UNIVERSIDADE NOVA DE LISBOA
Faculdade de Ciências e Tecnologia
Departamento de Engenharia Mecânica e Industrial

Laser welding of Shape Memory Alloys

Por: Luís Manuel Alberty Vieira

Dissertação apresentada na Faculdade de Ciências e Tecnologia da Universidade Nova de Lisboa para obtenção do grau de Mestre em Engenharia Mecânica

Orientadora: Prof.ª Doutora Rosa Maria Mendes Miranda

Co-orientador: Prof. Doutor Francisco Manuel Braz Fernandes

Lisboa

2010

Resumo

A necessidade de desenvolver técnicas avançadas de união para ligas com memória de forma tem-se revelado um assunto da maior importância, uma vez que as suas propriedades funcionais, nomeadamente o efeito de memória de forma e a superelasticidade, se revestem de enorme valor para aplicações actuais ou emergentes. De entre as ligas com memória de forma, o NiTi é a mais aplicada em campos tecnológicos tão diversos como a indústria biomédica, aerospacial e automóvel, o que se deve às suas características, como sejam: as elevadas biocompatibilidade e resistência à corrosão. Por estas razões, tem sido investigadas técnicas de ligação para estas ligas. No entanto, a sua ligação a outros materiais constitui um desafio cada vez maior permitindo explorar novos domínios de aplicação.

O principal objectivo deste estudo é compreender o efeito da soldadura laser em aspectos estruturais, mecânicos e funcionais, tanto em ligações similares envolvendo NiTi, como dissimilares. Foram produzidas juntas similares topo a topo utilizando um laser de Nd:YAG em modo contínuo e estudados os efeitos da direcção de laminagem na configuração de junta e dos parâmetros do processo nas caraterísticas das juntas. A soldadura dissimilar de NiTi com Ti-6Al-4V foi realizada com um laser de fibras operando em modo contínuo. Adicionalmente, soldaram-se arames de NiTi com aço inoxidável austenítico utilizando uma fonte laser de Nd:YAG operando em modo pulsado.

Foram projectados e produzidos sistemas de fixação e de protecção gasosa específicos para estas aplicações. Foram desenvolvidos e/ou adaptados métodos de ensaio para a avaliação da macro e microestructura, do comportamento mecânico cíclico e da capacidade de memória de forma. Utilizaram-se técnicas de análise como a Calorimetria Diferencial de Varrimento (DSC), a Microscopia Electrónica de Varrimento (SEM), EDS para identificação de espécies químicas e microdureza para avaliar as juntas soldadas.

Foram produzidas juntas soldadas sem defeitos de soldadura utilizando parâmetros de processo optimizados, as quais apresentaram elevada tensão de rotura (acima de 400 MPa), patamares superelásticos até níveis de deformação próximos de 8%, comportamento cíclico superior ao material base e fractura dúctil. Foi observada baixa tensão de rotura nas juntas dissimilares sobrepostas com aço inoxidável AISI 316LN, devido à fractura prematura pela zona afectada pelo calor, no lado do NiTi. Nas juntas topo a topo de NiTi com Ti-6Al-4V a zona revela uma estrutura de solidificação rápida do tipo dendrítica na qual se propagaram fissuras com origem em defeitos de soldadura, tais como falta de penetração.

Abstract

The demand of advanced joining techniques for shape memory alloys (SMA) has become of great importance, as their functional properties, namely shape memory effect (SME) and superelasticity (SE), present unique solutions for state-of-the-art applications. Among SMAs, NiTi is the most successfully used in various fields as biomedicine, aerospace and automotive applications, due to its unique properties such as biocompatibility and corrosion resistance. A significant effort form the scientific community, with improving results, has been put in joining NiTi in similar joints. However, the challenge is now joining NiTi to other materials, enlarging its fields of application.

The main objective of this study is to clarify the effect of laser welding in the structural, mechanical and functional behaviour of NiTi similar and dissimilar joints. Similar butt welds were produced using a continuous Nd:YAG laser source and both the effect of rolling direction and process parameters were studied. Dissimilar laser welding to Ti-6Al-4V was exploited by butt joining NiTi to this material using a Yb fiber laser source operating in continuous wave mode. Additionally, dissimilar welding of NiTi to Stainless Steel in wire shape was attempted using a Nd:YAG laser source operating in pulsed wave mode.

Special fixture and gas assist devices were designed and manufactured for laser welding. Testing methods were developed to evaluate the macro and microstructure, as well as the phase transformation temperatures, the mechanical single and cyclic behaviour and the shape recovery ability. Differential Scanning Calorimetry (DSC), Scanning Electron Microscopy (SEM), Energy Dispersive Spectroscopy (EDS), microhardness measurements, amongst other techniques were used to evaluate welded joints.

Optimized process parameters conducted to similar welded joints free of major welding defects presenting high ultimate tensile strength (above 400 MPa), superelastic plateaus up to strain levels close to 8%, superior cyclic behavior and ductile fracture. Dissimilar lap joints to AISI 316LN stainless steel exhibited low ultimate tensile strength due to premature fracture by the NiTi heat affected base material. The fusion zone of butt joints to Ti-6Al-4V was found to be mainly constituted by a rapid solidification dendritic structure in which cracks originated by welding defects, such as, partial penetration, were found to propagate.

Palavras-chave

Ligas com memória de forma, NiTi, Ti-6Al-4V, Aço Inoxidável, Soldadura laser, Nd:YAG, Laser de fibras, Superelasticidade, Efeito de memória de forma

Keywords

Shape memory alloys, NiTi, Ti-6Al-4V, Stainless steel, Laser welding, Nd:YAG, Fiber laser, Superelasticity, Shape memory effect

Agradecimentos

O autor gostaria de exprimir o seu mais profundo agradecimento aos seus orientadores, a Professora Doutora Rosa M. Mendes Miranda e o Professor Doutor Francisco M. Braz Fernandes, por toda a sua orientação científica, ensinamentos, por lhe terem proporcionado a oportunidade de integrar a equipa de um projecto de investigação, por lançarem os estudos nos meios da comunidade científica internacional e por último, mas não menos importante, pela sua amizade.

Por todo o apoio, o autor gostaria de agradecer ao fundo da FCT/MCTES para o projecto 'Joining micro to small scale systems in shape memory alloys using last generation infrared lasers' (PTDC/EME-TME/100990/2008).

Do grupo de Materiais Estruturais do CENIMAT, o autor dirige sinceros agradecimentos ao Dr. Karimbiri K. Mahesh, ao Professor Rui J.C. Silva, ao Mestre Luís Freitas, ao Dr. Corneliu Craciunescu e ao Professor Alexandre Velhinho, por toda a experiência laboratorial partilhada e pela recorrente disponibilidade para proceder a análises estruturais.

O autor gostaria de agradecer sinceramente ao Mestre Eurico G. Assunção pelo seu incansável apoio, particularmente durante a sua estadia em Inglaterra, em Maio de 2010. Um agradecimento é igualmente dirigido ao grupo de investigação de Engenharia de Soldadura da Universidade de Cranfield, nomeadamente aos Professores Stewart Williams e David Yapp, assim como ao Dr. Supriyo Ganguly, por disponibilizarem todos os materiais, equipamento e apoio técnico necessários à realização de ensaios de soldadura utilizando tanto um laser de Nd:YAG em modo pulsado como outro de fibras, em modo contínuo.

Uma palavra de agradecimento é dirigida ao Professor José Luís Ocaña, ao Dr. Dan Iordachescu e a toda a equipa técnica do Centro Laser da Universidad Politécnica de Madrid, por disponibilizarem a utilização de um laser de Nd:YAG com 3 kW operando em modo contínuo, bem como instalações e equipamentos para análise estrutural.

O autor gostaria de demonstrar o seu apreço ao Mestre Valentino Cristino do IST- Universidade Técnica de Lisboa pelo seu apoio na realização de ensaios preliminares de microdureza.

Do grupo de Materiais Electrónicos e Optoelectrónica, o autor gostaria de dirigir uma palavra de agradecimento à Professora Doutora Elvira M.C. Fortunato e ao Dr. Tito Busani pelas observações estruturais aí conduzidas, usando o equipamento de FIB.

Do grupo de Tecnologia Industrial do DEMI, o autor gostaria de exprimir a sua gratidão ao Professor Doutor J.J. Pamies Teixeira, à Mestre Carla M.M. Machado e aos técnicos de laboratório, os Srs. António G. Campos e Paulo Magalhães, por todo o seu apoio laboratorial, bem como amizade.

O autor não poderá deixar de referir o director do CEMUP, o Professor Doutor Carlos P. Moreira de Sá, bem como a responsável pelo laboratório de SEM da mesma instituição, a Dr.ª Daniela Silva, pela ajuda prestada na realização de observações em SEM e identificação de espécies químicas por EDS, em juntas dissimilares.

Por último, mas não menos importante, o autor deseja exprimir a sua mais honesta gratidão a todos os seus colegas e amigos que lhe dirigiram apoio e encorajamento, especialmente aos seu muito amigos, os Licenciados Paulo M. Ferreira, António G. Soares e o Mestre Daniel F. Martins.

Acknowledgements

The author would like to express his deepest gratitude to its supervisors, Professor Rosa M. Mendes Miranda and Professor Francisco M. Braz Fernandes, for all their scientific support, teachings, for giving the opportunity to be a part of a research team, for outputting the work in the scientific community, and at last, but not least, for their friendship.

For all support, the author would like to acknowledge the funding of FCT/MCTES for the project 'Joining micro to small scale systems in shape memory alloys using last generation infrared lasers' (PTDC/EME-TME/100990/2008).

From the CENIMAT Structural Materials Group, a sincere thanks to Dr Karimbiri K. Mahesh, to Professor Rui J.C. Silva, to the M.Sc. Luís Freitas, to Dr Corneliu Craciunescu and to Professor Alexandre Velhinho for all their laboratorial expertise and availability to perform structural observations.

The author would like to honest thank the M.Sc. Eurico G. Assunção for his tireless personal and technical support, especially during his journey to England, in May 2010. Thanks to the Welding Engineering Research Centre of the Cranfield University Professors Stewart Williams, David Yapp and Dr Supriyo Ganguly for providing all the materials, equipment and technical support needed to access laser welding using both Nd:YAG and Yb fiber power sources.

Sincere thanks to Professor José Luis Ocaña, Dr Dan Iordachescu and the technical staff of the Centro Láser at the Universidad Politécnica de Madrid for allowing the use of a 3 kW class Nd:YAG laser in continuous wave mode, as well as other facilities for materials analysis.

The author would like to show his appreciation to the M.Sc. Valentino Cristino from the IST-Technical University of Lisbon for his support accessing first microhardness measurements.

From the CENIMAT Electronic and Optoelectric Materials Group the author would like to acknowledge Professor Elvira M.C. Fortunato and Dr Tito Busani, for structural characterization done using the FIB equipment.

From the DEMI Industrial Technology Group the author would like to express gratitude to Professor J.J. Pamies Teixeira, the M.Sc. Carla M.M. Machado as well as to the technicians António G. Campos and Paulo Magalhães, for all their technical support and friendship.

The author can not forget the CEMUP director Professor Carlos P. Moreira de Sá and from the SEM laboratory, Dr Daniela Silva, for their help to perform structural SEM and EDS analysis on dissimilar joints.

At last, but not least, the author desires to express his most honest gratitude to all his colleagues and friends for their support and encouragement, especially to his great friends the bachelors Paulo M. Ferreira, António C. Soares and the M.Sc. Daniel F. Martins.

À minha mãe e à princesa Margarida

Contents

List of tables

List of figures

Abbreviations

A_f - Austenite finish temperature

A_s – Austenite start temperature

BPP – Beam parameter product

C^A – Austenite stress influence coefficient

C^M – Martensite stress influence coefficient

DC – Direct current

E – Young modulus/modulus of elasticity

E^A – Young Modulus of austenite

E^M – Young modulus of martensite

FPP – Focal point position

FZ – Fusion zone

HAZ – Heat affected zone

K - Quality laser parameter according to ISO 11149:1999

M^2 – Quality laser parameter according to ISO 11149:1999

M^d – Detwinned martensite

M_f – Martensitic finish temperature

M_s – Martensitic start temperature

M^t – Twinned martensite

MZ – Molten zone

NiTi – Nickel-Titanium intermetallic

OV – Overlap Percentage

P_b – Beam pressure

P_g – Gravity pressure

P_r – Recoil pressure

P_v – Vapour pressure

R – Deformed radius

R&D – Research and development

RD – Rolling direction

RSME – Measured shape recovery

SE – Superelasticity / Superelastic effect

SIM – Stress Induced Martensite

SMA – Shape memory alloy

SME – Shape memory effect

SS – Stainless Steel

T/t – Thickness

T_R – R-phase temperature

w – Width

γ – Y-axis coordinate / surface tension

ε_s – Bending strain

ε_x – Strain along x-axis

θ_f – Final angle

θ_i – Initial angle

ρ – Curvature radius relative to the neutral plane

σ_f – Detwinning finish stress

σ_s – Detwinning start stress

Nomenclature

BSE – Backscattered Electrons

DRX – X-Ray Diffraction

DSC – Differential Scanning Calorimetry

EBSD – Electron Backscatter Diffraction

EDM – Electrical Discharge Machining

EDS – Energy Dispersive X-Ray Spectroscopy

EELS – Electron Energy-Loss Spectroscopy

FIB – Focused Ion Beam

LASER – Light Amplification by the Stimulated Emission of Radiation

Nd:YAG – Neodymium-doped Yttrium Aluminium Garnet

SE – Secondary Electrons

SEM – Scanning Electron Microscopy

STEM – Scanning Transmission Electron Microscopy

TEM – Transmission Electron Microscopy / Transversal Electromagnetic Mode

TIG – Tungsten Inert Gas

Organizations

CENIMAT – Centro de Investigação de Materiais

DEMI – Departamento de Engenharia Mecânica e Industrial

FCT – Faculdade de Ciências e Tecnologia

UPM – Universidad Politécnica de Madrid

EWI – Edison Welding Institute

CU – Cranfield University

1. Introduction

Shape memory alloys (SMA) present a set of interesting characteristics for industrial applications though the complexity in obtaining and processing these alloys has limited its use in industry.

Nowadays industrial applications of SMAs are not comparable to conventional materials, mainly because difficulties come up when trying to machine them by conventional methods such as drilling, turning or milling, where significant tool wear is expected and partial degradation of material properties is almost inevitable. Advanced joining technologies for micromanufacturing and difficult-to-joint materials are required, as laser welding constitutes the first choice for welding SMAS, in both similar and dissimilar joints to other materials such as stainless steels and Titanium alloys.

Laser welding is on the market since the 70's and constitutes an efficient and accurate process that allows high rates of productivity with minimal thermal effect on base materials. However, despite advantages, laser welding of shape memory alloys is still challenging, requiring deep a study of its effects on functional properties, which requires extensive research work.

1.1 Motivation

It is fundamental that, in a near future, technology can provide effective production methods in order to place, definitively, shape memory alloys in the industrial context.

Before engineers responsible for product and process development may consider its application as a superior alternative to conventional methods, a strong effort in R&D work is still needed, to which this study aims to contribute.

1.2 Objectives

The aim of the present study, conducted within the framework of a FCT funded project, is to investigate the potential application of laser welding to join shape memory alloys either in similar and dissimilar joints for cutting-edge industrial applications.

Several laser beam sources, both in continuous and pulsed mode, were used to produce similar and dissimilar joints to stainless steel and Titanium alloys. The main scope of this study comprised the production and testing of NiTi similar joints, for which a process parameters study was developed and evaluation was performed aiming at structural, mechanical and functional characterization.

Preliminary studies in pulsed mode, which allows to better preserving material's properties, were conducted both on NiTi and Ti-6Al-4V regarding both similar and dissimilar joints. Several techniques, including Differential Scanning Calorimetry (DSC), Scanning Electron Microscopy (SEM), Energy Dispersive Spectroscopy (EDS) and uniaxial tensile testing, as well as, specially developed methods, were used to study the welded joints.

1.3 Thesis structure

This thesis is structured in six chapters. The first chapter contextualizes the study by presenting an introduction, as well as, the author's motivation and its objectives. In the second chapter a comprehensive presentation of shape memory alloys is done, in order to give background to understand the particularities of these nonconventional materials. The main types of shape memory alloys are presented and the thermoelastic martensitic transformation is introduced as the basis of their functional properties.

The third chapter addresses the state-of-the-art processes for joining shape memory alloys, and is specially focused on laser welding. Basic concepts are introduced and literature results concerning both similar and dissimilar joints are presented. The fourth chapter is devoted to the experimental set-up, and to the experimental approach, including test methods.

In chapter five results are presented alongside its discussion, keeping the logical order of the previous chapter, including structural observations attained by microscopy, tensile testing, fracture results and the identification of phase transformation temperatures, when applicable. Finally, in chapter six, conclusions are presented and identified further research needs.

2. Shape memory alloys

2.1. Introduction to SMAs

In literature, Shape Memory Alloys (SMAs) are categorized as “advanced materials”, alongside with composite materials, ceramics and others. In an industrial context they are known as functional materials, due to their peculiar and attractive properties such as Shape Memory Effect (SME) and Pseudoelasticity, which includes the Superelastic Effect (SE).

There are several types of SMAs. However, the NiTi alloy system which exhibits a thermoelastic reversible transformation, known as ‘martensitic transformation’ is the most widely studied and applied, and therefore, particularly the equiatomic NiTi alloys, for high performance to corrosion and fatigue. The martensitic transformation can be induced under specific conditions either by thermal or mechanical routines.

Although applied since the 70’s, some difficulties related to SMAs must be overcome, so that they can reach their full potential. Compared to conventional alloys such as steel and aluminum, they are still relatively expensive, mainly due to the nobility of some constituents, like Ni, Ti, Nb or Co. Aspects related to low workability and high sensibility to production parameters also contribute to increase production costs and must be overcome in a near future.

Despite these aspects, as consequence of R&D efforts, Shape Memory Alloys had been used with increasing success in a number of industrial fields, namely biomedical, automotive, aeronautical and many others of high added value, with incomparable advantages.

2.2. Historic review

Functional properties of SMAs, namely the Shape Memory Effect (SME) was, according to Otsuka and Wayman [1], first observed in Au-Cd alloys by Kurdjumov and Khandros in 1949, which introduced the martensitic transformation as a reversible thermoelastic process, different from the one found in the Fe-C system.

From 1951 to 1953, Chang & Read reported the same behaviour and its reversible nature on diffusionless transformations observed for a similar alloy system in 47.5 %Cd [2 to 4]. The shape memory effect remained unheralded until it has been discovered in NiTi by Buehler *et al.* at the Naval Ordnance Laboratory, in 1963 [5]. A near composition NiTi alloy was then named Nitinol, and has been used with great success in engineering since then.

SMAs were introduced to Orthodontics in 1972 by Andreasen *et al* [6], who proposed the use of superelastic Nitinol wire for the first time. Yet, in the 70’s, high temperature SMAs were developed

by alloying Ti with Pd, Pt and Au, obtaining higher transformation temperatures (>100 ºC). In the 80's, SMAs found other applications in medical purposes as Orthopedics, Radiology and guidewires technology [7]. In late 90's, NiTiCu alloys showed improved fatigue life attractive for cyclic applications [8].

Nowadays, new challenges for SMAs come from aerospace and energy industries, for actuators in tough applications involving high temperature and hostile environments. The use of SMAs as biomaterials for biomedical applications is another challenge.

2.3. Types of SMAs

A large family of SMAs has been growing since its first investigations in 50's, by alloying with different elements and attaining unique behaviors. A wide variety of properties is now available for almost any design requirement. SMAs are first classified by alloying elements, but operation temperature and desired behavior, beyond trade names are also common. The main types of SMAs according to composition are presented.

2.3.1. NiTi-based SMAs: Fe, Cu, Nb, Pt, Hf, Pd, Zr, Au, Co, Al, Mn and Cr alloyed

NiTi was first introduced with Nitinol and is known by its shape memory effect (SME), both one-way and two-way shape memory effect, as well as superelasticity. Due to its high resistance to corrosion and biocompatibility, has been used in biomedical applications with great success.

NiTi is in fact an intermetallic that exists at room temperature in a very narrow band of chemical composition - figure 2.1. The percentage of Ni is according to [9] known to change the transition temperatures above the equiatomic composition as shown in figure 2.2. Namely, on Ni-rich alloys, the increase of Ni percentage causes a drastic decrease of transformation temperatures. For Ti-rich alloys, composition does not affect the transformation temperatures, which can be explained by the solubility limit exhibited on the Ti-rich side of the Ti-Ni phase diagram depicted in figure 2.1 .

Ni-Ti alloys are commercially available in wire, strip, rod, bar and sheet, as well as foam and sintered powder. High % Ni has recently proven to enhance corrosion performance in harsh environments when compared to stainless steels. Third alloying elements often lead to considerable properties modifications, such as on transformation temperatures. Figure 2.3 summarizes the effect of third element on transformation temperatures, according to Otsuka and Ren [9]. It can be observed that alloying elements tend to decrease transformation temperatures, although Zr, Au, Pt, Hf and Pd conduct to higher transformation temperatures, so, in a wide alloying perspective, Pt, Hf and Pd are pointed out as candidates for high temperature shape memory alloys.

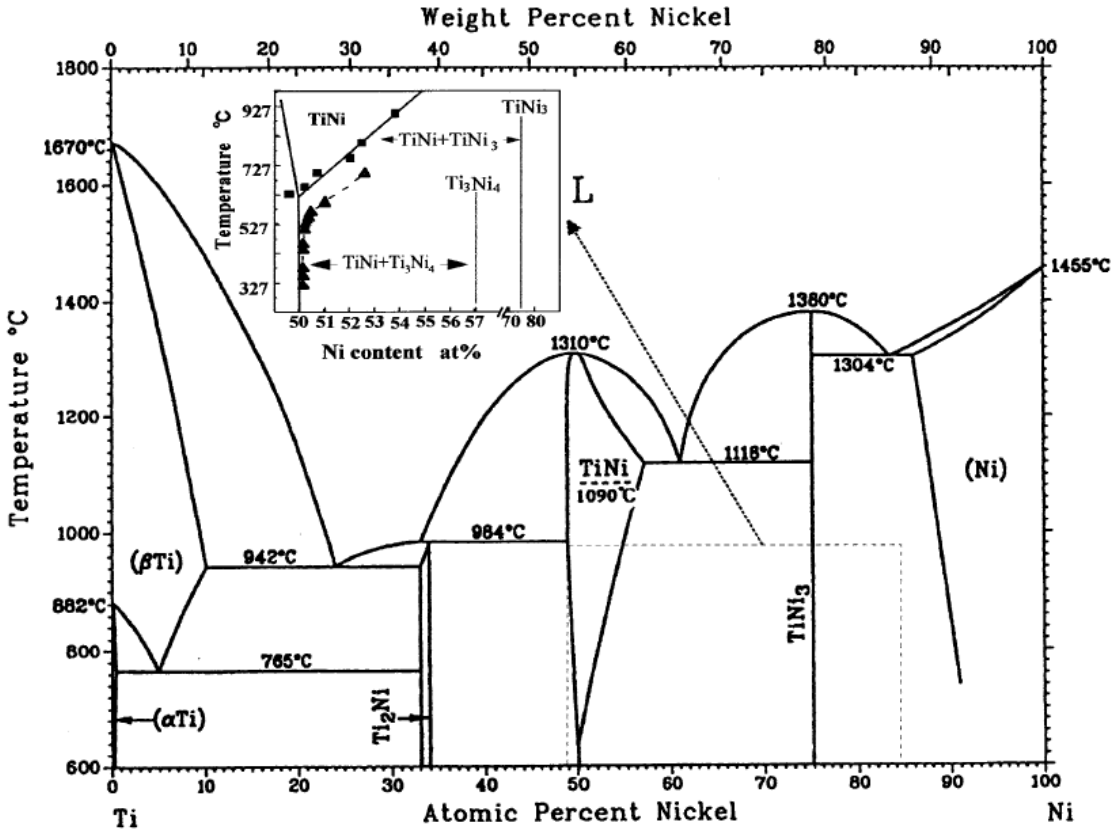

Figure 2.1 Binary Ti-Ni phase diagram [9]

Alloying elements can not only affect transformation temperatures, but also both the products and path can be affected. The addition of Fe leads to a two-step martensitic transformation, with the intermediate R-phase, instead of the typical single-step austenite to martensite transformation. The addition of Cu reduces the sensitivity of the transformation temperatures to composition, which are usually very high, allowing exploring shape memory effect around room temperature, making those alloys a usual choice to high force actuators, with copper contents between 5 and 10 %. In fact, in a hypothetical application, it is estimated that it would be necessary a modern DC brushless electric motor with a mass 5 to 10 times that of a SMA actuator, to perform the same amount of work.

Unlike when alloying with Cu, SMAs alloyed with Nb present high thermal hysteresis and, as a consequence, low response to wide temperature variations. This aspect makes these alloys suitable to be deformed at low temperatures and heated up to room temperature, without phase transformation. Alongside NiTis alloyed with Pt, Hf and Pd, are SMAs with high transformation temperatures (>100-800 ºC) that exhibit stable material properties. Unlike common NiTi alloys, their high cost, due to alloying elements like palladium and platinum, prevent them to become commercial. Furthermore, these alloys are limited by low transformation strains below 3 % due to low critical stresses for slip.

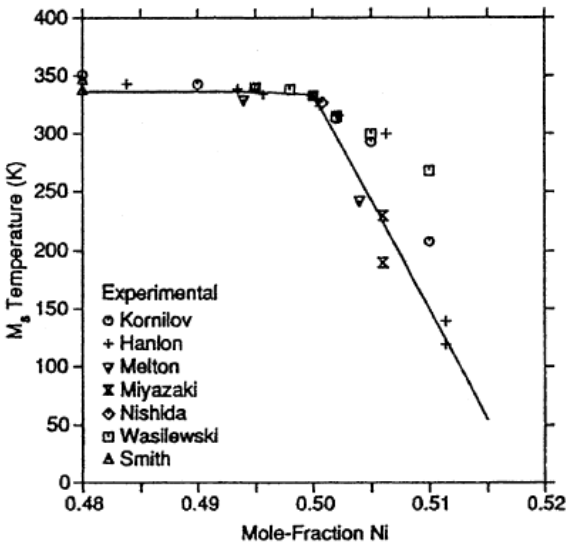

Figure 2.2 Influence of the Ni content on Ms temperature of NiTi binary alloys, according to different authors (points) and according to thermodynamic calculations (line) [9]

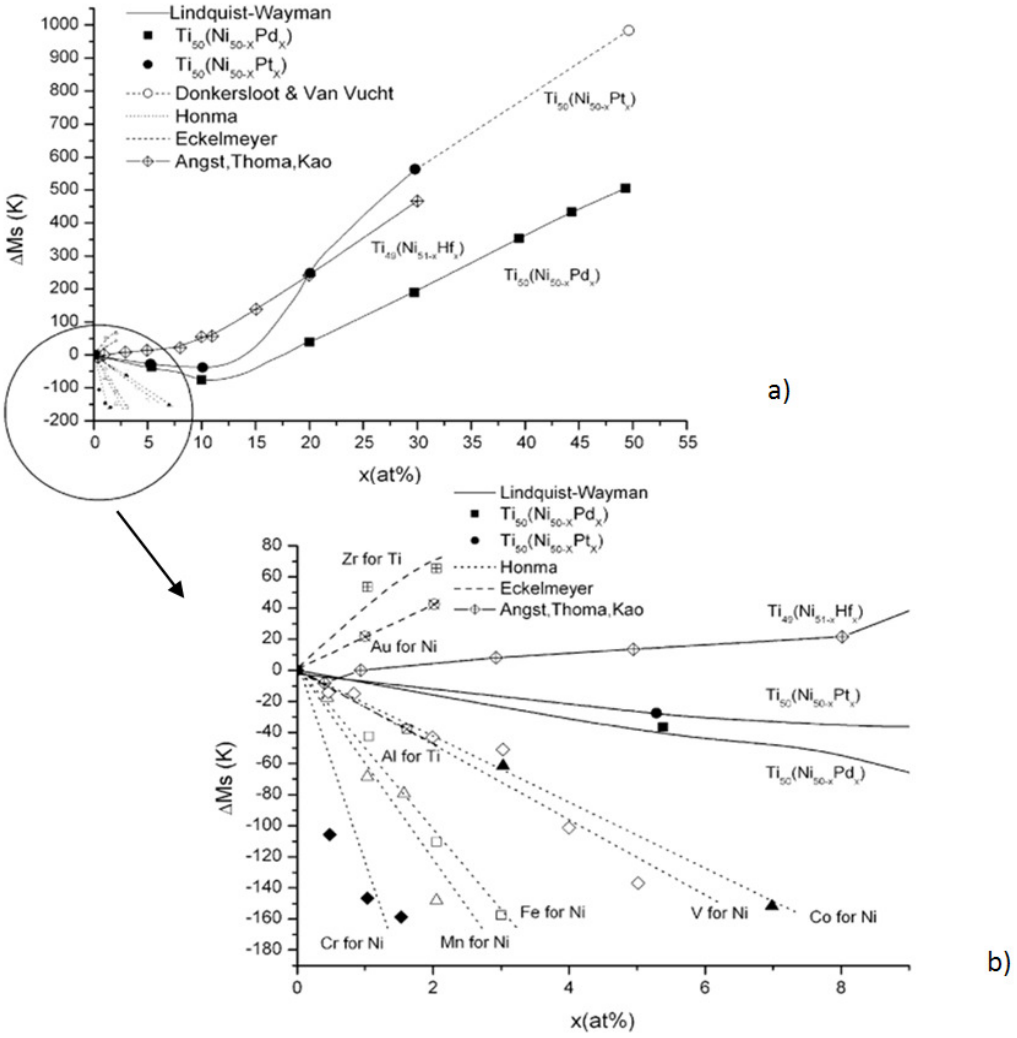

Figure 2.3 The effect of alloying elements Pt, Hf, Pd, Zr, Au, Co, V, Al, Fe, Mn and Cr on transformation temperatures of the binary Ni-Ti system: a) general view; b)detail of the previous. Adapted from [9]

2.3.2. Cu-based SMAs: CuZnAl and CuAlNi

These are less expensive than Ni-Ti based alloys and show less hysteresis and transformation temperatures highly dependent on the composition. They are an attractive alternative when good electrical and thermal conductivity are required, as well as good formability.

CuZn binary system shows good resistance to intergranular fracture due to its high ductility. They are austenitic at room temperature and the addition of Al result in increasing transformation temperatures (Ms may vary from -180 ºC to +100 ºC). Due to the tendency of the parent phase to decompose when overheated, they are limited to operating temperatures of about 100 ºC and stress levels of around 200 MPa, as a consequence of low critical stress for slip, reinforcing ductile behaviour.

Like CuZnAl alloys, changing the Al or Ni content on CuAlNi, the transition temperatures vary. Despite these variations, hysteresis remains constant. CuAlNi SMAs exhibit poor cyclic behaviour and ductility, leading to intergranular cracking, and frequently Al is replaced by Mn to increase ductility. Compared to CuZnAl, CuAlNi alloys reveal superior stability at high temperatures.

2.3.3. Iron-based SMAs: Mn, Si, Ni, Cr, Ti and Nb Fe-based alloys

Iron-based shape memory alloys have recently attracted much attention mainly for presenting high mechanical strength and good formability at low cost. Despite the advantages, these alloys are limited on functional properties. Shape memory effect can only be observed after thermomechanical training, involving several cycles of deformation and annealing under tension. A Fe-32Mn-Si SMA studied by Bouraoui *et al* [10] revealed transformation strains of about 4%, however superelasticity in never observed on Fe-based SMAs. Cold rolling and precipitation of both NbC and TiC are known to enhance shape memory performance on Nb and Ti containing alloys, as reported by [11].

2.4. Thermoelastic martensitic transformation

A Martensitic transformation is responsible for the shape memory effect (SME) and Superelastic Effect (SE) of SMAs. Unlike conventional materials, where it is possible to identify a point at which the atomic structure of crystals is permanently displaced during deformation, when deforming a SMA an internal displacement change in the crystal structure occurs (by shearing). This reversible phase transformation does not occur by diffusion, producing a constituent known as martensite from the austenite parent phase. This new phase has a different crystal structure and, therefore, different properties. In the binary Ni-Ti system, the martensitic transformation from B2 austenite → B19' martensite can occur either on one-step or two-step modes, dependent on composition and thermal or thermomechanical treatments, such as quenching and rolling [9,12].

The formation of martensite in a two-step transformation from the parent phase is presented in the schema of figure 2.4, in which the intermediate R-phase (b) is formed by shear of the parent B2 (110) planes along direction $[1\bar{1}0]_{B2}$. The martensite is attained from the R-phase by shear of B2 (001) planes, also along direction $[1\bar{1}0]_{B2}$.

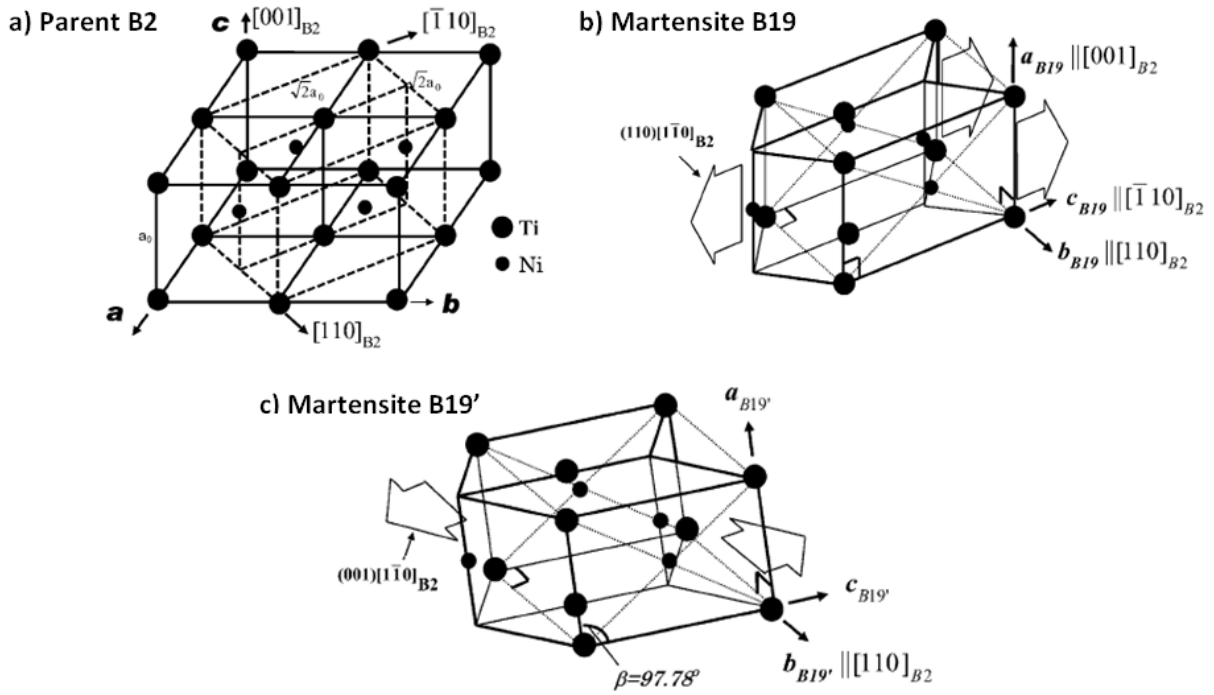

Figure 2.4 Crystallographic structures of a) Austenite – ordered B2, b) R-phase – orthorhombic B19 martensite and c) martensite – monoclinic B19' martensite. Adapted from [9]

Martensite can be formed through a series of crystallographic shear directions. Variant is the designation given to the orientation direction of each martensite crystal formed during the martensitic transformation. Two forms of martensite can be formed according to their variants assembly: twinned martensite, M^t, in which opposite shears from opposite variants cancel, and the macroscopic shape of the crystal block is preserved by forming a self-accommodating structure; detwinned martensite, M^d, in which a particular variant is dominant and, as a consequence, the shape is not preserved. Figure 2.5 a) and C) present a schema of the martensite conditions mentioned.

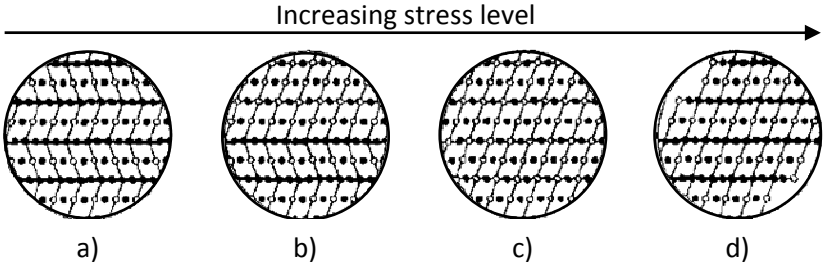

Figure 2.5 Microstructural changes on stressed NiTi: a) twinned martensite, b) partially twinned martensite, c) detwinned martensite and d) slipped martensite. Adapted from [13]

The martensitic transformation may occur only by temperature change, under zero stress, and four characteristic temperatures are associated with phase transformation: A_s, austenitic start temperature; A_f, austenitic finish temperature; M_s, martensitic start temperature and M_f, martensitic finish temperature. In the case of two-step transformations, the R-phase transition occurs at a temperature T_r, between M_s and M_f.

Upon cooling, a crystal structure which is initially austenite at $T>A_f$, starts changing to twinned martensite below M_s - figure 2.5 a) and finishes phase transformation at M_f. Two situations may occur: If a stress is applied, due to the mobility of martensite boundaries between variants the orientation of martensite crystals changes, choosing a set of variants that best accommodate the direction of resulting strain. Then detwinned martensite begins to be formed - figure 2.5 b) when $\sigma>\sigma_s$, being σ_s the detwinning start stress, and ends when the stress level is higher than the detwinning finish stress, $\sigma>\sigma_f$, not preserving the initial shape of the parent-phase - figure 2.5 c). Instead, if temperature rises, the reversal martensitic transformation occurs and the parent-phase, austenite, begins to be formed at $T>A_s$, finishing at $T>A_f$ and preserving the initial macroscopic shape.

2.5. Functional properties of SMAs

SMA's special properties are shape memory effect and Pseudoelasticity. Shape memory effect is a functional property and can be present as one-way shape memory effect, if shape recovery occurs upon heating, or as two-way shape memory effect, if also exhibited upon cooling. Two-way shape memory effect is attained by thermomechanical training. Pseudoelasticity also aims a functional property, the superelasticity or superelastic effect, and the rubber-like effect.

Shape memory effect can be observed on SMAs in general, either austenitic or martensitic at room temperature. However, superelasticity based on stress-induced transformation is only attainable starting from the parent phase.

2.5.1. Shape memory effect (SME)

In the previous case of stress applied to twinned martensite, with shape change after releasing the load due to formation of detwinned martensite, it is possible to fully recover the original shape, being only necessary to heat the alloy to a temperature above Af, according to the reverse phase transformation, from detwinned martensite to austenite. The process described above, caused by a mechanical load high enough to detwinn martensite followed by heating up to the parent phase, is the so-called Shape Memory Effect (SME), also referred in literature as one-way shape memory effect, and is schematically presented in figure 2.6.

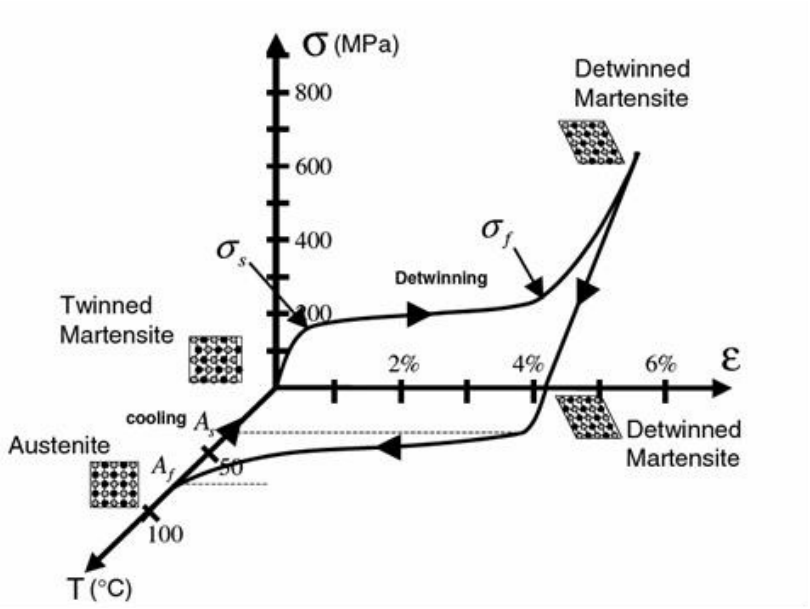

Figure 2.6 Schema of shape memory effect in a shape memory alloy. Adapted from [14]

To understand all possible transformation paths involving the martensitic transformation in a stress-temperature domain, for a given SMA with a particular composition and characteristic σ_s, σ_f, M_f, M_s, A_s and A_f, the following phase transformation diagram can be used:

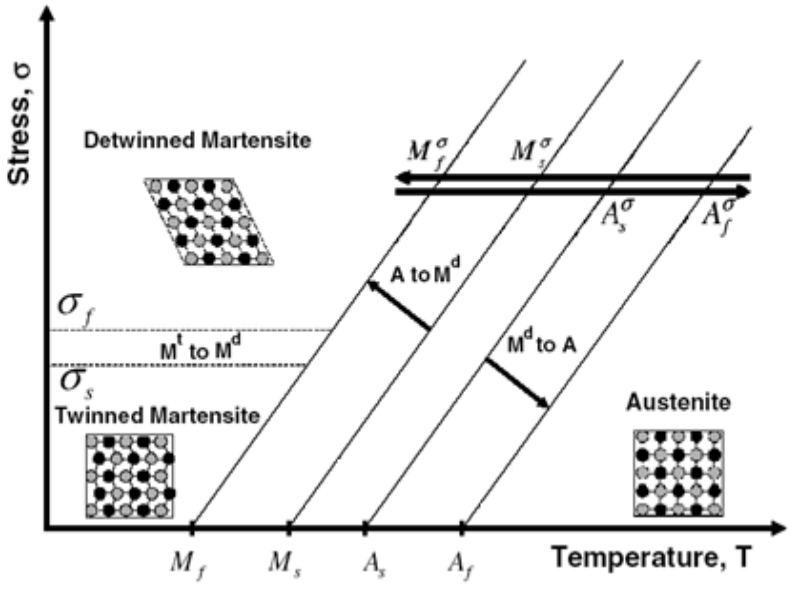

Figure 2.7 Phase transformation diagram of a SMA. Adapted from [14]

2.5.2. Pseudoelasticity and superelastic effect (SE)

Considering figure 2.7, it can be observed that, for a constant temperature in the parent-phase, it is possible to accomplish the martensitic transformation by just applying a mechanical load high

enough to overcome the martensitic finish transformation stress, at that temperature. The result of such load is stress-induced detwinned martensite with shape modification. This path is schematically presented in figure 2.8.

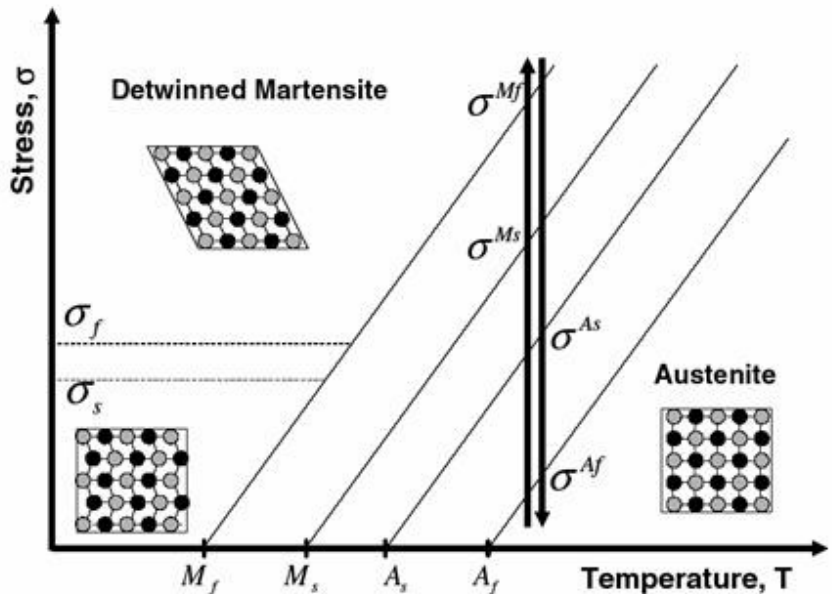

Figure 2.8 Schema of superelastic effect. Adapted from [14]

Since the thermoelastic martensitic transformation is a reversible process, if the stress level is lowered below $\sigma_{Af|T}$ by relieving the applied load, the reverse transformation occurs due to thermodynamic destabilization of martensite, and the original parent phase shape is recovered. The behavior described above is known as superelasticity, or simply, as superelastic effect. This effect can be represented in a stress-strain diagram, in which is possible to identify a hysteresis behavior (figure 2.9). The upper plateau occurs during the stress-induced martensitic transformation and the lower during the reverse transformation when unloading. The superelastic effect, as a functional property, make SMAs interesting for some specific applications when compared to conventional alloys, either for the large recoverable strains, or for the constant stress levels, or both.

In figure 2.9 the martensitic transformation in the NiTi shape memory alloy, Nitinol, is clearly identified by a change in the curve slope. Before and after the martensitic transformation the material behaves elastically, first as austenite and then as martensite, with different modulus of elasticity, E^A and E^M, respectively. In the stress-strain domain, the area between the two curves represents the energy dissipated in every complete cycle of transformation. Figure 2.10 shows, in a lattice perspective, the difference between the deformation mechanisms of a conventional stainless steel, which accommodates higher stress levels by irrecoverable slip, and a superelastic NiTi alloy, that accommodates higher deformation in a reversible process by shifting to twinned martensite.

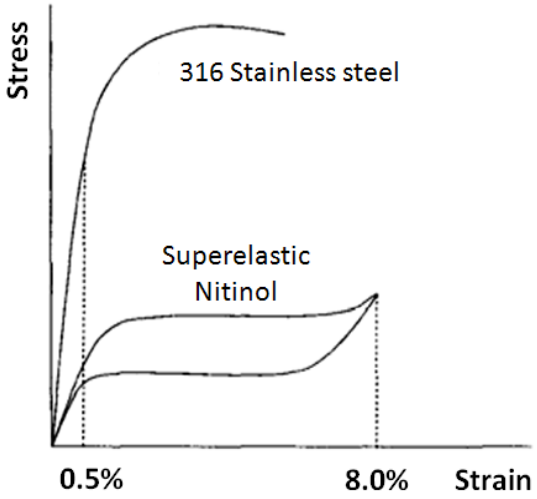

Figure 2.9 Stress-strain curve of conventional vs. superelastic alloys. Adapted from [15]

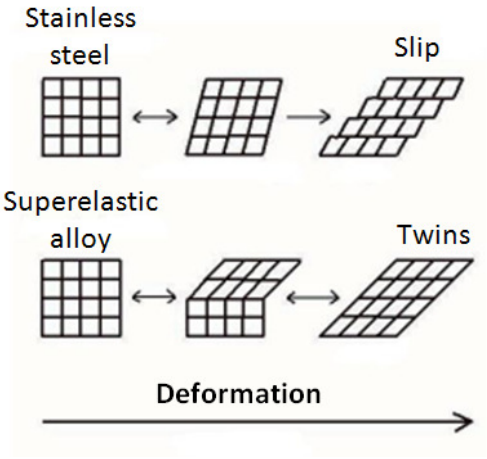

Figure 2.10 Schematic representation of lattice changes on stainless steel and NiTi caused by outer stress. Adapted from [16]

2.6 Training SMAs: two-way shape memory effect

For some particular applications of SMAs, it is required a repeated behavior under cyclic thermal loads. As a consequence, for a given SMA just two states should be clearly shown: one at low temperature and the other at high temperature, with different associated shapes.

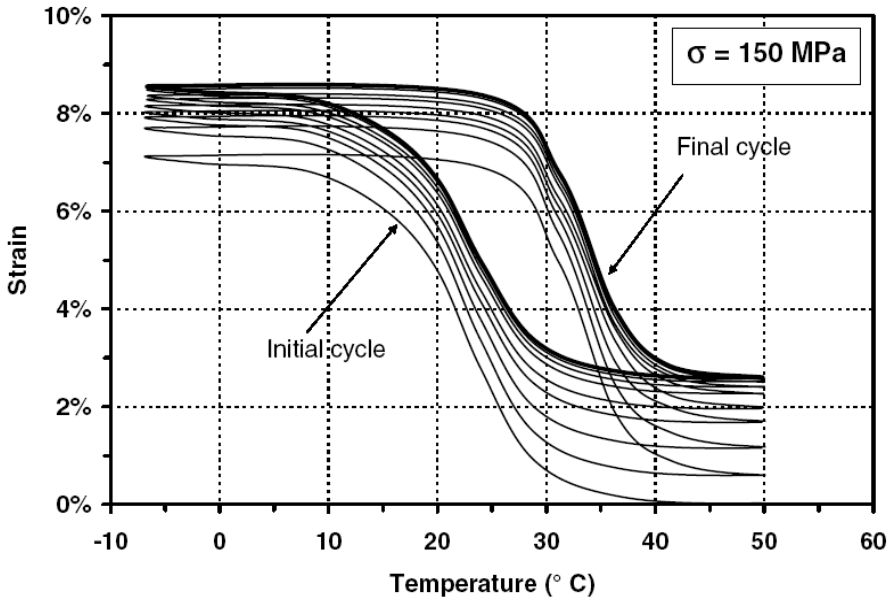

Figure 2.11 Training of a NiTi SMA. [14]

This behavior, known as two-way shape memory effect, is not a standard feature of commercial SMAs. It is achieved after a training process that consists of applying a large number of repeated

thermomechanical cycles, along a specific path. This training process causes changes in the microstructure to a desirable macroscopic behavior, achieved by material's hysteretic response stabilization, due to the absence of additional accumulation of inelastic strain, after a given number of cycles.

In fact, the two-way shape memory effect is a consequence of creating such an internal residual stress state that privileges determined variants during the martensitic transformation. As a consequence of such dependence, any change in the internal stress state will cause detraining (overloading, for example), effect known as 'amnesia'. A training process for a NiTi SMA wire at constant stress under thermal cycling loading is shown in figure 2.11.

2.7 Applications of SMAs

Shape memory alloys find applications over a wide range of industries, but successful applications are restricted to small added value markets in fast growing. The main reason is a lack of engineering techniques outside those markets, due to technical difficulties in scaling up techniques and materials, as well as, due to the difficulty of immediate visible benefits. However, the list of applications of SMAs has increased enormously during the 90's, which resulted in production increase and cost decrease. NiTi is by far the most applied SMA since it exhibits some of the most useful characteristics in terms of its active temperature range, hysteretic performance, recoverable strain and relatively simple thermal processing. This material is commercially available, however, its production is small compared to other metal commodities, as result of difficulties in the production process. Although its small production, most current applications require small amounts of material, increasing its viability.

2.7.1 Biomedical applications

The interest of the biomedical community on NiTi relies on its unique combination of shape memory effect, superelasticity and good biocompatibility, to fulfill demanding applications as for invasive surgical applications, amongst others. In this field, there is a need for joining technologies as laser welding to produce components in a micro scale [17].

Some successful applications reported are: Endovascular stents to expand blocked conduits in the human body introduced in a small and deformed shape that expands to an appropriate one in place - figure 2.13; vena-cava filters used in one of the outer heart chambers to trap blood clots introduced in a compact cylindrical form about 2.2 mm in diameter that in place is released to an umbrella shape – figure 2.14 ; strips to apply gentle outward pressure to small incisions to access the heart [7].

Figure 2.12 Orthodontic constant force wire [18]

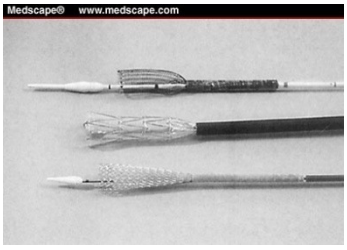

Figure 2.13 Endovascular stents [19]

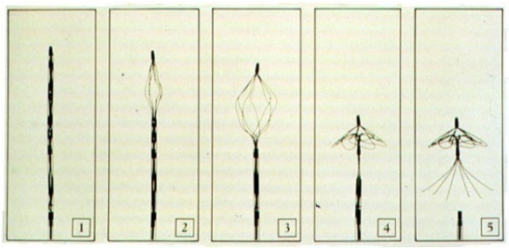

Figure 2.14 Simon filter: left –cylindrical shape; right – filter shape [20]

One of the first applications of NiTi, to orthodontics, is still a very promising and fast growing field. Combining NiTi with other non-smart materials allows obtaining selective components able to control the force applied on each teeth - figure 2.12, resulting in a superior and more effective therapy. The interest of joining different materials, e.g. SMAs and biocompatible stainless steels exists for biomedical applications.

2.7.2 Aerospace applications

Aerospace industry is well known for demanding state of the art materials and technologies and shape memory alloys are already employed with great success in specific demanding applications. They were used to create shrink-to-fit Nitinol metal couplings to join the hydraulic tubing of the F14 fight aircraft, which is made of titanium alloys and present poor weldability – similar to figure 2.15.

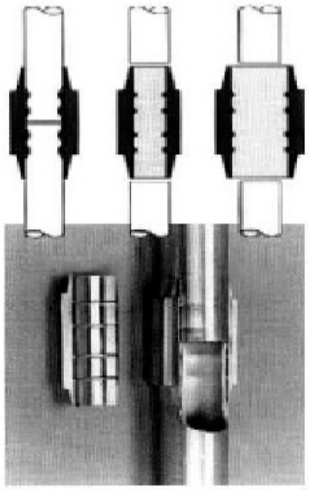

Figure 2.15 Schema of piping with shrink-to-fit NiTi metal couplings [21]

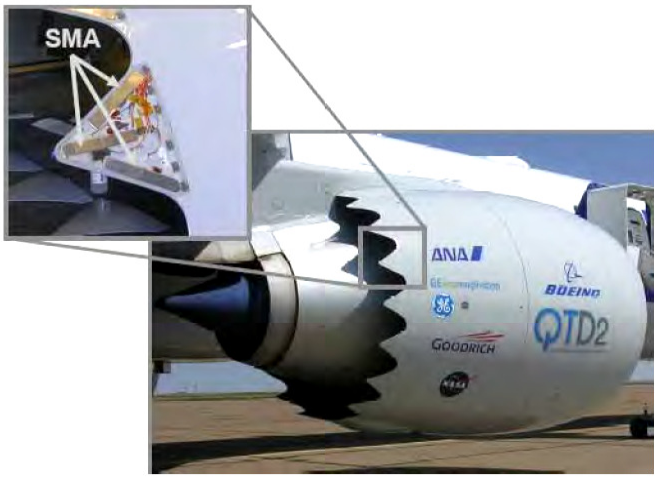

Figure 2.16 Commercial aircraft aero-engine showing adaptive serrated nozzle actuated by SMAs (top) [14]

Efforts are being made in the aerospace industry to implement SMAs in a large scale, with special interest in adaptive serrated nozzles for aero-engines that reduce noise pollution [22, 23]. Boeing,

General Electric Aircraft Engines, Goodrich Corporation, NASA and All Nippon Airways (ANA) developed a variable geometry chevron for jet noise reduction using SMAs (figure 2.16).

Smart materials lead to new design concepts, allowing fully integrated and distributed actuation by means of simple mechanisms that do not add weight.

Many other applications are being studied like the unique-body aircraft wing, without servo mechanisms including moving parts, only actuated by Nitinol wires introduced to create a highly flexible structure that is adjustable by remote current control. Made of a single continuous body, it reduces problems like the separation of the boundary layer. SMAs that resist to high temperatures like NiTi(Hf), NiTi(Nb), NiAl and Fe-based systems are also quite interesting and are under extensive research for aerospace applications.

2.7.3 Metalworking and automotive applications

A curious and simple engineering solution was developed by Predki *et al* [24] in Germany to adjust the clearance of taper roller bearings using SMAs and their extrinsic two-way effect ('fake' two-way effect). Bearings technology demand constant axial play and constant pre-loads, but thermal expansions between the inner and outer rings usually lead to a loss of pre-load or decreasing of axial play, leading to bearing failure. The solution, presented in figure 2.17 regards the bearing adjustment by axial movement, clamped between steel springs and NiTi specially trained elements.

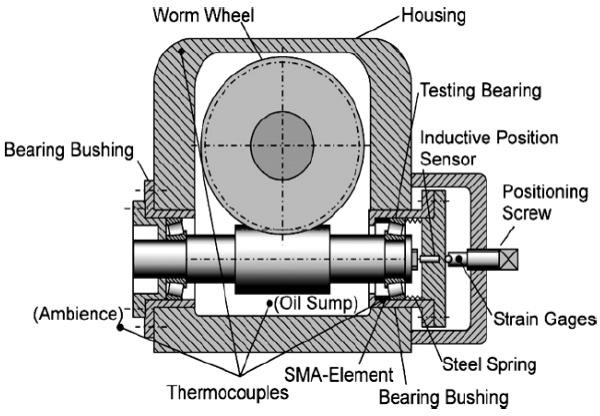

Figure 2.17 Worm gear with bearing bushings for clearance adjustment [24]

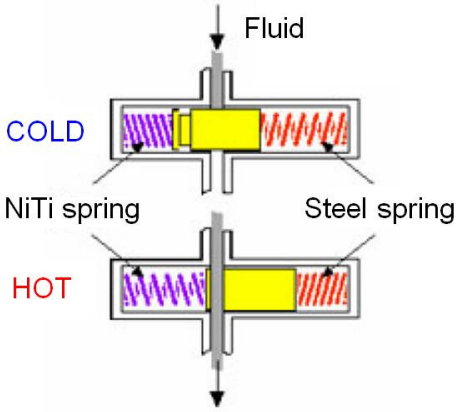

Figure 2.18 Thermostatic governor valve for shifting pressure control in automatic transmissions [25]

Figure 2.18 shows an automotive component that works on the same principles, using the shape memory effect to actuate a temperature dependent fluid valve. Although not visible, nowadays cars include a series of mechanisms actuated by SMAs. Figure 2.19 presents a number of applications of electrical SMAs actuators on automobiles: 1) foglamp adjustment; 2) engine hood latch; 3)

retractable headlight; 4) carburetor regulator; 5) engine control; 6) transmission control; 7) climate control; 8) wiper contact control; 9) mirrors adjustment; 10) seatbelt adjustment; 11) central latch; 12) shock absorber adjustment; 13) filler inlet lock; 14) trunk lock .

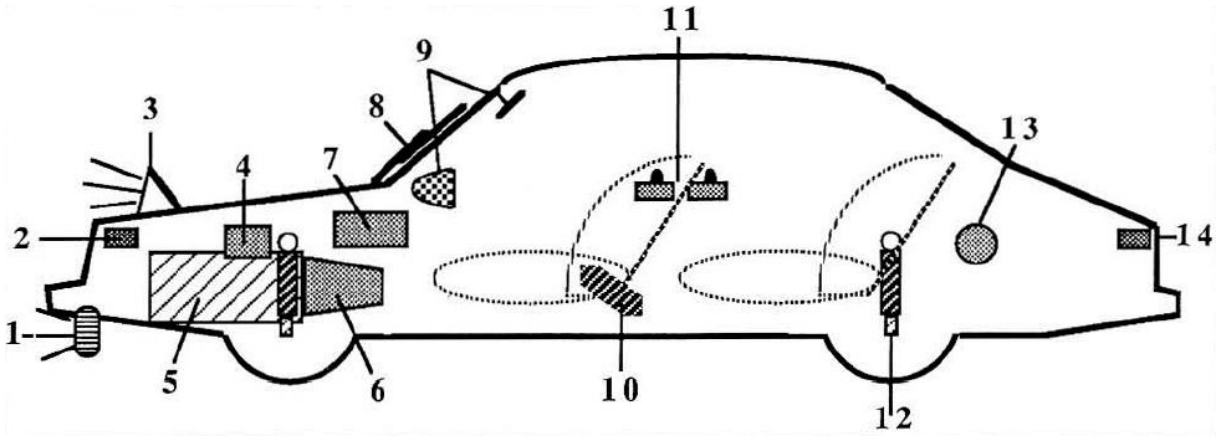

Figure 2.19 Application of electrical SMA actuators in automobiles [26]

2.7.4 Civil construction applications

Nowadays, Civil Engineers know that it takes more than just meeting the needs of functionality and load carrying under static conditions to design and build civil structures. The increasing demand of structures highly adaptive to changes in use, revealed the great potential of SMAs to enhance them. These pre-existing and new applications are being developed in field of civil engineering for damping, active vibration control and prestressing or post-tensioning of structures with fibers and tendons. Regarding these fields, according to Janke *et al* [27], Fe-based SMAs are refered as potential low cost alloys, in order to enhance viability in future applications.

2.8 Final note on this chapter

In this chapter a synthesis of SMAs types, characteristics and fields of application was presented. This is a growing area in terms of research in new types of alloys, as well as, on new applications. So, processing of these alloys is a major issue, in both producing techniques as melt spinning, powder metallurgy, etc., as well as, on joining, cutting and shaping for producing final products at acceptable costs.

3. Joining SMAs

3.1. Overview

The low workability of SMAs by conventional machining processes and their increasing application demands suitable joining techniques in order to obtain complex components.

In the last two decades the number of experiments reported in the literature concerning welding and joining techniques of shape memory alloys increased significantly. Traditional welding processes were mainly tested, but the increasing demand to perform more and more demanding tasks lead to the employment of state of the art technologies, like laser beams, which are revealing very promising results.

Welding SMAs is a challenge when compared to conventional welding techniques performed on steels or other well known alloys. Unlike those materials, SMA's response, mechanical properties and corrosion resistance are strongly dependent on chemical composition, microstructure and transformation temperatures between the base material and the joint region.

Dissimilar metal welds are in many aspects different from similar ones. Base material thermo-physical properties are usually different, leading to different heat transfer. During the process, composition varies across the weld pool, and it is not clear the interface between solid-liquid phases. Intermetallic compounds are formed and exotic convection processes may occur when base metal densities vary significantly. First studies about dissimilar weld of Ti and Ni conclude that results are strongly limited by the formation of brittle intermetallics that lead the weld to crack. Embrittlement occurs mainly due to high temperatures reaction of elements such as oxygen, nitrogen and hydrogen. Brittle intermetallics like Ti_2Ni and Ti_3Ni can also precipitate during solidification, having adverse effects on strength and shape memory characteristics.

In order to fulfill very specific needs of the medical industry, some welding experiments on dissimilar joints like NiTi/stainless steel or Hastealloys were performed. In the aerospace industry new parts, like gas turbine nozzles are being tested using NiTi and Ti-6Al-4V. They were previously joined by fasteners, but new methods are being developed to be integrally bonded [22].

Although previous studies on welding dissimilar joints involving SMAs created some pessimistic perspectives, a good solution has not yet been found. The main reasons that difficult weld joining are, as already referred, always related to overheating. Temperatures above the melting point and composition variation within the alloy, affect the SMAs performance.

As already identified by Chau *et al* [22], the development of new welding techniques to produce high strength joints between materials like NiTi and Ti-6Al-4V alloys is essential for the adoption of these materials in the aerospace industry.

3.2.Friction welding and resistance butt-welding

Friction welding is a solid state welding process that allows good control and prevention of grain growth and oxidization, so good mechanical properties can be achieved. However, when using this method, heat treatments are needed after welding in order to minimize the variation of transformation temperatures between the welds and the base metal.

First tests on resistance butt welding were performed in 1982 using thin wires of Ti-50 at. % Ni, welded without fusion or cast zone, in Japan [28]. The experiment consisted of feeding the welded parts (with little offset) with a welding current of 385-600 A during a short period of time, while applying a constant force between 50 and 200 N. The axial force during process closes possible grain boundary cracks, as well as oxidization is prevented by extrusion of the fusion zone. The shape memory effect of the welded part remained the same, and the tensile strength was about 80% of the base material. However, butt-weld joints require some work to trim extrusions and complex geometries are not allowed.

3.3. Tungsten Inert Gas – TIG

This welding technique usually causes an extended heat affected zone (HAZ), due to heat input delivered during the process. So, significant degradation of weld mechanical properties are frequently observed, as reported by Ikai *et al* [29].

Qiao *et al* [30] investigated the microstructure of the HAZ of a TIG welded Iron-based SMA (Fe-Mn-Si-Cr-Ni),using scanning electron microscopy (SEM) and X-ray diffraction, and reported no noticeable changes face to base material. The effect of welding on shape recovery was also examined by bending tests, leading to conclude that the TIG welded alloy exhibited almost the shape memory effect ability of the base material.

3.4. Ultrasonic welding

When joining SMAs the main key to success is basically to keep temperatures low, to minimize changes in the base material. Ultrasonic welding is a simple and promising technique that allows to control with great precision temperature peaks around the welding spots.

Budau *et al* [31] tested ultrasonic welding on bulk and ribbons made out of SMAs (Cu-Zn-Al & Ti-Ni-Cu), with similar and dissimilar materials, concluding that macrostructurally the weld are feasible.

Microstructural observations showed a good interface for bulk joints, but damages of the ribbons related to the welding process, as consequence of inappropriate welding parameters.

3.5. Plasma welding

Experiments with plasma welding of NiTi SMAs on similar and dissimilar joins were reported by Eijk *et al* [32] in 2003 and concluded that the welding process didn't affect the Ni/Ti ratio in the weld, on similar NiTi joints. However, the phase transformation temperatures changed, while the mechanical properties degraded. This study also revealed extreme difficulty to weld dissimilar joints of NiTi to stainless steel, due to brittle phase formation close to the fusion line, as NiTi tends to absorb elements from the steel.

3.6. Laser welding

3.6.1 Overview

Until mid 90's only CO_2 lasers were successfully used to join SMAs. By then some investigations started to employ, with promising results, the then modern Nd:YAG lasers. Also some experimental work about the preservation of shape memory properties and superelastic behavior started, revealing that almost identical properties between weld and base material could be achieved.

Those first CO_2 laser welds were mainly NiTi similar joints, and effects on mechanical behavior, shape memory, corrosion and other were then studied. Schlossmacher *et al* [33] studied the mechanical behavior of a Nd:YAG laser welded Ni-rich TiNi SMA (Ti-51.5 at. % Ni), performing tests on metal sheets 0,5 mm thick. Tuissi *et al* [34] evaluated the effect of Nd:YAG laser welding on the functional properties of Ni-49,6 at % Ti SMA. The effect of CO_2 laser welding on shape-memory and corrosion characteristics of an equiatomic and lightly Ni rich NiTi alloys was studied by Hsu *et al* [35]. Falvo *et al* [36] evaluated the mechanical and shape memory behavior of laser welded NiTi alloys.

Although both CO_2 and Nd:YAG lasers can perform laser welding on NiTi SMAs, more significant effects on mechanical strength and functional properties are observed in CO_2 welded joints (Hsu *et al* [35]), while Nd:YAG laser welded joints preserve good ultimate tensile strength and functional properties [33, 36 to 37].

Fatigue life of heat treated laser-welded NiTi SMAs has also been evaluated by Yan *et al* [17, 38] for wire shape on rotating-bending tests. Falvo *et al* [37] studied the functional behavior of a NiTi-welded joint, focused on the two-way shape memory effect. The influence of laser welding parameters on the microstructure and mechanical properties of laser welded NiTi alloy wires was only evaluated by Song *et al* [39]. Recent microstructural investigations of Nd:YAG laser welded dissimilar NiTi/AISI 304 stainless steel joints were performed by Gugel and Theisen in Germany [40].

3.6.2 Laser welding basics

Light Amplification by Stimulated Emission of Radiation, commonly known as LASER, was predicted in 1916 by Albert Einstein using a mathematical argument. Since its confirmation in 1928 by Rudolph Ladenburg, and the first working laser based on ruby invented by Theodore Maiman in 1960, has been used in state of the art applications. During the next 24 years more than 12 types of industrial lasers were invented, although concerning material processing applications, according to [41] the main are: carbon dioxide (CO_2), neodymium-yttrium aluminium garnet (Nd-YAG), excimer (KrF, ArF, XeCl), diode, disk and fiber lasers.

Lasers deliver energy in the form of electromagnetic radiation beams and their radiation is amongst the purest spectral forms of radiation available (for Nd:YAG, λ=1.06 µm). Laser radiation has three major characteristics: monochromaticity, coherence (spatial and temporal), a consequence of self-generated radiation by the stimulated emission phenomenon, and very low divergence. Metallic materials absorb laser radiation, specially at wavelengths below 1 µm, so developments in laser sources had a major objective of producing high power, low wavelength and good beam quality. Figure 3.1 depicts the absortivity of several industrial materials for different laser wavelengths.

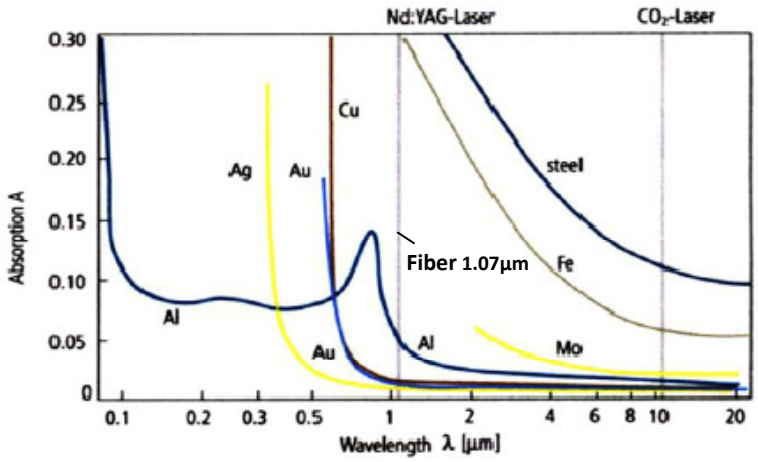

Figure 3.1 Absorption coefficient at laser wave lengths for common metals. Adapted from [42]

According to the ISO 11146:1999 standard, beam quality is often evaluated by several parameters, namely the beam parameter product, BPP, M^2 and K, which can be correlated by the following relations:

$$BPP = \frac{d_0}{2} \cdot \frac{\theta}{2} \tag{3.1}$$

$$K = \frac{\lambda}{\pi} . \frac{1}{BPP} \tag{3.2}$$

$$M^2 = \frac{1}{K} \tag{3.3}$$

Where d_0 is the focused beam diameter, θ the divergence angle and λ the wavelength.

Usually lasers are used in material processing applications as heat sources: lenses and mirrors are used to focus radiation, so that high energy densities are achieved. Focused to around 0,2 mm diameter, radiation from a 1kW CO_2 laser delivers around $3x10^4$ W/mm^2, which is 60 times more than an electric arc can produce.

When a laser beam is focused into a material surface, energy transfer occur in the electronic conduction band. If the energy is low, this conduction occurs mainly on the surface and in the interaction area melting of material occurs. Heat transfer is controlled by conduction (similar to arc welding) leading to large fusion and heat affected zones, as depicted in figure 3.2.

The displacement of the heat source and the forces acting on the molten pool, mainly the surface tension, which is determined by the chemical composition and the temperature of the pool, originate convection movements known as the Marangoni effect [41].

For high energy density, heat transfer on the surface is sufficient to melt and evaporate the material. When the material evaporates, the absortivity increases and temperature rises. A column of metallic vapor is formed in depth sustained by the surrounding molten metal that displaces with the laser source. The balance of pressures in the column is given by:

$$P_v+P_b+P_r=P_g+\gamma$$

Where P_v is the vapour pressure, P_b, is the pressure exerted by the laser beam, P_r, is the recoil pressure, P_g, is the gravity pressure and γ the surface tension of the molten metal.

Forces acting on this metallic vapor column tend to close it on the surface (where the surface tension is predominant) while vapour pressure tends to open it (figure 3.3). The balance of the pressures determine its shape, usually referred as a ‘keyhole’.

Generally, laser welding allow low heat inputs, therefore small HAZs and reduced distortions, narrow, precise and contamination-free welds, without the need of filler material. Nevertheless, the process requires the control of a set of parameters as shown in figure 3.4.

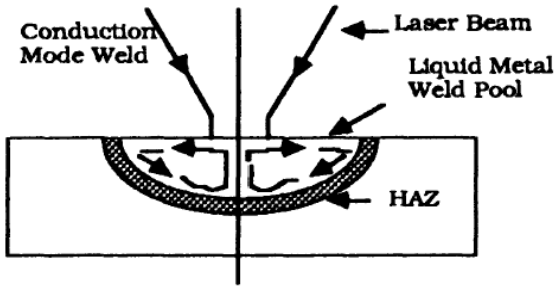

Figure 3.2 Conduction welding [41]

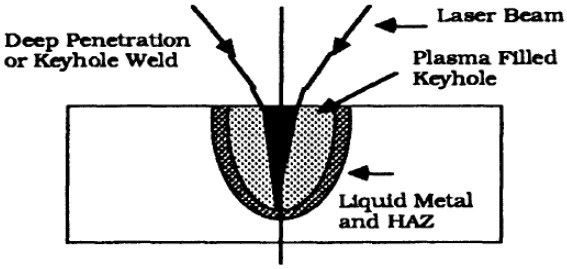

Figure 3.3 Keyhole welding [41]

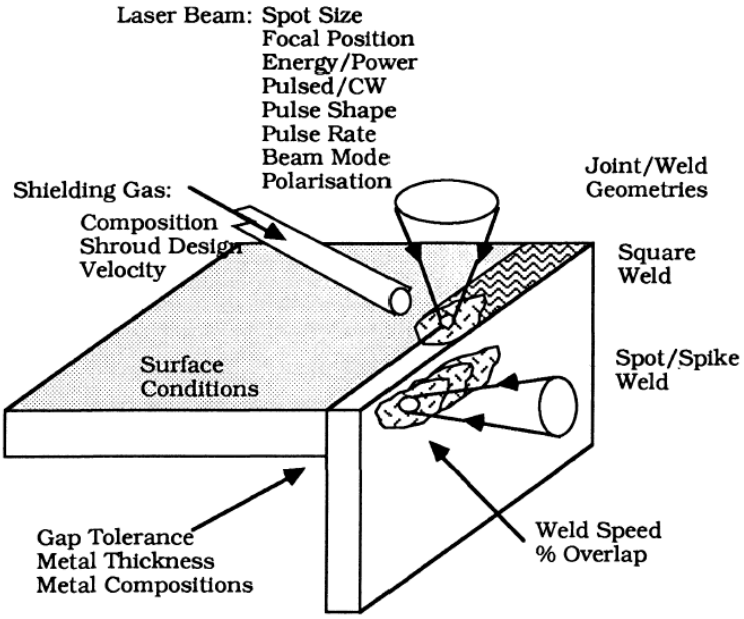

Figure 3.4 Main laser welding process parameters [41]

3.6.3 NiTi similar laser joints

3.6.3.1 Microstructure

Yan *et al* [17] observed the B2 structure (austenitic) in an as-welded state Ti-50.6 at. % Ni SMA with Ti_2Ni particles. No Ni_4Ti_3 precipitates, related to fatigue strength, were found in such conditions. Schlossmacher *et al* [33] confirmed this result on Ti-51.5 at. % Ni SMAs, and concluded that the Ni_4Ti_3 precipitates from the base material were completely dissolved in the fusion zone.

Song *et al* [39] when evaluating the influence of laser parameters on the microstructure of an as-joined NiTi SMA, observed in the fusion zone a columnar microstructure, due to low solidification rate. The microstructure of the heat affected zone consisted of coarse equiaxed grains and some

cracks were observed in the fusion zone. The weld quality was found strongly dependent on the microstructure, and related to laser power. The laser welded joints studied exhibited brittle fracture features like other previous studies indicated. However, laser welding process had little effect on the reverse martensitic transformation behavior of the welds.

Gugel and Theisen [43] reported a fusion zone mainly constituted by coarse grains on a NiTi SMA with 50.65 at. % Ni, passing into a zone of smaller and columnar grains. Epitaxial crystallization was observed at the fusion line with grain growth in the direction of heat flow. The heated-affected zone exhibited an equiaxed grain structure.

3.6.3.2 Effects on functional properties

Schlossmacher *et al* [33] observed on laser welded Ni-rich SMAs pronounced stress plateaus upon loading up to strains of about 6%, similar to the base material. Both austenitic and martensitic conditions were confirmed at the expected temperatures.

Tuissi *et al* [34] reported that modifications induced by Nd-YAG laser welding on a 49.6 at. % Ti preserved the original shape memory effect. However, tensile tests revealed ultimate tensile stresses lower than those observed in the base material and narrower pseudoelastic windows. On the other hand, Falvo *et al* [36] concluded that the shape memory effect of NiTi laser-welded wires is preserved for low strains (about 2,7%), while when increasing the total strain (about 6,2%) the behavior becomes different and the shape memory effect is affected by welding. Performance was reduced, making those joints not suitable for design of smart components under large tensile stress, requiring large strain recovery. These welds could be used in lighter applications at lower stress levels, requiring lower strain recovery.

Recently, Falvo *et al* [37] analyzed the functional behavior of NiTi-welded joints, concluding that the welding process, acting as a thermal treatment, affected the stress-strain response, reducing the effects of cold working and allowing to observe the characteristic stress-plateau. Results showed that the process is a suitable joining technique for NiTi smart actuators, despite the observed reduction in the overall performance.

3.6.3.3 Effects on mechanical properties

Generally, welding effects on SMAs lower the ultimate tensile stresses, as Tuissi *et al* [34] concluded when working on Ni-49.6 at. % Ti SMAs. Tensile tests on welded material revealed lower Young modules and a smoother transition between the elastic part of the curve and the lower stress-plateau. The explanation presented by the authors is that, probably, stress is accommodated by slip into the HAZ before reaching σ^{s} (twinned martensite to detwinned martensite). The same work refers

lower inelastic deformation values for welded material after free recovery. This may be due to weld defects and dislocations generated during loading in the HAZ.

Falvo *et al* [36] also observed a significant decrease in the mechanical ultimate tensile strength of joints, compared to the base material. Ultimate strength decreased about 52,7 %, while elongation to fracture was reduced about 41,6 %. Results showed a clear embrittlement due to the process; however the authors concluded that, in the overall, a ductile behavior was present since elongations to fracture of about 7 % were observed. The same work confirmed a clear reduction of martensitic stress-plateau has a consequence of slip in the HAZ.

Schlossmacher *et al* [33] reported the absence of embrittlement in the welding zone due to a dendritic microstructure predicted by others for joining techniques involving fusion in a laser welded Ti-51.5 at. %Ni SMA. Contrarily, microstructural investigations revealed ductile behavior up to fracture. However, results showed a reduction of about 20 % of the ultimate tensile strength, as well as, a decrease of about 67 % on elongation to fracture.

Fatigue life of heat treated laser-welded NiTi SMAs was evaluated by Yan *et al* [17, 38] for wire shape on rotating-bending tests. Results revealed that annealing at 400ºC for 1h can improve the fatigue strength. However, if annealed at 500 ºC during the same time, fatigue strength decreases. The study also associated the size of Ti_3Ni_4 precipitates to fatigue strength, which decreases when precipitates coarsen, so that heat treatments to produce smaller coherent precipitates may be used with improved results.

3.6.4 NiTi dissimilar laser joints

Dissimilar joints of NiTi SMAs to other alloys allow wider fields of application. Although a major problem occur when fusion welding NiTi to an iron-based alloy as the formation of oxides and brittle intermetallic phases of the type FeTi and Fe_2Ti that lead to cracks, generally on the NiTi side of the joint. Structural modifications in the fusion and heat affected zones affect the static strength, the functional performance and the failure region. In 1997 Wang, a senior Engineer at the EWI [44], reported preliminary tests regarding arc butt welding of Nitinol to nickel-based stainless steels, concluding that the use of a Ta interlayer nearly doubled the joint strength, which was limited by the Ta tensile strength. In 2003 Hall, also from the EWI [45], reported a patent pending method to produce high strength NiTi/Ferrous metals dissimilar welds, based on metal additions that suppress or alter the brittle phases, as tests conducted using Nd:YAG lasers revealed that functionality (superelasticity) was guaranteed on NiTi/ AISI 304 joints.

3.6.4.1 Microstructure

Gugel and Theisen [40] observed epitaxial growth of grains in NiTi/AISI 304 stainless steel joints, as well as fusion and heat-affected zones on the NiTi side - figure 3.5. According to XRD, EBSD, and TEM diffraction a predominant B2 structure (austenitic structure) was found in the fusion zone. Also round shaped oxycarbides and *TiC* carbides were found in the same zone. No heat-affected zone on the steel side was detected, where rich Fe_2Ti microstructure was observed (figure 3.6), as the grain size is much smaller compared to the center of the fusion zone.

Segregation of Ni, Cr and Fe occurred in the interdendritic regions, due to primary solidification of NiTi and successive reduction of Ti by precipitation of carbides, leading to inter-dendritic regions rich in TiC. X-Ray diffraction revealed a major B2 structure (austenitic) on the Ni-Ti side and fusion zone. Measurements made on the austenitic steel side confirmed the presence of the steel structure. Electron backscatter diffraction revealed small equiaxed grains of about 20 µm in the HAZ, smaller that those present in the base material, of about 30 µm. In the fusion zone massive grain growth was observed, while the grain structure of the austenitic steel was only slightly influenced. Additionally, by shifting the laser spot position a crack and pore free joint was obtained.

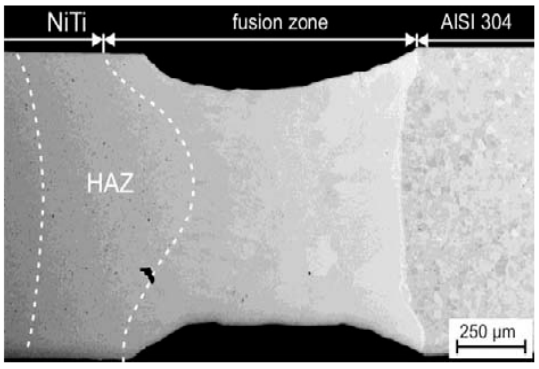

Figure 3.5 NiTi/AISI 304 joint [40]

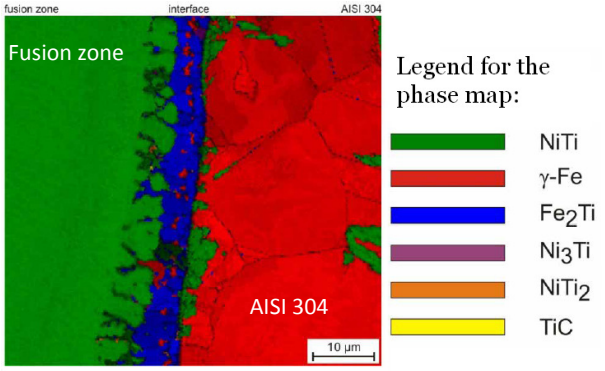

Figure 3.6 Phase map: interface FZ/AISI304. Adapted from [40]

Gugel *et al* [43] also welded NiTi to AISI 301 stainless steel without interlayer, and observed the formation of a HAZ on the NiTi side similar to those observed in NiTi similar welds, with an equiaxed grain structure. No coarse grains formation was observed in the fusion zone, which exhibited higher hardness values than the both of the base materials. Although not visible in optical microscopy, an HAZ was also present in the stainless steel side, as Vickers microhardness measurements revealed the presence of a recrystallized and softened relatively large area.

Vannod *et al* [46] studied the Nd:YAG laser welding of AISI 304 stainless steel and NiTi in pulsed wave mode, in which it is possible to observe extensive cracking along the weld centerline and the presence of Rutile - TiO_2, due to oxygen contamination.

3.6.4.2 Effects on functional properties

The superelasticity of dissimilar NiTi/AISI 301 welds was studied by Gugel *et al* [43], which reported cyclic transformation plateaus of about 1.7% (strain) at 500 MPa, when tested up to 2.5%. As the number of cycles increased, the transformation stresses decreased, and after 10 training cycles changes between successive cycles become very little, as an inelastic deformation was noticed - figure 3.7.

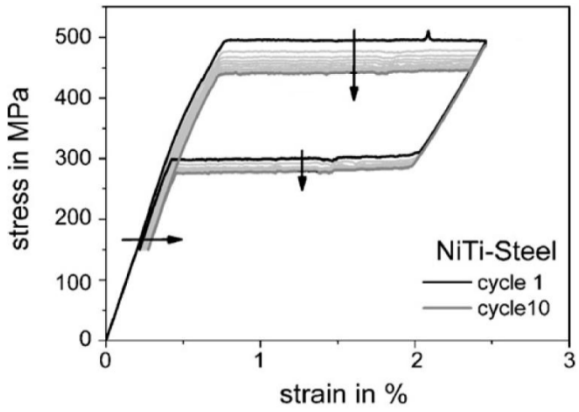

Figure 3.7 Cyclic stress-strain data of dissimilar NiTi/AISI 301 welds. Adapted from [43]

3.6.4.3 Effects on mechanical properties

Gugel *et al* [43] reported the fail of dissimilar NiTi/AISI 301 welds above the transformation plateau (at stress levels of 620 MPa and about 4% strain), as fracture occurred either by the steel HAZ, near the fusion line, pointing out to the presence of brittle phases that limited the ductility of the joint, or by the NiTi end fusion zone, what may occurred due to the presence of TiC precipitates and intermetallics containing Fe, Cr, Ni and Ti, leading to low-deformation brittle fracture.

3.7.Laser brazing

Brazing is an especially interesting joining technique when base materials present poor weldability by other methods. In SMA's context, preliminary studies revealed promising results on NiTi to stainless steel dissimilar laser brazed joints.

Qiu *et al* [47] developed experiments on lightly Ti-rich NiTi to austenitic stainless steel dissimilar joints, brazed with an Ag-based alloy. Results revealed a strong relation between heat input and the ultimate tensile strength and a loss of superelasticity was observed in the NiTi HAZ, which directly depends of heat input.

The significant influence of laser brazing parameters on joint behavior was also concluded by Li *et al* [48] when evaluated the properties of laser-brazed NiTis to SS orthodontic wires. The inverse dependence between heat input and preservation of functional properties on NiTi HAZ was again reinforced, as a strong reduction in microhardness measures in the FZ was also observed for higher inputs.

An increase in joint tensile strength was observed for higher powers; however shape recovery ratios decreased very significantly. Overall laser brazing is suitable technique for SMAs, however satisfactory joint properties are highly dependent of selecting proper brazing parameters.

3.8.Synthesis

In this chapter, a bibliographic research on the state of the art of SMAs joining techniques was presented. This is an intensive and innovative area of research. As no welding processes were seen to meet the requirements of SMAs, research is needed on:

- Welding procedures, namely those involving high energy density beams, as lasers.
- Microstructural analysis of welds that allow understanding the effects of the laser welding process on the modifications induced.
- Mechanical testing and SME evaluation.

4. Experimental work

As previously stated, the experimental work aimed to:

- Exploit laser joining processes of superelastic NiTi shape memory alloy in similar and dissimilar joints to stainless steel and Ti6Al4V alloy.
- Analyze microstructural evolution along the welded joints.
- Assess mechanical properties.
- Evaluate functional properties of SMAs welded joints.

4.1 Materials

4.1.1 NiTi shape memory alloys

Two different types of NiTi shape memory alloys from the same supplier were used in the present study: An S-alloy was used to produce similar NiTi/NiTi welds and an N-alloy was used on dissimilar NiTi/AISI 316 ones. Their characteristics are the following:

- Superelastic NiTi alloy (50.8 at. % Ni) plates of 1.0 ± 0.1mm and 0.50 ± 0.05 mm thicknesses from *Memory-Metalle GmbH* Alloy S (superelastic standard alloy). These alloys had an austenitic finish temperature of about 0 ºC, were flat annealed and surface oxide free. Plate dimensions were: 70x280x0.50 mm and 85x385x1.0 mm. Physical and mechanical properties are displayed in tables 4.1 and 4.2.

- Superelastic NiTi alloy (51 at. % Ni) 1 mm diameter wire from *Memory-Metalle GmbH* Alloy N (superelastic standard alloy). This alloy had an austenitic finish temperature of about 15 ºC and was annealed for stress relieve at 100 ºC for 10 min.

Table 4.1 Physical properties of NiTi shape memory alloys [49]

Melting point	Density	Thermal conductivity		Electrical resistivity	Thermal expansion factor	
		Martensite	Austenite		Martensite	Austenite
(ºC)	(kg/dm^3)	(W/m.K)	(W/m.K)	(μΩcm)	(x10^{-6} K^{-1})	(x10^{-6} K^{-1})
ca. 1310	6.45	ca. 9	ca. 18	50-110	ca. 6.7	10-11

Table 4.2 Mechanical properties of NiTi shape memory alloys [49]

Tensile modulus		Poisson ratio	Ultimate tensile strength		Tensile strain	
Martensite	Austenite		Cold worked	Fully annealed	Cold worked	Fully annealed
(GPa)	(GPa)	-	(MPa)	(MPa)	(%)	(%)
ca. 23-41	ca. 70-80	0.33	up to 1900	ca. 900	5-20	20-60

4.1.2 Titanium alloy

Ti-6Al-4V alloy was used to produce dissimilar welds and its properties are presented in tables 4.3 to 4.5.

Table 4.3 Chemical composition of the Ti-6Al-4V alloy [50]

wt. %								
C	Al	N	O	V	Fe	H	other	Ti
≤0.10	5.50-6.75	0.05	≤0.020	3.50-4.50	≤0.40	≤0.015	≤ 0.40	Balance

Table 4.4 Typical physical properties of Ti-6Al-4V [51]

Linear thermal expansion coefficient	Electrical resistivity	Thermal conductivity	Density
($x10^{-6}$ K^{-1})	(μΩm)	(W/m.K)	(g/cm^3)
8.6 (20-100ºC)	1.71	6.6-6.8	4.43

Table 4.5 Mechanical properties of Ti-6Al-4V rolled sheet [51]

Direction	thickness	Tensile strength	Yield strength	Elongation	Tensile modulus
	(mm)	(MPa)	(MPa)	(%)	(GPa)
Longitudinal	1.016	970	855	6.5	106
Transverse	1.016	1105	1105	7.5	145

4.1.3 Stainless steel

A low-carbon 1 mm wire austenitic stainless steel AISI 316 LN was used to produce dissimilar joints. Typical composition and properties are presented in tables 4.6 to 4.8.

Table 4.6 Typical chemical composition of AISI 316LN SS [52]

wt. %								
C	Mn	Si	Cr	Ni	P	S	Mo	N
≤0.03	≤2.00	≤1.00	16.0-18.0	10.0-14.0	≤0.045	≤0.03	2.0-3.0	0.10-0.16

Table 4.7 Typical physical properties of AISI 316LN SS [52]

Linear thermal expansion coefficient	Electrical resistivity	Thermal conductivity	Density
($x10^{-6}$ K^{-1})	(μΩm)	(W/m.K)	(g/cm^3)
15.9 (at 100ºC)	0.74	16.2 (at 100ºC)	8.0

Table 4.8 Mechanical properties of AISI 316LN SS [52]

Direction	Tensile strength	Yield strength	Elongation	Tensile modulus	Hardness
	(MPa)	(MPa)	(%)	(GPa)	(max. HRB)
Longitudinal	620	240	55	193	95

4.2 Sample preparation for joint design

4.2.1 NiTi similar joints

4.2.1.1 Joints for design evaluation

Samples were extracted from 1.0 mm thick plates along and across the rolling direction, using a precision cut-off machine *ATM GmbH model Brillant 221* equipped with a diamond wheel type *B102* from the same maker. Cutting parameters were set up to the following values: Speed - 3500 r.p.m; feed rate: 3 mm/min; lubricant: multipurpose cutting fluid. Butt joints geometry is presented in figure 4.1.

Samples were hand finished, chemically cleaned with a solution of HF: HNO_3:H_2O in the proportion of 1:5:10 in order to remove cutting moisture contamination and surface oxides. Figure 4.2 shows prepared samples.

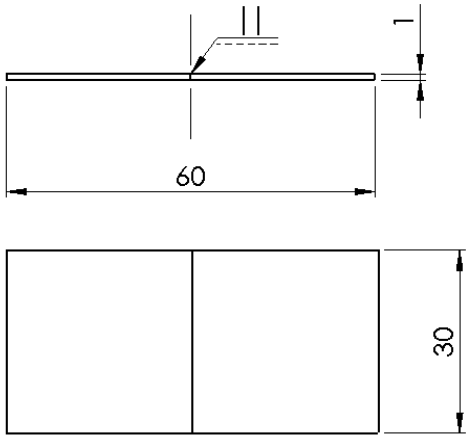

Figure 4.1 Joint configuration for design evaluation

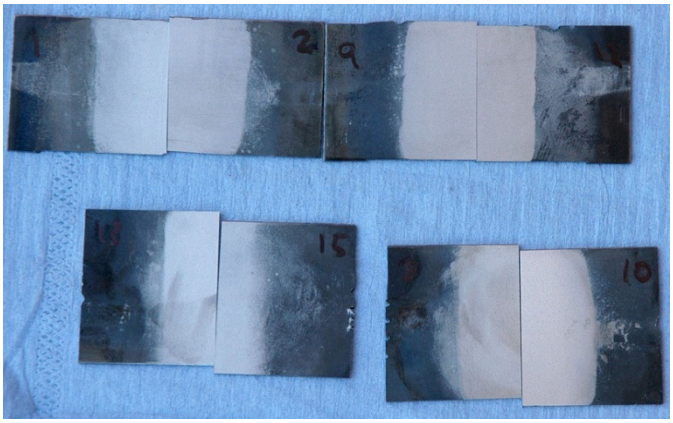

Figure 4.2 Samples for laser welding

4.2.1.2 Joints for parameters evaluation

The rolling direction was identified by visual inspection in the 1.0 and 0.5mm thick NiTi plates. The samples dimensions were set up to 35x35 mm, according to the geometry depicted in figure 4.3.

Samples dimensions allowed the extraction of the following specimens:

- 3 for ultimate tensile strength evaluation and cyclic behavior characterization.
- 1 for structural observations (optical and SEM).
- 1 for DSC analysis.
- 1 for shape memory effect evaluation.

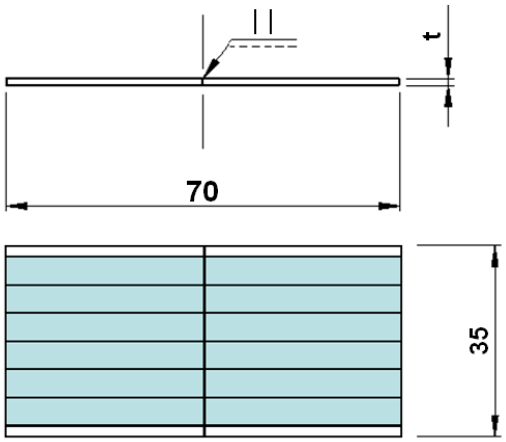

Figure 4.3 Joint configuration for parameters evaluation. t=0.5 and 1.0mm

The aim of the parameters evaluation study is to create joints that combine two sets of welding parameters (welding speed and power) at three levels, resulting in 9 welded specimens, which requires 18 single 35x35 mm square plates of each thickness. A reference marking system was adopted and the extraction was prepared according to the schemas of figures 4.4 and 4.5.

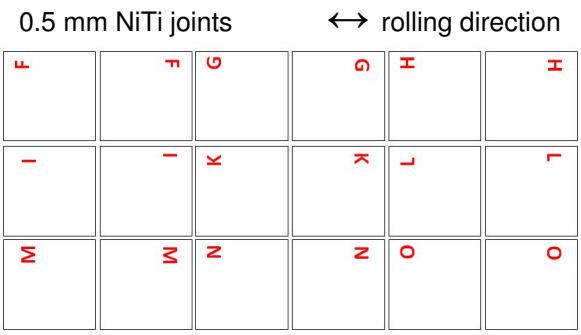

Figure 4.4 NiTi 0.5 mm joints for parameters evaluation references

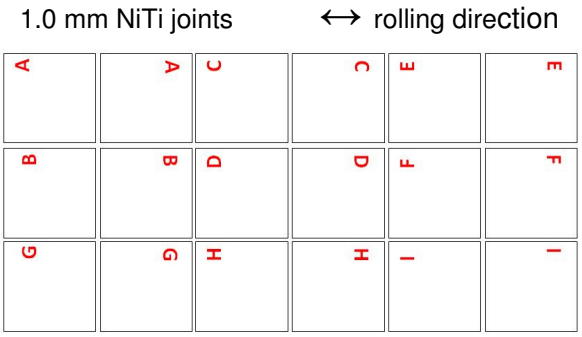

Figure 4.5 NiTi 1.0 mm joints for parameters evaluation references

Due to the dimensions of the initial plates (70x280x0.50 mm and 85x385x1.0 mm) and the number of cuts to perform, specimens were first roughly cut-off using a hand-operated guillotine. Preparation of faces to be welded consisted of grinding with a SiC wheel and finished as previously described.

4.2.2 Dissimilar joints

According to shape and intervenient alloys several dissimilar joint types were prepared from rough materials. Considerations taken into account for each group are described in the next sections.

4.2.2.1 NiTi N/AISI 316L lap joints

Samples for dissimilar NiTi N/AISI 316L joints were prepared from rough materials, both a wire shape. Materials were roughly cut-off 30mm long using a wire cutter and then were grinded with SiC paper of grit no. 400 to remove oxides. Lap joints were produced along the length direction overlapping about 10mm and welding on both sides, according to figure 4.6.

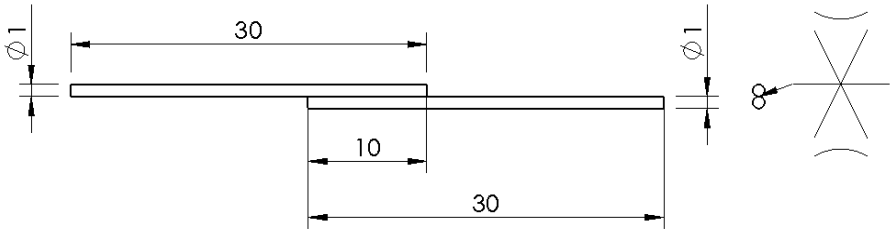

Figure 4.6 Joint schema for NiTi N/AISI 316L wire joints

4.2.2.2 NiTi for dissimilar butt joints

NiTi-S 1.0mm square 35x35 mm specimens were prepared to produce dissimilar joints with Ti-6Al-4V. The experimental procedure regarding the extraction and nature of samples is similar to the one described in item 4.2.1.2. However, references are different and for that reason, presented in figure 4.7.

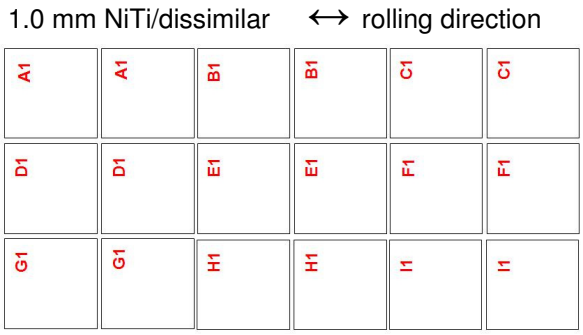

Figure 4.7 NiTi 1.0 mm plates for dissimilar welds

4.2.2.3 Ti-6Al-4V for dissimilar joints

Ti-6Al-4V square 35x35 mm plates 1.0mm thick were prepared at the *Cranfield University* premises. Specimens were roughly cut-off from as-received sheets using a hand-operated guillotine. The finishing operations consisted of top milling the butt joint edges (faces) and grinding by hand with SiC paper, assuring perfect contact with NiTi specimens.

Specimens were then cleaned with ethanol and chemically attacked with the same solution of HF: HNO_3:H_2O in the proportion of 1:5:10 in order to remove cutting fluid contamination and surface oxides.

4.3 Equipment

4.3.1 Laser sources

4.3.1.1 High power pulsed Nd:YAG laser

A pulsed Nd:YAG laser model JK300HPS from *GSI Lasers* was used at *Cranfield University* premises to produce preliminary tests on NiTi/NiTi similar joints, as well as, dissimilar NiTi/Ti-6Al-4V joints. The technical characteristics are presented in table 4.9.

Table 4.9 JK300HPS Pulsed Nd:YAG laser – technical data [53]

Max. average power at laser	Typical power at workpiece	Max. peak power	Max. Pulse energy	Max. frequency	Pulse width range	Shutter opening time	Fiber diameter
(W)	(W)	(kW)	(J)	(Hz)	(ms)	(Ms)	(µm)
300	250	9	56	1000	0.2-20	<50	300

The welding head shown in figure 4.8 was equipped with a 300 mm focal length fused-silica lens and focused to a spot diameter of 0.9 mm. The beam profile was analyzed in a beam profilometer and is presented in figure 4.9. It shows a Gaussian beam with a real beam diameter of 0.8866 mm. The clamping system containing samples was mounted on a X-Y remotely controlled table.

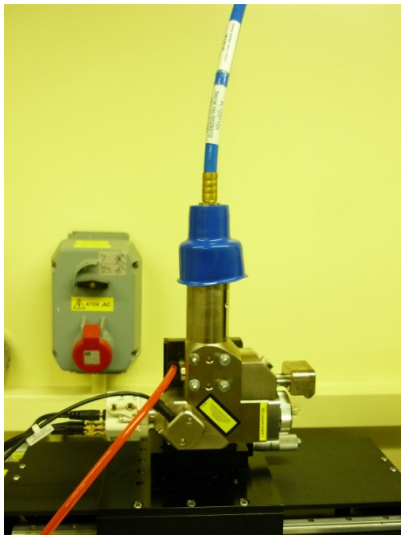

Figure 4.8 Pulsed Nd:YAG inner welding unit arrangement

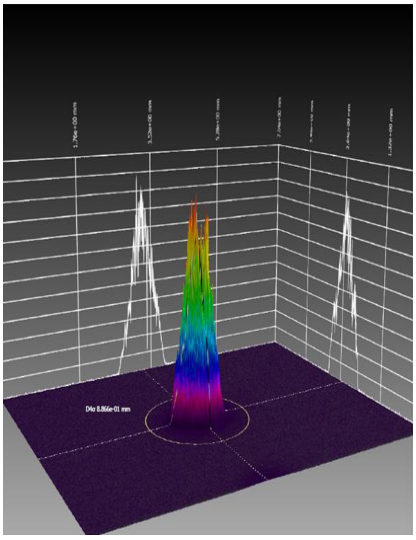

Figure 4.9 F300 measured pulsed beam profile - preview

4.3.1.2 High energy pulsed Nd:YAG laser

A *Rofin-Baasel* pulsed Nd:YAG *SWP 5002 Star Weld Performance* Manual Welding laser system was used by *Carrs welding Technologies* to perform dissimilar NiTi-N/AISI 316LN wire shape joints. The main technical characteristics are described in table 4.10 and the equipment is depicted in figure 4.10.

Table 4.10 *Rofin-Baasel* SWP5002 pulsed Nd:YAG laser - technical data [54]

Wavelength	1.06 µm
Nominal power	50 W
Pulse peak power	6 kW
Pulse energy	80 J
Pulse duration	0.5 – 50 ms
Pulse frequency	Up to 20 Hz
Focal beam diameter	0.3 - 2.0 mm

Figure 4.10 *Rofin-Baasel* SWP5002 pulsed Nd:YAG laser unit [55]

4.3.1.3 Continuous Nd:YAG laser

A *Rofin-Sinar* continuous Nd:YAG model DY033 diode-pumped laser was used at the *Universidad Politecnica de Madrid* to produce similar NiTi joints. The laser head movement was assured by an *ABB* robot remotely controlled. The main characteristics of the laser equipment are presented in table 4.11.

Table 4.11 *Rofin-Sinar* DY 033 CW Nd:YAG laser technical data [56]

Wavelength	1064 nm
Max. output power	3300 W
Number of cavities	6
Fiber diameter	400µm
Optical arrangement	
Tilt angle	3°
Focal length	ca. 160mm
Beam diameter	0.45mm
Intensity distribution	Gaussian

Figure 4.11 Inner Nd:YAG DY 033 laser equipment at *UPM* premises

4.3.1.4 High power fiber laser

An *IPG Photonics* Ytterbium fiber laser model YLR-8000 operating in continuous wave mode was used to produce dissimilar NiTi/Ti-6Al-4V at the *Cranfield University* laboratorial premises. The traveling of the laser welding head at the end of the process fiber is assured by a *FANUC* M-710iB/45 T robot remote controlled. The technical characteristics of the laser equipment are presented in table 4.12.

Table 4.12 IPG YLR-8000 Yb laser technical data [57]

Power		Up to 8kW
Wavelength		1070 nm
Feeding fiber diameter		200 µm
Process fiber diameter		300 µm
Optical arrangement		
Tilt angle		5°
1st Lens arrangement	Beam diameter	0.47 mm
	Focal distance	ca. 200 mm
2nd Lens arrangement	Beam diameter	0.73 mm
	Focal distance	ca. 300 mm

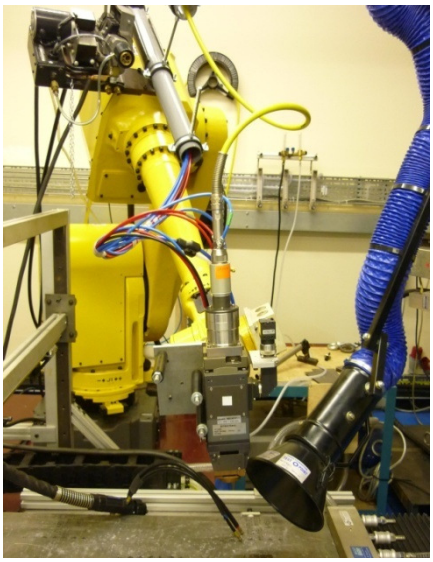

Figure 4.12 Yb fiber YLR-8000 laser at *Cranfield Unniversity* premises

4.3.2 Testing machines

The equipment used to perform mechanical and structural tests on welded specimens, namely a uniaxial tensile testing machine and a DSC equipment, are described below.

4.3.2.1 Tensile machine

A static tensile testing machine AUTOGRAPH *SHIMADZU* model AG500Kng equipped with a *SHIMADZU* load cell type SFL-50kN AG with total capacity of 50kN was used at *CENIMAT premises* to perform cyclic and to rupture tensile tests. Fixture to strip tensile specimens was attained by wedge grips.

4.3.2.2 DSC equipment

A *SETARAM* Differential Scanning Calorimeter (DSC) model DSC92 and a CS92 controller were used at *CENIMAT* premises to perform high and low temperature structural tests (liquid Nitrogen was employed on low-temperature tests).

4.3.3 Positioning devices

In order to guarantee perfect fit up and gas atmosphere control, a special jig was designed and manufactured at DEMI. Its main advantages are the following:

- Allows to firmly position the 0.5 and 1.0 mm thick plates for butt welding, avoiding distortions and allowing to apply an initial compressive force between opposite plates.
- Built-in channel provides gas assist to the root.
- Outer closed chamber with a lens window allows to control the atmosphere by over pressurizing with inert gas mixtures.

This positioning system and chamber were designed for similar and dissimilar joints with YAG lasers. It was also tested to assist the laser welding of dissimilar joints using a fiber laser. However, limitations concerning experimental details conducted to the design of another positioning mechanism and chamber, with the following improvements:

- Allows mounting start and ending plates to overcome transitory defects.
- Has a robust design and materials were selected to resist to high density radiation.
- A built-in selective exhaust system allows fumes to escape, keeping the purity of the inner atmosphere as face and root gas assist is provided separately, allowing flow control.
- The laser window was placed more far away from the defocused beam position, improving lens life.

The technical drawings which depict these two solutions are presented in annex B.

4.4 Experimental Approach

4.4.1 Similar NiTi/NiTi joints

The experimental approach concerning the main scope of the present work was the following: similar NiTi to NiTi joints were performed and evaluated aiming two different purposes: first the influence of joint's design in the overall mechanical performance and secondly the effect of welding parameters on structural, mechanical and functional aspects. Particular considerations, as well as explanations regarding the adopted experimental procedures, are made in each of the topics below.

4.4.1.1 Bead on plate welds for parameters evaluation

The determination of suitable process parameters for butt joints result from an iteration process conducted on the base material, which allows refining in order to achieve desired penetration, low incidence of defects like pores and cracks, oxidation control, adjust the extent of FZ and HAZ, etc.

In order to acquire experimental sensitivity to laser welding conditions, bead on plate welds were performed on the NiTi-S plate base material using the *Rofin-Sinar* Nd:YAG laser (see 4.3.1.3) operating in continuous wave mode. Several tests were performed varying processing parameters and gas injection system. NiTi 30x40x1.0 mm plates were mounted in a positioning JIG and gas was assisted by a flat nozzle - figure 4.13. An alignment laser was used and several bead on plate welds were produced according to parameters of table 4.13.

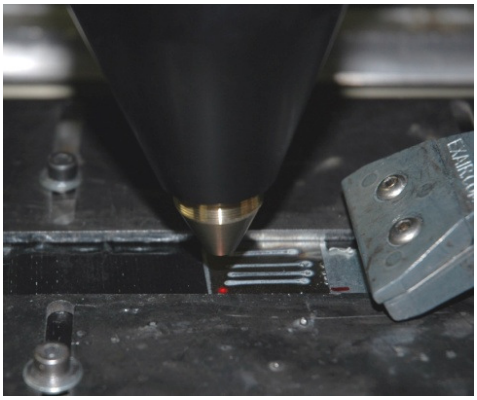

Figure 4.13 NiTi bead on plate welds

Table 4.13 Optimization of bead on plate laser weld parameters

Test number	Power	Welding speed	FPP	Beam spot ø	Shield gas flow		Gas assistance
					Face	Back	
	(W)	(mm/s)	(mm)	(mm)	(l/min)	(l/min)	
1	840	25	0	0.4	45	15	Flat tip
2	840	50	0	0.4	45	15	Flat tip
3	840	35	0	0.4	45	15	Flat tip
4	840	35	0	0.4	45	15	Flat tip[1]
5	840	30	0	0.4	45	15	Flat tip[1]
6	840	30	0	0.4	45	15	Chamber

4.4.1.2 Joints for design evaluation

Similar NiTi-S/NiTi-S butt joints for design evaluation were performed regarding the knowledge acquired with the preliminary bead on plate welds. The set up of proper welding parameters was found to be an iterative process. Welds were conducted on 30x30x1 NiTi-S plates using the *Rofin-Sinar* Nd:YAG laser (see 4.3.1.3) operating in continuous wave mode. Opposite plates were firmly fixed to a rigid mounting table by a screw fixture system shown in figure 4.14. A red laser was used for specimens alignment prior to butt welding, according to parameters of table 4.14, along and across the rolling direction. A special chamber was built *in situ* and overpressurized with Argon - figure 4.15. Figure 4.16 shows a similar butt joint in the welding place, after the chamber had been removed.

Table 4.14 NiTi butt joints for design evaluation - welding parameters

Power	Welding speed	FPP	Beam spot ø	Shield gas flow		Gas assistance
				Face	Back	
(W)	(mm/s)	(mm)	(mm)	(l/min)	(l/min)	
910	25	0	0,4	45	15	Chamber

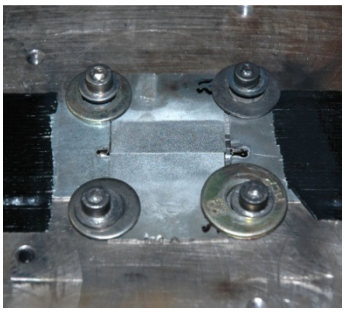

Figure 4.14 Fixture system

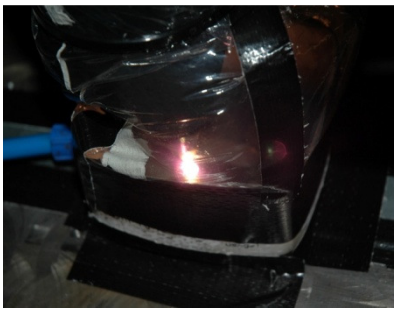

Figure 4.15 Welding running in Argon atmosphere - chamber

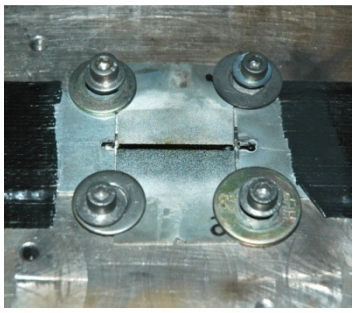

Figure 4.16 Butt joint – chamber removed

4.4.1.3 Joints for parameters evaluation

A comprehensive study regarding parameters evaluation was performed on NiTi-S plates with dimensions of 35x35x1.0 and 35x35x0.5 mm (see 4.2.1.2) using the *Rofin-Sinar* Nd:YAG laser (see 4.3.1.3) operating in continuous wave mode. Fixture and alignment of 1.0 and 0.5 mm plates was attained using a positioning system specially designed for that purpose (see 4.3.3) which assures that opposite plates were in the same plane and tight to each other, due to a small compressive force applied by the mechanism.

Back gas protection was assisted through a narrow pocket in the base of the positioning device, as face protection was assured by a chamber, which was feed laterally flowing in the welding direction and secondarily coaxially with the beam through an air knife. Due to technical limitations concerning maximum gas flow both Helium and Argon were used simultaneously to create an inert atmosphere. The chamber was opened at top (no lens were mounted) limiting the aperture to preserve the inner atmosphere - figure 4.17.

The focal point position was figured out by programming the robot to execute a ramp routine around the theoretical focal distance of the optical system on a thin metal sheet and visually observing the effect of beam diameter variation.

Two series of preliminary tests were made before butt welding and consisted of a number of bead on plate welds. Conditions and parameters are presented in tables 4.15 and 4.16.

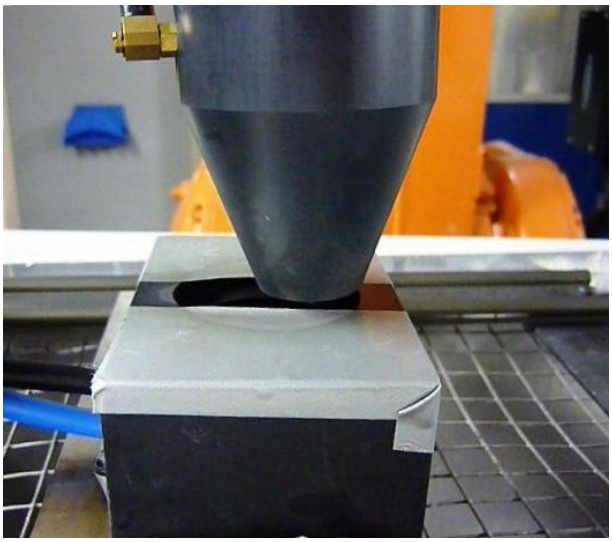

Figure 4.17 Welding of similar NiTi joints for parameters evaluation

Table 4.15 NiTi bead on plate welds for parameters evaluation – 1st parameters set

1st Series - Bead on plate							
Test number	Power	Welding speed	FPP	Beam spot ø	Argon		Helium
					Air knife	Laterally	Back
	(W)	(mm/s)	(mm)	(mm)	(bar)	(l/min)	(l/min)
1	990	25	0	0.45	-	-	100
2	990	25	0	0.45	8	-	100
3	1320	25	0	0.45	8	-	100
4	1320	25	0	0.45	8	-	100

Table 4.16 NiTi bead on plate welds for parameters evaluation – 2nd parameters set

2nd Series - Bead on plate							
Test number	Power	Welding speed	FPP	Beam spot ø	Argon		Helium
					Air knife	Laterally	Back
	(W)	(mm/s)	(mm)	(mm)	(bar)	(l/min)	(l/min)
1	1320	25	0	0.45	8	-	50
2	990	25	0	0.45	8	-	50
3	990	15	0	0.45	8	-	50
4	1485	20	0	0.45	8	-	50

Laser welding of 1.0 and 0.5 mm butt joints was performed according to the joint design stated before (see 4.2.1.2). Conditions and operational parameters are presented in tables 4.17 and 4.18.

Table 4.17 1.0mm butt joints for parameters evaluation – welding conditions

Plates reference	Power	Welding speed	Heat input	FPP	Beam spot ø	Argon		Helium
						Air knife	Laterally	Back
	(W)	(mm/s)	(J/cm)	(mm)	(mm)	(bar)	(l/min)	(l/min)
A-A	990	25	396	0	0.45	7.5	40	50
B-B	990	20	495	0	0.45	7.5	40	50
C-C	990	15	660	0	0.45	7.5	40	50
D-D	1485	30	495	0	0.45	7.5	40	50
E-E	1485	25	594	0	0.45	7.5	40	50
F-F	1485	20	743	0	0.45	7.5	40	50
G-G	1980	44	450	0	0.45	7.5	40	50
H-H	1980	40	495	0	0.45	7.5	40	50
I-I	1980	35	566	0	0.45	7.5	40	50

Table 4.18 0.5 mm butt joints for parameters evaluation – welding conditions

Plates reference	Power	Welding speed	Heat input	FPP	Beam spot ø	Argon		Helium
						Air knife	Laterally	Back
	(W)	(mm/s)	(J/cm)	(mm)	(mm)	(bar)	(l/min)	(l/min)
F-F	726	30	242	0	0.45	7.5	40	50
G-G	726	35	207	0	0.45	7.5	40	50
H-H	726	40	181	0	0.45	7.5	40	50
I-I	790	30	263	0	0.45	7.5	40	50
L-L	790	40	197	0	0.45	7.5	40	50
K-K	790	50	158	0	0.45	7.5	40	50
M-M	858	50	172	0	0.45	7.5	40	50
N-N	858	60	143	0	0.45	7.5	40	50
O-O	858	70	122	0	0.45	7.5	40	50

Concerning the welding process, gas assist was opened about 20s in advance, in order to fully remove the air inside the chamber, and then removed 15s after welds had finished. Due to practical limitations, it was not possible to quantify the amount of gas flowing through the air knife, however in tables 4.15 to 4.18 the Argon pressure is presented as a reference for future work.

4.4.1.4 Preliminary studies in pulsed mode

In order to acquire expertise regarding laser welding of NiTi alloys in pulsed mode, the pulsed *GSI* Nd:YAG laser was used to produce four series of NiTi-S bead on plate welds. The fixture system adopted was the same of the previous paragraph (see 4.3.3) which was mounted on an X-Y axis travelling optical table, ensuring precise process control, mechanical stability and gas protection during the process – figures 4.18 and 4.19. A mixture of Argon with 5% Hydrogen flowing at 15 l/min was used to create the shielding atmosphere inside the chamber in which was mounted a window lens, fully transparent to radiation, in order to preserve the inner environment. Hydrogen was used having in mind its reaction with Oxygen, protecting the weld pool from severe oxidation. An alignment laser was used to position the weld beads, as can be seen in figure 4.19.

Figure 4.18 Pulsed mode Nd:YAG experimental setup

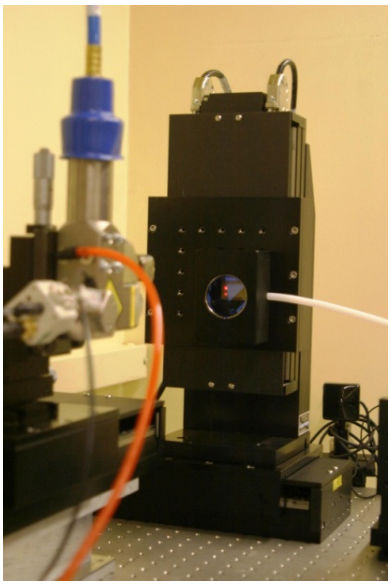

Figure 4.19 Detail of setup – alignment

The relation found in the literature [41, 58], between frequency (f), spot diameter (d_s), welding speed (V) and percent overlap ($\%OV$) was used to correlate the welding parameters for pulsed mode:

$$f = \frac{100V}{(d_s)(100 - \%OV)} \qquad \textbf{(4.1)}$$

The measured beam profile for the fused silica lens is presented in figures 4.20 and 4.21.

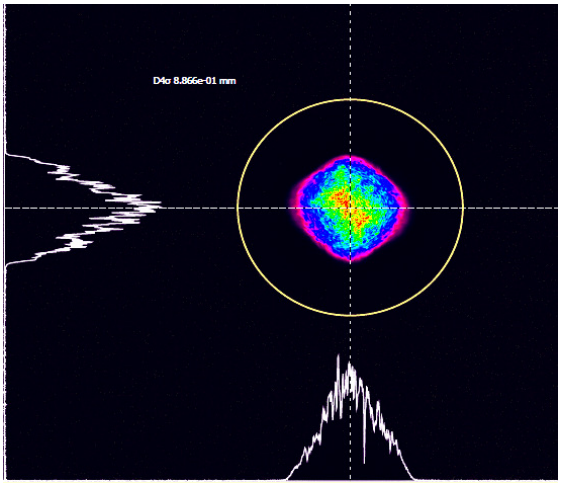

Figure 4.20 F300 lens beam profile - top

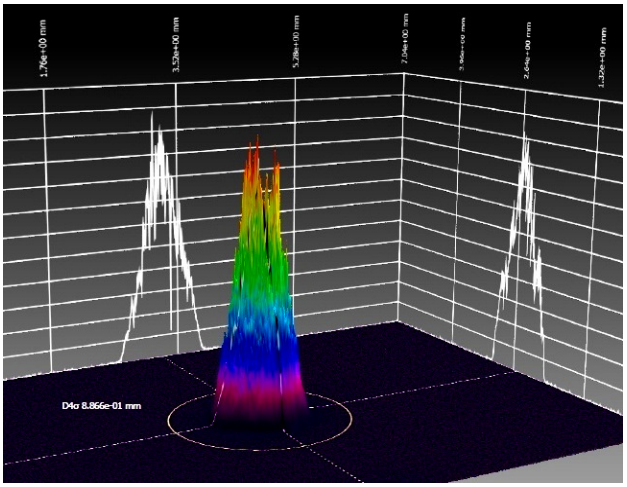

Figure 4.21 F300 lens beam profile - perspective

Laser welding of 25x25x1.0mm NiTi-S plates was performed according to parameters of next tables.

Table 4.19 1st series of bead on plate welds parameters

1st Series of NiTi pulsed welds									
Test number	Energy	Pulse duration	Welding speed	OV	Frequency	FPP	Beam spot ø	Power	Intensity
	(J)	(ms)	(mm/s)	(%)	(Hz)	(mm)	(mm)	(W)	(MW/cm^2)
1	55.0	20.0	1.1(3)	50	2.5	0	0.9	2750	0.40
2	41.5	15.0	1.1(3)	50	2.5	0	0.9	2767	0.40
3	27.0	10.0	1.1(3)	50	2.5	0	0.9	2700	0.40
4	55.0	15.0	1.1(3)	50	2.5	0	0.9	3667	0.61
5	55.0	15.0	1.1(3)	50	2.5	0	0.9	3667	0.61
6	55.0	10.0	1.1(3)	50	2.5	0	0.9	5500	0.86
7	48.0	17.5	1.1(3)	50	2.5	0	0.9	2743	0.40
8	48.0	17.5	1.1(3)	50	2.5	0	0.9	2743	0.40

Table 4.20 2nd series of bead on plate welds parameters

2nd Series of NiTi pulsed welds									
Test number	Energy	Pulse duration	Welding speed	OV	Frequency	FPP	spot ø	Power	Intensity
	(J)	(ms)	(mm/s)	(%)	(Hz)	(mm)	(mm)	(W)	(MW/cm^2)
1	55	10	0.81	10	1.0	0	0.9	5000	0.78
2	55	10	0.72	20	1.0	0	0.9	5000	0.78
3	55	10	0.63	30	1.0	0	0.9	5000	0.78
4	55	10	0.54	40	1.0	0	0.9	5000	0.78
5	55	10	0.45	50	1.0	0	0.9	5000	0.78
6	55	10	0.36	60	1.0	0	0.9	5000	0.78
7	55	10	0.27	70	1.0	0	0.9	5000	0.78
8	55	10	0.18	80	1.0	0	0.9	5000	0.78

Table 4.21 3rd series of bead on plate welds parameters

3rd Series of NiTi pulsed welds									
Test number	Energy	Pulse duration	Welding speed	OV	Frequency	FPP	spot ø	Power	Intensity
	(J)	(ms)	(mm/s)	(%)	(Hz)	(mm)	(mm)	(W)	(MW/cm^2)
1	41	15	0.81	10	1.0	0	0.9	2733	0.43
2	41	15	0.72	20	1.0	0	0.9	2733	0.43
3	41	15	0.63	30	1.0	0	0.9	2733	0.43
4	41	15	0.54	40	1.0	0	0.9	2733	0.43
5	41	15	0.45	50	1.0	0	0.9	2733	0.43
6	41	15	0.36	60	1.0	0	0.9	2733	0.43
7	41	15	0.27	70	1.0	0	0.9	2733	0.43
8	41	15	0.18	80	1.0	0	0.9	2733	0.43

Table 4.22 4th series of bead on plate welds parameters

4th Series of NiTi pulsed welds									
Test number	Energy	Pulse duration	Welding speed	OV	Frequency	FPP	spot ø	Power	Intensity
	(J)	(ms)	(mm/s)	(%)	(Hz)	(mm)	(mm)	(W)	(MW/cm^2)
1	10	20	4.5	50	10	0	0.9	500	0.0786
2	12	20	4.5	50	10	0	0.9	600	0.0940
3	14	20	4.5	50	10	0	0.9	700	0.1100
4	16	20	4.5	50	10	0	0.9	800	0.1250
5	18	20	4.5	50	10	0	0.9	900	0.1414

4.4.2 Dissimilar joints

NiTi Dissimilar joints to stainless steel and titanium were carried out using a Nd:YAG laser operating both in continuous and pulsed wave modes, as well as a continuous Ytterbium fiber laser. Both wire and plate shapes were tested with the Nd:YAG laser source regarding the acquisition of know-how for eventual applications. Only plates were welded using the fiber laser. Laser welding followed the lines of dissimilar joint design (see 4.2.2); however some weldments were preceded by exploratory work regarding bead on plate welds in order to identify the best windows of parameters.

4.4.2.1 NiTi/AISI 316LN wire joints

The pulsed *Rofin-Baasel* Nd:YAG laser (see 4.3.1.2) was used to produce the dissimilar NiTi-N/AISI 316 LN ø 1 mm lap joints, according to the joint design described before (see 4.2.2.1). Argon was injected through a nozzle creating an inert protective atmosphere. Dissimilar joints were produced according to parameters presented in table 4.23.

Table 4.23 NiTi/AISI 316LN dissimilar wire joints – welding parameters

Power	Welding speed	Frequency	FPP	Beam spot ø	Argon flow	Assist gas
(W)	(mm/s)	(Hz)	(mm)	(mm)	(l/min)	
50	5.0	6.0	+ 0.7 [1]	0.7	8	nozzle

[1] '+' means above the surface

4.4.2.2 Ti-6Al-4V bead on plate welds for parameters evaluation

Regarding plate shape, some know-how had already been acquired for bead on plate welding of NiTi in pulsed wave mode (see 4.4.1.4), from preliminary tests. Bearing in mind the dissimilar welding of NiTi to Ti-6Al-4V, autogenous weld spots as well as bead on plate welds were performed on 35x70x1.0 mm Ti-6Al-4V plates. For that purpose the *GSI* Nd:YAG laser (see 4.3.1.1) was used in pulsed wave mode and a mixture of Argon with 5% of Hydrogen was used as protective atmosphere.

The same positioning device (see 4.3.3) used in the NiTi experiments, with root built-in gas assistance and chamber was used to do the experiment, in which was mounted a window. The lens fully transparent to radiation allowed preserving the inner atmosphere (from outer Oxygen). The set-up was similar to the one of figures 4.18 and 4.19. A flow of 10l/min, 5l/min lower than the one used on NiTi was selected and used during the experiment, which was conducted according to the parameters listed in table 4.24.

Table 4.24 Ti-6Al-4V autogenous tests – welding parameters

Test number	Energy	Pulse duration	Welding speed	OV	Frequency	FPP	spot ø	Power	Intensity
	(J)	(ms)	(mm/s)	(%)	(Hz)	(mm)	(mm)	(W)	(MW/cm^2)
1	27	20	4.5	50	10	0	0.9	1350	0.21
2	27	10	4.5	50	10	0	0.9	2700	0.42
3	68	20	Single	-	1	0	0.9	3400	0.53
4	40	20	Single	-	1	0	0.9	2000	0.31
5	35	20	Single	-	1	0	0.9	1750	0.28
6	30	20	Single	-	1	0	0.9	1500	0.24
7	35	20	2.25	50	5	0	0.9	1750	0.28
8	30	20	2.25	50	5	0	0.9	1500	0.24

4.4.2.3 Dissimilar NiTi/Ti-6Al-4V joints

Laser welding of dissimilar NiTi/Ti-6Al-4V was made using two experimental approaches: the first consisted of using the *GSI* Nd:YAG (see 4.3.1.1) pulsed laser, as the second was performed with the *IPG* Ytterbium fiber laser operating in continuous wave mode. Previous pulsed mode tests revealed a tendency for dust metal vapours to sputter into the lens inner surface, due to the small distance from the weld pool.

A new feature consisting of a Polypropylene ø 50 mm pipe 150 mm long, which in one end was installed the fused-silica lens, was adapted to the camber opening, improving the lens protection. At the same time a rip 30 mm long was opened near the end, allowing fumes to be exhausted without the risk of incoming Oxygen.

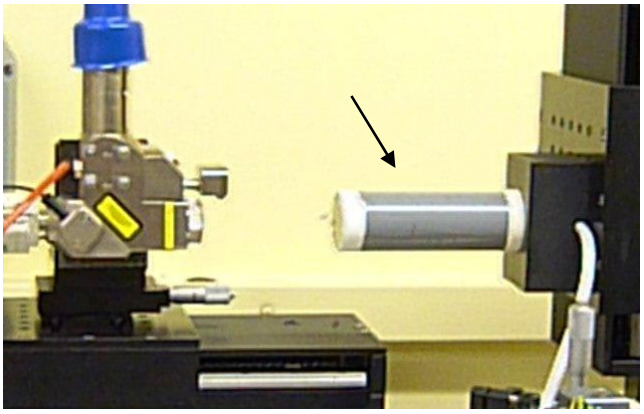

Figure 4.22 Updated experimental arrangement for dissimilar NiTi/Ti-6Al-4V welding - The arrow indicates the new feature

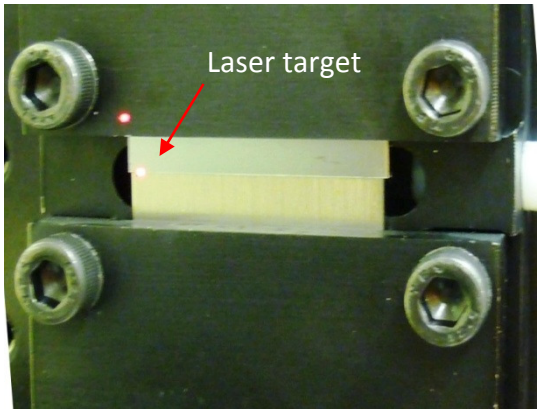

Figure 4.23 Alignment set-up – the arrow indicates the real laser target

The new setup is presented in figure 4.22. The gas protection used in the pulsed experiments consisted of the same mixture of Argon with 5% of Hydrogen. However, in some of the continuous wave tests, an extra Argon source was added, due to the observation of extensive oxidation. Welding of dissimilar butt joints was performed as designed (see 4.2.2.2 and 4.2.2.3) and the alignment was carefully carried out along the division line (50% spot for each side) using a red laser - Figure 4.23. The pulsed wave welding was performed according to parameters in the following tables.

Table 4.25 1st series of dissimilar NiTi/Ti-6Al-4V plate welds – welding parameters

1st Series of NiTi/Ti-6Al-4V welds									
Energy	Pulse duration	Welding speed	OV	Frequency	FPP	spot ø	Power	Intensity	Gas flow
(J)	(ms)	(mm/s)	(%)	(Hz)	(mm)	(mm)	(W)	(MW/cm^2)	(l/min)
55	20	1.1(3)	50	2.5	0	0.9	2750	0.43	15

Table 4.26 2nd series of dissimilar NiTi/Ti-6Al-4V plate welds – welding parameters

2nd Series of NiTi/Ti-6Al-4V welds									
Energy	Pulse duration	Welding speed	OV	Frequency	FPP	spot ø	Power	Intensity	Gas flow
(J)	(ms)	(mm/s)	(%)	(Hz)	(mm)	(mm)	(W)	(MW/cm^2)	(l/min)
48	17.5	1.1(3)	50	2.5	0	0.9	2743	0.43	15

Table 4.27 3rd series of dissimilar NiTi/Ti-6Al-4V plate welds – welding parameters

3rd Series of NiTi/Ti-6Al-4V welds									
Energy	Pulse duration	Welding speed	OV	Frequency	FPP	spot ø	Power	Intensity	Gas flow
(J)	(ms)	(mm/s)	(%)	(Hz)	(mm)	(mm)	(W)	(MW/cm^2)	(l/min)
55	20	1.1(3)	50	2.5	0	0.9	2750	0.43	Max.

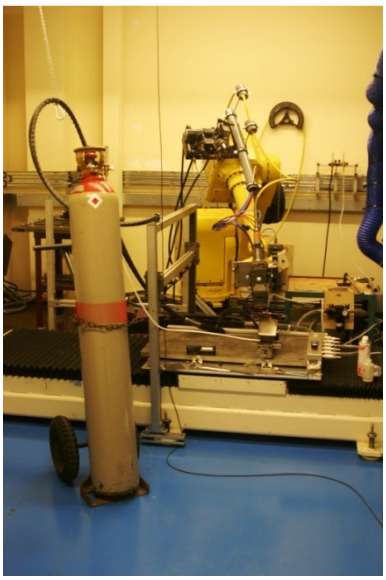

Figure 4.24 Fiber laser facilities

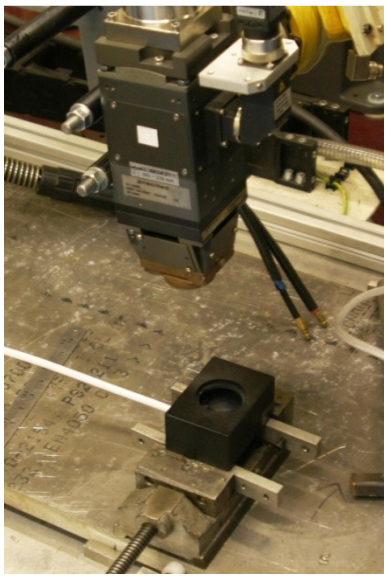

Figure 4.25 1st Fiber laser Experimental arrangement

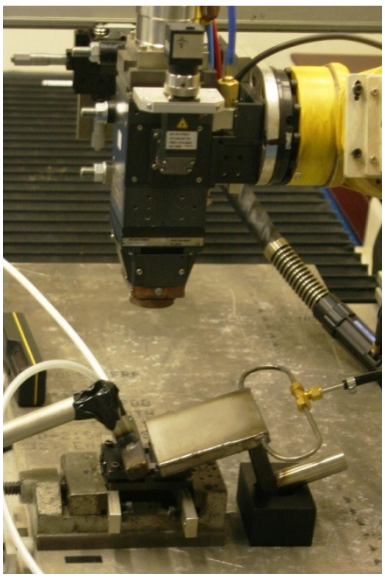

Figure 4.26 2nd Fiber laser Experimental arrangement

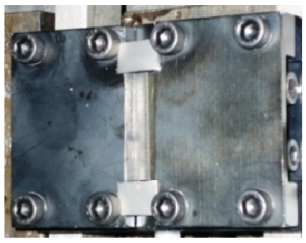

Figure 4.27 Start and end plates

Figure 4.24 presents the facilities where the dissimilar NiTi/ Ti-6Al-4V butt joints were welded in continuous wave mode using the Ytterbium fiber laser (yellow robot, at the back) and the special gaseous mixture (bottle in first plan). Due to the observation of severe oxidation several gas assistance configurations were tested: figure 4.25 shows the first, composed only by the classical jig and open chamber (gas feeding through the white pipe); the second was composed by the jig system with root gas assistance and the chamber was replaced by two additional systems, a flat nozzle (figure 4.26-right) and a spreader, both providing Argon. The fused-silica lens was not used due to the high energy intensity of the near focused beam, which would easily overheat and permanently damage this component.

Due to programming limitations of both laser and robot starting, first trials presented a hole in the start and ending points. The practical solution found for the problem was to introduce two small Ti-6Al-4V plates slightly overlapped with the butt joint at the start and ending points, protecting those regions by absorbing the laser burst. Figure 4.27 shows the solution during an alignment. Laser welding conditions and parameters are presented in the next tables.

Table 4.28 4th series of dissimilar NiTi/Ti-6Al-4V plate welds – welding parameters

4th Series of NiTi/Ti-6Al-4V welds							
Gas assistance mode	Start/end plates	Power	Welding speed	Heat input	FPP	Beam spot ø	Gas flow
		(W)	(mm/s)	(J/cm)	(mm)	(mm)	(l/min)
1st	No	900	25	360	0	0.47	15

Table 4.29 5th series of dissimilar NiTi/Ti-6Al-4V plate welds – welding parameters

5th Series of NiTi/Ti-6Al-4V welds							
Gas assistance mode	Start/end plates	Power	Welding speed	Heat input	FPP	Beam spot ø	Gas flow
		(W)	(mm/s)	(J/cm)	(mm)	(mm)	(l/min)
1st	Yes	1100	16.7	559	0	0.47	15

Table 4.30 6th series of dissimilar NiTi/Ti-6Al-4V plate welds – welding parameters

6th Series of NiTi/Ti-6Al-4V welds								
Plates ref.	Gas assistance mode	Start/end plates	Power	Welding speed	Heat input	FPP	Beam spot ø	Gas flow
			(W)	(mm/s)	(J/cm)	(mm)	(mm)	(l/min)
H1	1st	Yes	900	25.0	360	0	0.47	15
I1	1st	Yes	900	21.7	415	0	0.47	15
O1	1st	Yes	900	16.7	539	0	0.47	15

Table 4.31 7th series of dissimilar NiTi/Ti-6Al-4V plate welds – welding parameters

7th Series of NiTi/Ti-6Al-4V welds									
Plates ref.	Gas assistance mode	Start/end plates	Power	Welding speed	Heat input	FPP	Beam spot ø	Gas flow [2]	
								Face	back
			(W)	(mm/s)	(J/cm)	(mm)	(mm)	(Bar)	
G1 face	2nd	Yes	900	25.0	360	0	0.73	15	2
G1 root	2nd	Yes	900	33.(3)	270	0	0.73	15	2
F1	2nd	Yes	1000	16.7	599	0	0.73	15	2

4.4.3 Testing methods

4.4.3.1 Microstructure observations

Macro and microstructural observations were carried out on both similar and dissimilar welds. An experimental procedure for sample preparation was developed due to the lack of information in literature. The procedure is presented in annex C.

Optical observations were made in an *Olympus* CX40 microscope equipped with a DP21 video camera. SEM observations were both performed on a *ZEISS* DSM 962 ESM equipped with an Oxford *Instruments* INCAX-Sight EDS system and a *FEI Quanta* 400 FEG ESM equipped with an *EDAX* Genesis X4M EDS analyzer.

[2] Due to technical limitations it was not possible to measure the flow of this experiment for being over the range; however the pressure is presented as a reference for other trials and future work.

4.4.3.2 Microhardness measurements

Microhardness measurements were performed both on similar and dissimilar laser welded joints. Vickers microhardness profiles along the base material/welded zone/base material on transverse sections were attained on similar joints for design evaluation using a *Struers Duramin-1* micro indentation tester applying a test load of 500 mN.

Vickers microhardness measurements were performed on transverse sections of welded joints for parameters evaluation 1.0 and 0.5 mm thick, using a Mitutoyo *HM-112* microhardness tester by applying a test load of 1000 mN.

According to the standards [59] indentations were performed away more than three diagonals from each other and from the boarders.

4.4.3.3 Differential Scanning Calorimetry - DSC

DSC tests were performed on welded specimens aiming to characterize of the fusion zone and the base materials in terms of zero-stress structural transformation temperatures. Tests were carried on the *SETARAM* DSC92 calorimeter and CS92 controller unit (see 4.3.2.2). Liquid Nitrogen was used to cool down the system to about -90°C. DSC samples were extracted only from 1.0 mm thick laser welded similar butt joints, which initially had the geometry presented in figures 4.28 and 4.29 (dimensions in millimetres are only indicative).

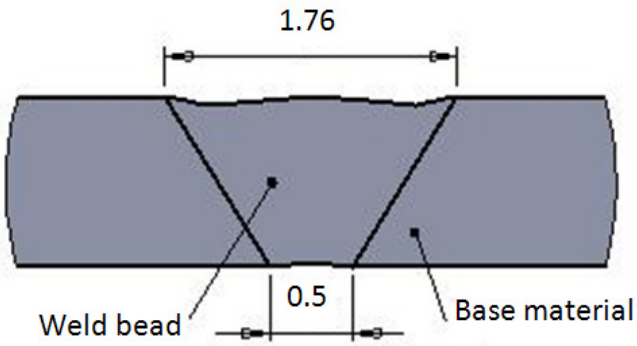

Figure 4.28 Typical dimensions of weld beads

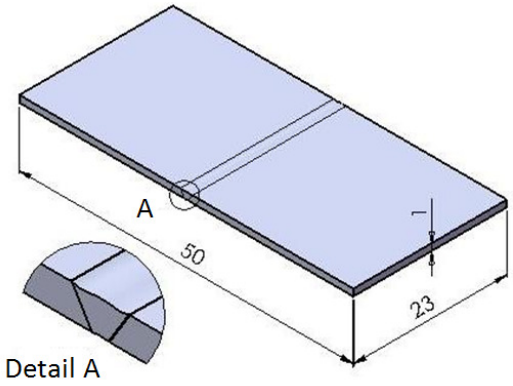

Figure 4.29 Schema of welded joints

For DSC testing, according to laboratorial experience, samples shall weigh at least about 60mg. According to geometry, considering material's density 6.5 g/cm^3 and the weld bead transversal area of about 1 mm^2, the minimum bead length that shall be removed for DSC tenting of the fusion zone is about 10 mm.

The weld beads were removed from butt joints using an *ATM Brilliant* precision cut-off machine and finished by hand, grinding with SiC paper of grit no. 400, in order to isolate only the FZ material. The weld beads were then cut into sections 3 mm long in the precision cut-off machine, in order to fit the DSC probe container. Chemical etching was performed to remove the mechanically affected film (in depth) using the HF 10% + HNO_3 45% + H_2O 45% in volume solution for about 10 minutes. Chemical neutralization was made with ethanol.

Samples from base materials were prepared by a similar procedure, providing a reference for further discussion. Fusion zone and base material samples' weigh are presented in table 4.32.

Table 4.32 DCS Samples weigh measurements

Sample type	Measured mass
	x 10^{-6} kg
NiTi – S 1.0 mm thick Base material for design evaluation	96.3 ± 0.05
Fusion zone material Joints for design evaluation	48.1 ± 0.05
NiTi – S 0.5 mm thick Base material for parameters evaluation	93.3 ± 0.05
NiTi – S 1.0 mm thick Base material for parameters evaluation	87.2 ± 0.05
Fusion zone material Joints for parameters evaluation	77.2 ± 0.05

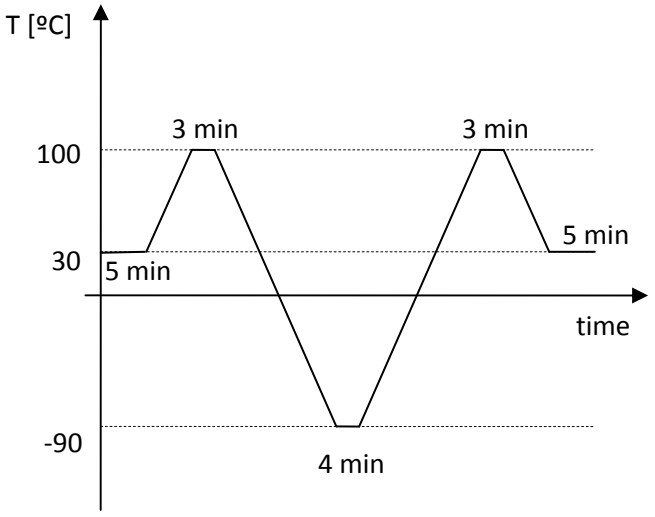

Figure 4.30 DSC programmed thermal cycle

The thermal cycle presented in figure 4.30 was programmed for testing both the fusion zone and base material DSC specimens. Both heating and cooling rates of 7^{o} C/min were used.

4.4.3.4 Uniaxial static tensile testing

Uniaxial static tensile tests were performed both on similar and dissimilar laser welded joints, as well as, on base materials. The effect of rolling direction was evaluated in terms of global mechanical behavior, regarding similar joints for design purposes. Prismatic section tensile specimens were prepared using the *ATM* precision cut-off machine with a diamond wheel, according to the geometry shown in figure 4.31, where 't' means thickness and 'w' width.

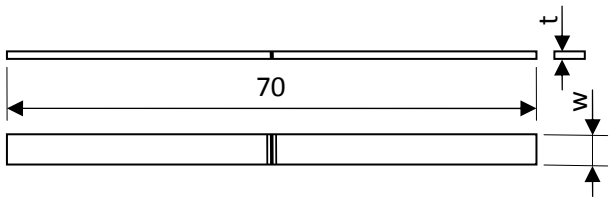

Figure 4.31 Geometry of similar tensile specimens

Due to geometrical limitations two configurations were adopted for plate shape tensile specimens, which are presented in table 4.33. Dissimilar wire shape specimens were tested as-welded.

Table 4.33 Geometry parameters of plate shape tensile specimens

Joint type	t	w
	mm	mm
Similar for design evaluation	1.0	4.0
Similar for parameters evaluation	1.0	3.0
Similar for parameters evaluation	0.5	3.0

Due to the nature of the different studies that were carried out, which involved a very different number of tensile specimens (parameters evaluation required about 6 times more), two techniques were used to extract the specimens from welded joints.

Tensile specimens for design evaluation, made from joints welded along and across the rolling direction were prepared using the *ATM* cut-off machine using the following parameters: rotational speed of 3500 rpm, feed rate of 3 mm/min, while cooling was attained with abundant cutting fluid.

The production time of tensile specimens for design evaluation was found out very high, about 55 min/unit, as materials waste on clamping and alignment methods was significant: considering scale went to about 43%. A special EDM tool was developed for overcoming such limitations (see annex D) improving the production time to 20 min/unit as waste was reduced to 31%. Regardless time and materials consumed along the design, engineering and production processes, an almost wear-free custom tool for proper production of tensile specimens, also regarding future work, was made.

An EDM *ALIC* DT-168 machine was used and the operational parameters for producing tensile specimens for parameters evaluation are presented in table 4.34. EDM specimens were finished by hand, grinding with SiC paper of grit no. 240.

Table 4.34 EDM Operational parameters

Pulse width	Off time	Voltage	Current		Gap	Stepper sensibility
			Rough	Finish		
level	level	(V)	level	level	level	level
100	2	100	10 [3]	4	8	5

Tensile tests were performed at room temperature on the *SHIMADZU* tensile testing machine (see 4.3.2.1) at low strain rates, both on cyclic and to failure routines, according to [14] not exceeding 0.05 %/s, which results on a testing speed of 1.0 mm/min for specimens initially 35.0 mm long between grips. Tests were performed both on the base materials and welded joints, in the case of joints and materials for design evaluation, both along and across the rolling direction.

Regarding tensile testing of welded joints for design evaluation and respective base materials, more than 30 specimens were tested. Successful tests are presented in tables 4.35 and 4.36.

[3] Current density of level 10 is about 4.5 A/cm^2

Table 4.35 Tensile testing references of base materials - similar joints for design evaluation

Tensile specimens for design evaluation							
Base materials							
Testing direction	Test type		Reference	Specimen geometry			Testing speed
				Thickness	Width	Length	
				(mm)	(mm)	(mm)	(mm/min)
Across	Failure		# 1	1.05	3.85	31.70	1.00
	Cyclic	Short	# 1	1.05	2.55	35.25	1.00
		Long	# 1	1.05	2.55	34.50	1.00
			# 2	1.05	2.55	36.00	1.00
			# 3	1.05	2.55	36.00	1.00
			# 4	1.05	2.15	35.60	1.00
			# 5	1.05	2.15	35.75	1.00
			# 6	1.05	2.15	35.90	1.00
Along	Failure		# 1	1.05	3.50	18.85	1.00
	Cyclic	Short	Lack of testing materials				
		Long					

Table 4.36 Tensile testing references of welded similar joints for design evaluation

Tensile specimens for design evaluation							
Welded specimens							
Welding direction	Test type		Reference	Specimen geometry			Testing speed
				Thickness	Width	Length	
				(mm)	(mm)	(mm)	(mm/min)
Across	Failure		# 1	1.05	3.85	34.50	1.00
			# 2	1.05	3.55	32.60	1.00
			# 3	1.05	3.15	30.70	1.00
	Cyclic	Short	# 1	1.05	3.00	34.50	1.00
		Long	# 1	1.05	3.00	38.25	1.00
			# 2	1.05	3.00	38.50	1.00
			# 3	1.05	3.00	39.00	1.00
Along	Failure		# 1	1.05	4.60	35.10	1.00
			# 2	1.05	4.25	35.45	1.00
			# 3	1.05	1.25	43.00	1.00
	Cyclic	Short	# 1	1.05	2.95	38.30	1.00
		Long	Lack of testing materials				

Table 4.37 Tensile testing references of 1.0 mm thick similar joints for parameters evaluation

Tensile specimens for parameters evaluation					
Welded specimens 1.0 mm thick					
Test type	Reference	Specimen geometry			Testing speed
		Thickness	Width	Length	
		(mm)	(mm)	(mm)	(mm/min)
Failure	A – A # 1	1.10	2.95	39.00	1.00
	A – A # 2	1.10	2.95	39.80	1.00
	B – B # 1	1.10	3.00	39.60	1.00
	B – B # 2	1.10	3.00	39.70	1.00
	C – C # 1	1.10	2.95	39.70	1.00
	C – C # 2	1.10	2.95	39.70	1.00
	D – D # 1	1.10	3.00	39.75	1.00
	D – D # 2	1.10	3.00	39.70	1.00
	E – E # 1	1.10	2.95	39.75	1.00
	E – E # 2	1.10	2.85	39.90	1.00
	F – F # 1	1.10	2.95	39.90	1.00
	F – F # 2	1.10	3.00	39.80	1.00
	G – G # 1	1.10	2.95	39.75	1.00
	G – G # 2	1.10	2.95	39.65	1.00
	H – H # 1	1.10	2.90	39.65	1.00
	H – H # 2	1.10	2.95	39.85	1.00
	I – I # 1	1.10	2.95	39.85	1.00
	I – I # 2	1.10	2.95	39.80	1.00

Table 4.38 Tensile testing references of 0.5 mm thick similar joints for parameters evaluation

Tensile specimens for parameters evaluation					
Welded specimens 0.5 mm thick					
Test type	Reference	Specimen geometry			Testing speed
		Thickness	Width	Length	
		(mm)	(mm)	(mm)	(mm/min)
Failure	F – F # 1	0.50	2.85	39.90	1.00
	F – F #2	0.50	2.95	40.00	1.00
	G – G # 1	0.50	2.80	39.80	1.00
	G – G # 2	0.50	2.90	39.75	1.00
	H – H # 1	0.50	2.80	39.75	1.00
	H – H # 2	0.50	2.95	39.85	1.00
	I – I # 1	0.50	2.80	39.90	1.00
	I – I # 2	0.50	2.70	39.65	1.00
	K – K # 1	0.50	2.85	39.80	1.00
	K – K # 2	0.50	2.80	39.80	1.00
	L – L # 1	0.50	2.80	39.75	1.00
	L – L # 2	0.50	2.80	39.80	1.00
	M – M # 1	0.50	2.85	39.90	1.00
	M – M # 2	0.50	2.80	39.75	1.00
	N – N # 1	0.50	2.85	39.90	1.00
	N – N # 2	0.50	2.95	39.80	1.00
	O – O # 1	0.50	2.85	39.90	1.00
	O – O # 2	0.50	2.85	39.75	1.00

Table 4.39 Tensile testing references of wire shape AISI 316LN specimens

AISI 316 LN base material				
Test type	Reference	Specimen geometry		Testing speed
		Diameter	Length	
		(mm)	(mm)	(mm/min)
Failure	# 1	1.00	28.25	1.00
	# 2	1.00	30.00	1.00
	# 3	1.00	30.20	1.00

Table 4.40 Tensile testing references of dissimilar wire shape joints

Dissimilar NiTi/AISI 316 LN shear joints				
Test type	Reference	Specimen geometry		Testing speed
		Welded length	Length	
		(mm)	(mm)	(mm/min)
Failure	# 1	9.63	31.00	1.00
	# 2	9.94	31.00	1.00
	# 3	9.95	31.00	1.00

4.4.3.5 SME evaluation

The experimental method for evaluating the shape memory effect ability of welded joints is based on bending and free-recovery testing. The testing procedure consists of bending a test piece in the martensitic condition, inducing lattice detwinning, followed by the remove of load and heating up to the parent phase, in a SME loop. Amongst the techniques reported in literature for SME evaluation ([34, 36 to 37]), bending tests represent a simple solution that does not require the use of complex testing machinery. Bending and free-recovery tests are particularly appropriate when specimens are martensitic either at or near room temperature [28] once that deformation can be applied at that temperature as free-bending can be attained only by heating up the deformed sample. Although not so straightly such testing method can also be applied to superelastic alloys, however cooling below M_f previous to bending is required. Despite being martensitic or austenitic at room temperature, characteristic DSC curves of the material must be known before programming any shape memory effect testing procedure.

Regarding the evaluation of shape memory ability on laser welded superelastic NiTi, the bending and free-recovery testing procedure was pointed out as the simplest and more attainable technique once that testing should take into account the evaluation of such properties over a relatively large number of cycles. The method was described in 1982 by Nishikawa *et al* [28] and is presented in figure 4.32.

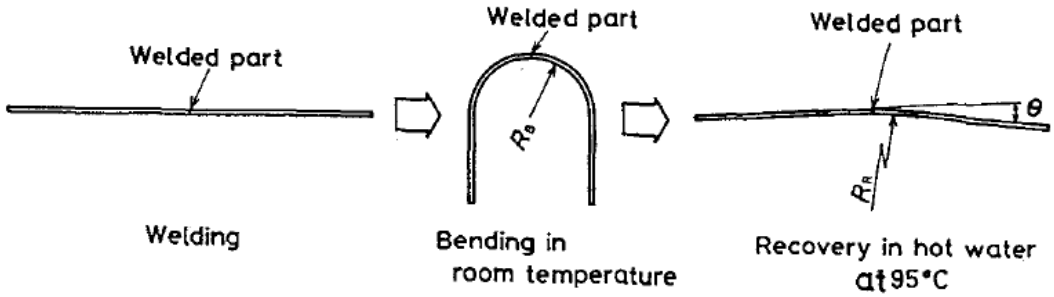

Figure 4.32 The bending and free-recovery method for martensitic alloys. Schema by [28]

The fundamentals of such testing method lie on the elastic pure bending theory, which is briefly presented in figure 4.33 and 4.34.

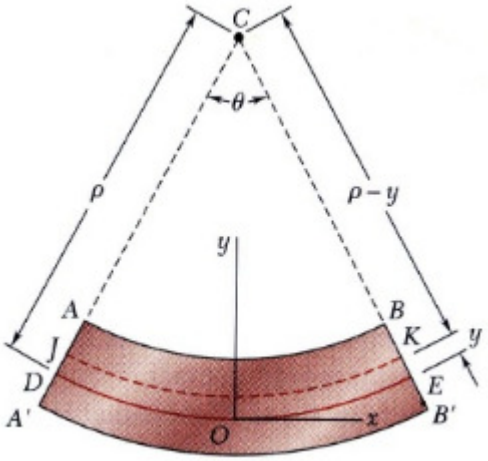

$$\varepsilon_x = -\frac{y}{\rho} \qquad \textbf{(4.2)}$$

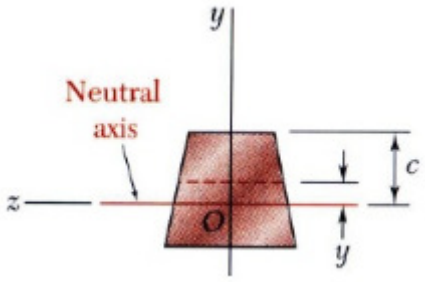

Figure 4.33 Schema of pure bending [60]

Figure 4.34 Bending section view [60]

According to equation 4.2, strain varies linearly over thickness, suggesting that higher strains occur on the inner and outer surfaces, while in the neutral plane strain equals zero (y=0).

The detwinning of martensite is known to be an anisotropic process, which behaves very differently from tension to compression [61]. Considering only the general tensile behavior of martensite, at strain levels close to 4 %, a significant amount of variant reorientation already occurred (see figure 2.6) as macroscopic apparent permanent deformation can be observed.

Considering the case of testing a specimen from the 1.0 mm thick laser weld joints for design evaluation, being desirable a maximum strain level of 4%, the parameters are y=-0.5 mm; ε_x=0.04, and equation 4.2 gives:

$$\varepsilon_x = -\frac{y}{\rho} \leftrightarrow \rho = -\frac{y}{\varepsilon_x} \rightarrow \rho = \frac{0.5}{0.04} = 12.5\ mm$$

The evaluation of shape recovery ability was studied in 1992 by Lin *et al* [62], which adopted the procedure shown in the schema of figure 4.35. R_{SME} was called the measured shape recovery and such concept was adopted to evaluate the shape memory effect ability on this study. For that purpose was developed a special mechanism that allows bending superelastic specimens dipped in liquid nitrogen.

Depending on DSC results the return to the parent phase can be achieved either by warm up to room temperature or using a thermalized bath. The permanent deformation angle, θ_f, will be evaluated either by photograph/profile projection analysis or direct measurement using a precision gauge.

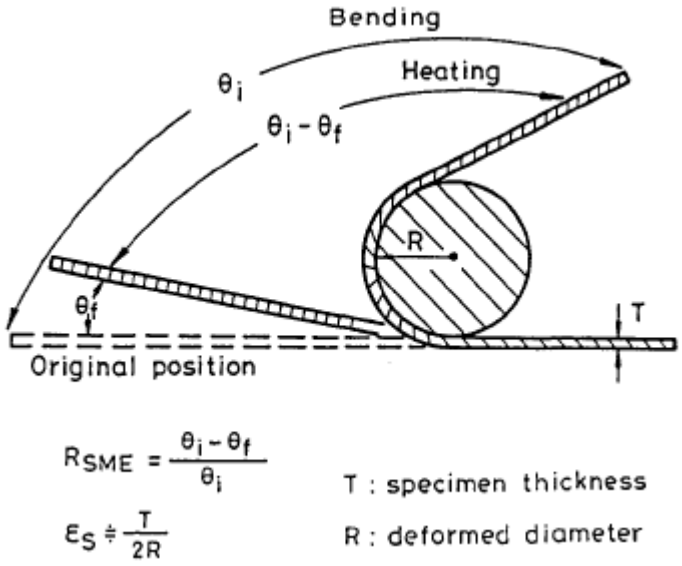

Figure 4.35 Schematic illustration of SME bending [62]

5. Results and discussion

The experimental results are now presented and discussed. According to the previous structure, results follow the logical flow presented in the experimental work, thereby were sorted in two main groups: Results from similar and from dissimilar joints.

5.1 Similar joints

5.1.1 Bead on plate welds results

The purpose of these welds was to evaluate parameters and operational conditions, such as the gas assistance mode. Macrostructural observations were carried on etched transverse sections of these welds by optical microscopy, which are next presented.

5.1.1.1 Metallographic observations

Macrographs of some of the weld beads are presented from figures 5.1 to 5.5. Partial penetration was in some cases attained due to excessive welding speed, as shown in figure 5.1. The microstructure of the fusion zone was constituted by coarse epitaxial grains. Extensive porosity was often observed in the fusion zone. Frequently, the extent of the heat affected zone is not clear.

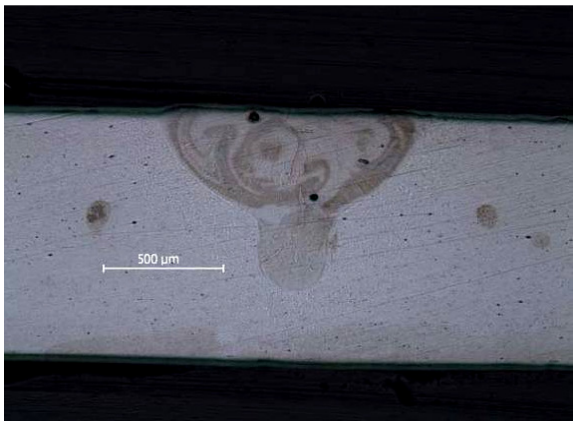

Figure 5.1 NiTi bead on plate #2

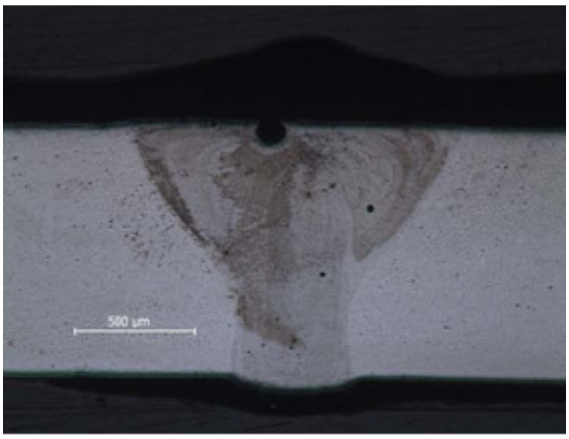

Figure 5.2 NiTi bead on plate #3

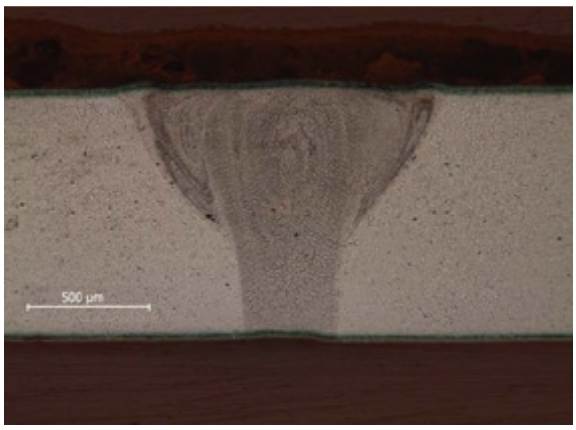

Figure 5.3 NiTi bead on plate #4

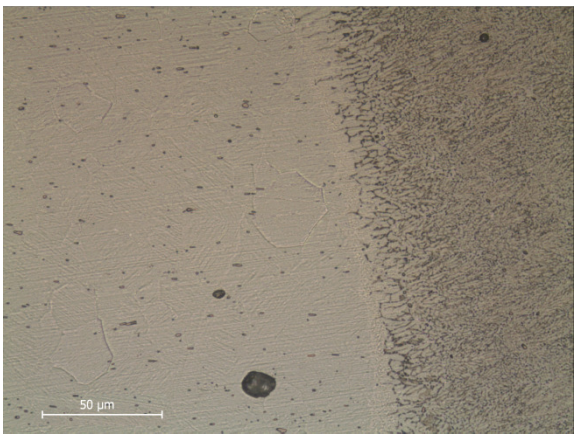

Figure 5.4 Transition Zone of bead #4

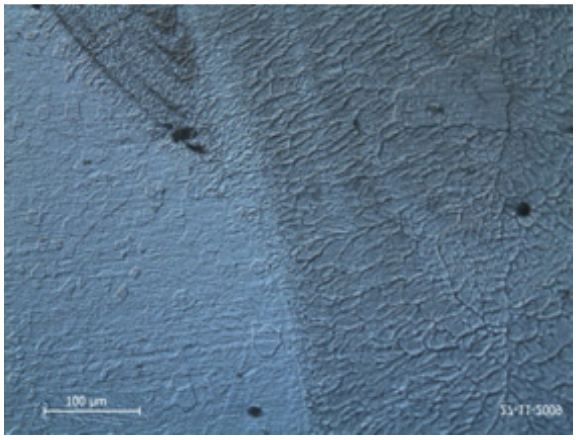

Figure 5.5 NiTi bead on plate #6 – dark field

From previous figures it can be seen that keeping the laser power constant and only changing the welding speed, very different weld geometries can be obtained and defect formation can be controlled. The gas protection chamber was found to be crucial to prevent porosities. A more efficient system was developed within this study as described previously. From these results the importance of the heat input was reinforced and studied.

5.1.2 Results from joints for design purposes

The welded joints for design purposes were the most extensively studied, thus a number of results from extensive testing are presented in the next paragraphs.

5.1.2.1 Structural observations

The as-welded similar joints for design evaluation were first observed by means of SEM. Figure 5.6 presents a top view of the weld face, revealing the presence of extensive porosity in the centre of the welded zone, which can be observed at higher magnification in figure 5.7. Figure 5.6 also allows

observing the presence of peculiar solidifying structures in the interface between the base material and the fusion zone, growing along the heat flow direction, as figure 5.8 shows in detail. Those structures which only were observed on the top surface are related to the solidification rate which strongly depends on the welding speed and boundary conditions [41]. Figure 5.9 presents an observation carried out on a weld bottom face, where it is possible to identify the presence of severe oxidation in the weld centreline. Despite oxidation, no porosity was observed in the root.

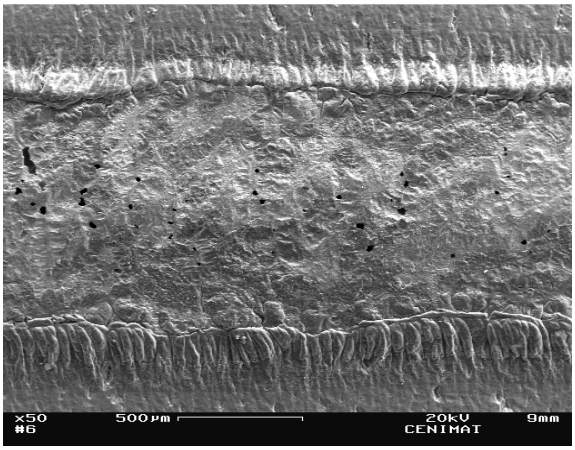

Figure 5.6 SEM observation of the top of a similar weld at low magnification

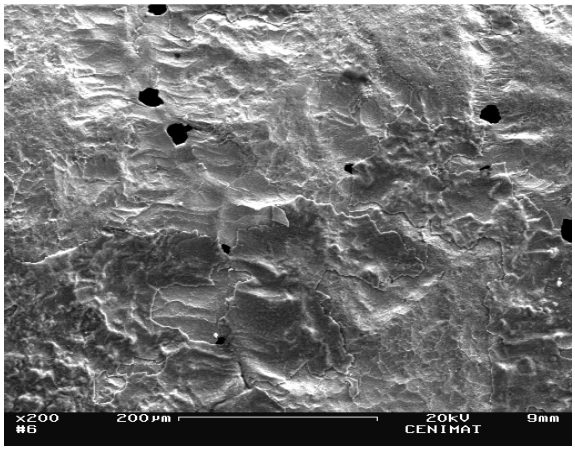

Figure 5.7 SEM observation on the top of the weld centre revealing extensive porosity

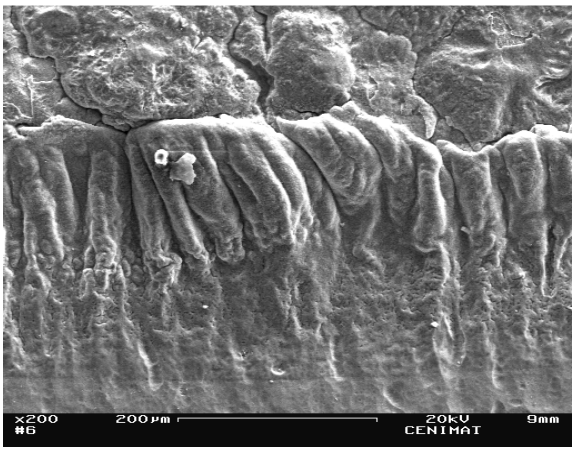

Figure 5.8 SEM top observation of the transition zone revealing peculiar structures on similar welds

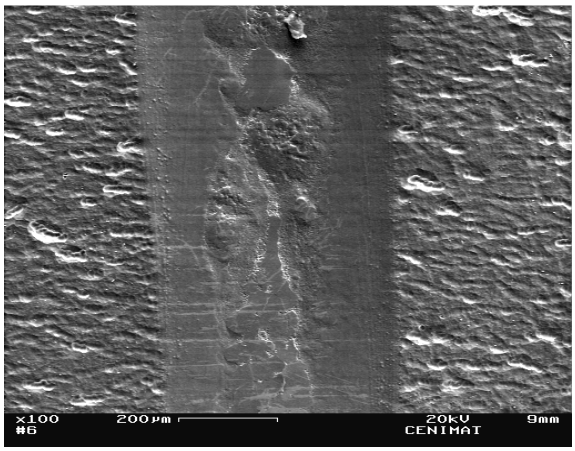

Figure 5.9 SEM observation at the bottom of a similar weld

Macro and microstructural observations were carried on transverse sections of welded joints, by optical microscopy and SEM. Concerning structural issues alike features were found in both similar and dissimilar welded zones, a consequence of extensive recrystallization.

Macrographs from a joint welded across the rolling direction are presented in figures 5.10 and 5.11, in which are identified the welding zones (concluded based on structural and further hardness observations). Microstructural details are presented next.

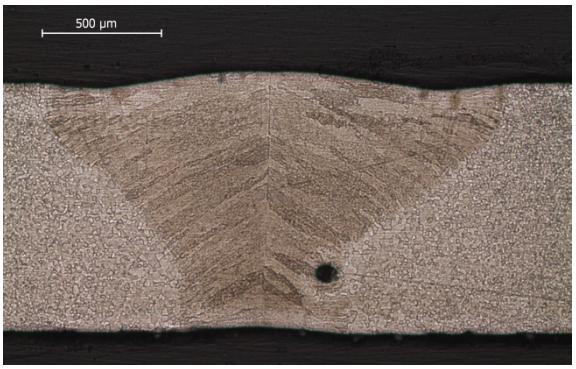

Figure 5.10 Macrograph of a similar joint for design evaluation welded across the RD

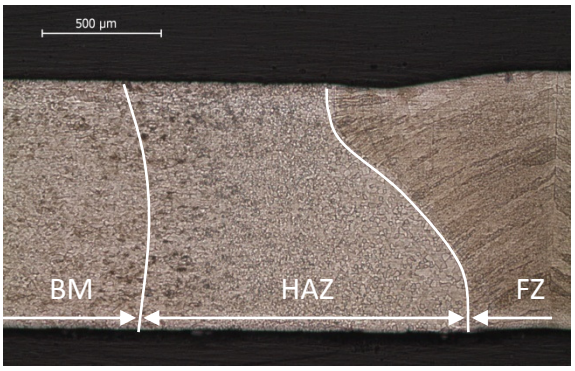

Figure 5.11 Macrograph of a similar joint for design evaluation welded across the RD – welding zones identified

Figure 5.12 depicts the microstructure of the base material, which presents a fine grained annealed austenitic structure. Figure 5.13 presents the microstructure of the HAZ where coarse equiaxed grains can be observed and figure 5.14 shows the transition between the HAZ and the fusion zone. The fusion zone presents epitaxial columnar grains developed from the base material to the weld centreline. The microstructure of this zone, which is mainly constituted of NiTi is very fine due to rapid solidification (figure 5.15). Similar observations were reported by others [33, 39, 43]. Similar structures were observed by [17, 33].

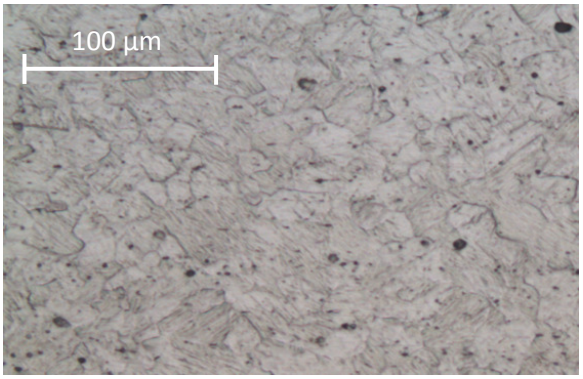

Figure 5.12 Microstructure of the base material

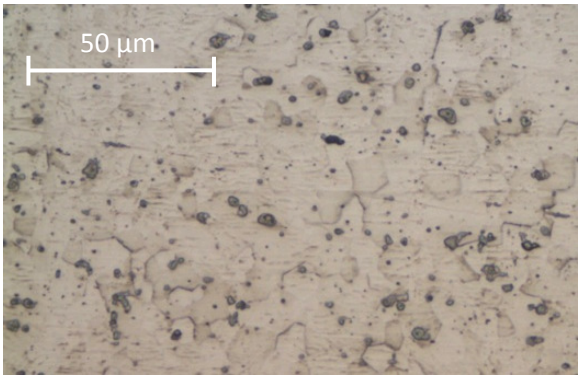

Figure 5.13 Microstructure of the HAZ

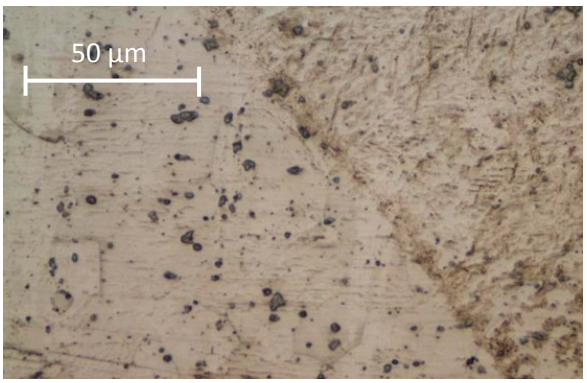

Figure 5.14 Micrograph of the transition zone

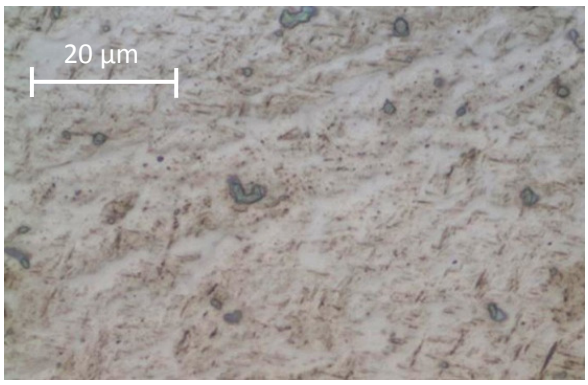

Figure 5.15 Microstructure of the fusion zone

SEM observations were also carried on transverse sections of similar joints, pointing out to the same conclusions attained by optical microscopy about grain size and growth direction both in the HAZ and FZ. Figure 5.16 presents the microstructure of the HAZ revealed by secondary electrons, which is mainly constituted by equiaxed grains and small precipitates. The microstructure of the fusion zone was observed by means of backscattered electrons and is presented in figure 5.17, which confirms its very fine structure and columnar grain growth to the centreline.

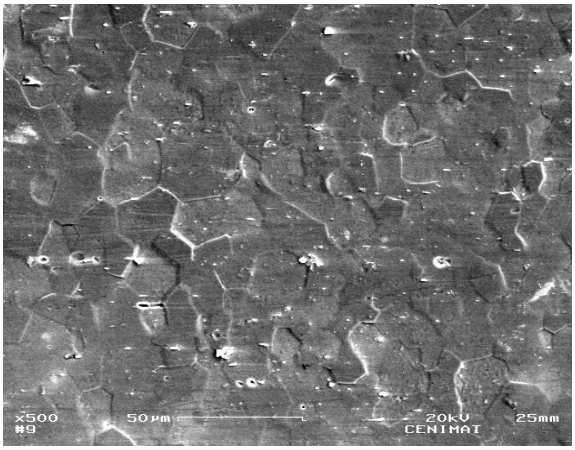

Figure 5.16 SEM observation of the HAZ on a transverse section of a similar specimen

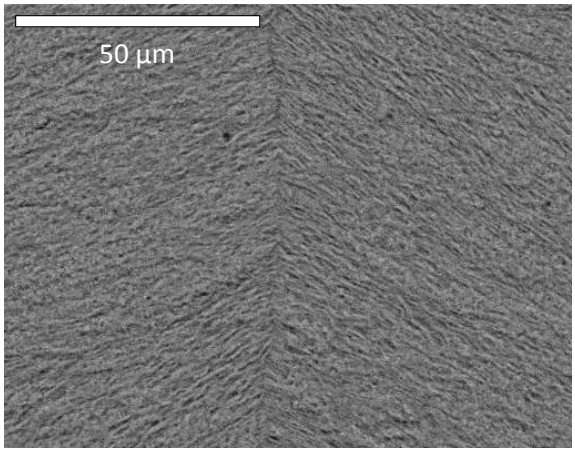

Figure 5.17 SEM observation of the FZ on a transverse section of a similar specimen

EDS analysis was carried on the transverse sections observed before. First measurements were performed in order to confirm the chemical elements present in the fusion zone and, as expected, both Ni and Ti were found in significant amounts in specimens welded along and across the rolling direction. No other metallic elements were found in the weld, as presented in figure 5.18.

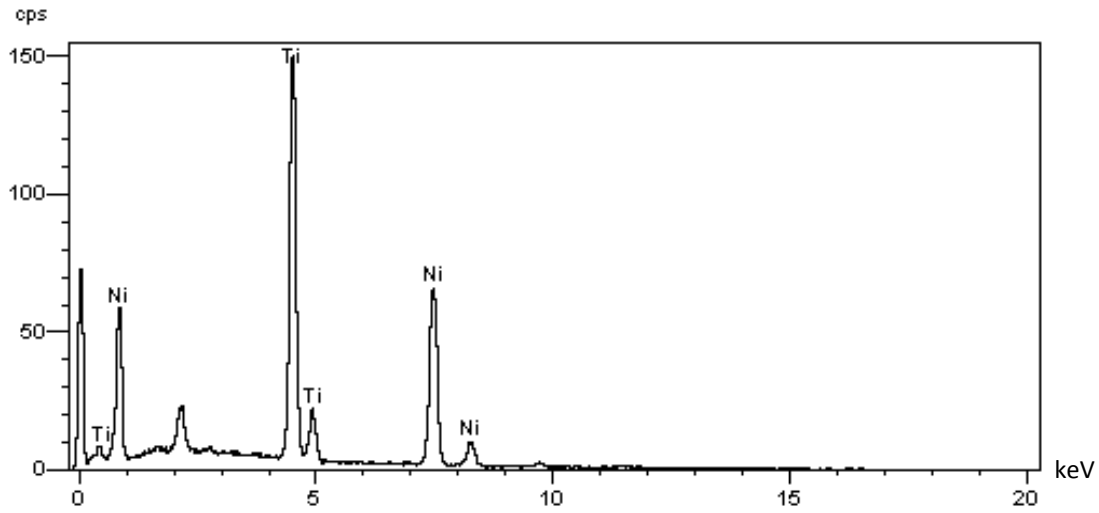

Figure 5.18 EDS Spectrum of the weld metal

EDS measurements were also performed both in the HAZ, FZ and in the transition zone, in order to figure out the relative chemical composition of some constituents.

Figure 5.19 presents a SEM observation of the HAZ attained by backscattered electrons. EDS chemical analysis was performed on the points marked from 1 to 4. Figure 5.20 shows a similar observation in the transition zone, where several EDS measurements were also made.

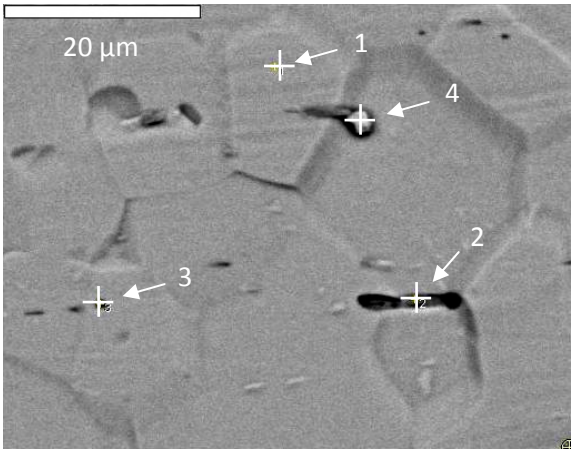

Figure 5.19 SEM observation of the HAZ showing EDS measurements locations

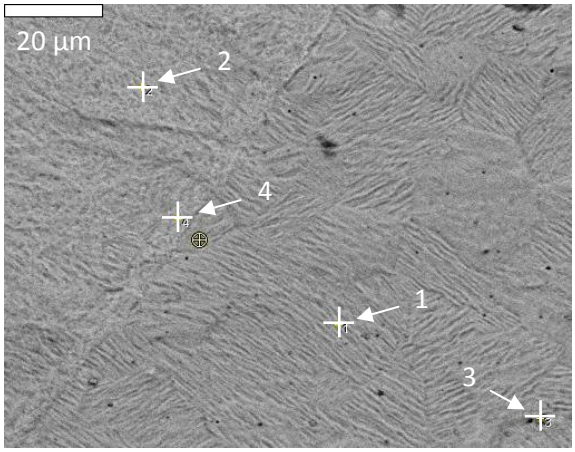

Figure 5.20 SEM observation of the transition zone showing EDS measurements locations

Regarding figure 5.19 the chemical EDS measurements of points 1 to 3 are presented in figure 5.21, as their main constituents are Ni and Ti. The composition of the structure marked as 4 was pointed out as copper, so that probably it is just a particle embedded during grinding or polishing.

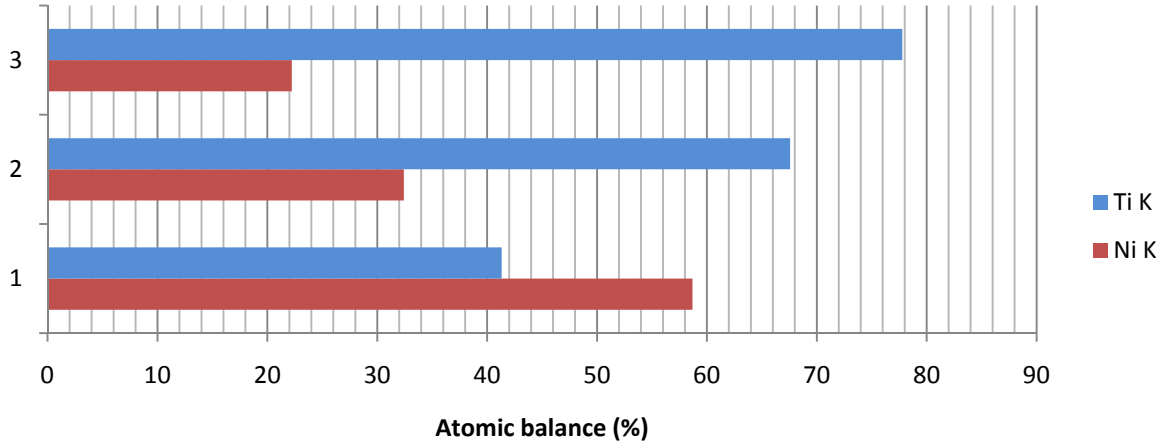

Figure 5.21 EDS analysis results of points marked in figure 5.19

Semi-quantitative data presented in figures 5.21 and 5.22 was balanced for two elements (Ti and Ni) and the signal was acquired with a system resolution of 108 eV. Considering figure 5.19 and figure 5.21 it can be observed that point 1 most likely corresponds to NiTi, which points out that an error of about 8% can be expected, even when acquiring the signal from a large area. Point 2 presents a Ti composition about two times the Ni content, suggesting the presence either of a $Ti_4Ni_2O_x$ oxide or most likely of a Ti_2Ni intermetallic precipitate elongated by the effect of cold-work.

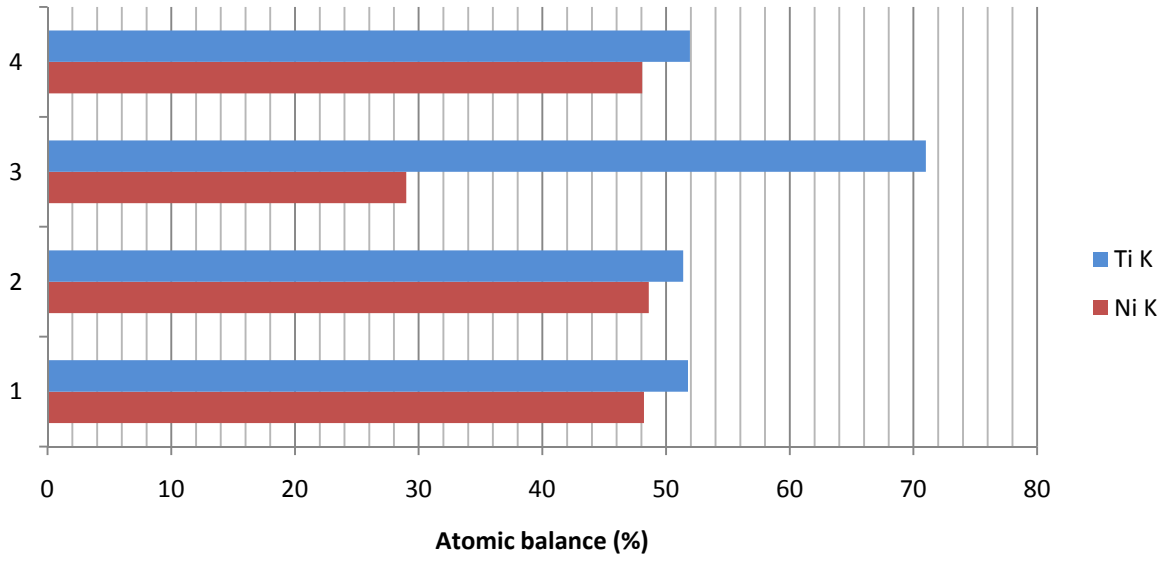

Figure 5.22 EDS measurements results of figure 5.20

Figure 5.22 suggests that in figure 5.20 both the composition of the HAZ, the transition zone and the FZ is nearly equiatomic NiTi (points 1, 2 and 4). Point 3 aims a small darker structure, which according

to EDS results is most likely Ti_2Ni. Assuming that both TiC and Ti_2Ni exist in the base materials, with fusion welding of the NiTi matrix above 1310°C the Ti_2Ni precipitates melt at about 1015°C, however the same is most likely not true for Titanium carbides, which melt around 3170°C. Most likely, as optical and electronic microscopy support, both very small and scattered TiC particles from the base material may be present in the fusion zone, however may also be present bigger Ti_2Ni intermetallic precipitates, although formed during cooling.

Scanning EDS analysis was performed along two lines, one in the transition zone and another in the weld centre, which are presented with the respective balanced Ti and Ni composition spectra in figures 5.23 and 5.24. From the results it can be concluded that the welded zone is a NiTi matrix in which can exist small Ti_2Ni precipitates and, eventually, smaller TiC particles.

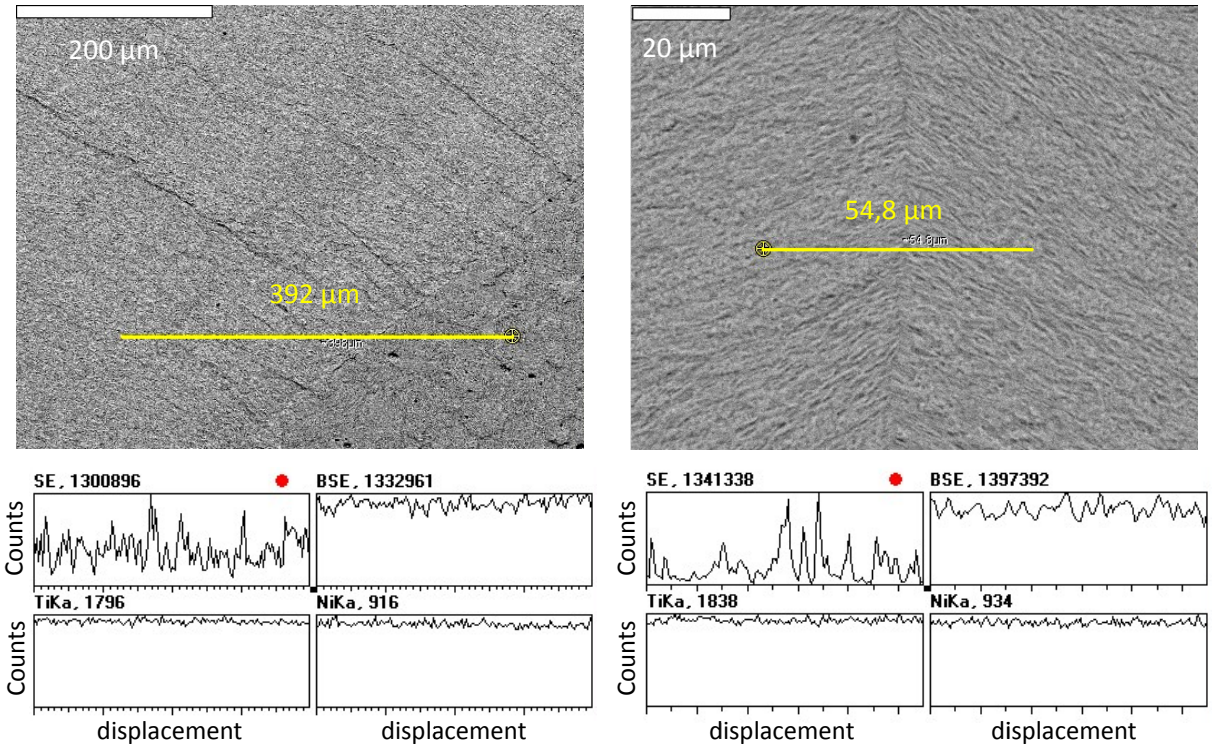

Figure 5.23 EDS line scanning on the transition zone and respective spectrum of Ti and Ni.

Figure 5.24 EDS line scanning on the weld centreline and respective spectrum of Ti and Ni

5.1.2.2 Microhardness measurements

Vickers microhardness measurements were carried out on transverse sections of specimens welded along and across the rolling direction, by applying a test load of 500 mN.

Figure 5.25Figures 5.25 and 5.26 present the resulting hardness profiles combined with transverse sections macrographs of welded joints. It is possible to identify in both profiles symmetry that clearly

distinguishes the weld zones. A typical decrease in hardness values of about 50 MHV0,05 can be observed in the transition between the heat affected zone and the fusion zone.

A continuously increasing trend of hardness is observed when approaching the non-affected base material, from the fusion zone, essentially due to the effect of grain size. Some scattering may be observed due to the small load applied, which conducted to extreme sensivity, although no brittle phases were identified in the fusion zone.

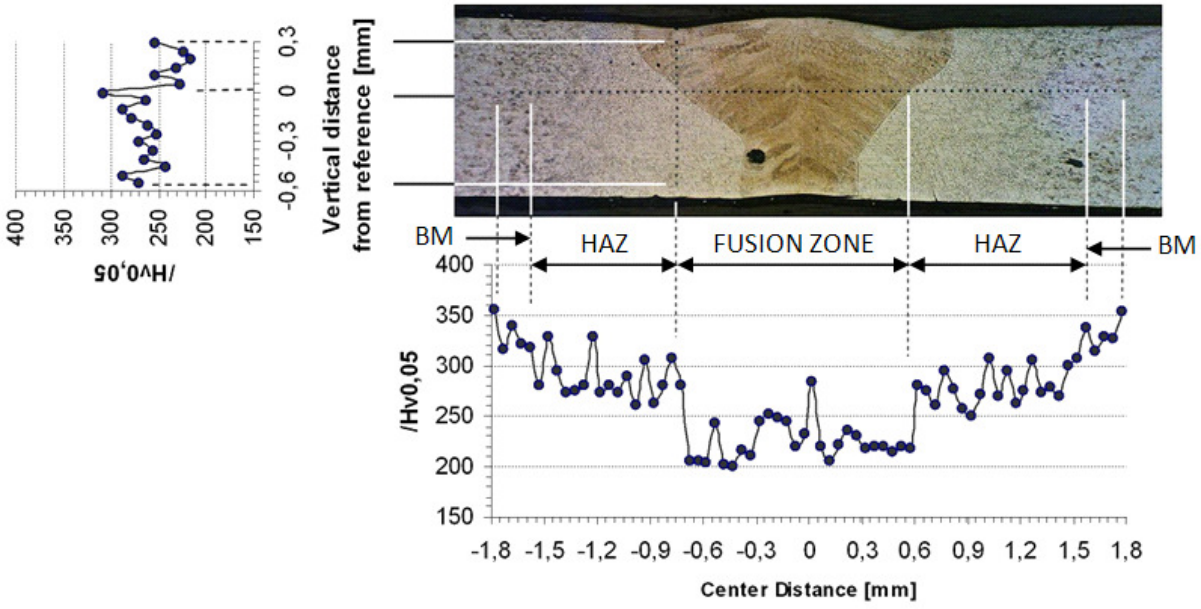

Figure 5.25 Microhardness profile of a specimen welded across the rolling direction

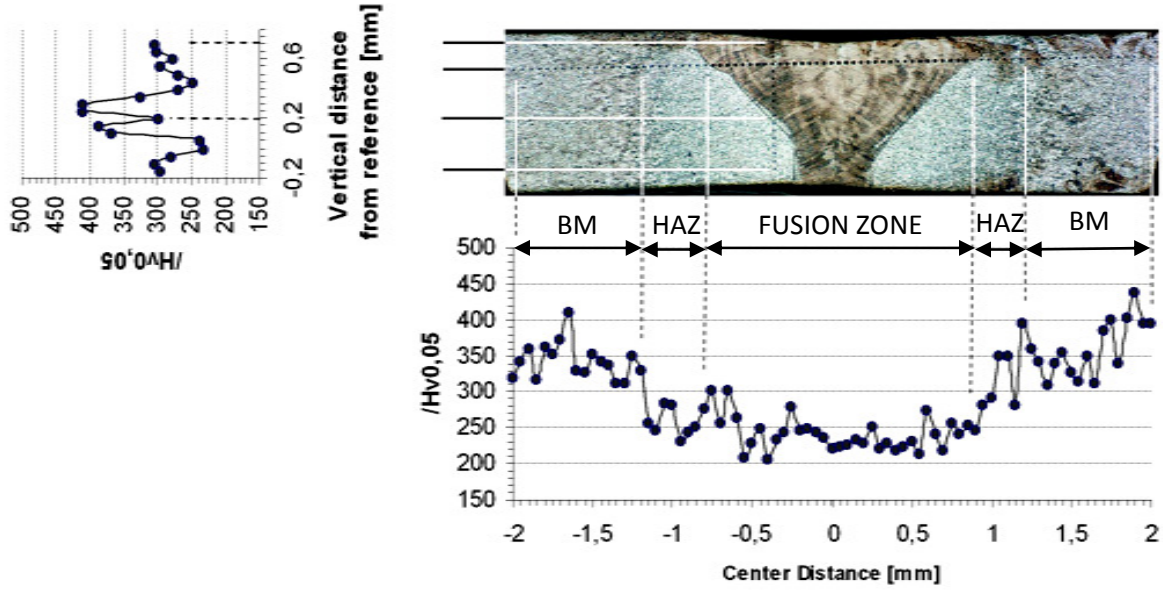

Figure 5.26 Microhardness profile of a specimen welded along the rolling direction

5.1.2.3 DSC measurements

The transformation temperatures measured by DSC on the base material and the weld metal, to identify the main phase transformations with temperature, for a zero-stress condition, and are depicted in figure 5.27 and summarized in table 5.1.

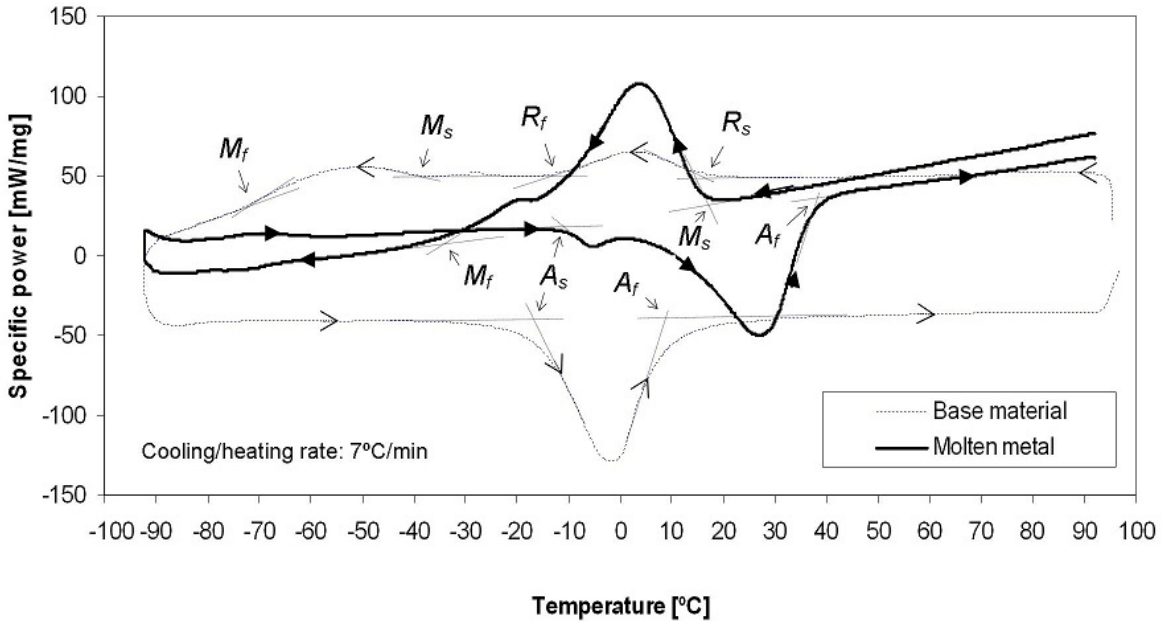

Figure 5.27 DSC measurements of base and weld material of similar joints for design evaluation

Table 5.1 DSC results from similar joints for design evaluation

	R_s	R_f	M_s	M_f	A_s	A_f
	ºC	ºC	ºC	ºC	ºC	ºC
Base material	15	-14	-39	-71	-17	9
Molten metal	-	-	17	-34	-11	37

The DSC curve of the base material identifies a two-step transformation from austenite B2 structure to r-phase and then from r-phase to martensite B19'. However, the sample removed from the fusion zone exhibits two relevant B2 to B19' and B19' to B2 transformation upon cooling and heating, respectively. That behavior, different from base material, suggests the occurrence of two distinct martensitic transformations on molten metal, at slightly different temperatures, evidencing the existence of two distinct regions with different compositions. Comparing the endothermic peaks, it can be observed that the martensitic transformation of the main constituent, responsible for the

most significant heat flow, occurs at a higher temperature range, compared to the smaller volume fraction region.

A similar, although not so evident behavior (about twice less spaced in temperature), was observed in the DSC results of Tuissi *et al* [34]. In that work the base material exhibited the same typical two-step martensitic transformation on cooling described before, although laser welding was attained in pulsed mode, and the reason for the difference may be in the process arrangement.

Is well known from literature that the martensitic transformation temperature is strongly dependent upon composition [9], particularly the increase of Ni content above the equiatomic condition causes a significant decrease in transformation temperatures.

In fact, Titanium is known for exhibiting high reactivity, oxidizing easily at high temperature if an inert gas protection is not completely ensured during fusion welding. This leads to the formation of Ti depleted (Ni-richer) solid solution regions (in a minor volume fraction compared to the remaining fusion zone) that may be quenched as such to room temperature. The resulting Ni-richer (minor volume fraction) region would present lower transformation temperatures.

5.1.2.4 Tensile tests

Tensile tests were performed both on base material and specimens from similar joints for design evaluation, according to the conditions presented in tables 4.35 and 4.36. The mechanical properties measured on the base material are dependent on tensile direction, that is, when the material was tested along the rolling direction, higher ultimate tensile strength and elongation to fracture were observed, due to anisotropy induced by cold-rolling. This effect, as well as the superelastic plateaus typical of SMA at stress levels of about 400, can be observed in figure 5.28, which depicts the tensile tests conducted to failure on the base materials, tested both along and across the rolling direction.

The results of tensile testing performed to failure on specimens welded across and along are presented in figures 5.29 and 5.30 (nomenclature according to table 4.36). Welded specimens present lower tensile stress and strain to rupture than the base material, which is mainly due to the unfavorable microstructure of the fusion zone and welding defects such as porosities. However, they exhibited approximately the same stress level for the plateau of the stress induced austenite to martensite transformation. The rupture of the welded joints took place at strain levels in the range of 8 to 12%, just before the SIM would start to increase to be elastically deformed and the stress level at the base material started increasing more significantly.

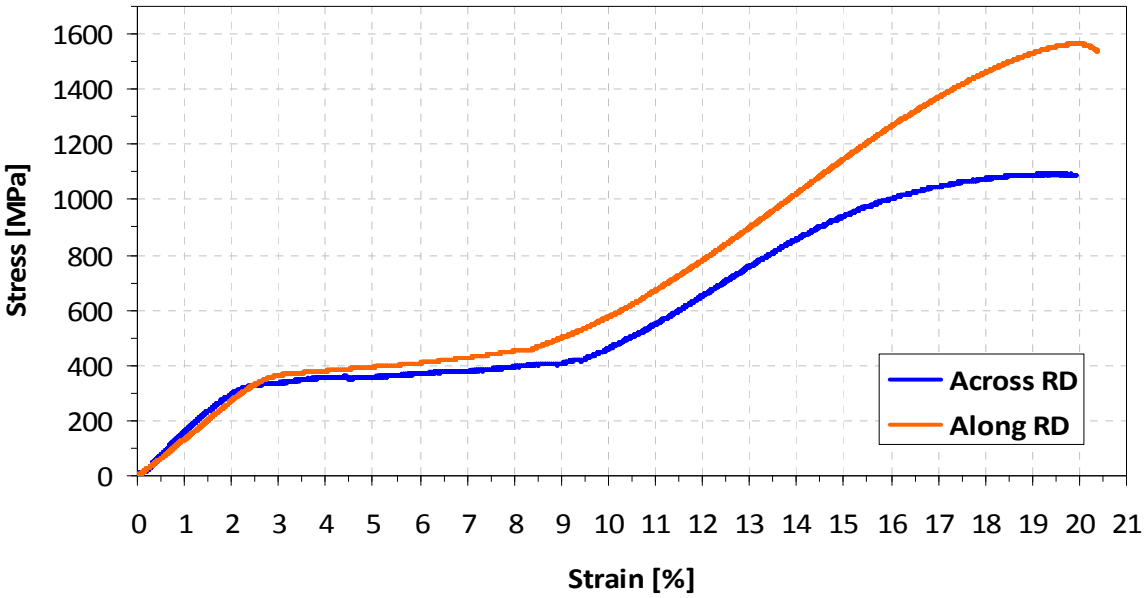

Figure 5.28 Tensile results of base materials tested up to failure

Comparing results from figures 5.29 and 5.30 it is possible to observe that specimens welded across the rolling direction presented slightly superior ultimate tensile strength and consequent superior elongation to rupture, when compared to specimens welded along the rolling direction.

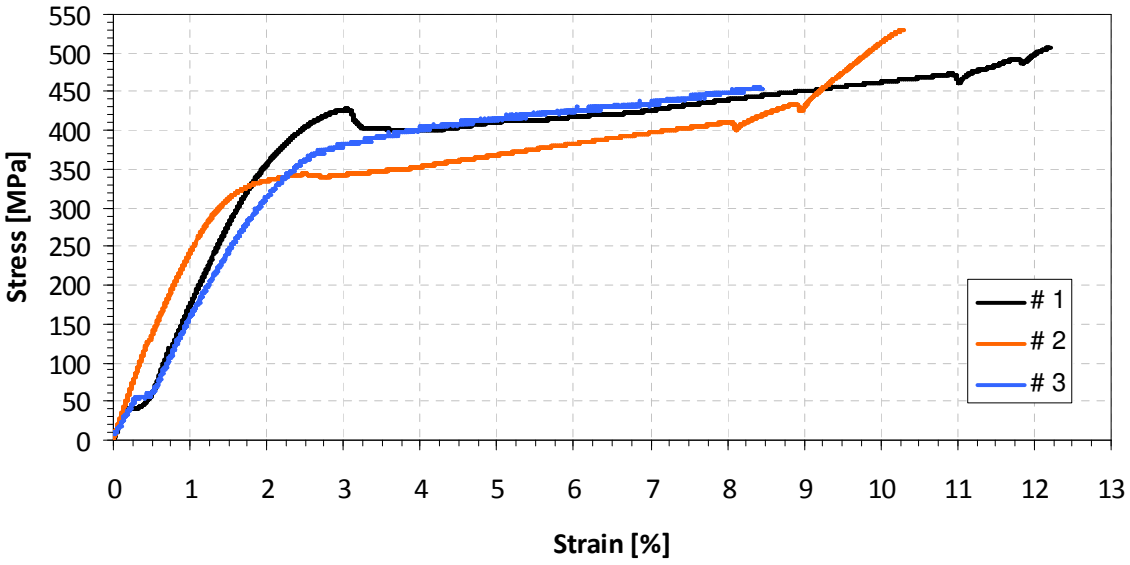

Figure 5.29 Tensile results of specimens welded across the rolling direction

The ultimate tensile properties of welded joints are presented in table 5.2. Some scattering of results can be observed on welded specimens due to internal small defects such as porosities, which were observed in some welded specimens.

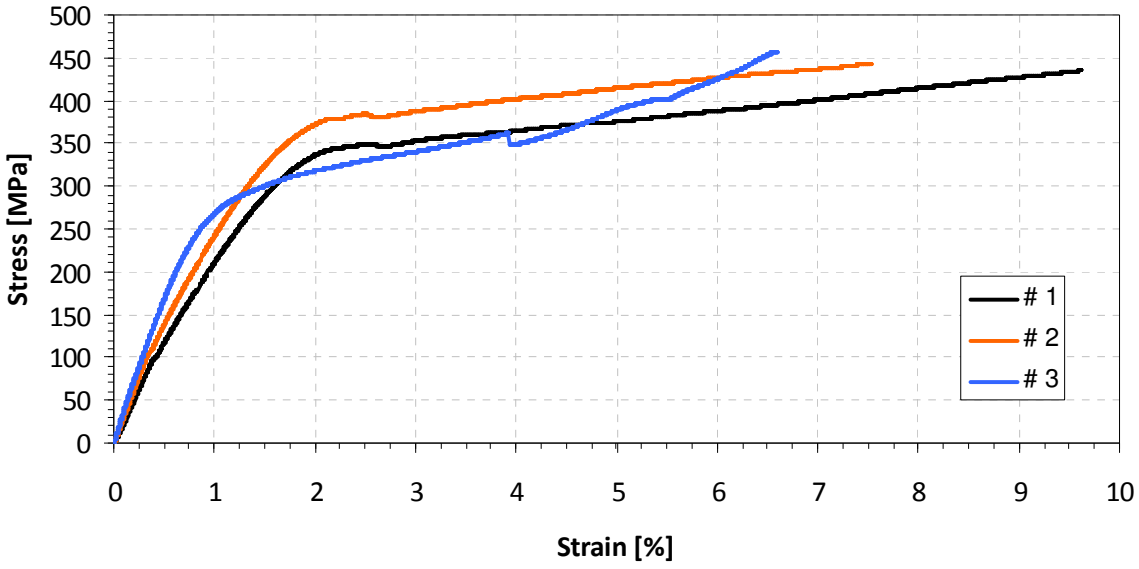

Figure 5.30 Tensile results of specimens welded along the rolling direction

From figures 5.29, 5.30 and table 5.2 it is possible to confirm that specimens welded across the rolling direction attained mean strength levels about 50 MPa and 2.5 % higher than specimens welded along the rolling direction.

Table 5.2 Mechanical properties of welded specimens

Welding direction relative to rolling	Tensile strength	Elongation to fracture
	MPa	%
Across	498±37	10.44±1.69
Along	445±12	7.90±1.55

In terms of smart design involving superelasticity, is required repeatable cyclic behaviour along a loading path, for a large number of cycles. In fact related to each cycle changes occur in the microstructure and accumulation of inelastic strain, which tend to stabilize over continuous transformation cycles, leading to the stabilization of the pseudoelastic hysteretic response.

The cyclic tensile behaviour both of base material and welded specimens was first tested in three cycles up to 8% strain. Results are presented in figures 5.31 to 5.33.

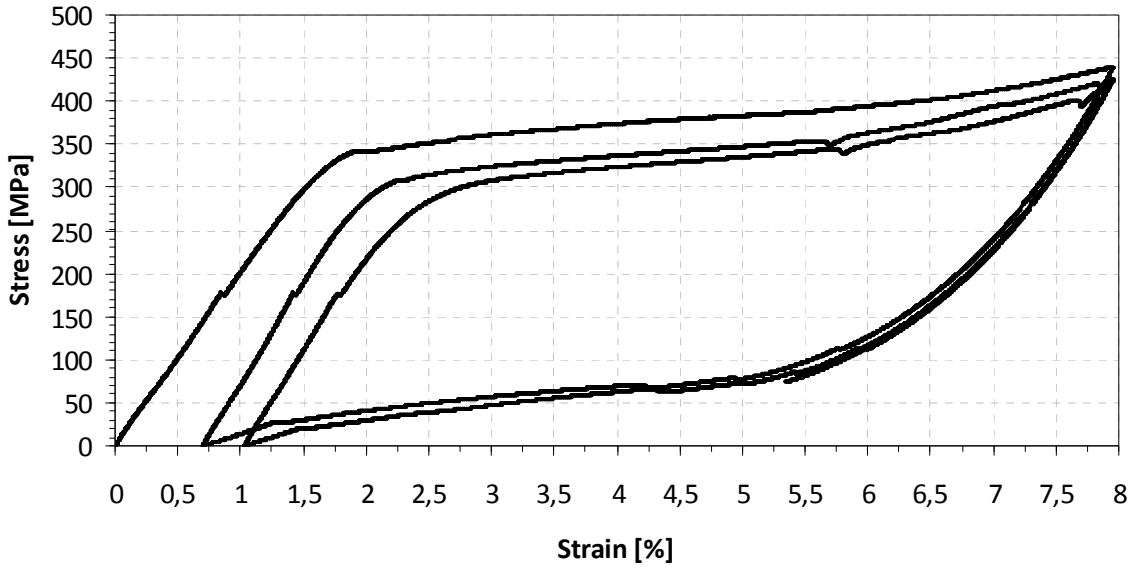

Figure 5.31Short cyclic testing of base material up to 8%

Results from mechanical cycling reveal that the superelastic behaviour of laser welded joints is similar to base material's, even when straining up to 8%, which induce stress levels near to the ultimate tensile strength of welded joints (shown in figures 5.29 and 5.30). It can be observed that for the number of cycles tested the mechanical response is far from stabilizing, which is suggested by the significant accumulation of inelastic strain in the last two cycles.

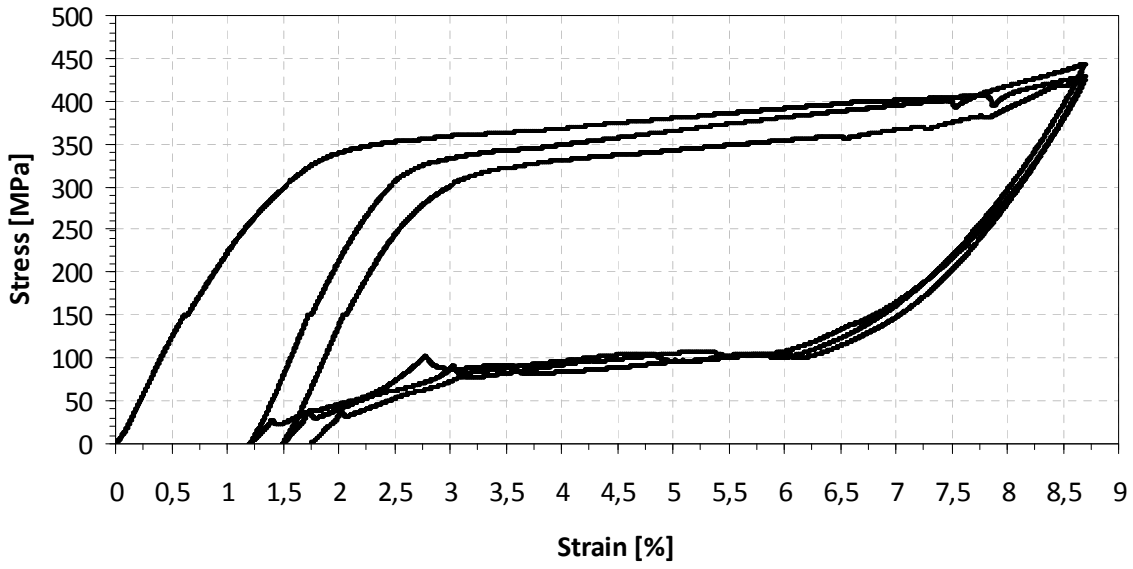

Figure 5.32 Short cyclic testing up to 8% of a similar joint welded across the rolling direction

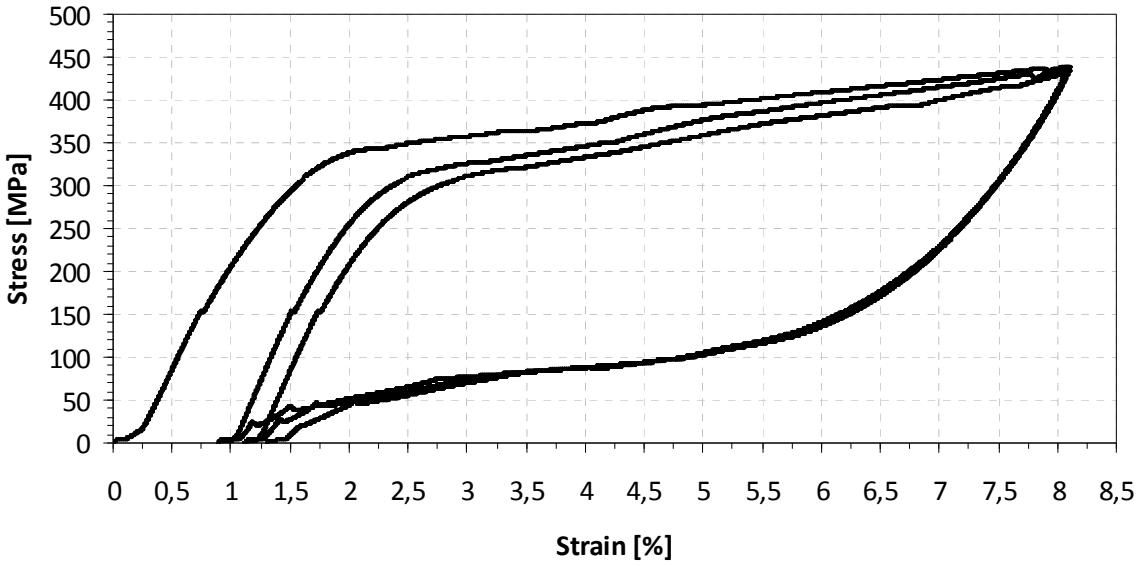

Figure 5.33 Short cyclic testing up to 8% of a similar joint welded along the rolling direction

In order to evaluate the stabilization of the pseudoelastic hysteretic response both the base material and welded specimens were submitted to tensile cycling over 30 cycles to each of the following strains: 4%, 6% and 8%, totalizing 90 cycles for each sample. Results from base material are depicted in figures 5.34 to 5.36. Results from welded joints are presented in figures 5.37 to 5.39.

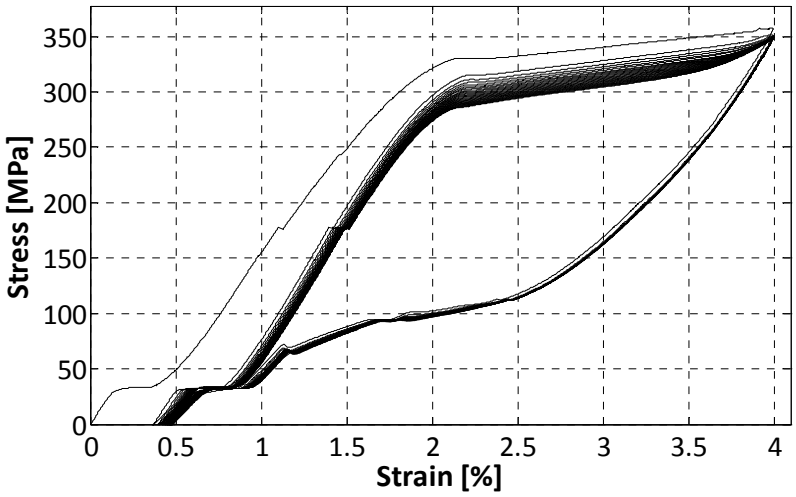

Figure 5.34 Long tensile cycling of the base material up to 4%

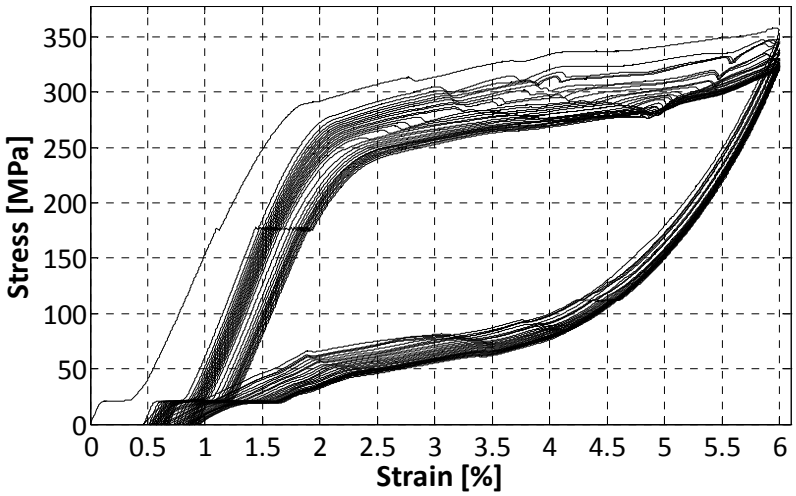

Figure 5.35 Long tensile cycling of the base material up to 6%

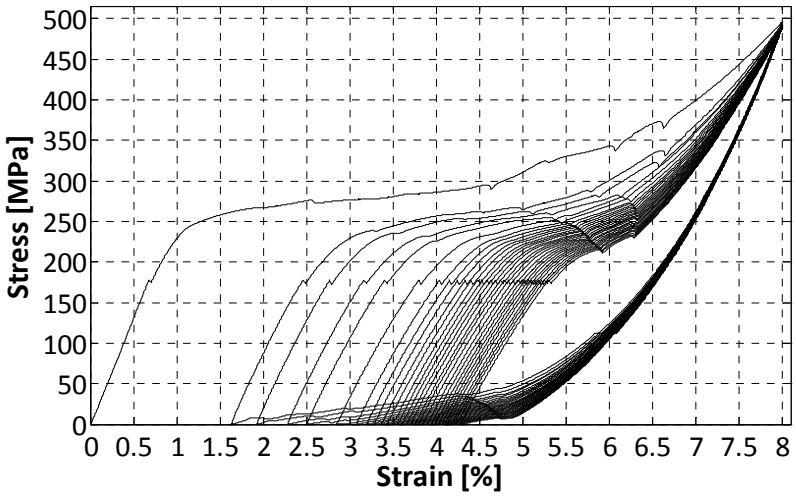

Figure 5.36 Long tensile cycling of the base material up to 8%

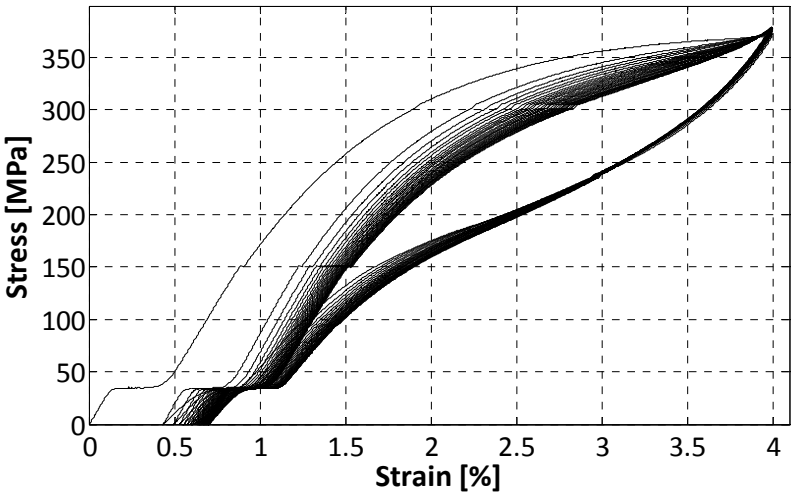

Figure 5.37 Long tensile cycling of a welded joint up to 4%

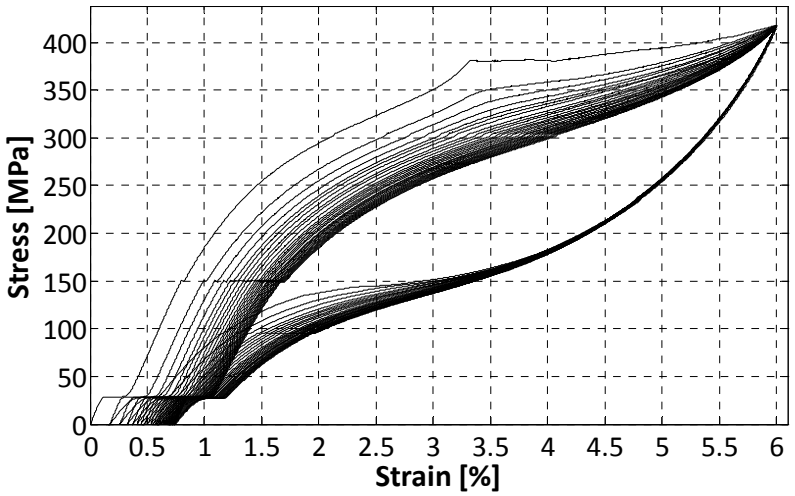

Figure 5.38 Long tensile cycling of a welded joint up to 6%

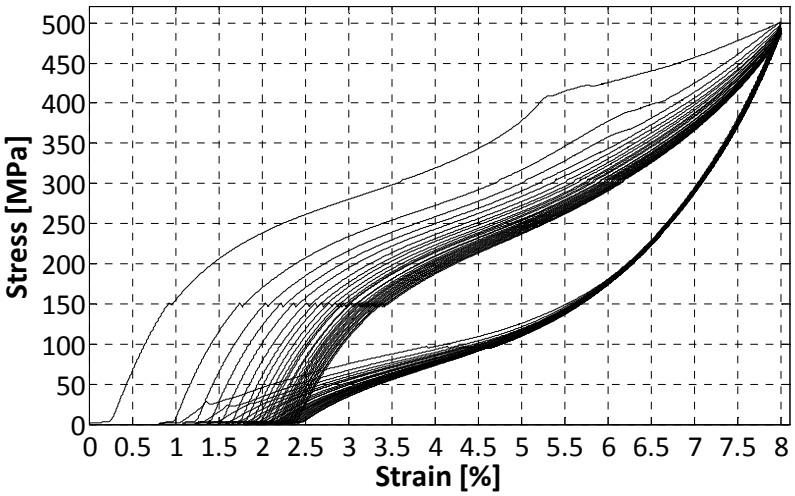

Figure 5.39 Long tensile cycling of a welded joint up to 8%

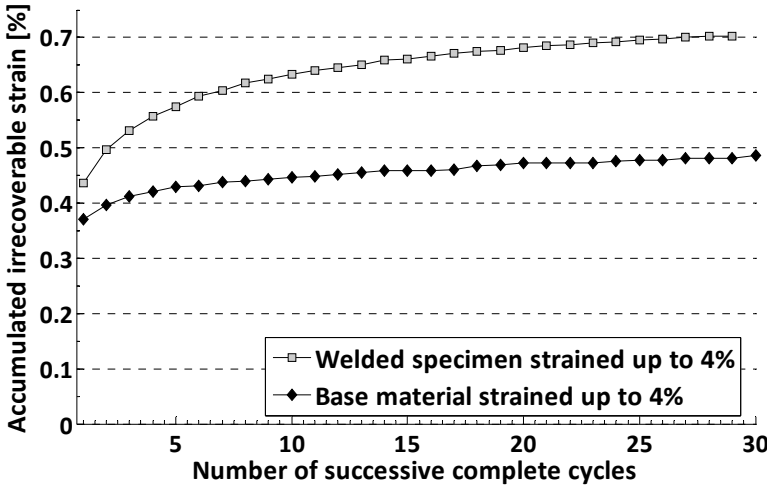

Figure 5.40 Comparative accumulation of inelastic strain between base material and welded specimens strained up to 4%

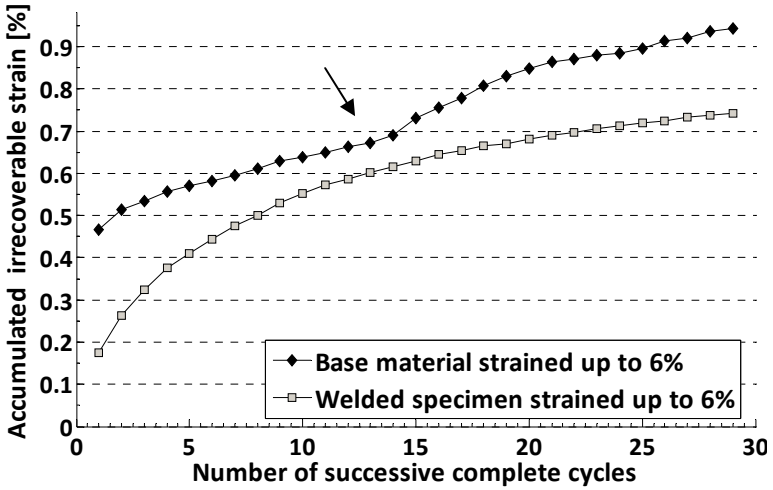

Figure 5.41 Comparative accumulation of inelastic strain between base material and welded specimens strained up to 6%

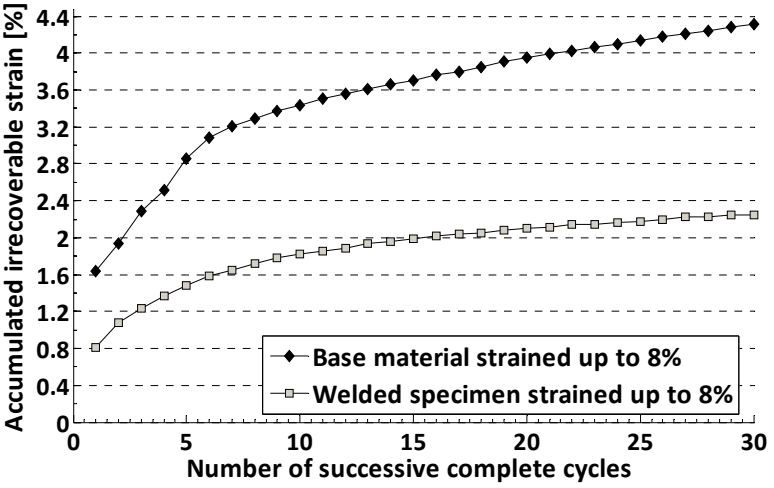

Figure 5.42 Comparative accumulation of inelastic strain between base material and welded specimens strained up to 8%

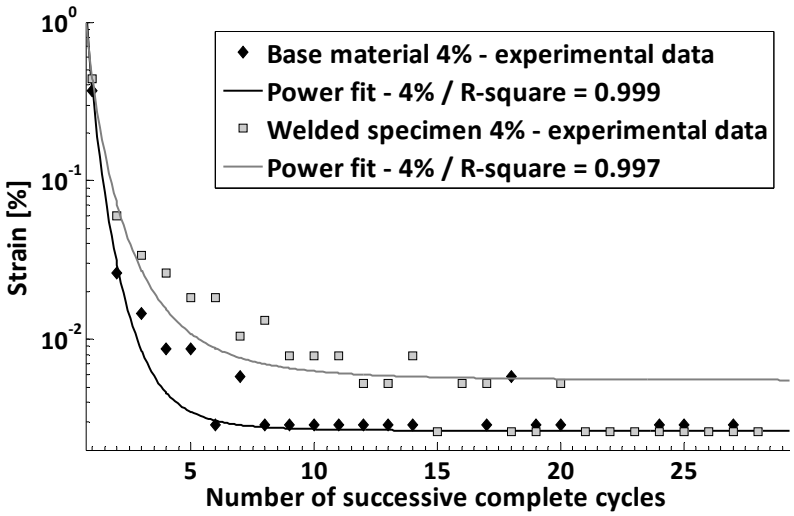

Figure 5.43 Evolution of inelastic strain over the number of cycles for base material and welded specimens strained up to 4%

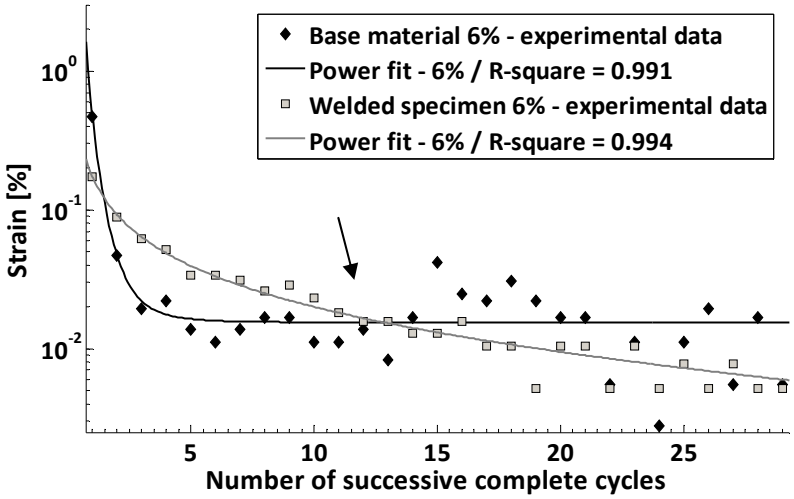

Figure 5.44 Evolution of inelastic strain over the number of cycles for base material and welded specimens strained up to 6%

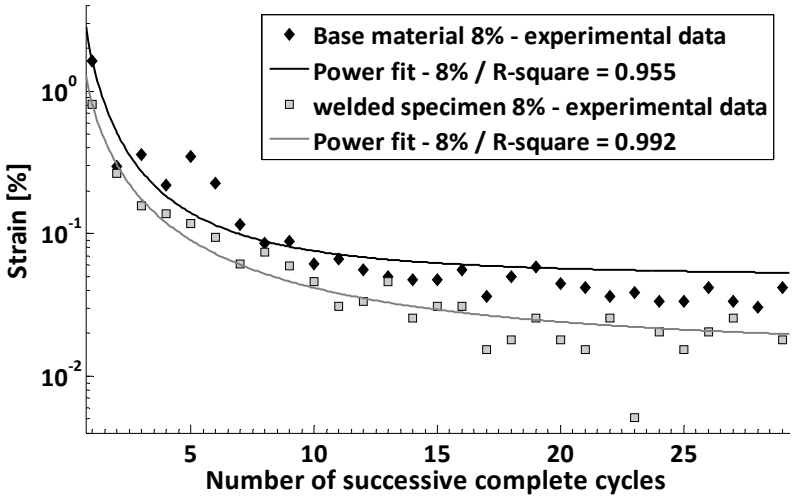

Figure 5.45 Evolution of inelastic strain over the number of cycles for base material and welded specimens strained up to 8%

Both from base material and welded specimens results (figures 5.34 to 5.39) it is possible to verify the convergence of the hysteretic loops from the first cycle (on the left) to the last (darker on the right). The weld bead originates a softening effect at the beginning and the end of the superelastic plateau, resulting in more elongated loops, with less area and consequently less energy. This smoother transition was also observed by others [34] and was identified as a consequence of stress accommodated by slip in the heat affected zone, just before reaching the transformation plateau.

The inelastic strain was found to accumulate differently from base material to welded specimens, as figures 5.34 to 5.39 suggest. So, a comprehensive study was carried out in order to evaluate, for each condition tested, the accumulation of inelastic strain over successive cycles, both on the base material and on the welded specimens. An analysis routine was programmed in MATLAB to evaluate the accumulation of inelastic strain, as figure 5.46 illustrates. It consisted of calculating the zero-stress points of the discrete series that constituted the plots and then data was used to generate accumulated and evolutionary plots. The program is presented in annex F.

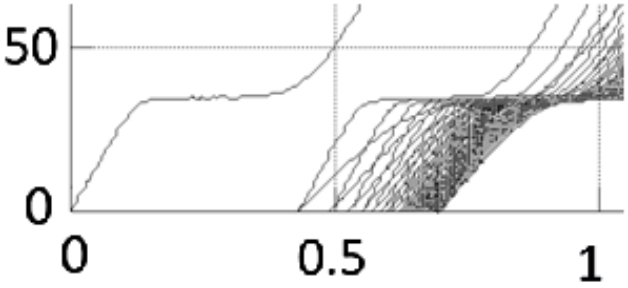

Figure 5.46 magnification of figure 5.37 depicting the accumulation of inelastic strain

Results from that study are presented in figures 5.40 to 5.43 in terms of irrecoverable strain accumulation. It can be observed that for cycles involving lower strain levels, such as in figure 5.40, the base material has a superior ability of strain recovering, presenting lower inelastic strain accumulation over the cycles.

However, data presented in figures 5.41 and 5.42 suggest that for higher strain cycles the opposite effect occurs. In figure 5.42 it can be observed that after 30 cycles the base material accumulated twice the inelastic strain accumulated by the welded specimen. Similarly to figure 5.40, Falvo *et al* [37] reported an increasing trend for welded specimens to present higher values of plastic accumulated deformation over training cycles, although they applied a thermomechanical cycle to evaluate the two-way shape memory effect.

A similar behaviour was also reported by Khan *et al* [**1**], although specimens were strained up to 6%. The base material exhibited lower levels of inelastic strain accumulation over 50 cycles. However, it must be emphasized that in this study, the tests were conducted at a strain rate twice the one reported by [58].

In order to evaluate how differently the mechanical response of base material and welded specimens tends to converge, the amount of inelastic strain observed in each successive cycle was plotted in a

logarithmic scale, and results are presented in figures 5.43 to 5.45. A power rule of the type $f(x) = ax^b + c$ was seem to best fit the experimental data. Fitting parameters are presented in table 5.3 and a correlation parameter (R^2) above 0.99 was obtained in all fits.

Table 5.3 Curve fitting parameters – Power fits

Fitting	a	b	c	R^2
Base material – 4%	0.3683	-3.7880	0.002642	0.9986
Welded specimen – 4%	0.4304	-2.7280	0.005483	0.9964
Base material – 6%	0.4512	-3.8550	0.015470	0.9910
Welded specimen – 6%	0.1756	-0.8825	-0.002989	0.9942
Base material – 8%	1.5570	-1.7710	0.049260	0.9550
Welded specimen – 8%	0.7858	-1.4520	0.013870	0.9919

Figures 5.43 to 5.45 point out that, for tensile cycling involving larger elongations, the welded joint revealed the ability of converging faster to the stabilized response, accumulating less inelastic strain on each successive cycle, than the base material does (figure 5.45). For cycles tested to lower strains (figure 5.43), it was observed the opposite behaviour, as figures 5.41 and 5.44 clearly show the inversion of that initial trend (marked with arrows in both figures).

The explanation for that behaviour relies in the thermal cycle that was applied to the material of the welded zone during the process. The fusion zone was fully recrystallized, which typically results in the suppressing of the R-phase and the consequent optimization of the superelastic response, which are of great importance for higher strain levels.

5.1.2.5 Fracture

The fracture surface of a welded tensile specimen forced to failure after six cycles up to 5% was observed by SEM and is depicted in figure 5.47. Rupture was noticed to occur in all specimens by the weld centreline like Khan *et al* [58] have reported. Specimen revealed a ductile fracture, as also observed by [33, 58, 63], which is supported by figures 5.48 and 5.49, where it is possible to identify both the presence of voids and equiaxed deep dimples, the last associated to intense plastic deformation during rupture on mode I.

The exposed surfaces however may not accurately reflect the behaviour of the phases involved in the fracture process, as some residual martensite might be present, due to the formation of SIM in the

crack-tip zone [64]. That is known to in some dynamic loading circumstances increase the fracture toughness of superelastic NiTi specimens [65] and helps to support the high resistance of welded specimens to extensive cycling, as observed before.

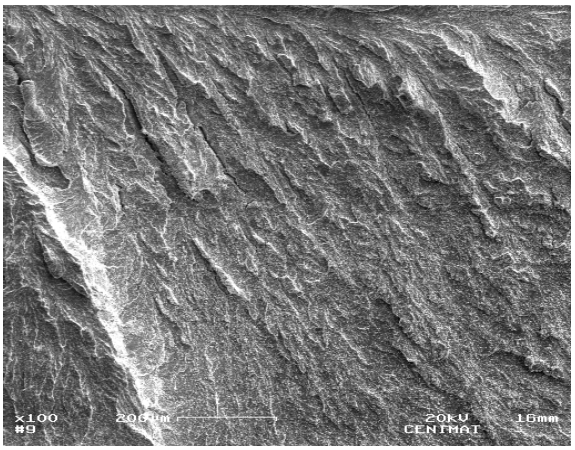

Figure 5.47 SEM observation of the fracture surface showing no evidence of cleavage (100X)

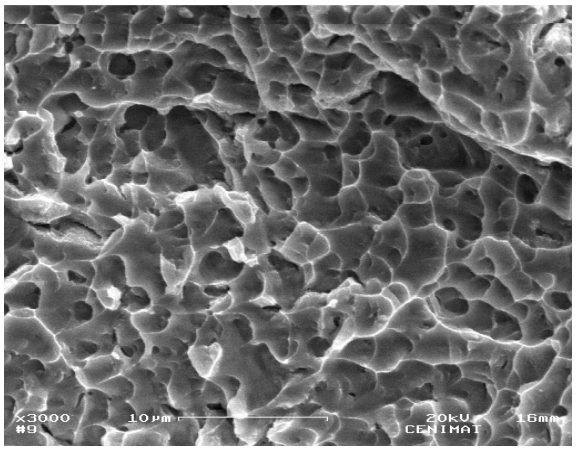

Figure 5.48 SEM detail of the dimpled ductile fracture surface (3000X)

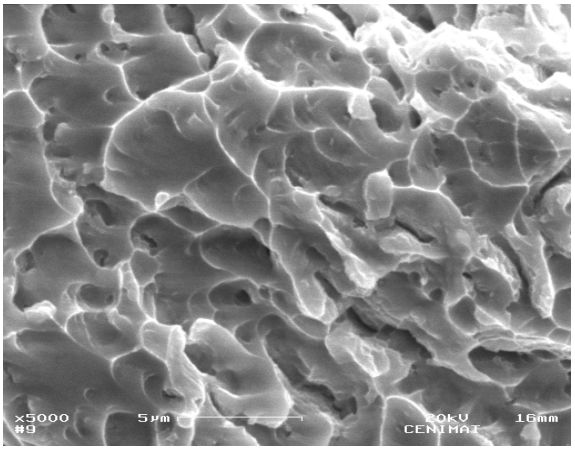

Figure 5.49 SEM observation of grown voids in the dimpled surface (5000x)

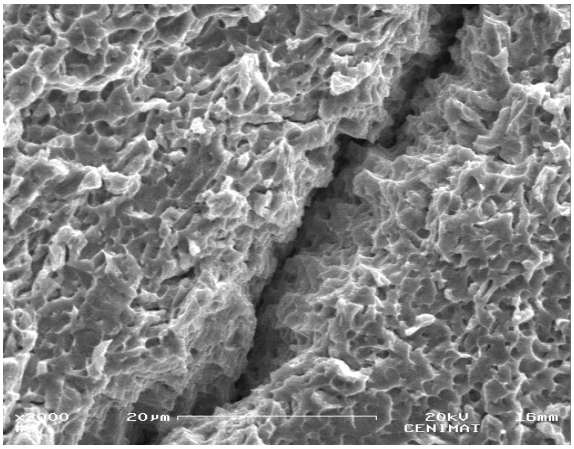

Figure 5.50 SEM observation showing evidences of secondary cracking along the tensile testing direction

Nucleation of voids, growth and coalescence are known to have their origin on either precipitates or microporosities [66]. As concluded before, intermetallic precipitates may exist in the FZ, although microporosities are the main cause of failure, as their undeniable existence was confirmed by scanning electron microscopy carried on top surfaces of welds. In those observations was noticed special incidence along the weld centre, what partially explains why rupture occurred by that region, and not by the HAZ, like Maletta *et al* [63] have experienced.

Extensive observation was performed on the sample, revealing that the same microfracture ductile mechanisms were present, without signs of cleavage. The presence of those ductile mechanisms, as

well as the hypothetical formation of SIM, help to support the high mechanical strength observed on tensile tests (strain levels as high as 8% even after a cyclic background of 60 cycles).

As can be observed in figures 5.47 and 5.50, what seem to be deep parallel secondary intergranular cracks were found scattered throughout the dimpled surface. Such observations may derive from the propagation of secondary microcraks, also observed by [65], a consequence of continuous changing of the local stress state during the fracture process.

5.1.3 Results from joints for parameters evaluation

5.1.3.1 The influence of welding parameters on the weld bead geometry

The influence of welding parameters on the geometry of weld beads was evaluated by measuring the width of the face and root, using an optical microscope equipped with a digital camera and measuring software. The measurements, which are presented in annex E, were correlated with the heat input (heat input=power/welding speed) and power. The few tests performed conducted to significant scattering, particularly on 0.5 mm thick plate tests, although some conclusions can be extracted for 1.0 mm plates and are presented in figures 5.51 and 5.52.

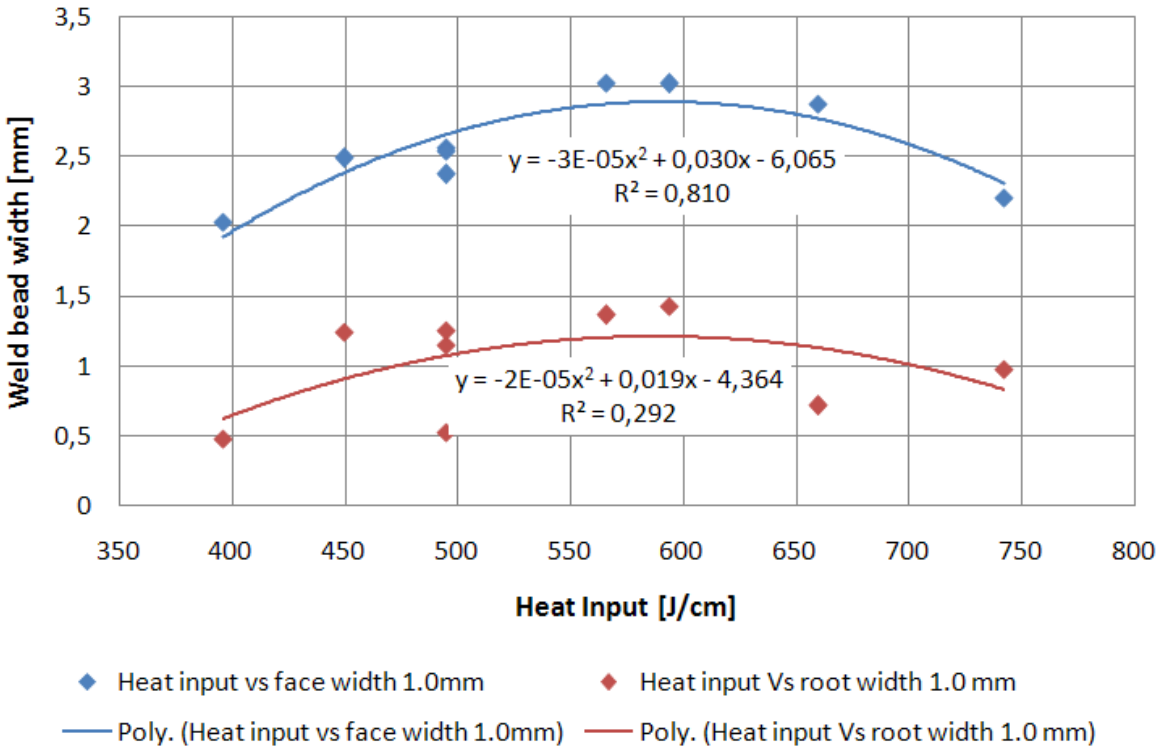

Figure 5.51 Graph showing the relation between the heat input and the weld bead with on 1.0 mm thick plates

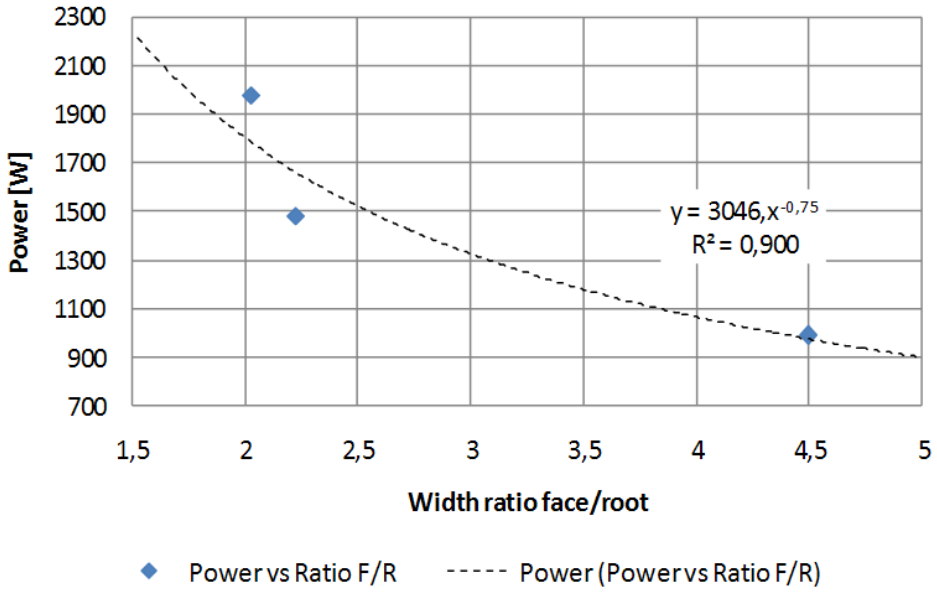

Figure 5.52 Relation of welding power and the width ratio between face and root for the same heat input

From figure 5.51 it is possible to conclude that the weld bead width can be related to the heat input, although not linearly. A very low correlation factor was found for the root width data, mainly due to the accumulation of measurement errors. Both measurements on the face and on the root reveal a negative polynomial relation, which point out that the weld bead width tends to icrease until about 600 J/cm, both on the face and the root, and from that point on a significant decrease is observed. That behavior can be related to the welding mode: until the maximum verified at about 600 J/cm conduction mode is mainly present and thereafter higher heat input leads to keyhole welding, narrowing both the face and back of the weld bead.

Although easy to understand, previous conclusions strongly depend on experimental conditions such as gas assistance, fixture mode, materials, etc., and for that reason only general aspects are discussed. Figure 5.52 illustrates how peculiar the effect of parameters arrangement on the geometry of the weld bead may be: a dimensionless parameter given by the ratio between the width of the weld bead on the face and back was plotted versus the power of three measurements, which exhibited the same heat input. That ratio may be interpreted as a parameter for evaluating penetration, and the theoretical value 1 would mean pure keyhole welding and full penetration.

It can be observed that higher power levels conduct to lower ratios, which means that for the same heat input power decides the welding mode. Although not involving the heat input concept, Steen [41] stated that the relation between the welding speed and penetration is strongly dependent on power, which corroborates the experimental conclusions presented.

5.1.3.2 Structural observations

Both the macro and the microstructure of selected specimens was observed by optical microscopy, as selection was carried out based on mechanical tensile testing results (strength and ductility parameters) balanced with the interest of observation based on parameters arrangement (maximum and minimum heat inputs). Four 1.0 mm thick samples were selected to be observed and are presented from figures 5.53 to 5.56. Complementary micrographs can be found in annex G.

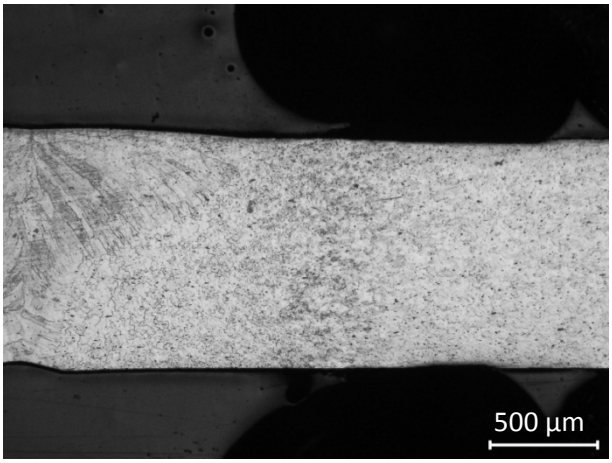

Figure 5.53 Macrograph of A-A 1.0 mm thick similar joint showing the welded zones

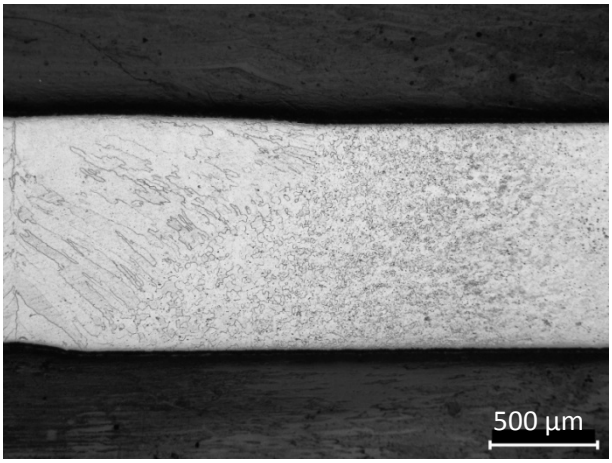

Figure 5.54 Macrograph of C-C 1.0 mm thick similar joint showing the welded zones

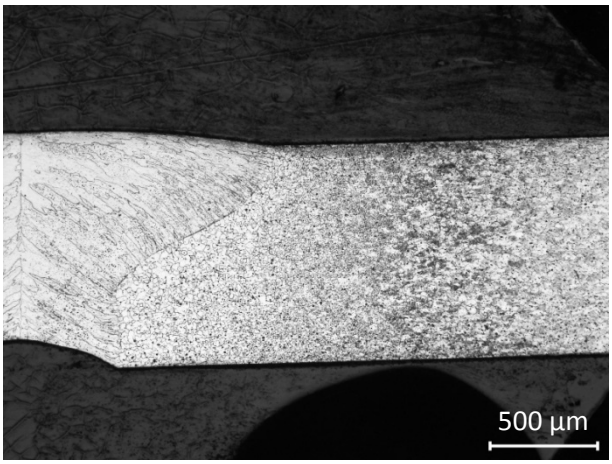

Figure 5.55 Macrograph of F-F 1.0 mm thick similar joint showing the welded zones

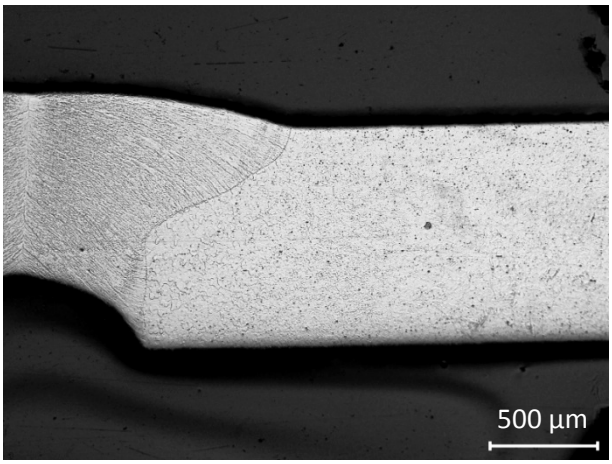

Figure 5.56 Macrograph of H-H 1.0 mm thick similar joint showing the welded zones

Also four 0.5mm thick samples were selected to be observed and results are presented from figure 5.57 to 5.60.

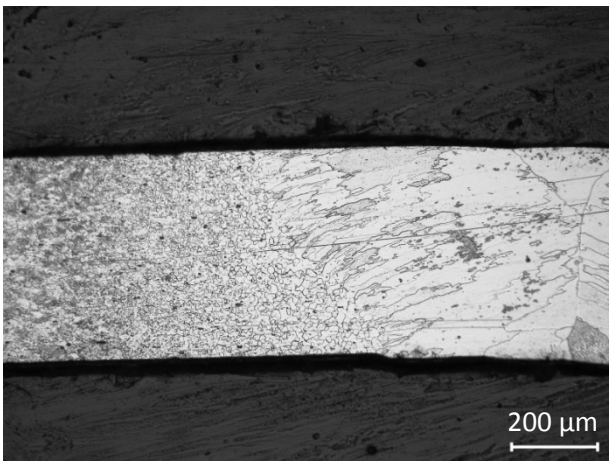

Figure 5.57 Macrograph of F-F 0.5 mm thick similar joint showing the welded zones

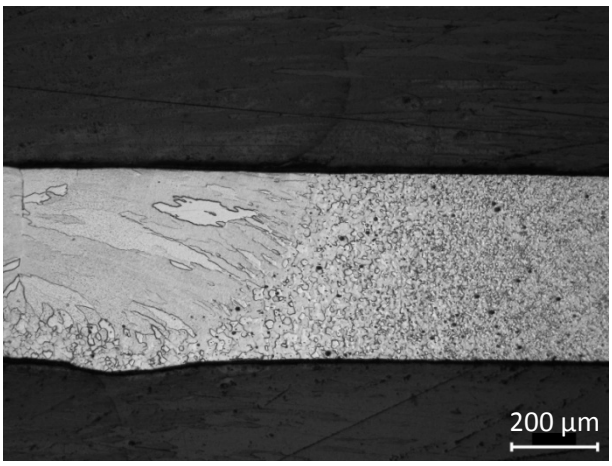

Figure 5.58 Macrograph of G-G 0.5 mm thick similar joint showing the welded zones

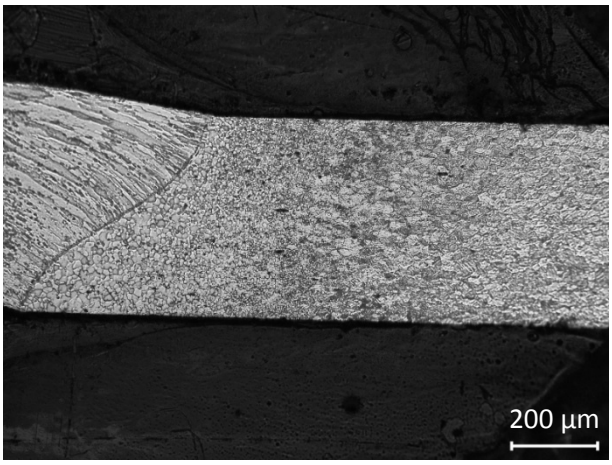

Figure 5.59 Macrograph of N-N 0.5 mm thick similar joint showing the welded zones

Figure 5.60 Macrograph of O-O 0.5 mm thick similar joint showing the welded zones

In every single sample presented before it is possible to identify a microstructure similar to the one described for similar joints for design evaluation. Away from the weld bead is presented the cold-rolled base material, with oriented grains and precipitates aligned with the rolling direction; coming from the base material a typically darker region appears, which delimits the base material from the heat affected zone, which is constituted by coarser equiaxed grains and some precipitates; from the favorably oriented grains of the HAZ grow columnar epitaxial grains in the welded zone, along the heat flow direction, converging to a generally well defined centreline.

Regarding the 1.0 mm thick plates, the effect of the welding parameters (please see table 4.17) can be evaluated by considering as a first indicator the heat input: welds of figures 5.53 and 5.54 were attained with the same power conditions, although the heat input of the welded joint depicted in figure 5.53 was only about 60% of the heat input used to attain the one of figure 5.54, resulting in a

narrower weld bead (although with full penetration), with a considerably finer microstructure in the fusion zone, which may have a significant effect on tensile properties.

Comparing figure 5.55 and 5.56 it can be observed that although the first was welded with a significantly higher heat input (150%) a narrower weld bead was attained, due to lower power. This effect was already pointed out in the previous paragraph, concerning the effect of the welding parameters on the weld bead geometry. Despite the geometrical issues, the heat input has a strong influence on the microstructure as concluded before. Figure 5.55 exhibits a coarser microstructure than figure 5.56 due to higher heat input.

Regarding the 0.5 mm specimens similar observations can be made, although due to lower thickness small changes in the welding parameters conduct to major differences. The macrograph of figure 5.57 was attained with the same power of the one presented in figure 5.58, although a variation of only just about 15% in the welding speed (and consequently in the heat input) was enough to change from full (figure 5.57) to partial penetration in conduction mode(figure 5.58).

The specimens which macrographs are presented in figures 5.59 and 5.60 were welded with the same power and although not visible on the macrograph, the higher heat input of figure 5.59 conducted to a wider weld bead, as expected. The micrographs reveal the inexistence of significant porosity, although both figures 5.59 and 5.60 present extensive accumulation of undissolved precipitates near the weld centre (darker regions).

SEM observations were carried on transverse sections of etched joints, and results are presented from figure 5.61 to 5.70. The base material microstructure is presented in figures 5.61 and 5.62 where it is possible to observe elongated grains containing residual martensite oriented along several variants. Elongated precipitates were found scattered in the base material, as figure 5.63 illustrates. The EDS chemical analysis of such features is presented in figure 5.72, which reveals the presence of a Ti_2Ni precipitate in a NiTi matrix (the measured zones are marked with colored arrows), hypothetically, once that the $Ti_4Ni_2O_x$ has the same structure and are frequently confused.

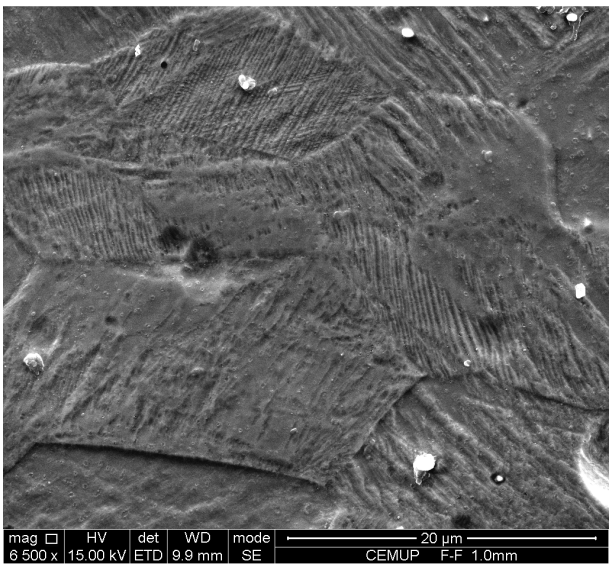

Figure 5.61 SEM observation of the microstructure of the base material of 1.0 mm thick specimens showing elongated grains

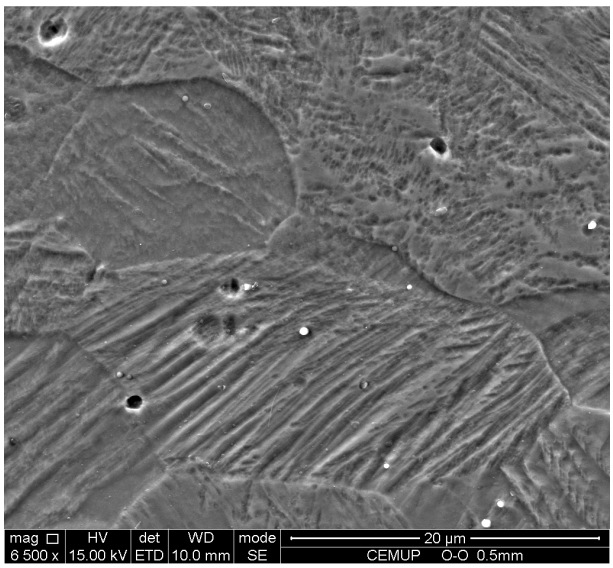

Figure 5.62 SEM observation of the microstructure of the base material of 0.5 mm thick specimens showing elongated grains

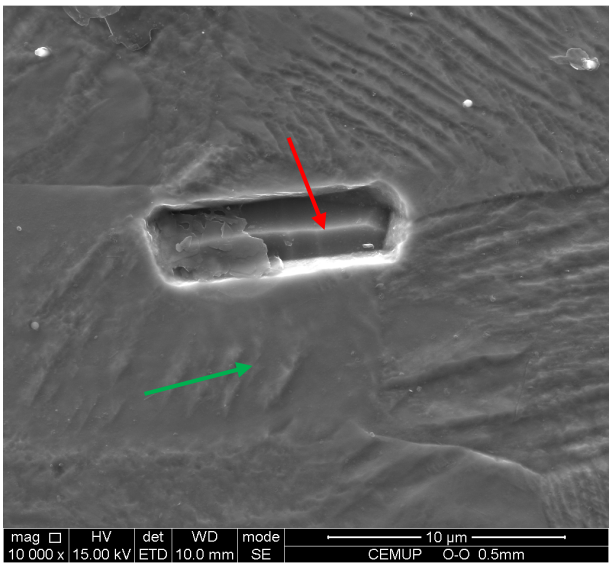

Figure 5.63 SEM observation of a precipitate in the base material of 0.5 mm thick specimens showing EDS analysis markers

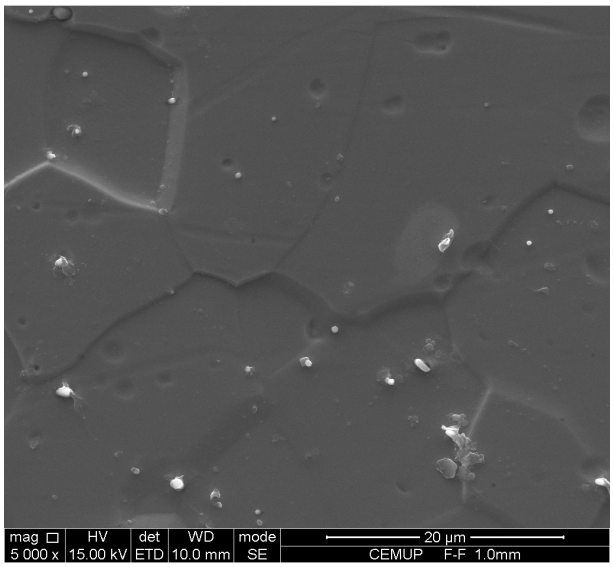

Figure 5.64 SEM observation of the HAZ of a specimen 1.0 mm thick showing equiaxed grains and precipitates

The heat affected zone presented in figure 5.64 was found similar both in 0.5 and 1.0 mm thick specimens, and mainly constituted of equiaxed grains and scattered small precipitates. A magnification of one of those precipitates is presented in figure 5.65. EDS chemical analysis was performed on the marked zones and results, which are presented in figure 5.71 , showed the presence of a TiC carbide in a NiTi matrix. Figure 5.66 depicts the transition zone of a 1.0 mm thick specimen welded with high heat input (F-F) where the epitaxial columnar grain growth from the HAZ can be observed, as well as lower incidence of precipitates in the FZ.

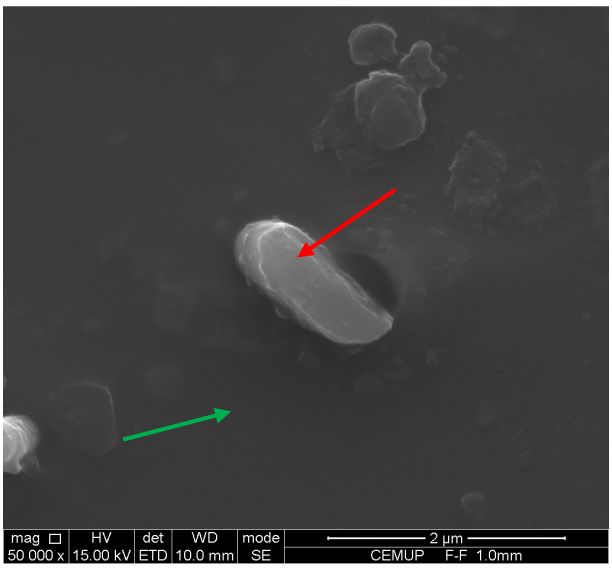

Figure 5.65 SEM observation of an elongated precipitate in the HAZ of a specimen 1.0 mm thick showing EDS analysis markers

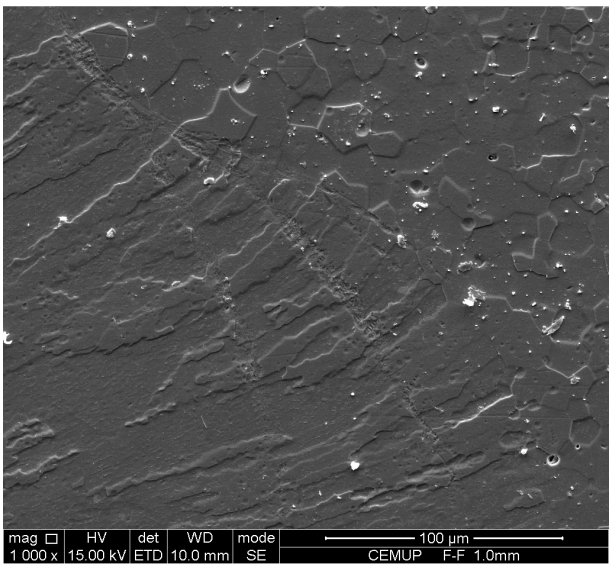

Figure 5.66 SEM observation of the transition zone showing high incidence of precipitates in the HAZ and equiaxed grain growth in the FZ

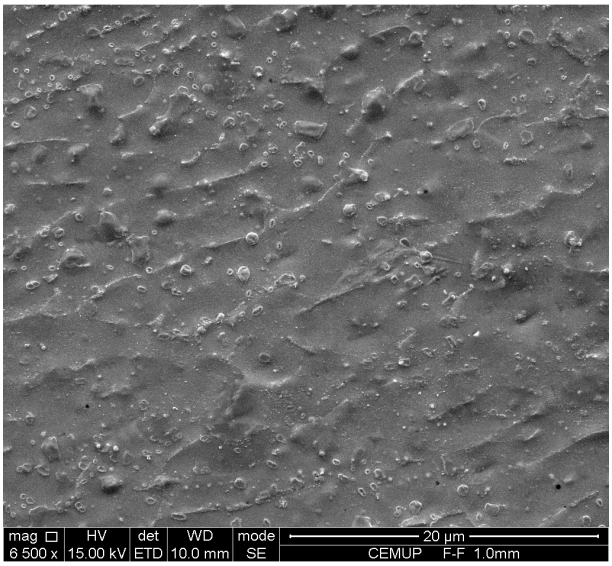

Figure 5.67 SEM observation of the FZ of a high heat input 1.0 mm thick specimen

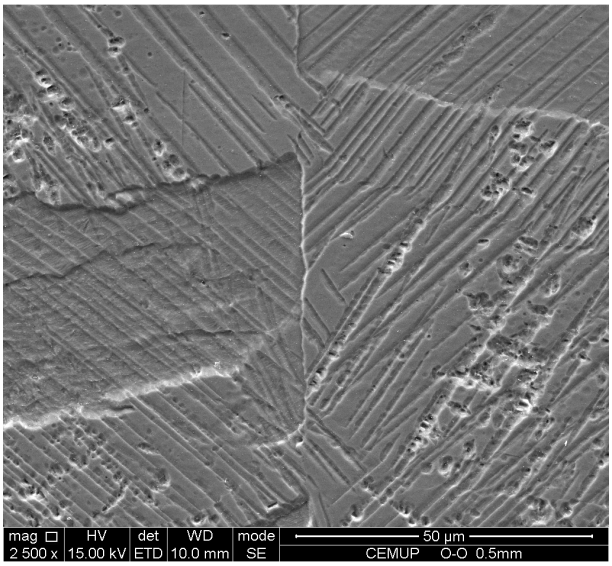

Figure 5.68 SEM observation of the weld centreline of a low heat input 0.5 mm specimen (O-O 0.5 mm) showing symmetric needle structures

A magnification of one grain from the fusion zone of the same sample is presented in figure 5.67, where high homogeneity can be observed. However, the fusion zone of the 0.5 mm thick O-O joint revealed the presence of a needle like structure symmetric to the weld centreline, as can be observed in figure 5.68.

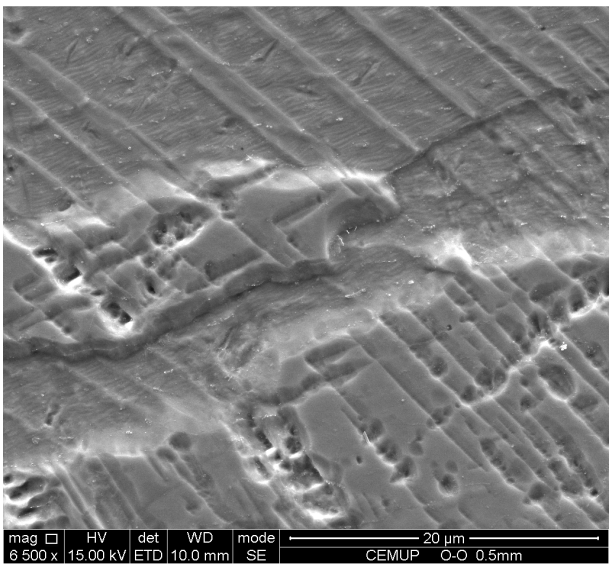

Figure 5.69 SEM observation of the FZ of a low heat input 0.5 mm specimen (O-O 0.5 mm) showing equiaxed grains with needle structures and some corroded scattered spots

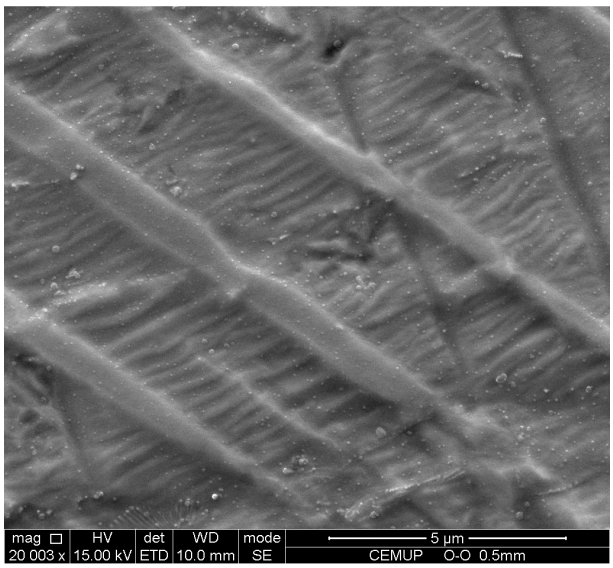

Figure 5.70 SEM observation of needle structures in the FZ of a 0.5 mm thick specimen (O-O) welded with low heat input

Such acicular structures can be observed in detail in figures 5.69 and 5.70. They were found to develop all macroscopically parallel inside the same grain, as grain boundaries sometimes slightly affect orientation. Studies develop by Martins *et al* [67 to 68] reported the preferential development of [110] oriented B2 grains on sputtered NiTi SMA thin films. The development of parent phase grains with the [110] orientation aligned with the rolling direction was studied by Shu *et al* [69].

The growth of columnar grains of the fusion zone, as depicted in figure 5.66, has its origin on favorably orientated grains from the heat affected zone. In this particular case, probably due to low heat input and preservation of the parent-phase structure, a preferential growth of the [110] oriented grains was observed. In these conditions, the observation of a transverse section of a weld bead would reveal the (001) planes of the crystallographic lattice.

Shrinkage induced by weld beads solidification has probably induced the partial transformation of favorably oriented grains, according to the local stress state, which has resulted in the formation of a large number of favorably oriented martensite macrobands, due to high grain uniformity. During this process some variants become locked, due to local changes of stress state, which can be observed in figure 5.68 and was also reported by Brinson *et al* [70].

In summary, the particular welding conditions (heating and cooling) of specimen O-O conducted to the observation on a transverse section ((001) oriented plane) of the O-O 0.5 mm thick joint a partially twinned martensite lattice along alike variants, pointed out as the result of preferential grain growth along the [110] heat flux direction. However, further investigation (like TEM tests) is still necessary to better support such conclusions.

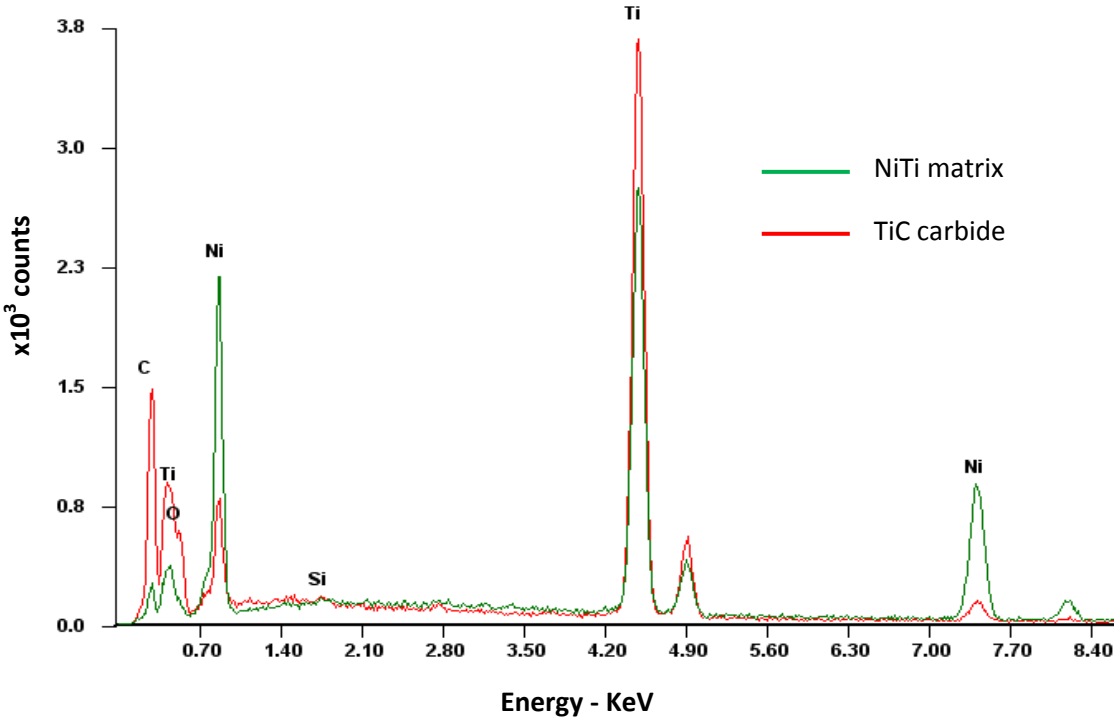

Figure 5.71 EDS comparative analysis of regions marked in figure 5.65

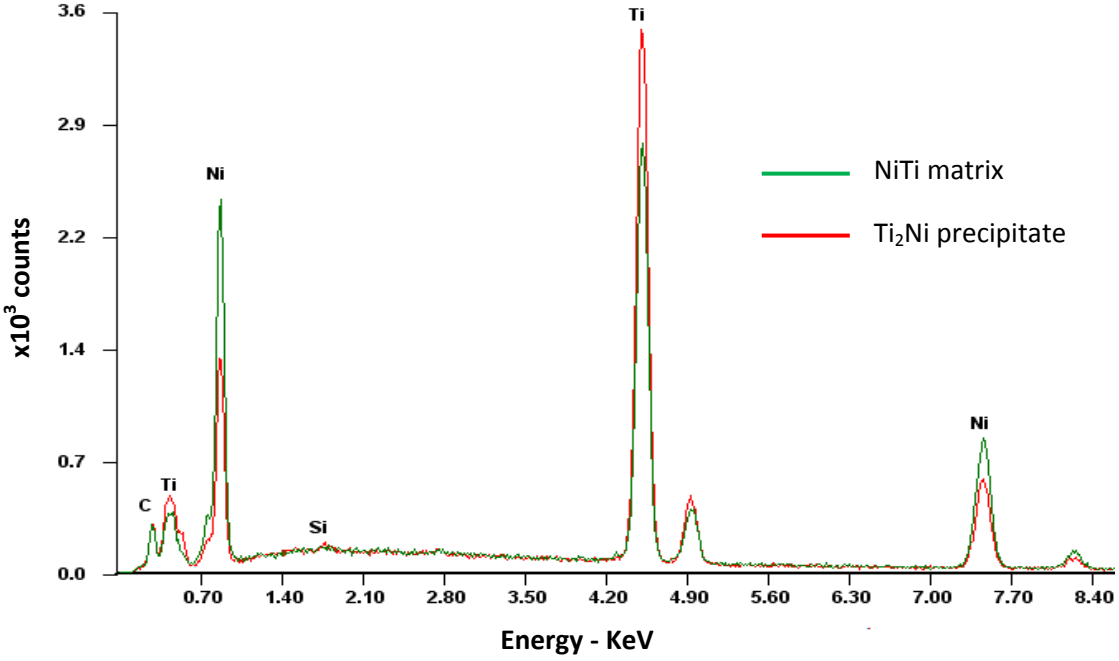

Figure 5.72 EDS comparative analysis of regions marked in figure 5.63

5.1.3.3 Microhardness measurements

Hardness measurements were performed on same samples presented before for structural observations, from figure 5.53 to 5.60. Results from hardness measurements were combined with micrographs showing the indentation marks allowing to identify the weld regions: hardness profiles in 1.0 mm thick joints are presented in figures 5.73 to 5.76; profiles in 0.5 mm thick joints are depicted in figures 5.77 to 5.80.

Table 5.4 presents average results regarding the analysis of hardness measurements in the fusion zone and the base metal. No relation was found between the average hardness of the fusion zone and the welding parameters arrangement, what may be explained by the relatively small size of the indentations compared to the grain size in that region. An increase of about 110/HV0.1 was found between the fusion zone and the base metal, both on 1.0 and 0.5 mm thick welded specimens.

The hardness measurements of the heat affected zone were not analyzed by the same procedure, once that can be easily observed that the profiles are strongly dependent on the path chosen. However, it is possible to conclude from all hardness measurements on that region that a continuous trend of hardness increasing is verified from the fusion zone to the base material, a consequence of the progressive grain refinement. No brittle phases were identified by microhardness measurements either on 1.0 or 0.5 mm thick laser welded joints.

Table 5.4 Average hardness measures - 1.0 and 0.5 mm thick specimens for parameters evaluation

1.0 mm thick			0.5 mm thick		
reference	*Fusion zone*	*Base metal*	*reference*	*Fusion zone*	*Base metal*
	HV0.1	HV0.1		HV0.1	HV0.1
A – A	199	320	F – F	220	331
C – C	203	320	G – G	222	314
F – F	202	313	N – N	233	324
H – H	215	325	O – O	233	373

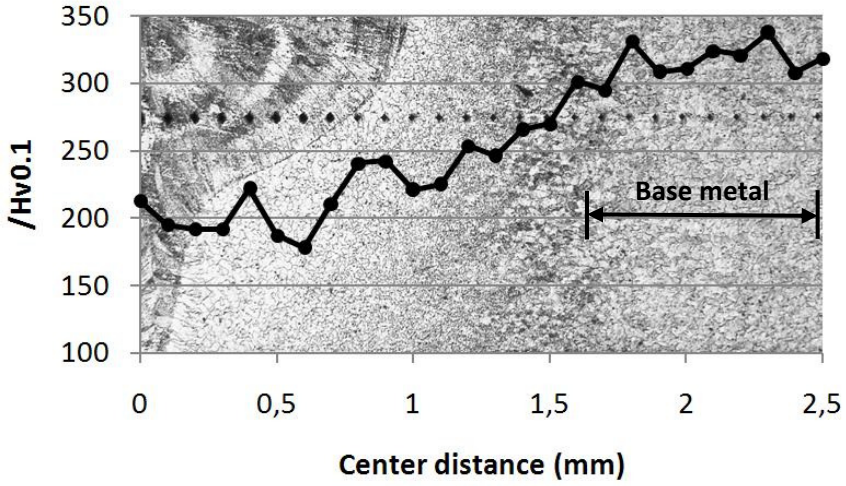

Figure 5.73 A-A 1.0 mm thick joint microhardness profile

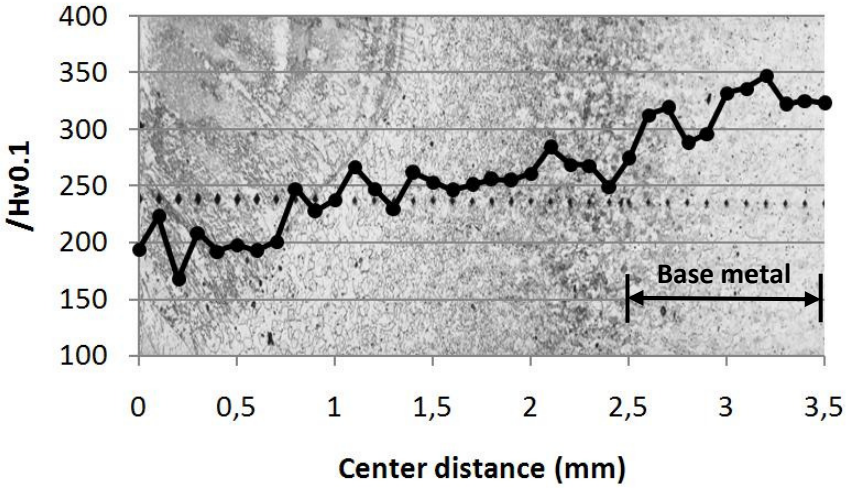

Figure 5.74 C-C 1.0 mm thick joint microhardness profile

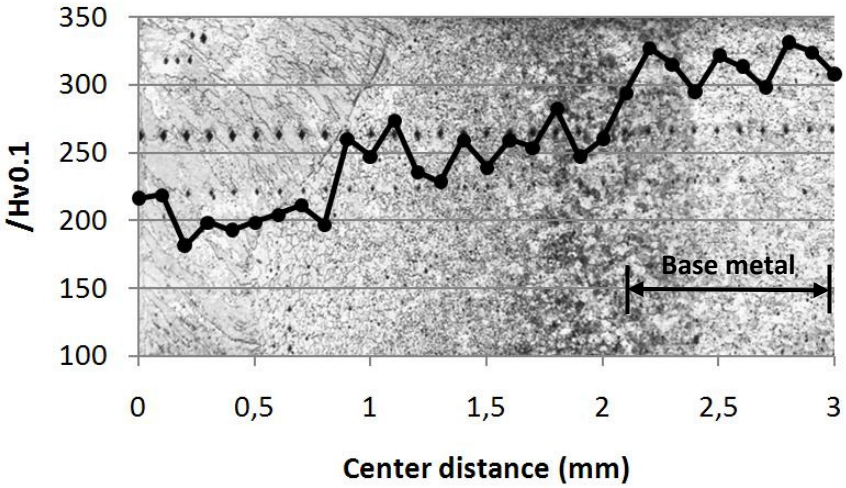

Figure 5.75 F-F 1.0 mm thick joint microhardness profile

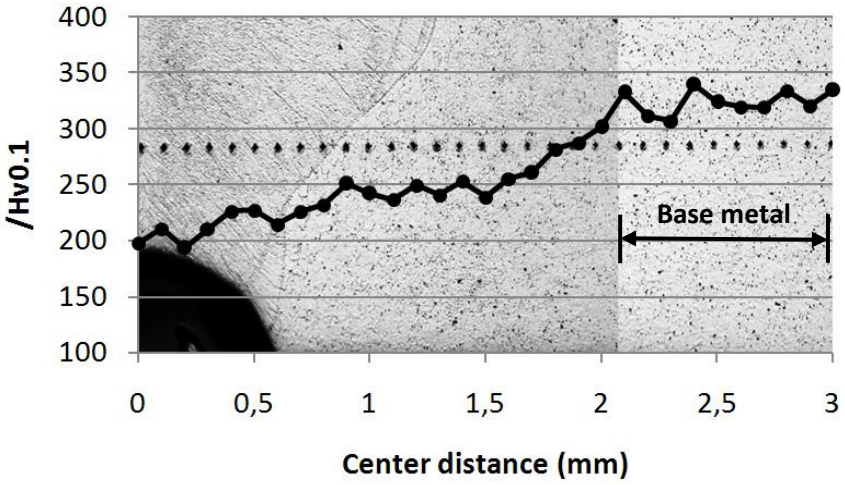

Figure 5.76 H-H 1.0 mm thick joint microhardness profile

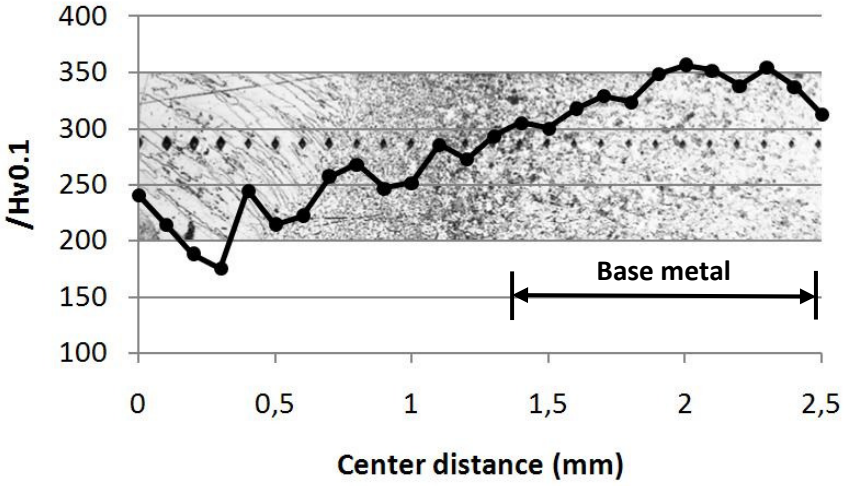

Figure 5.77 F-F 0.5 mm thick joint microhardness profile

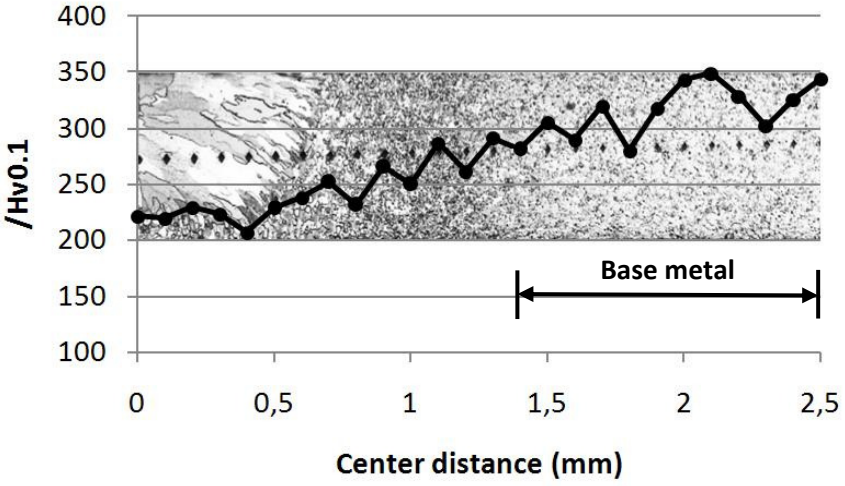

Figure 5.78 G-G 0.5 mm thick joint microhardness profile

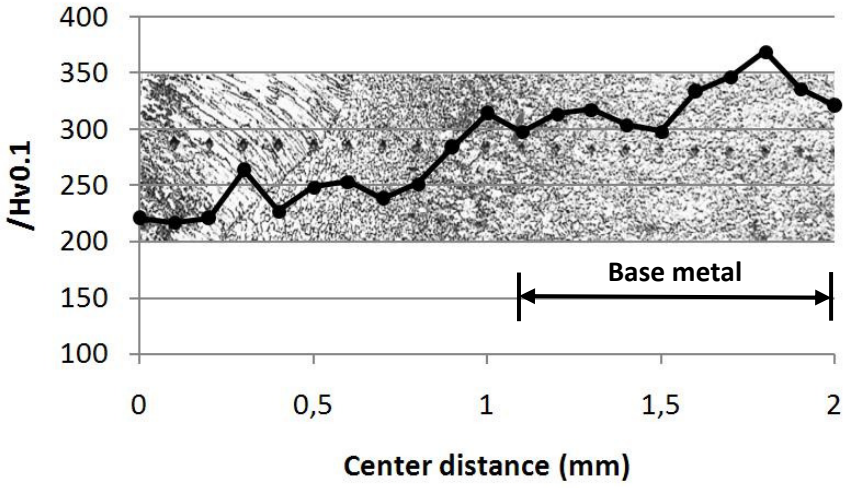

Figure 5.79 N-N 0.5 mm thick joint microhardness profile

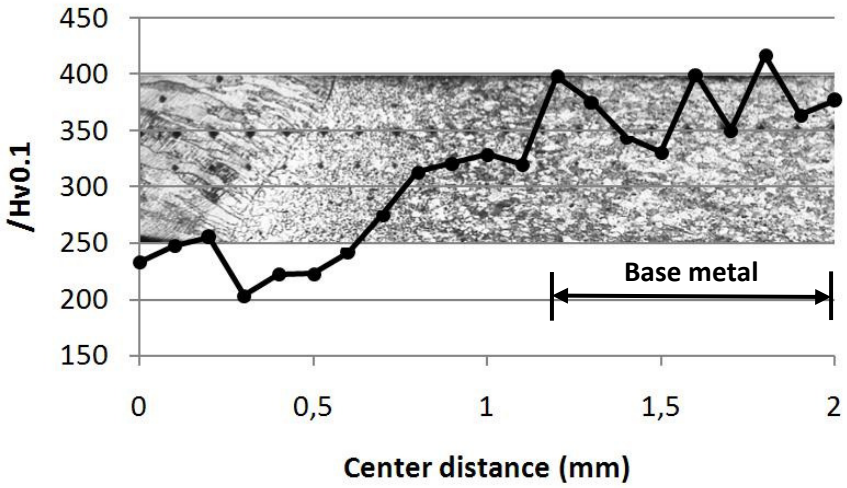

Figure 5.80 O-O 0.5 mm thick joint microhardness profile

5.1.3.4 DSC measurements

DSC measurements were performed in the base material, according to table 4.32, in order to evaluate transformation temperatures. Results allowed identifying the main phase transformations with temperature, for a zero-stress condition. The key transformation temperatures that resulted from DSC measurement analysis on the base metal, are identified in figures 5.81 and 5.82 and are presented in table 5.1. According to table 4.32 it can be observed that DSC measurements were planned to the weld metal; however, such tests were not attained due to unexpected failure of the testing equipment.

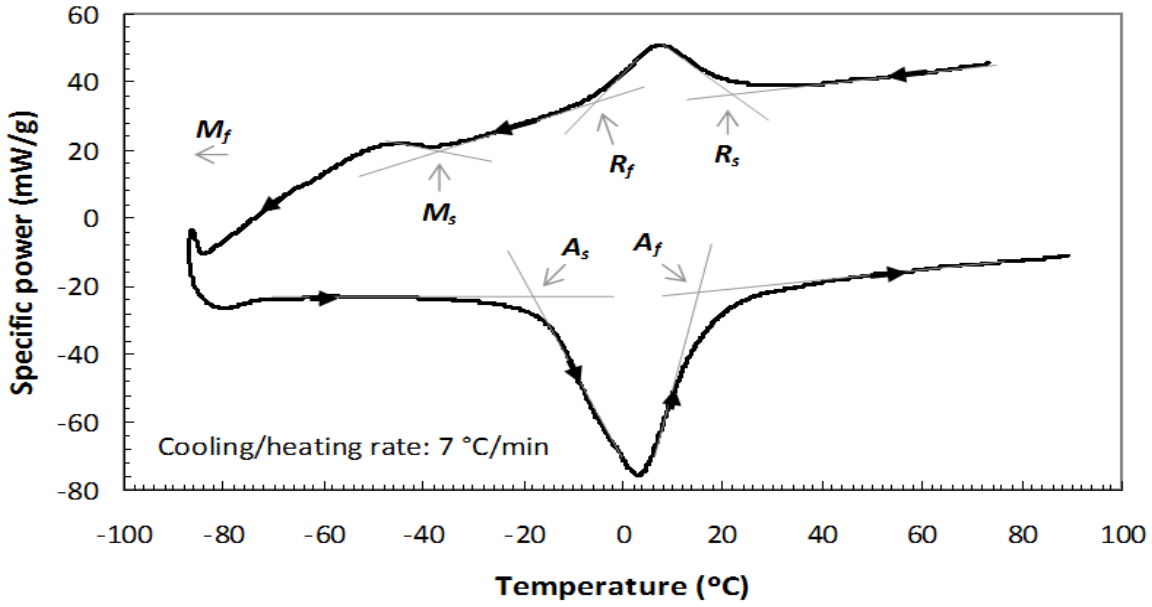

Figure 5.81 DSC measurement from the 0.5 mm thick base material with transformation temperatures identified

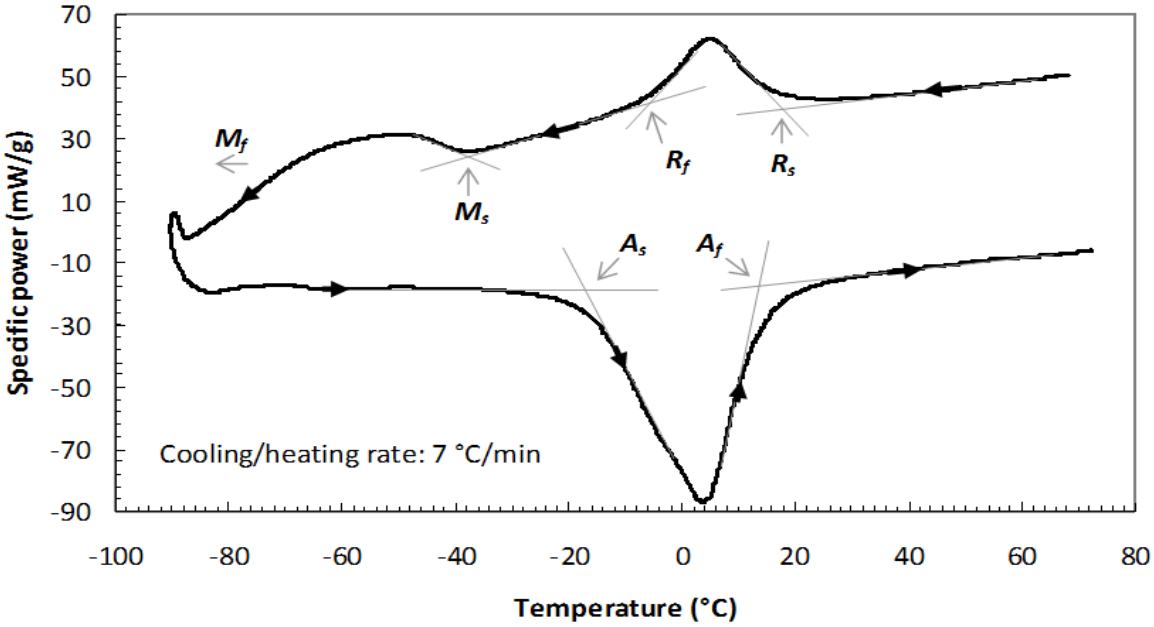

Figure 5.82 DSC measurement from the 1.0 mm thick base material with transformation temperatures identified

Table 5.5 DSC results from similar joints for parameters evaluation

	R_s	R_f	M_s	M_f	A_s	A_f
	ºC	ºC	ºC	ºC	ºC	ºC
Base material 0.5mm thick	22	-6	-38	<-80	-18	6
Base material 1.0mm thick	18	-6	-36	<-80	-18	14

From DSC measurements of figures 5.81 and 5.82 can be concluded in both materials the presence of a two-step martensitic transformation on cooling, identified by the two peaks, with the following transformation sequence from high to low temperature: parent-phase austenite B2 → r-phase martensite B19 → martensite B19'. In the reverse path, upon heating, is identified a single-step martensitic transformation, from the low temperature martensite B19' to the high temperature B2 austenite, identified in both figures for a single endothermic peak above -18 ºC. The described behavior is typical of NiTi SMAs partially annealed after cold working, and was also reported by others [34].

In both measurements, it was not possible to identify exactly the martensite finish temperature, M_f. However, from the results it is seen to be less than -80 ºC.

From table 5.5 it can be noticed that at room temperature, about 25 ºC, some residual martensite may exist in the base material, which indeed was observed by light and electron microscopy, the last presented both in figures 5.61 and 5.62.

5.1.3.5 Tensile tests results

Tensile testing up to rupture was one of the first tests performed on welded specimens in order to select the most promising ones for further analysis. Once that constituted such an important factor for parameters evaluation, selected plots from all testing conditions are presented from figure 5.83figures 5.83 to 5.90. The testing conditions and references which were presented in tables 4.37 and 4.38 can now be used to identify the plots. The remaining results are presented in annex H.

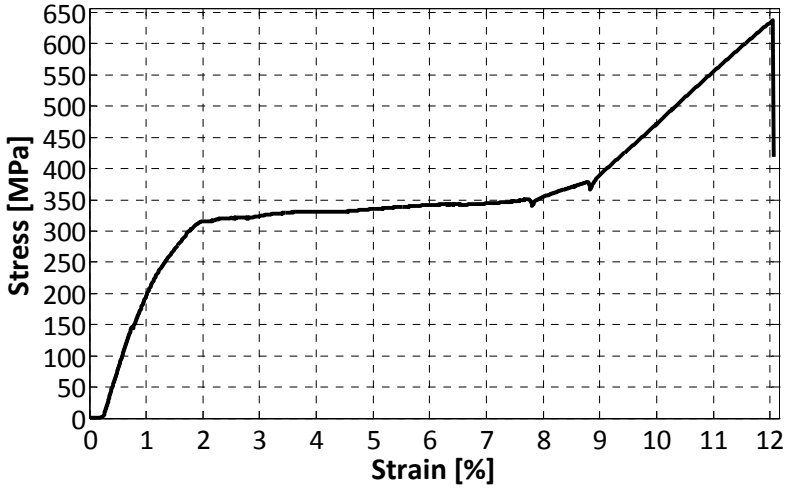

Figure 5.83 Tensile test result of the 1.0 mm thick A – A # 2 specimen

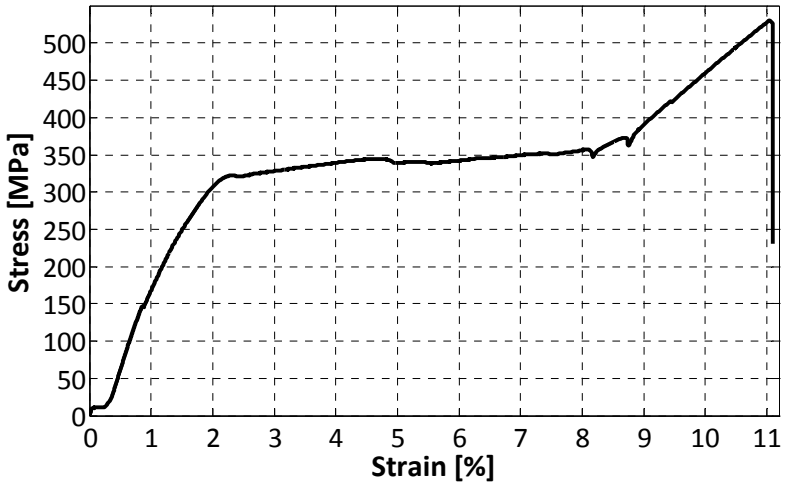

Figure 5.84 Tensile test result of the 1.0 mm thick C – C # 1 specimen

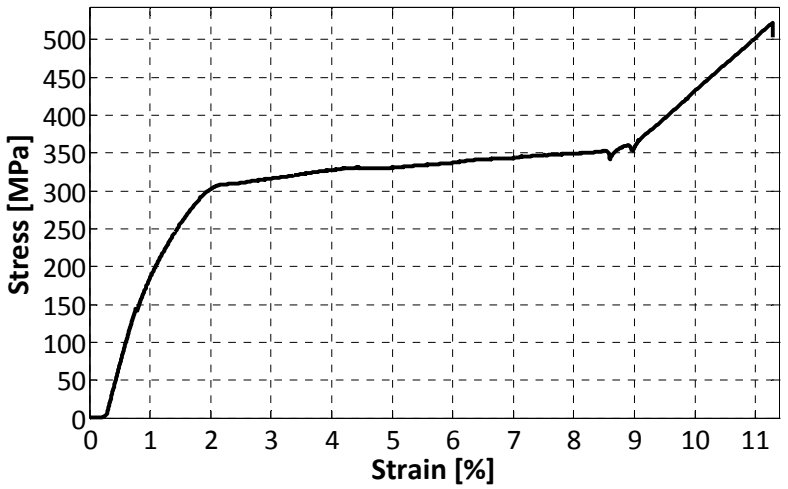

Figure 5.85 Tensile test result of the 1.0 mm thick F – F # 2 specimens

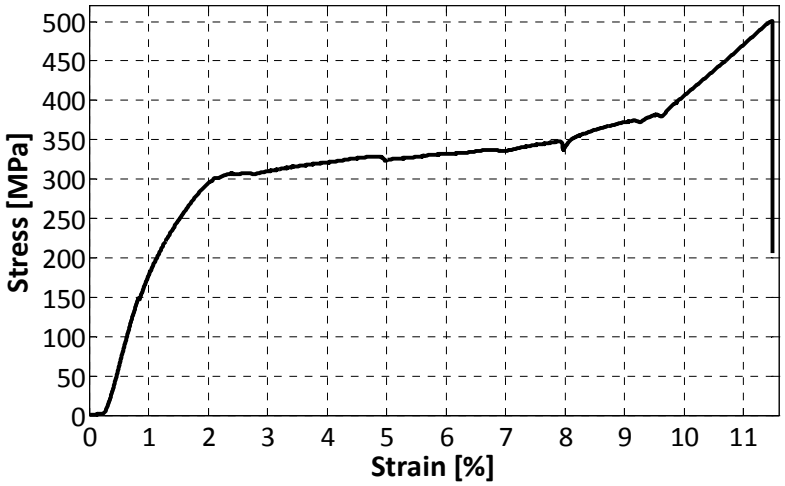

Figure 5.86 Tensile test result of the 1.0 mm thick H – H # 1 specimen

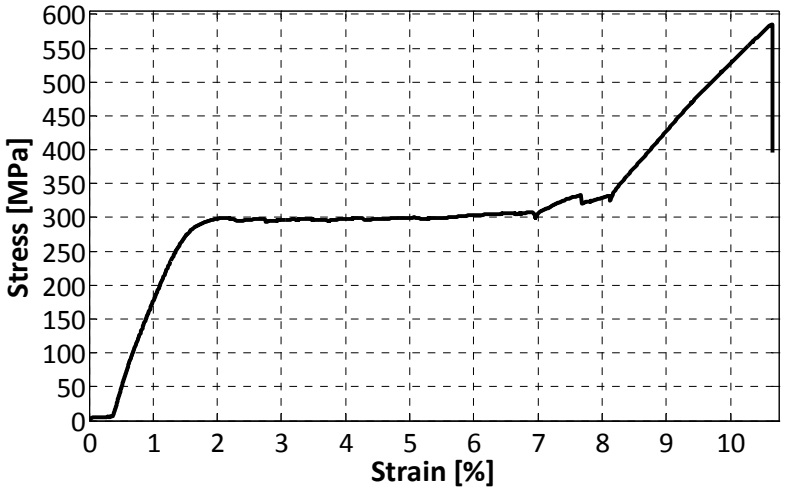

Figure 5.87 Tensile test result of the 0.5 mm thick F – F # 1 specimen

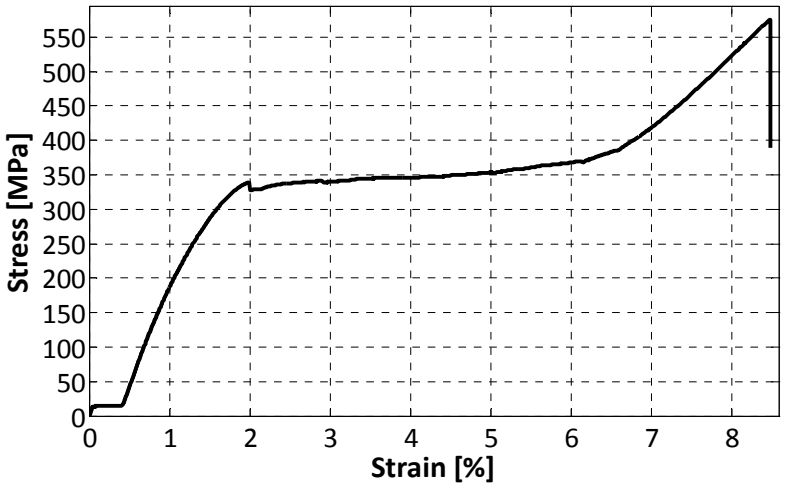

Figure 5.88 Tensile test result of the 0.5 mm thick G – G # 1 specimen

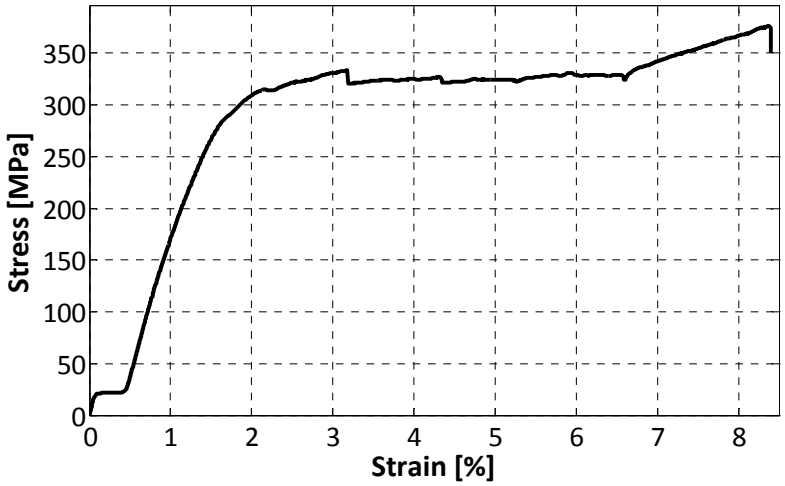

Figure 5.89 Tensile test result of the 0.5 mm thick N – N # 1 specimen

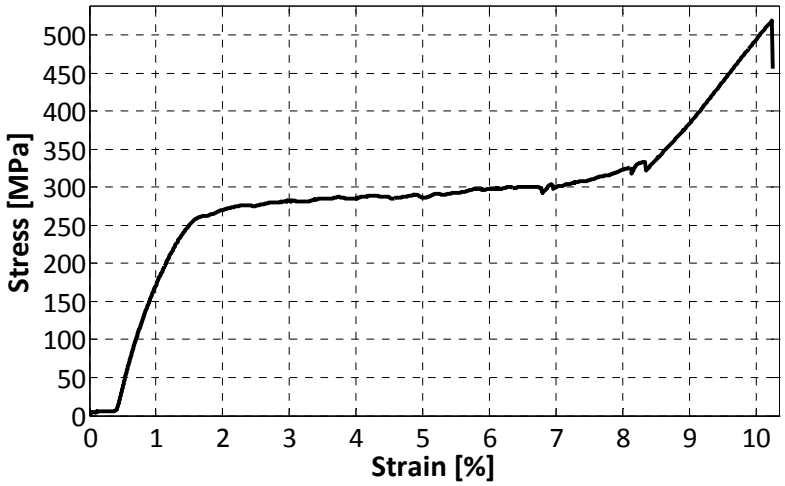

Figure 5.90 Tensile test result of the 0.5 mm thick O – O # 2 specimen

The strength and ductility parameters extracted from the tensile tests results reported previously, as well as, from the plots presented in annex H, are synthesized in table 5.6. Four joints of each thickness were selected for further analysis according to tensile strength and parameters arrangement (high and/or low power or heat input). Selected joints are underlined in table 5.6.

Table 5.6 Strength and ductility parameters of similar specimens for parameters evaluation

1.0 mm thick			0.5 mm thick		
reference	*Ultimate tensile strength*	*Elongation to fracture*	*reference*	*Ultimate tensile strength*	*Elongation to fracture*
	MPa	%		MPa	%
A – A # 1	630.78	11.94	F – F # 1	585.44	10.65
A – A # 2	636.94	12.06	F – F #2	576.95	10.29
B – B # 1	480.87	10.21	G – G # 1	575.00	8.48
B – B # 2	510.61	10.61	G – G # 2	468.28	7.52
C – C # 1	530.24	11.10	H – H # 1	381.61	4.92
C – C # 2	433.55	9.80	H – H # 2	397.46	6.20
D – D # 1	481.63	10.13	I – I # 1	361.96	8.58
D – D # 2	469.51	10.31	I – I # 2	294.44	2.44
E – E # 1	337.44	6.52	K – K # 1	333.33	8.23
E – E # 2	320.57	2.75	K – K # 2	366.96	8.34
F – F # 1	466.87	10.69	L – L # 1	339.29	8.17
F – F # 2	521.78	11.29	L – L # 2	311.16	3.14
G – G # 1	438.94	10.44	M – M # 1	319.12	6.26
G – G # 2	344.76	7.79	M – M # 2	297.23	2.80
H – H # 1	500.78	11.49	N – N # 1	376.32	8.39
H – H # 2	324.15	4.52	N – N # 2	322.12	7.18
I – I # 1	312.79	3.83	O – O # 1	441.23	9.44
I – I # 2	394.45	10.26	O – O # 2	518.77	10.24

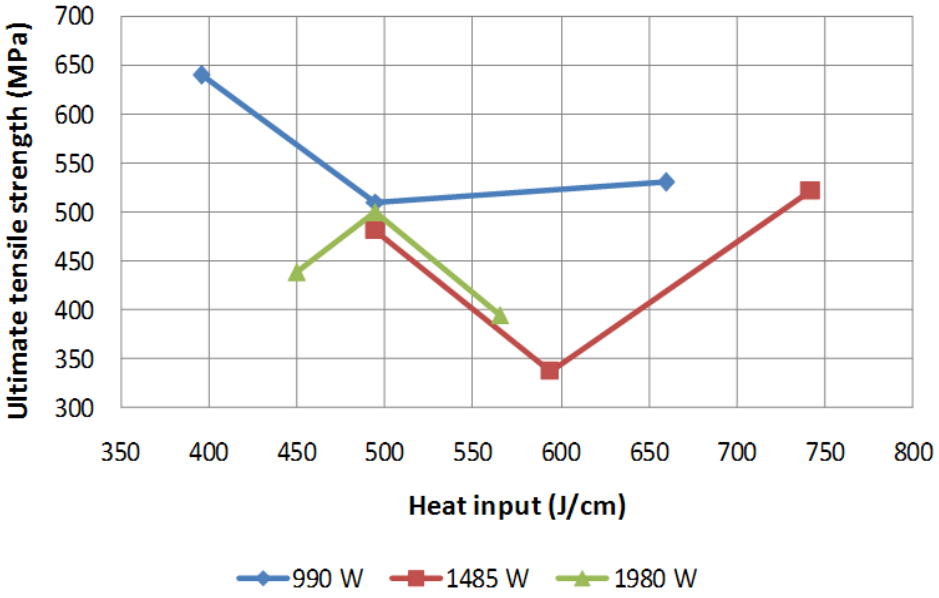

Figure 5.91 Tensile strength vs heat input at each power - 1.0 mm thick joints

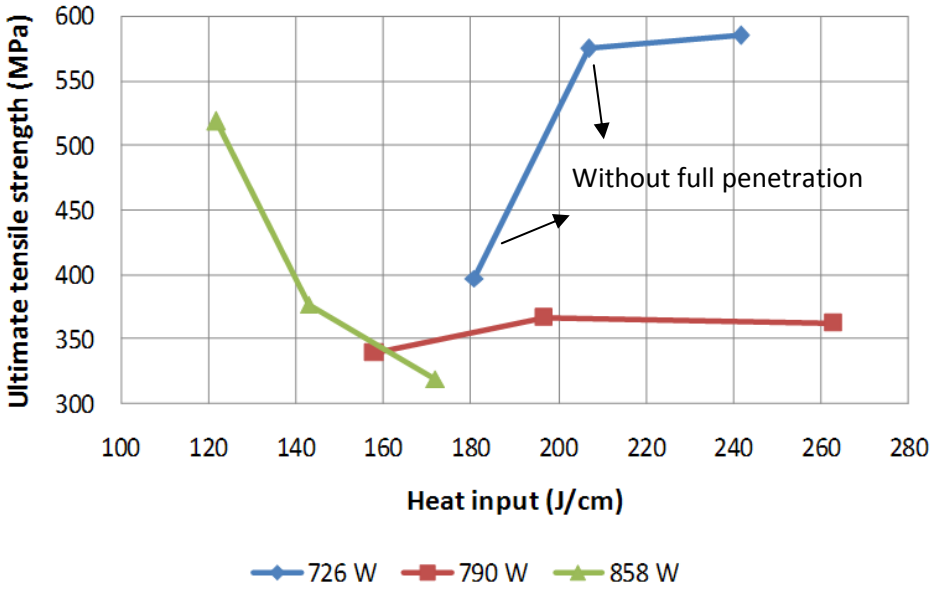

Figure 5.92 Tensile strength vs heat input at each power – 0.5 mm thick joints

Results of table 5.6 were crossed with the parameters arrangement (tables 4.17 and 4.18) resulting the plots of figures 5.91 and 5.92 for 1.0 mm and 0.5 mm thick specimens, respectively. In figure 5.91 it can be seen that 1.0 mm thick joints exhibit high tensile strength when low laser power and low heat input is used. The same effect is observed at higher welding speeds and low power. Despite the few tests presented, maximum tensile strength was observed for samples welded with 990 W. Additionally, most of the cycling specimens (five out of seven) exhibit tensile strengths above the transformation plateau stress level. (about 350-400 MPa for base material and welded joints as seen

in figure 5.83). From the structural observations, it was seen that the microstructure obtained in the fusion zone of laser welds with low heat input is very fine, as expected, since the total time for heating and cooling prevents excessive grain coarsening. Considering the Hall-Petch relation for polycrystalline materials, finer microstructures lead to higher tensile strength, as experimentally observed. However, the laser power has a stronger effect on tensile strength than the heat input, as seen from figure 5.91, and must not be excluded. This is mainly due to the effect of laser power on the weld bead width, which for this material has a relevant effect on its mechanical behavior.

Regarding laser welding of 0.5 mm thick samples, figure 5.92 points out two ways to attain higher strength joints: the first, with lower laser power (726 W), is achieved in the transition from conduction to keyhole welding, involving parameters arrangement with high heat input; the second is employing higher power (858 W), although a higher welding speed is required to reduce the heat input. Although some conclusions may be attained from these observations, it is important to reinforce that the present study is not an exhaustive one, and other factors were kept constant, such as boundary conditions regarding the fixture system, the gas protection system, surface finish, amongst others, must not be neglected when extrapolating this conclusions.

An attempt was made to correlate the sum of face and root widths with the ultimate tensile strength and a strong, almost linear, relationship was found for the 1.0 mm thick plate welds, which is presented in figure 5.93. A similar study was attempted for 0.5 mm thick plates, but the measurement error combined with the conduction/keyhole transition mode unabled this study.

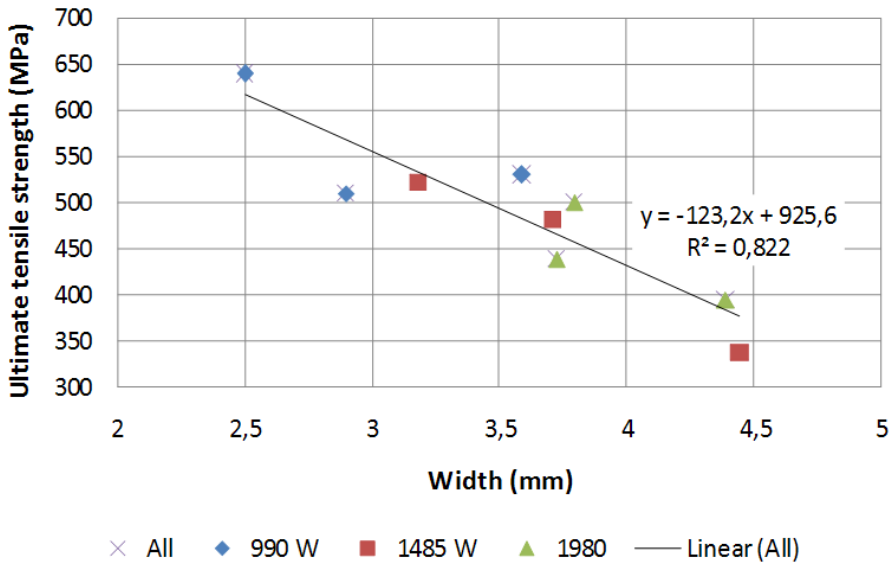

Figure 5.93 Relation between the weld bead width and the tensile strength of 1.0 mm thick joints

Once again it is possible to verify the effect noticed before (when studying the effect of the parameters arrangement on the geometry of welded beads) as power, despite the heat input, has a

straight influence on the width of weld beads. The width is an experimental consequence both of power and heat input (welding speed), and representing the global process arrangement was found in practice to relate more accurately to measured strength that theoretical parameters.

5.1.4 Results from preliminary study in pulsed mode

The results from preliminary tests conducted in pulsed mode are presented, and their analysis is focused on the effect of the parameters arrangement on the welding mode, geometry of the weld beads, and structural aspects. According to data from tables 4.19 to 4.22, experimentation was set according to four series of parameter arrangements. Results will be presented by the same logical order.

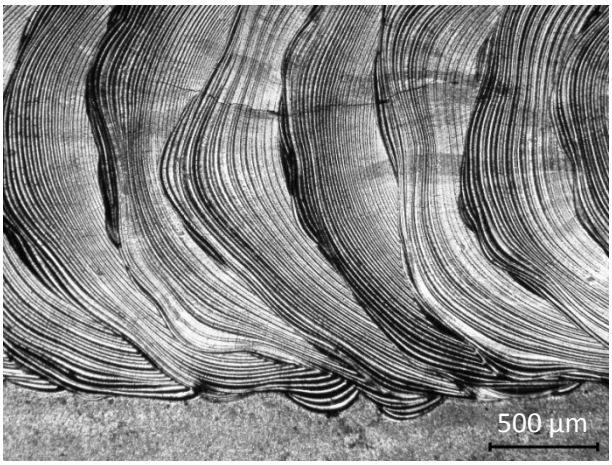

Figure 5.94 NiTi pulsed mode weld - 1st series - bead on plate # 1 – top observation

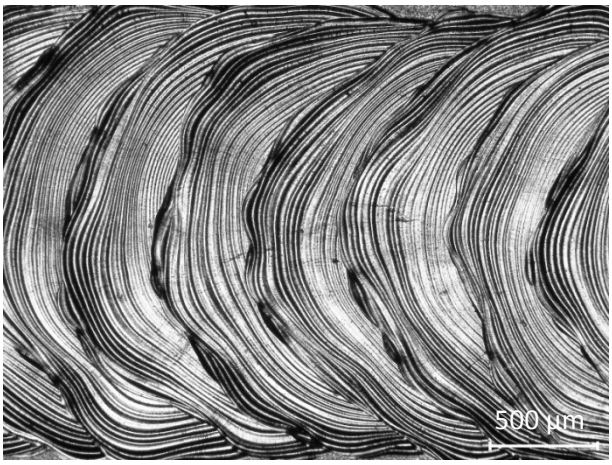

Figure 5.95 NiTi pulsed mode weld - 1st series - bead on plate # 2 – top observation

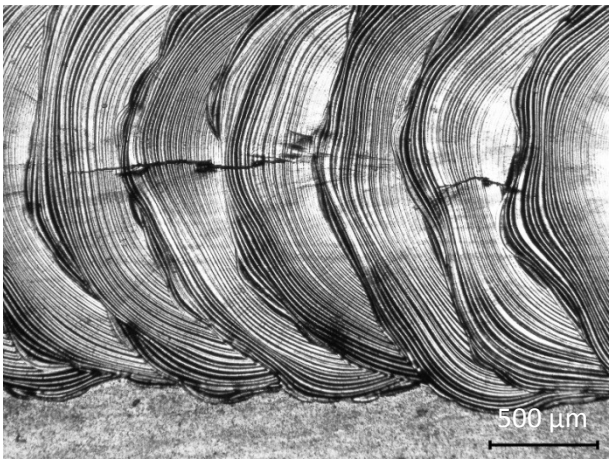

Figure 5.96 NiTi pulsed mode weld - 1st series - bead on plate # 5 – top observation

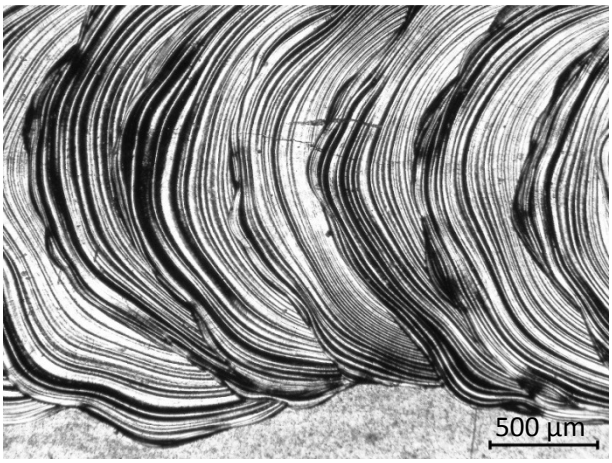

Figure 5.97 NiTi pulsed mode weld - 1st series - bead on plate # 6 – top observation

Regarding the 1st series of NiTi pulsed mode bead on plate welds, which were all attained using the same welding speed and frequency, top observations were carried on welded specimens by light microscopy and are presented from figures 5.94 to 5.101. The remaining observations are presented in annex I.

From previous results it can be observed the occurrence of cracks along the weld beads centreline, which will be studied later in this work. However, no cracks were observed in the roots of welded specimens.

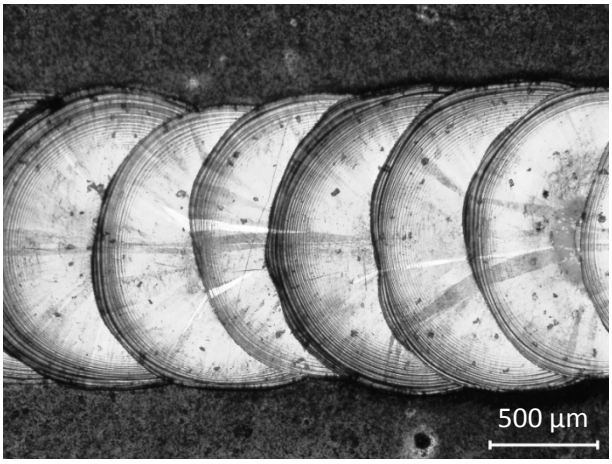

Figure 5.98 NiTi pulsed mode weld - 1st series - bead on plate # 1 – back observation

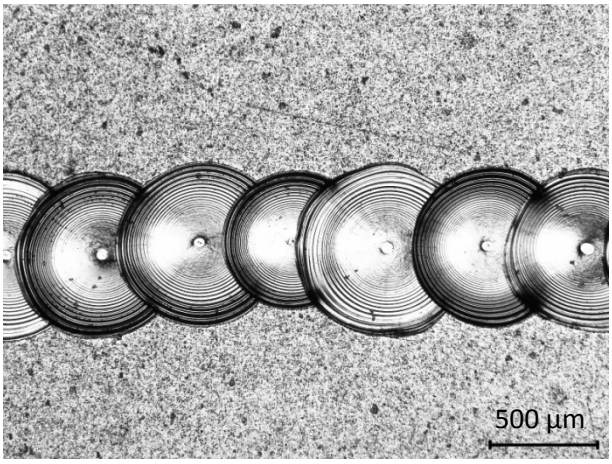

Figure 5.99 NiTi pulsed mode weld - 1st series - bead on plate # 2 – back observation

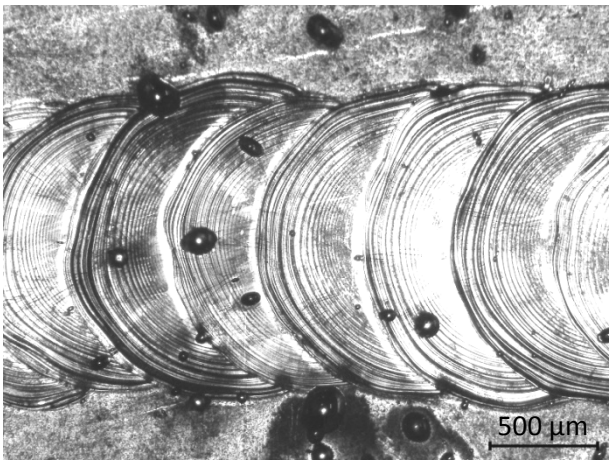

Figure 5.100 NiTi pulsed mode weld - 1st series - bead on plate # 5 – back observation

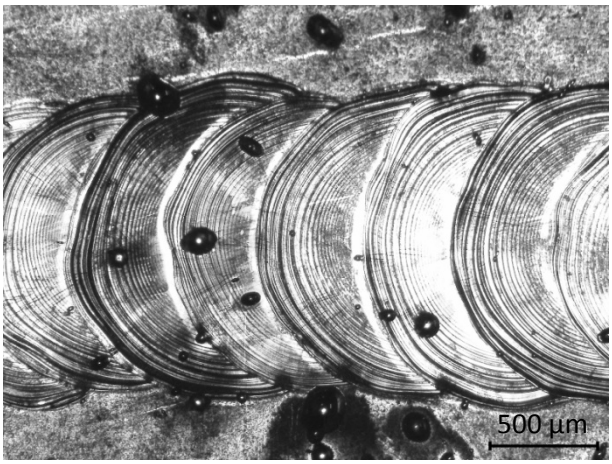

Figure 5.101 NiTi pulsed mode weld - 1st series - bead on plate # 6 – back observation

In the tests performed, welding speed was kept constant and the energy of each pulse was the result of power times the pulse duration. From previous figures it was observed the effect of the pulse energy in penetration: figures 5.99 and 5.100 show macrographs of weld roots with the same pulse duration; however sample depicted in figure 5.100 was welded with about 33 % more power than the one in figure 5.99, which resulted in a significantly wider root (about twice).

The pulse energy was found, from previous results, to be the leading parameter controlling the penetration, which can be confirmed by comparing figures 5.98, 5.100 and 5.101: all had the same pulse energy, 55 J, and although varying power up to twice, the root width was the same.

It can be observed in table 4.19 that the weld beads #7 and #8 were obtained with the same welding parameters, however the last one was performed using a recently cleaned lens, which was found to have a strong effect on penetration (due to laser beam attenuation and defocusing caused by dirt), according to the figures of annex I.

The effect of overlapping at constant frequency was studied both for high and low power, according to the parameters arrangement of tables 4.20 and 4.21, concerning the 2nd and the 3rd series of NiTi pulsed mode bead on plate welds. Results are presented in figures 5.102 to 5.107.

The occurrence of centreline cracking can be observed in several weld beads, which probably is due to the critical accumulation of shrinkage stress during solidification, when the weld is not strong enough to support the stress. Alloys solidifying through a wide temperature range, like NiTi, are particularly susceptible to this problem [41].

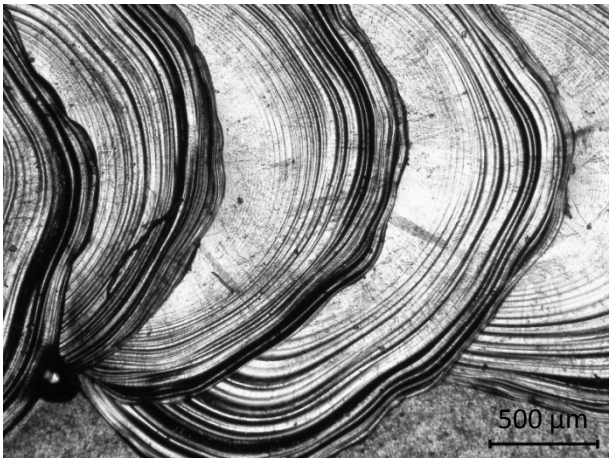

Figure 5.102 NiTi pulsed mode weld - 2nd series - bead on plate # 1 – top observation

Figure 5.103 NiTi pulsed mode weld - 2nd series - bead on plate # 6 – top observation

Figure 5.104 NiTi pulsed mode weld - 2nd series - bead on plate # 8 – top observation

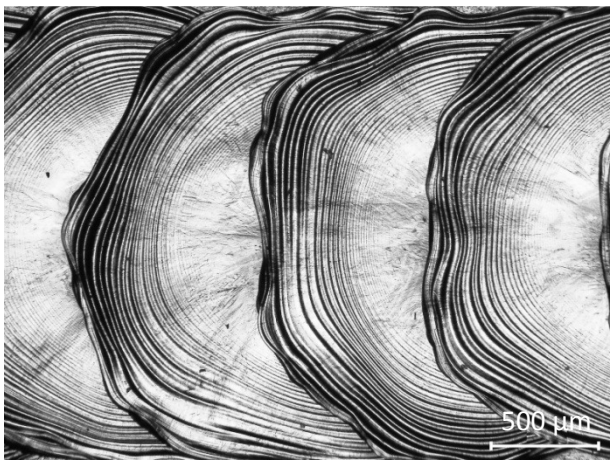

Figure 5.105 NiTi pulsed mode weld - 3rd series - bead on plate # 1 – top observation

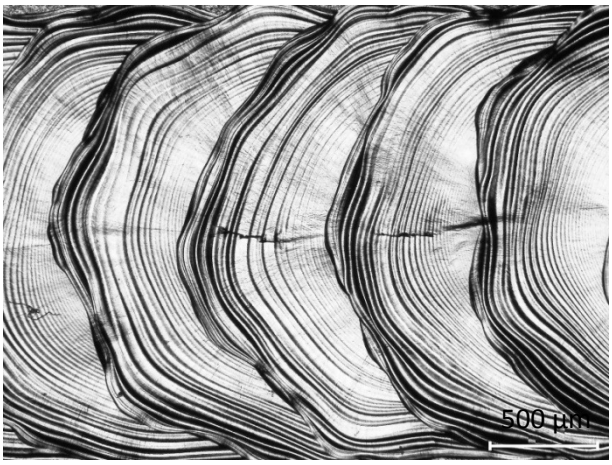

Figure 5.106 NiTi pulsed mode weld - 3rd series - bead on plate # 3 – top observation

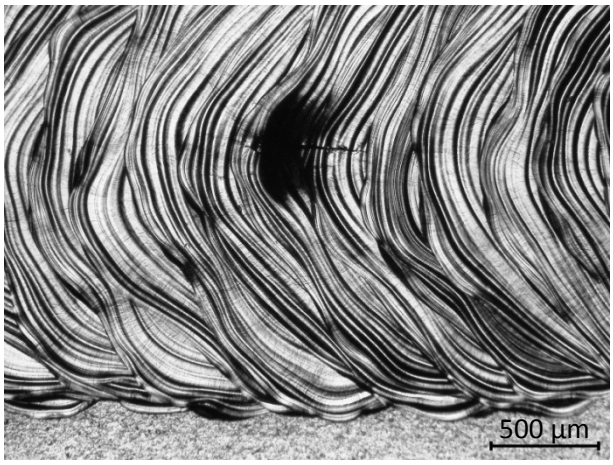

Figure 5.107 NiTi pulsed mode weld - 3rd series - bead on plate # 7 – top observation

Regarding the parameters presented in tables 4.20 and 4.21, it can be observed that the process variables can be summarized to the following independent ones: pulse energy, welding speed and frequency, maintaining constant the focal point position and beam diameter.

Considering that the frequency is also constant, a simple evaluation parameter given by the combination of the two variables was used to correlate the parameters arrangement with the occurrence of centreline cracking. The parameter used to evaluate the occurrence of cracking, herewith referred as 'cracking parameter', *CP*, (Wm) is given by eq. 5.1:

$$CP = pulse\ energy \times welding\ speed \qquad (5.1)$$

The calculated CP values are presented in table 5.7 for the overlapping study regarding the 2nd and 3rd series of NiTi bead on plate welds. Analyzing the macrographs from previous figures and identifying the cracking occurrences, the corresponding CPs are underlined in table 5.7.

From the calculated CP parameter, it can be observed that cracking occurs always in the range of 9.90 to 25.83. Moreover, in terms of crack incidence, figures 5.104 and 5.107 are quite similar, and the cracking parameters only vary about 10% despite the significant difference in power. Apparently, there is an agreement of this parameter with experimental results, though extrapolation of this conclusion to other conditions must be regarded with precaution, as they are based on few experimental results and further work is needed to understand how cracking is dependent on the welding parameters arrangement.

Table 5.7 Cracking parameter of the 2nd and 3rd series of NiTi bead on plate welds

High power – 2nd series				Low power – 3rd series			
Test number	*Energy*	*Welding speed*	*CP*	*Test number*	*Energy*	*Welding speed*	*CP*
	J	mm/s	W.m		J	mm/s	W.m
1	55	0.81	44.50	1	41	0.81	33.21
2	55	0.72	39.60	2	41	0.72	29.52
3	55	0.63	34.65	3	41	0.63	25.83
4	55	0.54	29.70	4	41	0.54	22.14
5	55	0.45	24.75	5	41	0.45	18.45
6	55	0.36	19.80	6	41	0.36	14.76
7	55	0.27	14.85	7	41	0.27	11.07
8	55	0.18	9.90	8	41	0.18	7.38

The results from the 4th series of NiTi pulsed mode bead on plate welds are depicted in figures 5.108 to 5.113. These experiments were conducted keeping all parameters constant except the pulse energy, a consequence of varying power. Figure 5.108 shows a top view of the weld beads. The pulse energy was increased constantly form 10 to 18 J, and again it can be concluded its straight effect on penetration: from figures 5.108 to 5.113 the penetration progressively increases as the width of the weld beads converges (figure 5.112).

In the weld beads attained with higher energies it is possible to observe columnar grain growth from the successively wider HAZ towards the weld centreline, although parameters arrangement led

always to conduction mode. Figures 5.112 and 5.113 show that the experiment was conducted in pulsed mode, and it is possible to observe two distinct crystallization zones, each of them related to the successive pulses. According to figure 5.108, the outer FZ region of both figures was formed first, as the inner region resulted from recrystallization induced by the following pulse, which explains the more equiaxed grain structure that can be observed in this region.

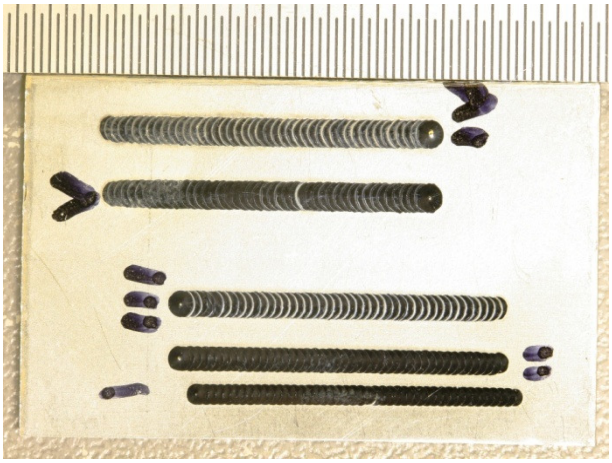

Figure 5.108 4th series of NiTi pulsed mode beads on plate – top observation showing numbered beads

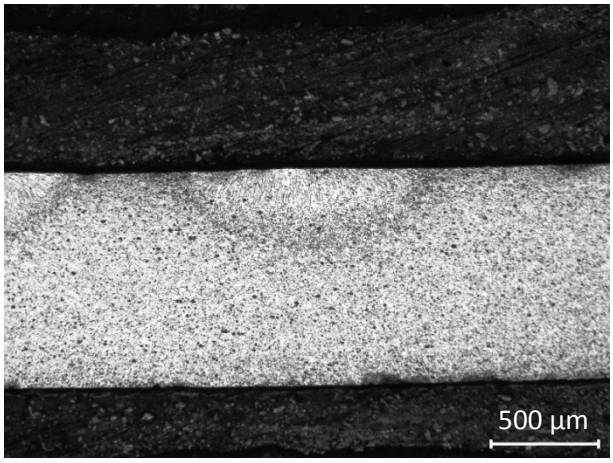

Figure 5.109 4th series of NiTi pulsed mode beads on plate – macrograph of weld bead #1

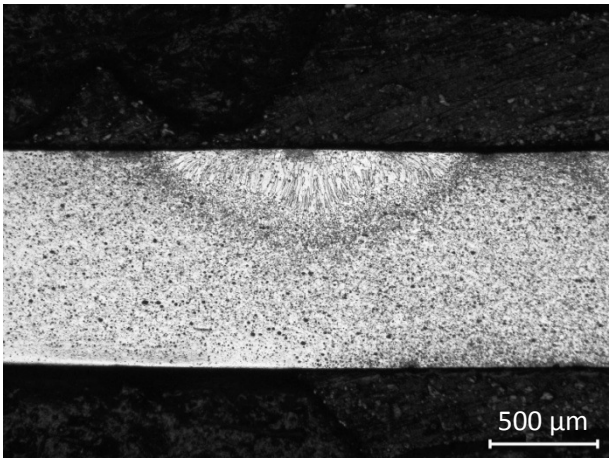

Figure 5.110 4th series of NiTi pulsed mode beads on plate – macrograph of weld bead #2

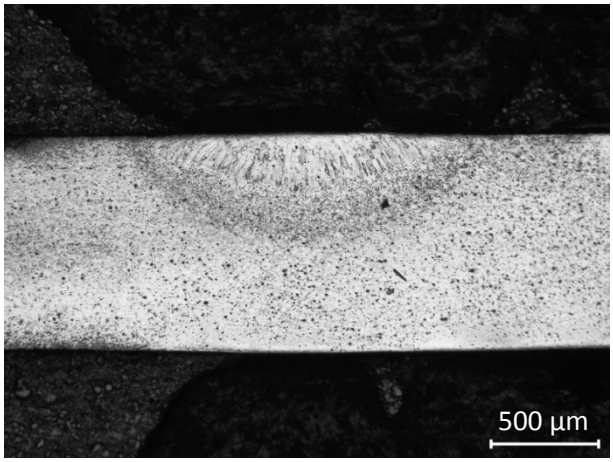

Figure 5.111 4th series of NiTi pulsed mode beads on plate – macrograph of weld bead #3

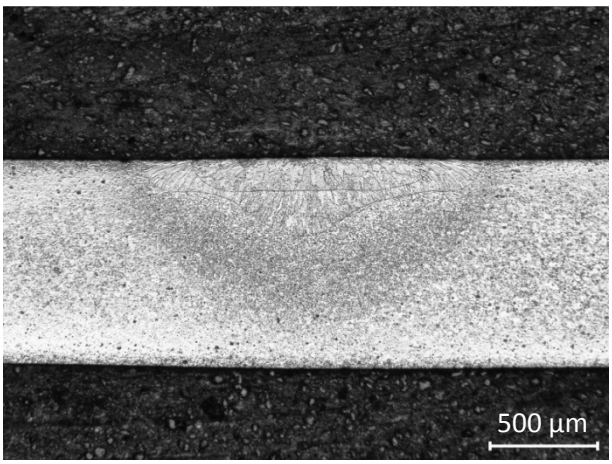

Figure 5.112 4th series of NiTi pulsed mode beads on plate – macrograph of weld bead #4

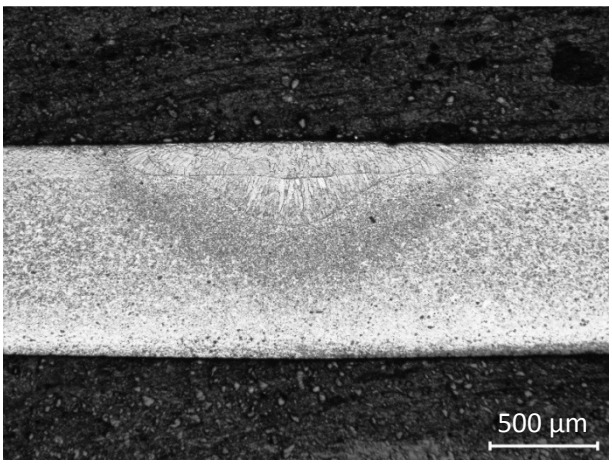

Figure 5.113 4th series of NiTi pulsed mode beads on plate – macrograph of weld bead #5

5.2 Dissimilar joints

The results from the preliminary investigations on dissimilar joints are now presented. Although dissimilar welds do not constitute the main scope of the present work, results are presented and analyzed according to the experimental plan, constituting a starting point for further developments.

5.2.1 Results from dissimilar wire shape NiTi/AISI 316LN joints

Dissimilar NiTi to AISI 316LN lap joints were attained according to the experimental procedures described before (see 4.4.2.1). Structural observations and mechanical testing were performed on welded joints and results are presented below.

5.2.1.1 Structural observations

Light microscopy observations were carried out on transverse sections of welded specimens and results are depicted in figures 5.114 and 5.115. Figure 5.114 presents a macrograph where it is possible to identify the welded region, darker in the middle of both base materials. The stainless steel was not affected by the etching solution and looks brighter; however, NiTi wire is identified in figure 5.114. The three small arrows identify the fusion region that resulted from the first pass. The technique was found to be unsuitable and specimens were reused for double pass joints.

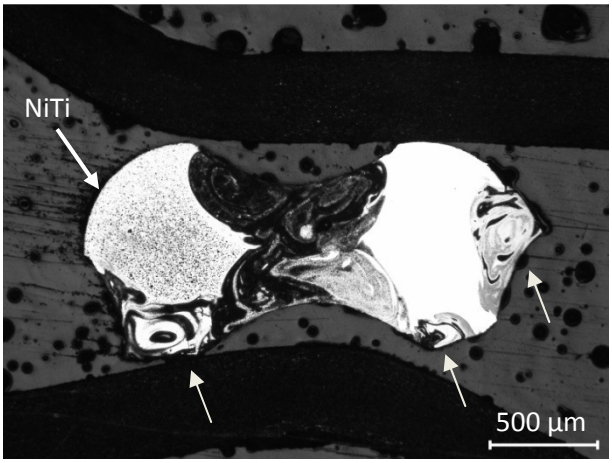

Figure 5.114 Macrograph of the dissimilar NiTi/AISI 316LN lap joint showing the welded zones and identifying the NiTi side

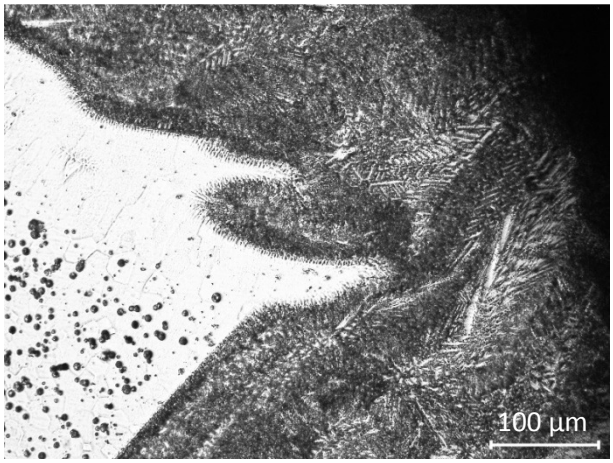

Figure 5.115 micrograph of the dissimilar NiTi/AISI 316LN lap joint showing the interface between the NiTi base material (left) and the fusion zone dendritic microstructure

Figure 5.115 presents a micrograph of the interface between the NiTi and the fusion zone. As other reported [40] a HAZ was observed in the NiTi side, constituted of equiaxed grains, from which columnar grains grow towards the dendritic microstructure of the fusion zone.

SEM observations were performed on the same transverse section and backscattered electrons revealed the structures depicted in figures 5.116 and 5.117.

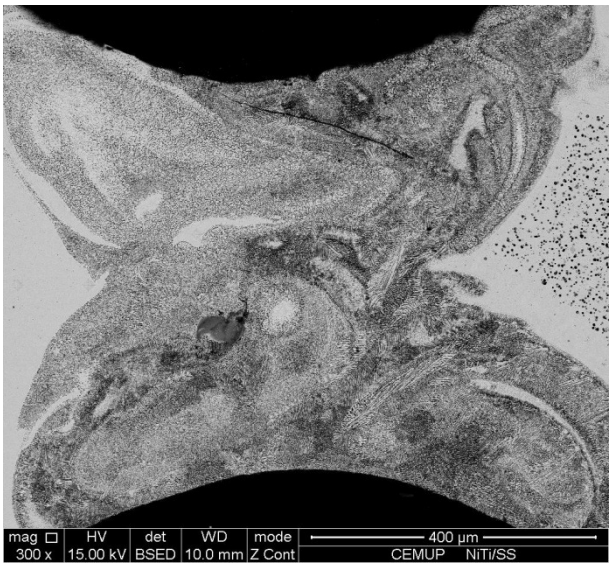

Figure 5.116 SEM observation of a transverse section of the dissimilar NiTi/AISI 316LN lap joints showing the welding zones

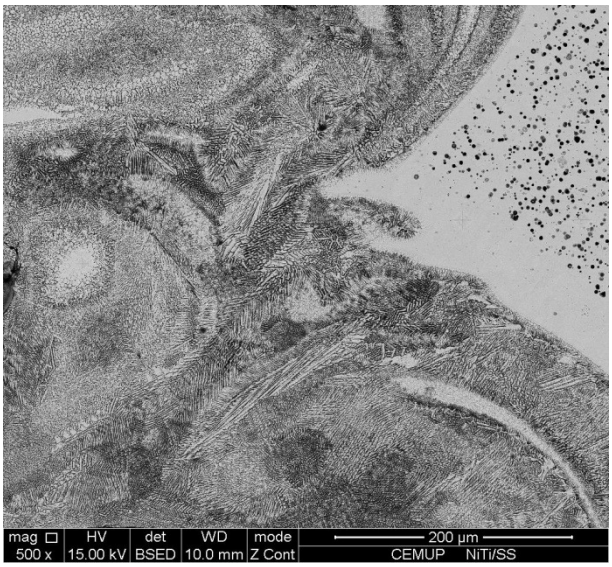

Figure 5.117 SEM observation of a transverse section of the dissimilar NiTi/AISI 316LN lap joints showing the fusion zone dendritic structure and the transition to the NiTi side

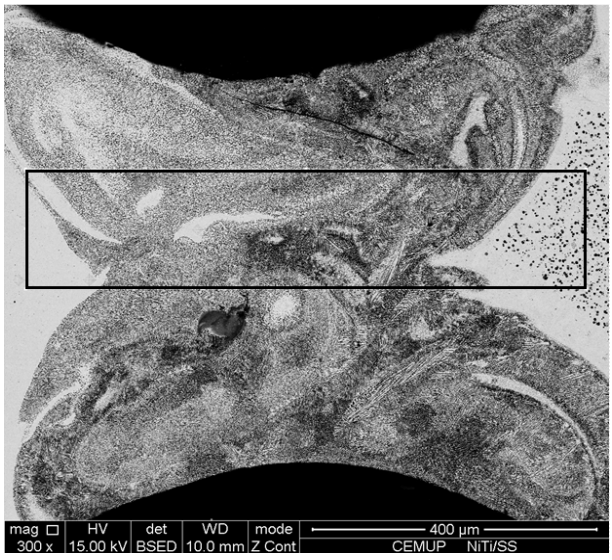

Figure 5.118 SEM observation on the welded zone of the dissimilar NiTi/AISI 316LN lap joints showing the area were chemical elements mapping was performed.

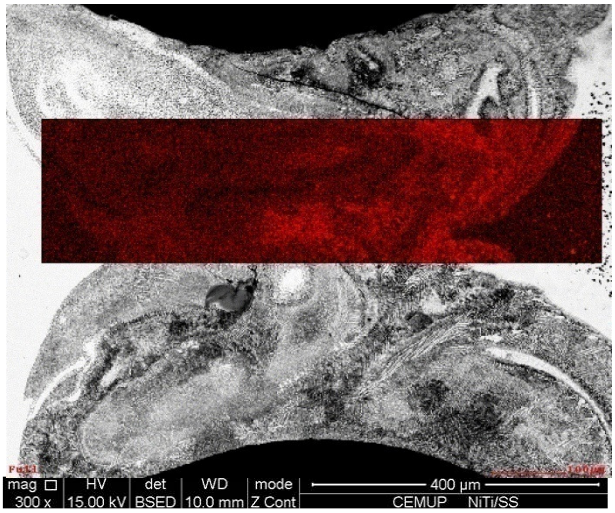

Figure 5.119 SEM observation on the welded zone of the dissimilar NiTi/AISI 316LN lap joints showing the EDS mapping of Carbon in red

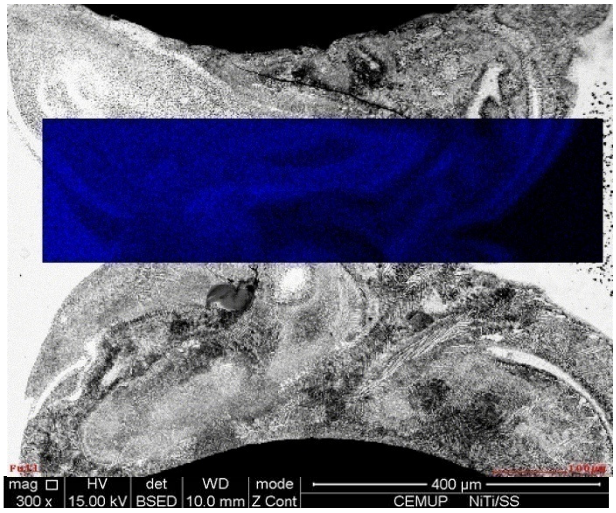

Figure 5.120 SEM observation on the welded zone of the dissimilar NiTi/AISI 316LN lap joints showing the EDS mapping of Chromium in blue

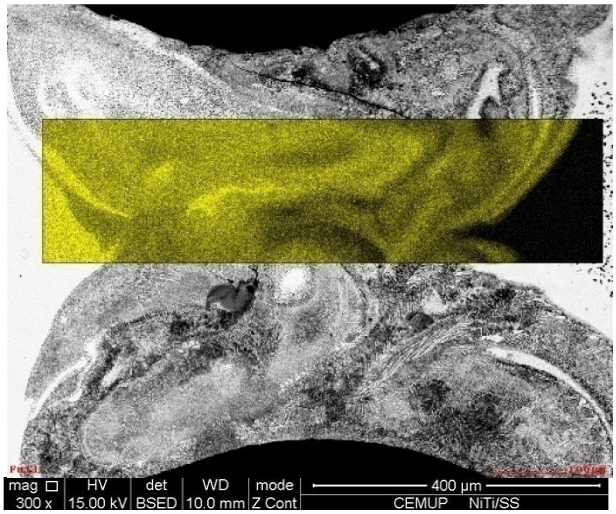

Figure 5.121 SEM observation on the welded zone of the dissimilar NiTi/AISI 316LN lap joints showing the EDS mapping of Iron in yellow

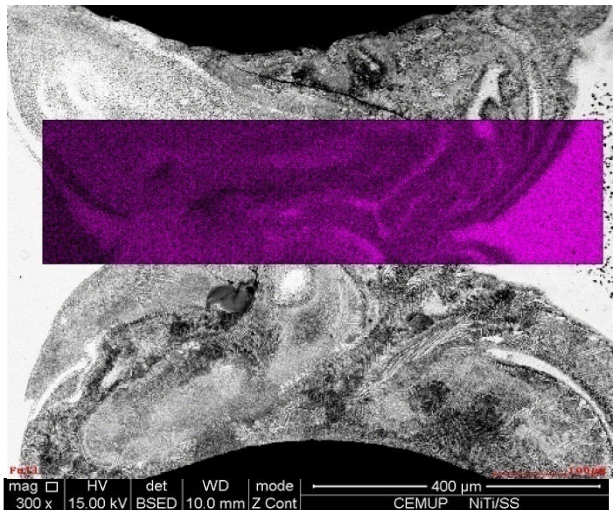

Figure 5.122 SEM observation on the welded zone of the dissimilar NiTi/AISI 316LN lap joints showing the EDS mapping of Nickel in pink

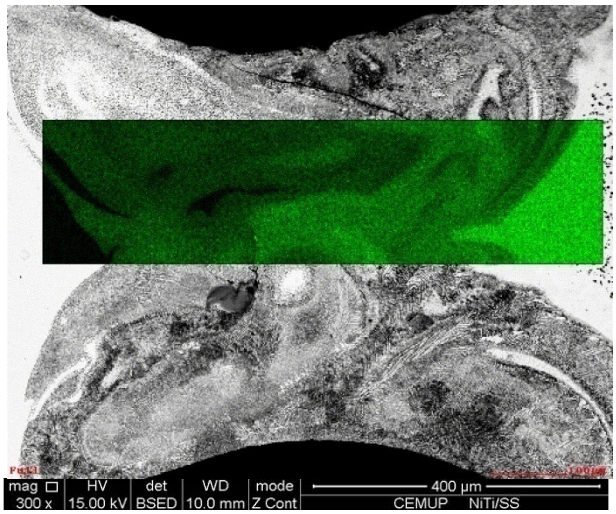

Figure 5.123 SEM observation on the welded zone of the dissimilar NiTi/AISI 316LN lap joints showing the EDS mapping of Titanium in green

EDS mapping of chemical elements was performed on the transverse sections of welded joints within an area depicted in figure 5.118. From figure 5.119 to 5.123 are presented the chemical EDS maps of Carbon, Chromium, Iron, Nickel and Titanium, respectively.

Carbon was found in both base materials; dispersed in stainless steel and spotted in NiTi. It was also found to be present in the darker constituents of the FZ (mainly on the NiTi side), when observed by backscattered electrons. Chromium was found in the stainless steel and spread trough out the FZ,

mainly in the brighter structures on the stainless steel side (when observed by backscattered electrons).

Iron was found to in the FZ. Nickel was identified in both base materials, in larger amounts on the NiTi side. It was also found spread all over the FZ, in the grey dual-phase dendritic regions of figure 5.118.

Titanium was seen in the NiTi base material, as well as, spread all over the FZ. Significant amounts were identified in the darker dendritic structures in the NiTi side of figure 5.118. It aws also found to co-exist with significant amounts of Nickel and Carbon.

Maps combining several of the previous elements were also obtained from EDS analysis on the transverse section, which are presented from figure 5.124 to 5.126. A color legend of chemical elements is also presented at the right of each map.

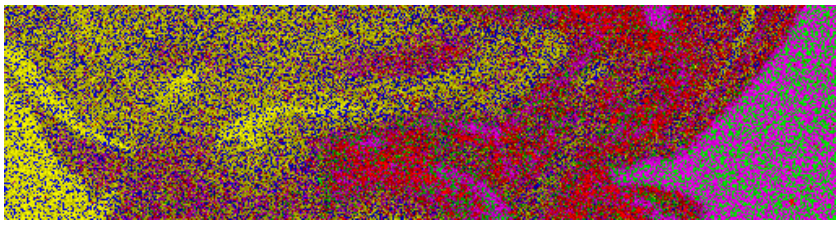

Figure 5.124 EDS mapping of C, Ti, Cr, Fe and Ni inside the window of the FZ of a dissimilar NiTi/AISI 316LN joint depicted in figure 5.118

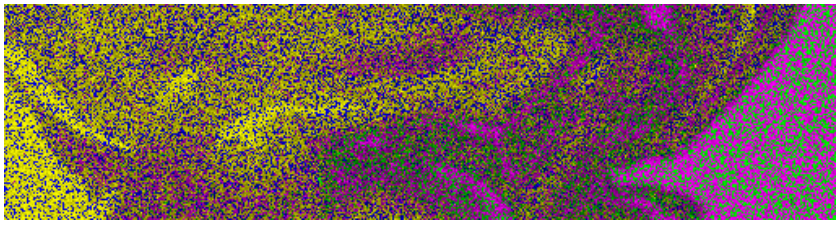

Figure 5.125 EDS mapping of Ti, Cr, Fe and Ni inside the window of the FZ of a dissimilar NiTi/AISI 316LN joint depicted in figure 5.118

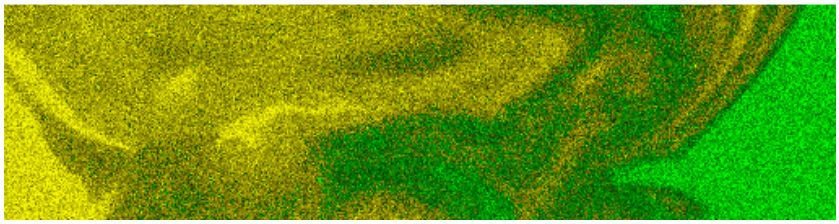

Figure 5.126 EDS mapping of Ti and Fe inside the window of the FZ of a dissimilar NiTi/AISI 316LN joint depicted in figure 5.118

In the FZ Titanium was found to combine either with Nickel or Carbon, while in the NiTi base material is always combined with Nickel. Chromium was found scattered both in the stainless steel base material and in the FZ, mostly combined with Iron. Results from previous maps were combined with a SEM BSE observation and some conclusions are presented in figure 5.127.

Gugel and Theisen [40] have reported the presence of brittle Fe_2Ti scattered with Fe in the transition from the FZ to the stainless steel. It was not possible to identify that phase by this method, however in some locations it can be observed significant amounts of Iron combined with less Titanium, with scattered Iron-rich regions.

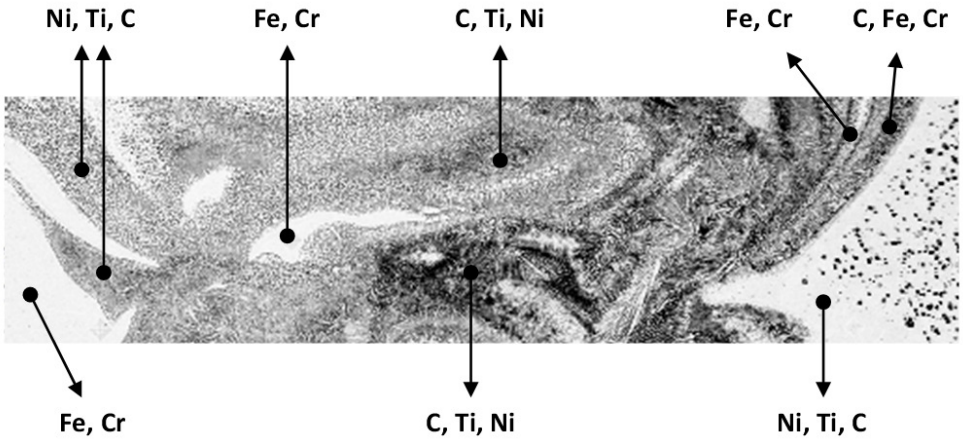

Figure 5.127 SEM backscattered electrons observation of the fusion zone of a dissimilar NiTi/AISI 316LN lap joint showing the main chemical composition of some regions, identified by EDS maps (elements are presented according to relevance in the selected region)

The dendritic structures of figure 5.127 seem to be mainly composed by Ni, Ti and C in different amounts. The darker ones have both high Carbon and Titanium, suggesting the presence of Titanium carbides, as reported by Gugel and Theisen [40]. Despite the conclusions drawn from the previous EDS maps, further investigations such as finer EDS measurements, XRD and TEM is needed to accurately characterize the complex welded zone of such dissimilar NiTi to AISI 316 stainless steel joints.

5.2.1.2 Microhardness measurements

Vickers microhardness measurements were performed on transverse sections of welded specimens, and the resulting profile, combined with a macrograph identifying both the welding regions and the indentation marks, is presented in figure 5.128.

From the hardness profile it can be concluded that is not clear the existence of a HAZ in the NiTi side, despite the microstructural observations, since that the transition region from the NiTi base material

to the dendritic structure of the fusion zone presents higher hardness than the base material. The fusion zone is characterized by very hard phases and the brighter phase shown in figure 5.128 was found to be the hardest.

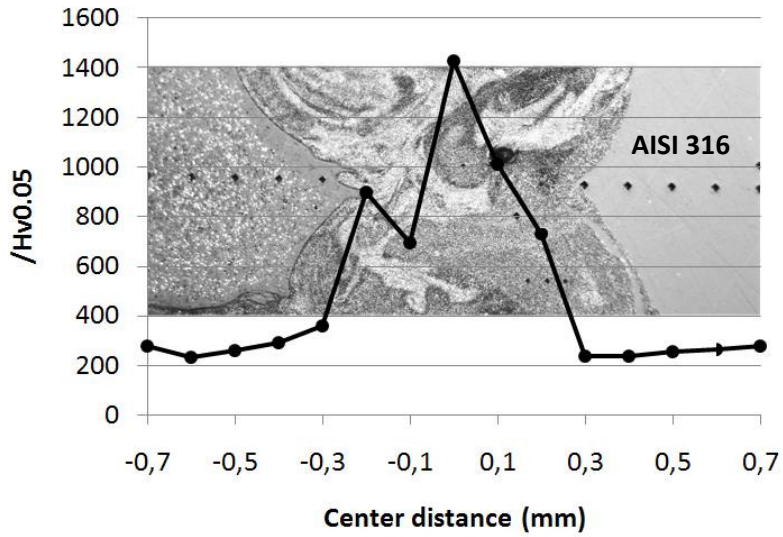

Figure 5.128 Microhardness profile along the weld regions of a NiTi/AISI 316LN lap joint

5.2.1.3 Tensile tests

The NiTi/AISI 316LN wire shape lap joints were tested as fragile fracture (evidence from visual observations) occurred always (three specimens tested) by the heat affected zone on the NiTi side, as Gugel *et al* [43] also experienced. Results from tensile testing performed on the base materials and welded joints are summarized in table 5.8, as their mean values are presented at the right.

Table 5.8 Tensile results of NiTi/AISI 316LN wire shape dissimilar joints

Reference	σ_u	ε_u	$\overline{\sigma}_u$	$\overline{\varepsilon}_u$
	MPa	%	MPa	%
AISI 316LN #1	1623	3.80	1671	3.90
AISI 316LN #2	1719	4.30		
AISI 316LN #3	1671	3.60		
NiTi/AISI 316LN #1	271	1.18	281	1.16
NiTi/AISI 316LN #2	334	1.33		
NiTi/AISI 316LN #3	239	0.96		

From previous results it can be concluded that premature rupture occurred, as the martensitic transformation plateau was never observed, due to the very low ultimate tensile strength achieved by the welded joints.

5.2.2 Results from dissimilar joints to Ti-6Al-4V

5.2.2.1 Bead on plate pulsed mode welds

Preliminary bead on plate welds were produced according to the parameters presented in table 4.24. Full penetration was achieved with 1750 W, pulse energy of about 35 J and welding speed of 135 mm/min (weld bead #7). The result from optical observations carried on the top face obtained with the mentioned parameters is presented in figure 5.129. As it can be observed, a joint free of cracks was produced, with a fusion zone presenting coarse grains that grow across adjacent spots, in the direction of heat flow.

Figure 5.130 shows an optical observation carried on the top face of a weld bead produced with lower power and about twice the welding speed of the previous one (weld bead #1). No full penetration was attained, as the combination of low heat input due to low energy and high welding speed affected the geometry, that is shorter total heating and cooling time. Particularly, the effect of discontinuous crystallization between successive spots, which is visible on the top faces, is much more pronounced than in figure 5.129, as grains are noticeably less coarse. Complementary figures are presented in annex I.

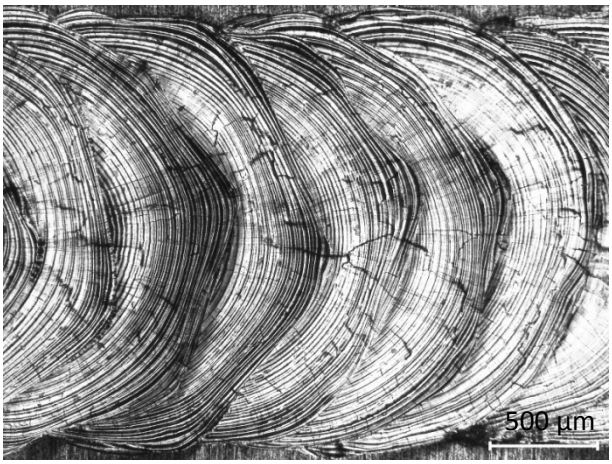

Figure 5.129 Optical observation of the Ti-6Al-4V bead on plate weld #7 showing top face

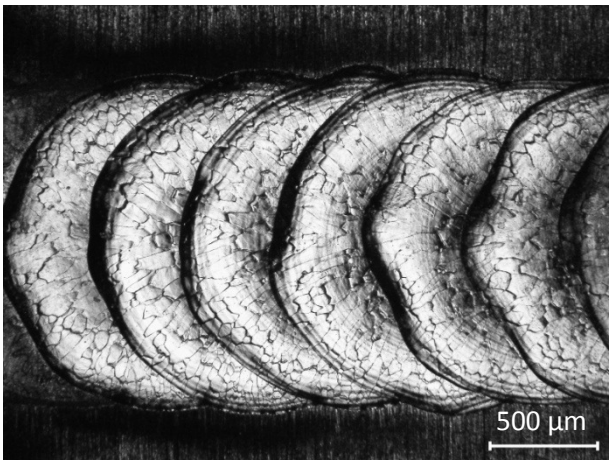

Figure 5.130 Optical observation of the Ti-6Al-4V bead on plate weld #1 showing top face

5.2.2.2 Dissimilar NiTi/Ti-6Al-4V butt welds

Dissimilar pulsed welds were produced according to the processing parameters of tables 4.25 to 4.27. Without exception, the 1st, 2nd and 3rd series of welds cracked completely by the weld centreline during cooling, before had after been removed from the fixture system.

The next series were performed in continuous wave mode, according to the parameters of tables 4.28 to 4.31.The 4th series resulted in laser cutting, due to excessive heat input. The 5th series samples were welded using both start and ending plates, as well as, higher heat input than the previous. Extensive cracking occurred upon cooling in the weld centreline, also before specimens had been removed from the fixture system.

Both the 6th and 7th series resulted in welded joints without macroscopic evidence of cracking. Optical observations revealed that all welds from the 6th series did not achieve full penetration, as partial cracking was observed in the fusion zone of some joints. The macrostructure of the fusion zone is presented in figure 5.131, where the partial penetration can be observed, as well as, the existence of heat affected zones both in the Ti-6Al-4V and NiTi sides. The fusion zone is mainly constituted by a rapid solidification dendritic structure, in which can be observed the Marangoni effect. The transition zone FZ/Ti-6Al-4V is colored darker due to a different orientation of the dendritic structure, as well as due to the severe removal of the interdendritic material (including segregations) observed after etching.

The microstructure of the fusion zone is depicted in figure 5.132, were it is possible to observe crack propagation, which were found to initiate in the root, propagating along the Ti-6Al-4V transition zone, most probably due to the combination of solidification shrinkage, dendritic microstructure and partial penetration.

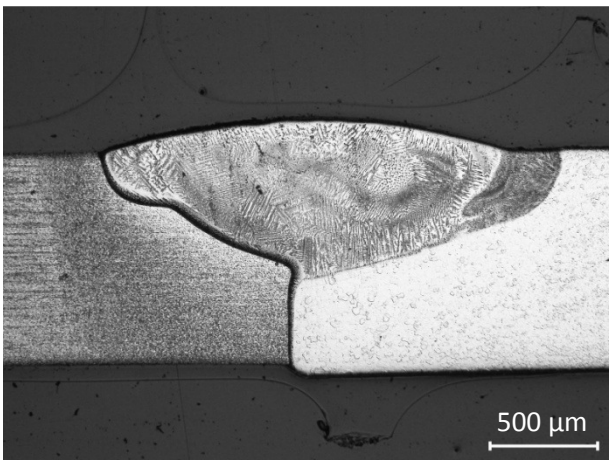

Figure 5.131 Macroscopic observation carried on the 6th series (ref O1) dissimilar Ti-6Al-4V welded joint, presenting the NiTi base material at right and showing partial penetration

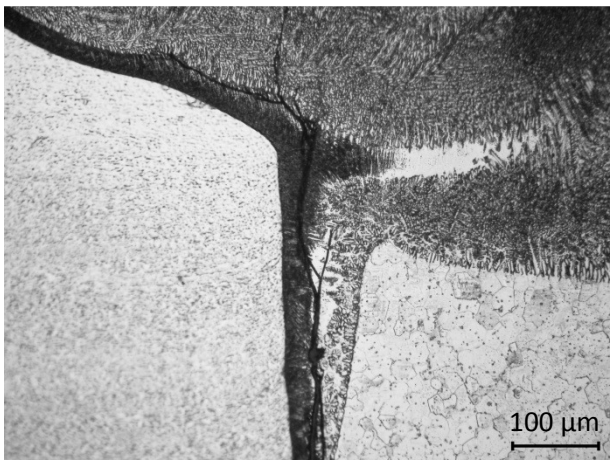

Figure 5.132 Optical observation of the welded zone carried on a transverse section of the 6th series (ref. H1) dissimilar Ti-6Al-4V welded joint, showing cracking in the fusion zone

SEM observations carried on this sample revealed the fusion zone microstructure shown in figure 5.133, in which it is possible to identify extensive cracking near the Ti-6Al-4V transition zone, as well as, the dendritic solidification structure of the fusion zone.

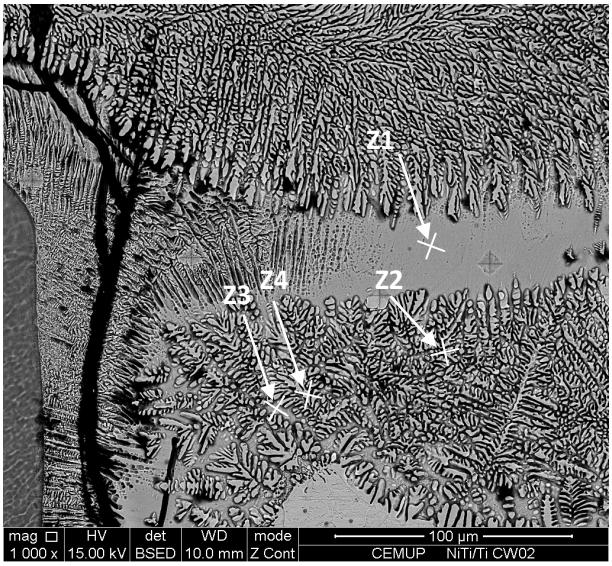

Figure 5.133 SEM BSED observation on the welded zone of the 6th series (ref. H1) dissimilar Ti-6Al-4V welded joint, showing extensive cracking and the spots of EDS chemical analysis

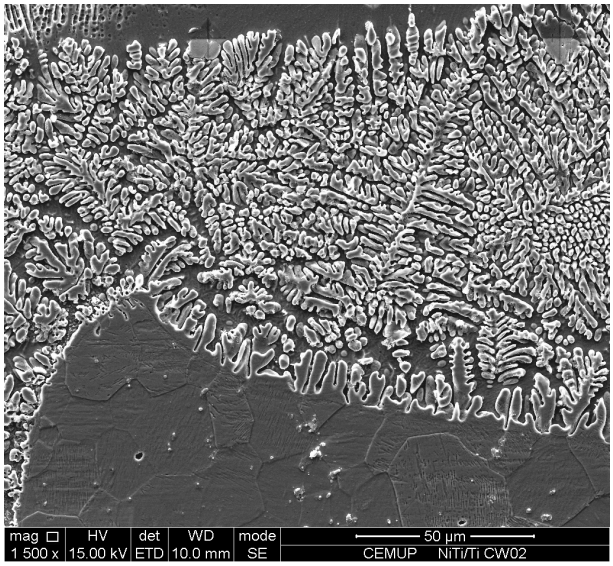

Figure 5.134 SEM SE observation on the transition zone of the 6th series (ref. H1) dissimilar Ti-6Al-4V welded joint, showing dendritic structures in the NiTi side

Semi-quantitative analysis with EDS was performed in the regions marked in figure 5.133 and results are presented in table 5.9. The marks on figure 5.133 correspond to the following:

- Interdendritic regions: Z3, (Z1)
- Dendritic arms: Z2, Z4

Table 5.9 EDS chemical semi-quantitative analysis - Ti-6Al-4V dissimilar joint of figure 5.133

at. %				
Reference	Al k	Ti k	V k	Ni k
Z1	4.52	61.8	0.59	33.09
Z2	1.49	48.84	0.00	49.67
Z3	1.76	62.34	0.11	35.70
Z4	1.08	49.14	0.00	49.79

From previous results it can be concluded that the interdendritic regions of the fusion zone are probably composed by the Ti_2Ni intermetallic alongside with other elements such as Aluminum and Vanadium. The dendritic arms, despite the penetration of the electron beam and consequent matrix effect on such small structures, seem to be mainly constituted by NiTi alongside Aluminum. In fact, figure 5.134 shows the growing of dendrites from the NiTi HAZ microstructure. No Vanadium was identified in the dendritic arms.

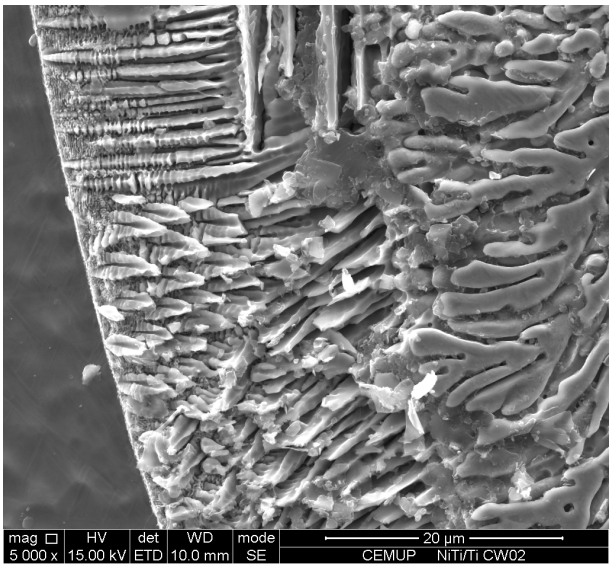

Figure 5.135 SEM BSED observation on the transition zone of the 6th series (ref. H1) dissimilar Ti-6Al-4V welded joint, showing the dendritic interface in the Ti-6Al-4V side

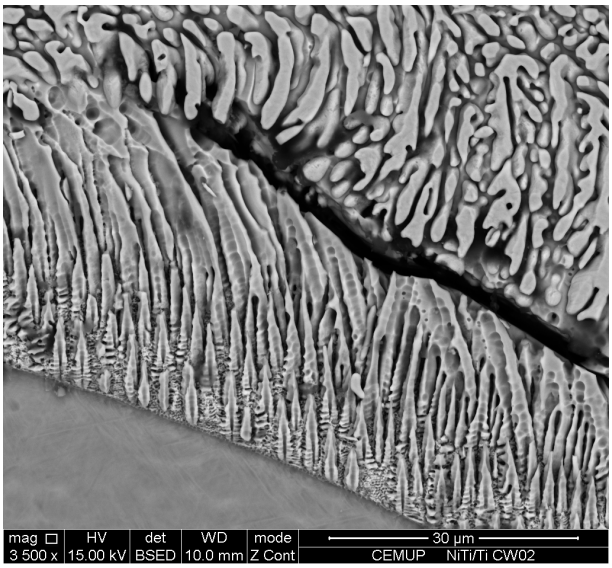

Figure 5.136 SEM BSED observation on the transition zone (Ti-6Al-4V side) of the 6th series (ref. H1) dissimilar Ti-6Al-4V welded joint, showing crack propagation trough dendritic interfaces with different orientations

The microstructure of the Ti-6Al-4V transition zone was observed by SEM and figure 5.135 reinforces the conclusions from optical observations, suggesting the presence of an interface between two

dendritic solidification structures, a consequence of materials flow during solidification. From the Ti-6Al-4V side emerges a very fine dendritic microstructure, which is constrained by the coarser rapid solidification structure of the fusion zone. Cracks were found to develop along this interface, as figure 5.136 shows.

5.2.2.3 Microhardness measurements

Vickers microhardness measurements were performed on the transverse section of the 6th series H1 specimen, by applying a test load of 500 mN. The resulting hardness profile was combined with a macrograph of the welded zone and the result is depicted in figure 5.137.

Microhardness results corroborate the presence of a HAZ both in the NiTi and Ti-6Al-4V sides, noticed in the NiTi side by a small reduction in the hardness measurements, mainly due to the grain size effect, and by slightly higher hardness values in the Ti-6Al-4V side, due to the formation of α' martensite from the parent β phase, due to the rapid thermal cycle, also reported by [71 to 72].

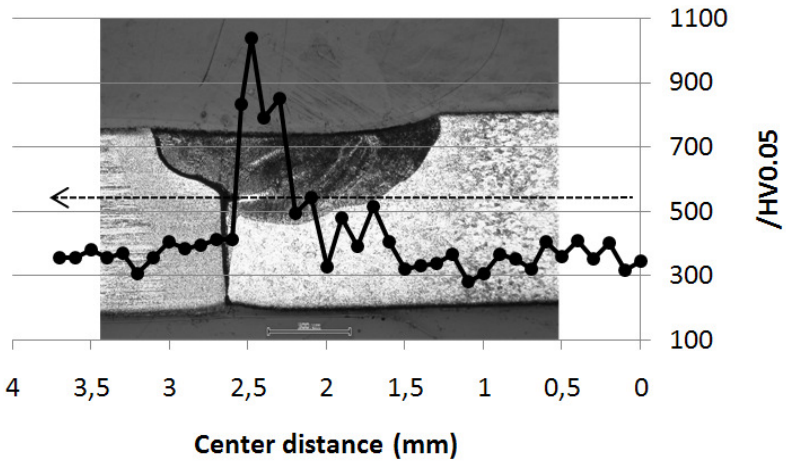

Figure 5.137 Vickers microhardness profile combined with a macrograph of the welded zone of a dissimilar weld to Ti-6Al-4V from the 6th series (ref. H1). A dashed arrow indicates the microhardness indentation path, starting in the NiTi side.

From figure 5.137 it can be observed that the fusion zone present the higher hardness, as the region identified as Z1 in figure 5.133, pointed out before as most probably Ti_2Ni, as well as, small amounts of Al and Ti. This region was found to be the most brittle phase, exceeding 1000 /HV0.05.

6. Conclusions and future work

The effect of laser welding on the structural, mechanical and functional properties of NiTi similar and dissimilar welded joints was studied. Several laser power sources both operating on continuous and pulsed mode were used. Similar 0.5 and 1.0 mm, as well as, 1.0 mm thick dissimilar joints to Ti-6Al-4V and 1.0 mm wire shape lap joints to AISI 316 LN were produced.

Similar welded joints free of major defects were produced using optimized process parameters. However, microstructural investigations revealed the presence of small and scattered pores. Tensile tests conducted on 1.0 thick similar butt joints for design evaluation revealed superior ultimate tensile strength and elongation to fracture of specimens welded across the rolling direction. Despite the presence of small defects, ductile fracture occurred at stress levels that allow exploring the superelastic effect to recoverable strain levels close to 8%. The superelastic plateaus were observed on welded specimens at the same stress level of those exhibited by the base material, at about 350-400 MPa.

Functionally, DSC tests performed on the molten metal revealed a single step B2->B19' transformation, as characteristic temperatures were found to increase. The stabilization of the mechanical hysteretic response of welded joints was compared to the base material, to strain levels up to 8%. For tensile cycling involving strains above 6%, welded specimens were found to present superior mechanical behavior by presenting larger recoverable strain levels. This behavior is mainly a consequence of the microstructure of the welded zone. Although not favorable for the ultimate tensile strength exhibited by the welded joints, which was found to be inversely proportional to the extent of the welded zone, had the effect of enhancing the cyclic functionality.

Microstructural investigations carried on transverse sections of welded joints revealed the presence of a fusion zone mainly constituted by coarse columnar grains aligned with the heat flow direction. The fusion zone was found to be constituted by a NiTi matrix, where a scattered distribution of small TiC particles was sometimes observed. Ti_2Ni like particles were identified amongst the coarse equiaxed grains of the heat affected zone. Microhardness measurements revealed a hardness decrease of about 40% in the fusion zone compared to the base material, mainly due to the effect of grain size.

Dissimilar lap joints to AISI 316 LN stainless steel were produced using a Nd:YAG laser source operating in pulsed wave mode exhibited low ultimate tensile strength. Although the presence of brittle phases in the fusion zone was confirmed, fracture occurred by the NiTi heat affected zone,

which may be explained by the heat-affected microstructure and critical local stress state induced by the mechanical test.

Microstructural observations carried out on dissimilar butt joints to Ti-6Al-4V produced using a Yb fiber laser operating on continuous wave mode revealed the presence of a dendritic rapid solidification structure in the fusion zone, mainly constituted by NiTi and Ti_2Ni like phases. Cracks were found to propagate by the interface between the fine dendritic microstructure of the Ti-6Al-4V and the coarser rapid solidification structure of the fusion zone.

Preliminary studies in pulsed mode both in NiTi and Ti-6Al-4V revealed an intensive cracking sensitivity to process parameters, as future work is still required to take advantage of pulsed mode laser welding benefits.

Regarding future developments, the SME ability of welded joints still must be evaluated using the bending and free-recovery method presented and the testing device designed and produced for that purpose.

The future of NiTi applications relies on developing suitable joining techniques to other materials. Based on the know-how acquired within this study, an improved fixture system and welding chamber were designed aiming to produce dissimilar butt joints both to Titanium highly biocompatible alloys and to austenitic stainless steels. This new device, amongst other improvements, allows mounting start and ending plates for butt welding, includes a selective exhaust system that preserves the inner atmosphere and was designed to improve lens life.

For these reasons, by overcoming the limitations experienced with the first system, functional dissimilar joints are expected to be attained by continuously optimizing the process conditions and trying new techniques to minimize cold cracking, such as pre-heating.

7. References

[1] Otsuka, K.; Wayman, C.M., *Shape Memory Materials*. Cambridge, UK: Cambridge University Press, 1998.

[2] Chang, L.C., "Atomic Displacements and Crystallographic Mechanism in Diffusionless Transformation of Gold-Cadmium Single Crystals containing 47.5 atomic percent Cadmium," *Acta Crystallographica*, vol. 4, pp. 320-324, 1951.

[3] Chang, L.C.; Read, T.A.;, "Plastic deformation and diffusionless phase changes in metals - The Gold-Cadmium beta phase," *AIME Transactions*, vol. 191, pp. 47-52, 1951.

[4] Chang, L.C.; Read, T.A.; Wechsler, M.S.;, "Reversible single-crystal rocking-curve broadening," *Acta Crystallographica*, vol. 6, p. 567, 1953.

[5] W.J. Buehler, J.V. Gilfrich, and R.C. Wiley, "Effect of Low-Temperature Phase Changes on the Mechanical Properties of Alloys near Composition TiNi," *Journal of Applied Physics*, vol. 34, pp. 1475-1477, 1963.

[6] Andreasen, George F.; Brady, Patrik R.;, "A Use Hypothesis for 55 Nitinol Wire for Orthodontics," *The Angle Orthodontist*, vol. 42, no. 2, pp. 172-177, 1972.

[7] Pelton, A.R.; Stockel, D.; Duerig, T.W.;, "Medical Uses of Nitinol," in *International Symposium on Shape Memory Materials*, vol. 327-328, Kanazawa, Japan, 2000, pp. 63-70.

[8] Miyazaki, S.; Mizukoshi, K.; Ueki, T.; Sakuma, T.; Liu, Y.;, "Fatigue life of Ti-50 at. % Ni and Ti-40Ni-10Cu (at.%) shape memory alloy wires," *Materials Science and Engineering A*, no. 273-275, pp. 663-685, 1999.

[9] Otsuka, K.; Ren, X.;, "Physical Metallurgy of Ti-Ni-based shape memory alloys," *Progress in Materials Science*, vol. 50, pp. 511-678, 2005.

[10] Bouraoui, T.; Jemal, F.;, "Tensile Properties of a Fe-32Mn-6Si Shape Memory Alloy," *Strength of Materials*, vol. 40, no. 2, pp. 203-211, 2008.

[11] N. Stanford and D.P. Dunne, "Effect of NbC and TiC precipitation on shape memory in an iron-based alloy," *Journal of Materials Science*, vol. 41, pp. 4883-4891, 2006.

[12] Miyazaki, S.; Otsuka, K.;, "Deformation and transformation behavior associated with the r-phase in Ti-Ni alloys," *Metallurgical Transactions A17A*, pp. 53-63, 1986.

[13] Shaw, John A.; Kyriakides, Stelios;, "THERMOMECHANICAL ASPECTS OF NiTi," *Journal of the Mechanics and Physics of Solids*, vol. 43, no. 8, pp. 1243-1281, 1995.

[14] Lagoudas, Dimitris C.;, *Shape Memory Alloys: Modeling and Engineering Applications*. USA: Springer, 2008.

[15] Morgan, N.B.; Broadley, M.;, "Taking the art out of smart! - Forming processes and durability issues for the application of NiTi shape memory alloys in medical devices," in *Materials & Processes for Medical Devices Conference*, Anaheim, California, 2004, pp. 247-252.

[16] Ryhanen, Jorma, *BIOCOMPATIBILITY EVALUATION OF NICKEL-TITANIUM SHAPE MEMORY METAL ALLOY*. OULU, OULUN YLIOPISTO, May 1999. [Online]. HYPERLINK "http://herkules.oulu.fi/isbn9514252217/"

[17] Yan, X.J.; Yang, D.Z.; Liu, X.P.;, "Influence of heat treatment on the fatigue life of a laser-welded NiTi alloy wire," *Materials characterization*, vol. 58, pp. 262-266, 2007.

[18] FURUKAWA TECHNO MATERIAL CO. (2010, August) Shape memory alloys and super-elastic alloys Furukawa NT Alloys. [Online]. HYPERLINK "http://www.fitec.co.jp/ftm/english/nt-e/appli/medi.htm"

[19] Mauro, M.A.; Koehler, R.E.; Baron, T.H.;, "Advanves in gastrointestinal intervention: the treatment of gastroduodenal and colonrectal obstructions with metallic stents," *Radiology*, vol. 215, pp. 659-669, 2000.

[20] NiTinol Medical Technologies, Inc., Boston, MA, Promotional material.

[21] Stockel, Dieter;, "Forming of Nitinol - A Challenge," in *New Developments in Forging Technology*, Freemont, California, 2001, pp. 119-134.

[22] Chau, E.T.F.; Friend, C.M.; Allen, D.M.; Hora, J.; Webster, J.R.;, "A technical and economic appraisal of shape memory alloys for aerospace applications," *Materials Science and Engineering A*, vol. 438-440, pp. 589-592, 2006.

[23] Mabe, James H.; Calkins, Frederick T.; Butler, George;, "Boeing's Variable Geometry Chevron, Morphing Aerostructure for Jet Noise Reduction," in *47th AIAA/ASME/ASCE/AHS/ASC Structures, Structural Dynamics and Meterials Conference*, Newport, Rhode Island, 2006.

[24] Predki, Wolfgang; Knopik, Adam; Bauer, Bjorn;, "Engineering applications of NiTi shape memory alloys," *Materials Science and Engineering*, no. 481-482, pp. 598-601, 2008.

[25] Stoeckel, Waram;, "Use of NiTi Shape Memory Alloys for Thermal Sensor-Actuators," in *SPIE* , San Diego, 1991, p. 382.

[26] Stoeckel, Dieter;, "Shape Memory Actuators for Automotive Applications," *Materials & Design*, vol. 11, pp. 302-307, December 1990.

[27] Janke, L.; Czaderski, C.; Motavalli, M.; Ruth, J.;, "Applications of shape memory alloys in civil engineering structures - Overview, limits and new ideas," *Materials and Structures*, vol. 38, pp. 578-592, June 2005.

[28] Nishikawa, M.; Tanaka, H.; Kohda, M.; Nagaura, T.; Watanabe, K.;, "Behaviour of welded part of Ti-Ni shape memory alloy," *Journal of Applied Physics*, vol. 43, no. 12, pp. 839-844, December 1982.

[29] Ikai, A.; Kimura, K.; Tobushi, H.;, "TIG Welding and Shape Memory Effect of TiNi Shape Memory Alloy," *Jounal of intelligent Material Systems and Structures*, vol. 7, no. 6, pp. 646-655, 1996.

[30] Quiao, Zhixia; Li, Lianjin; Wang, Dongat; Li, Zongmin;, "Microstructure and shape memory recovery characteristics in a TIG-Weld Fe-Mn-Si-Cr-Ni shape memory alloy," in *International conference on smart materials and nanotechnology in engineering, SPIE*, Chine, 2007, pp. 642-330.

[31] Budau, Victor; Oanca, Octavian; Craciunesau, Corneliu M.;, "Macro and Microscopic Aspects observed on ultrasonic welding of shape memory alloys," *Annals of the University of Oradea, Fascicle of Management and Technological Engineering*, vol. VII(XVII), România, 2008.

[32] Eijk, Casper van Der; Fostervoll, Hans; Sallom, Zuhair K.; Akselsen, Odd M.;, "Plasma welding of NiTi to NiTi, Stainless Steel and Hastealloy C276," in *ASM Materials Solutions 2003 Conference*, Pittsburg, Pennsylvania, USA, October 2003, pp. 13-15.

[33] Schlossmacher, P.; Haas, T.; Schussler, A.;, "Laser-Welding of a Ni-Rich TiNi Shape Memory Alloy: Mechanical behaviour," *Journal De Physique IV*, vol. IV, pp. 251-256, 1997.

[34] Tuissi, A.; Besseghini, S.; Ranucci, T.; Squatrito, F.; Pozzi, M.;, "Effect of a Nd:YAG laser welding on the functional properties of the Ni-49.6 at % Ti," *Materials Science and Engineering A*, no. 273-275, pp. 813-817, 1999.

[35] Hsu, Y.T.; Wang, Y.R.; Wu, S.K.; Chen, C.;, "Effect of CO2 Laser Weld on the Shape-Memory and Corrosion Characteristics of TiNi alloys," *Metallurgicall and Materials Transactions A*, vol. 32A, pp. 569-576, March 2001.

[36] Falvo, A.; Furgiuele, F.M.; Maletta, C.;, "Laser welding of a NiTi alloy: Mechanical and shape memory behaviour," *Materials Science and Engineering A*, no. 412, pp. 235-240, 2005.

[37] Falvo, A.; Furgiuele, F.M.; Maletta, C.;, "Functional behaviour of a NiTi-Welded joint: Two-way shape memory effect," *Materials Science and Engineering A*, no. 481-482, pp. 647-650, 2008.

[38] Yan, X.J.; Yang, D.Z.; Qi, M.;, "Rotating-bending fatigue of a laser-welded superelastic NiTi alloy wire," *Materials Characterization* , no. 57, pp. 58-63, 2006.

[39] Song, Y.G.; Li, W.S.; Li, L.; Zheng, Y.F.;, "The influence of laser parameters on the microstructure and mechanical properties of the as-joined NiTi alloy wires," *Materials Letters*, no. 62, pp. 2325-2328, 2008.

[40] Gugel, H.; Theisen, W.;, "Microstructural investigations of laser welded dissimilar Nickel-Titanium-steel joints," in *ESOMAT 2009 - 8th European Symposium on Martensitic Transformations* , Prague, Czech Republic, 2009, pp. 1-6.

[41] Steen, William M.;, *Laser Material Processing*, 3rd ed.: Springer, 2003.
[42] Gahan, B.C.;, "New high-power fiber laser enables cutting edge research," *Laser Technology*, pp. 29-31, Winter 2004.
[43] Gugel, H.; Schuermann, A.; Theisen, W.;, "Laser welding of NiTi wires," *Materials Science and Engineering A*, no. 481-482, pp. 668-671, 2008.
[44] Wang, Ge;, "welding of Nitinol to Stainless Steel," EWI, Columbus, Ohio, Short report October 1997.
[45] Hall, Peter;, "Welding of Titanium and Titanium Based Alloys to Ferrous Metals (Patent Pending) Notification of Availability for Licensing," EWI, Columbus, Ohio, Summary Report of Coorporative Research Program 46446IRD, 2003.
[46] Vannod, J.; Hessler-Wyser, A.; Rappaz, M.;, "Nd:YAG laser joining between stainless steel and nickel-titanium shape memory alloys," in *EMC 2008, Vol 2: Materials Science*, Aachen, Germany, 2008, pp. 501-502.
[47] Qiu, X.M.; Li, M.G.; Sun, D.Q.; Liu, W.H.;, "Study on brazing of TiNi shape memory alloy with stainless steels," *Journal of Materials Processing Technology*, vol. 176, pp. 8-12, 2006.
[48] Li, M.G.; Qiu, X.M.; Sun, D.Q.; Yin, S.Q.;, "Properties of laser-brazed joint of NiTi shape memory alloy and stainless steel orthodontic wires," *The Orthodontic Cyberjournal*, retrieved from http://www.oc.j.com/oct05/LaserbrazedNiTi.htm on 17 February 2010.
[49] INFO-SHEET No. 13: NiTinol Alloy Types, Conditions and Surfaces. (2010, August) Memory-Metalle GmbH. [Online]. HYPERLINK "http://www.memory-metalle.de/html/03_knowhow/PDF/MM_13_alloytypes_e.pdf"
[50] ASTM International, *ASTM B 381-10 Standard Specification for Titanium and Titanium alloy Forgings*, DOI: 10.1520/B0381-10, Ed. West Conshohocken, 2010.
[51] ASM INTERNATIONAL, *Volume 2 - Properties and Selection: Nonferrous Alloys and Special-Purpose Materials*, 2nd ed.: The Materials Information Company, 1992.
[52] ASM INTERNATIONAL, *Vol 1 - Properties and Selection: Irons, Steels, and high Performance Alloys*, 2nd ed.: The materials Information Company, 1992.
[53] GSI Group. (2010, August) GSI JK Lasers : JK300PS and JK300HPS. [Online]. HYPERLINK "http://www.gsiglasers.com/UserFiles/Documents/DS.JK300PS,%20300HPS.0610HR.pdf"
[54] (2010, August) ROFIN 'The family of manual welding lasers'. [Online]. HYPERLINK "http://www.rofin.com/fileadmin/user_upload/produkte/Handschweisslaser/Bro_ManualWelding_E_final.pdf"
[55] Suzuho. (2010, on August) Jewelry Making Machine & Tools. [Online]. HYPERLINK "http://www2.ocn.ne.jp/~suzuho/re-za-page.htm"
[56] Rofin-Sinar. (2010, August) Diode pumped Nd:YAG Laser DY series. [Online]. HYPERLINK "http://www.consorziotecnopolo.it/convegni/convegno3/Laser%20a%20Nd-YAG%20a%20diodi,%20S.Draghi,%20ROFIN.PDF"
[57] IPG Photonics. (2010, August) Ytterbium YLR series: HP Brochure. [Online]. HYPERLINK "http://www.ipgphotonics.com/Collateral/Documents/English-US/HP_Brochure.pdf"
[58] Khan, M.I.; Panda, S.K.; Zhou, Y.;, "Effects of Welding Parameters on the Mechanical Performance of Laser Welded Nitinol," *Materials Transactions*, vol. 49, no. 11, pp. 2702-2708, 2008.
[59] International Organization for Standardazation, *International Standard ISO 6507-1:2005 - Metallic materials - Vickers hardness test*.
[60] Beer, Ferdinand P.; Johnston, E. Russel Jr.; DeWolf, John T.;, *Mechanics of Materials*, 4th ed.: The McGraw-Hill Companies, Inc, 2006.
[61] Liu, Yong;, "Detwinning process and its anisotropy in shape memory alloys," in *SPIE Symposia of Smart Structures and Materials*, Newport Beach, CA, USA, 4th March 2001, pp. 82-94.
[62] Lin, H.C.; Wu, S.K.;, "Strengthening Effect on Shape Recovery Characteristic of the Equiatomic TiNi Alloy," *Scripta Metallurgica et Materialia*, vol. 26, pp. 59-62, 1992.
[63] Maletta, C.; Falvo, A.; Furguiele, F.; Barbieri, G.; Brandizzi, M.;, "Fracture Behaviour of Nickel-Titanium Laser Welded Joints," *Journal of Materials Engineering and Performance*, vol. 18,

no. 5-6, pp. 569-573, 2009.
[64] Gollerthan, S.; Young, M.L.; Baruj, A.; Frenzel, J.; Schmahl, W.W.; Eggeler, G.;, "Fracture mechanics and microstructure in NiTi shape memory alloys," *Acta Materialia* , vol. 57, pp. 1015-1025, 2009.
[65] Jiang, Fengchun; Vecchio, Kenneth S.;, "Fracture of Nitinol under Quasistatic and Dynamic Loading," *Metallurgical and Materials Transactions A*, vol. 38A, pp. 2907-2915, 2007.
[66] ASM International, *Volume 12 - Fractography*, 2nd ed.: The Materials Information Company, 1992.
[67] Martins, R.M.S; Schell, N.; Borany, J. von; Mahesh, K.K.; Silva, R.J.C.; Braz Fernades, F.M.;, "Structural evolution of magnetron sputtered shape memory alloy Ni-Ti films," *Vacuum*, vol. 84, pp. 913-919, 2010.
[68] Martins, R.M.S.; Schell, N.; Reuther, H.; Pereira, L.; Mahesh, K.K.; Silva, R.J.C.; Braz Fernades, F.M.;, "Texture development, microstructure and phase transformation characteristics of sputtered Ni-Ti Shape Memory Alloy films grown on TiN," *Thin Solid Films*, no. doi: 10.1016/j.tsf.2010.07.078, 2010.
[69] Shu, Y.C.; Bhattacharya, K.;, "The influence of texture on the shape memory effect in polycrystals," *Acta Metallurgica*, vol. 46, no. 15, pp. 5457-5473, 1998.
[70] Brinson, L. Catherine; Schmidt, Ina; Lammering, Rofl;, "Stress-induced transformation behavior of a polycrystalline NiTi shape memory alloy: micro and macromechanical investigations via in situ optical microscopy," *Journal of the Mechanics and Physics of Solids*, vol. 52, pp. 1549-1571, 2004.
[71] Baeslack, W.A.; Becker, D.W.;, "Fusion zone fracture behavior of weldments in Alpha-Beta Titanium Alloys," *Metallurgical Transactions A*, vol. 10A, pp. 1803-1806, April 1979.
[72] Costa, Alexandra; Miranda, Rosa; Quintino, Luísa; Yapp, David;, "Analysis of Beam Material Interaction in welding of Titanium with Fiber Lasers," *Materials and Manufacturing Processes*, vol. 22, pp. 798-803, October 2007.
[73] Casillas, A.L., *MÁQUINAS FORMULÁRIO TÉCNICO*, 2nd ed., Leda Mitico Uchida, Ed. São Paulo, Brasil: Editôra Mestre jou, 1963.
[74] Copper 101 OFE OFHC. (2010, August) SEQUOIA BRASS & COPPER. [Online]. HYPERLINK "http://sequoia-brass-copper.com/alloy_101_ofe_copper.htm"
[75] Kohl, Walter H.;, *Handbook of materials and techniques for vacuum devices*, 1st ed., H.F. Dylla, Ed. New York, USA: American Institute of Physics, 1995.
[76] Perrin Walkin and William H. Tarn, Eds., *Handbook of Metal Etchants*. Boca Raton, Florida: CRC Press, 1991.
[77] Clemex Technologies Inc. (2010, August) ATM Clemex Brillant 221- Technical data. [Online]. HYPERLINK "http://jeng-bo.com.tw/products/material/metalography/pdf_files/Brillant%20221.pdf"
[78] Lucas dos Santos, Christian Mariani;, *PhD Thesis- LIGAS Ni-Ti RICAS EM Ni: Tratamento Térmico, Termomecânico e Efeito de Micromemória de Forma*. Rio de Janeiro, Brasil: Instituto Militar de Engenharia, 2006.
[79] International Organization for Standardization, *ISO 6892 - 1 : 2009 - Metallic Materials - Tensile testing Part 1: Method of testing at room temperature*., 2009.
[80] Simon, G.; Gratzke, U.; Kroos, J.;, "Analysis of heat conduction in deep penetration welding with a time-modulated laser beam," *Journal of applied physics D*, vol. 26, pp. 862-869, 1993.
[81] Kannatey-Asibu, Elijah;, *Principles of laser materials processing*.: Wiley, April 2009.

8. Annexes

A – Construction materials

This group is formed by the materials employed to produce the tools that were specially developed to assist directly the welding process, such as positioning systems and protective chambers, to obtain specimens from welded joints, such as EDM tools or testing devices, like the one that was developed to evaluate the shape memory effect of welded specimens by bending and free-recovery evaluation.

Used to produce components, their properties are not extensively explored, although general purpose considerations regarding design and production are presented.

Mild Steel

Hot-rolled bar shape 70x15 mm mild steel Ck45, available at the DEMI laboratorial premises, was used to produce a jig fixture device that was used to assist the positioning of plates when laser welding. The chemical composition as well as some aspects relevant for machining are presented in tables 1 and 2. Marked items (*) mean that parameters were selected according to tooling.

Annex A Table 1 Typical chemical composition of AISI 1045 Steel [2]

Ck45 (DIN) AISI 1045 Steel – Typical Chemical Composition (wt)			
C	Mn	P	S
%	%	max. %	max. %
0.43-0.50	0.60-0.90	0.040	0.050

Annex A Table 2 Mechanical and machining aspects of AISI 1045 mild steel [2], [3]

Tensile strength	Hardness	Cutting speed*	Feed/tooth*
MPa	HB	m/min	mm
570	163	60	0.020

Stainless Steel

Round-shaped ø 150mm AISI 304 stainless steel rod was used to machine the main body of a bending and free-recovery device developed for testing the shape memory effect of welded specimens. The chemical composition as well as aspects relevant for machining are presented in tables 3 and 4. Marked items (*) mean that parameters were selected according to tooling.

Annex A Table 3 Typical chemical composition of AISI 304 SS [2]

wt						
C	Mn	Si	Cr	Ni	P	S
max.%	max. %	max. %	%	%	%	max. %
0.08	2.00	1.00	18.0-20.0	8.0-10.5	0.045	0.03

Annex A Table 4 Mechanical and machining aspects of AISI 304 SS [2]

Tensile strength	Hardness	Cutting speed*	Feed/tooth*
MPa	HB	m/min	mm
515	123	120	0.030

Electrolytic Copper

Square shape 40x40mm electrolytic copper bar and ø10 mm rod were used to produce the EDM tool that was employed to extract tensile specimens from welded joints. The chemical composition as well as aspects relevant for machining are presented in table 5 and 6. Marked items (*) mean that parameters were selected according to tooling.

Annex A Table 5 Typical chemical composition of electrolytic copper [4]

Electrolytic copper ASTM B170 Grade 1 – Typical Chemical Composition (wt)																
Cu	Sb	As	Bi	Cd	Fe	Pb	Mn	Ni	O	P	Se	Ag	S	Te	Sn	Zn
min %	≤ ppm (all except Cu)															
99.99	4	5	1	1	10	5	0.5	10	5	3	3	25	15	2	2	1

Annex A Table 6 Machining considerations for electrolytic copper [2], [5]

Electrolytic copper ASTM B170 Grade 1 – machining			
Tensile strength	Hardness	Cutting speed*	Feed/tooth*
MPa	HRB	m/min	mm
375	45	40	0.006

B – Fixture systems technical drawings

The technical drawings of the fixture systems and chambers used for laser welding are now presented. The first system was built in the technical premises of the DEMI section of Industrial Technology. The second was projected based on the know-how of butt welding, aiming dissimilar butt welding both to stainless steel and Ti alloys.

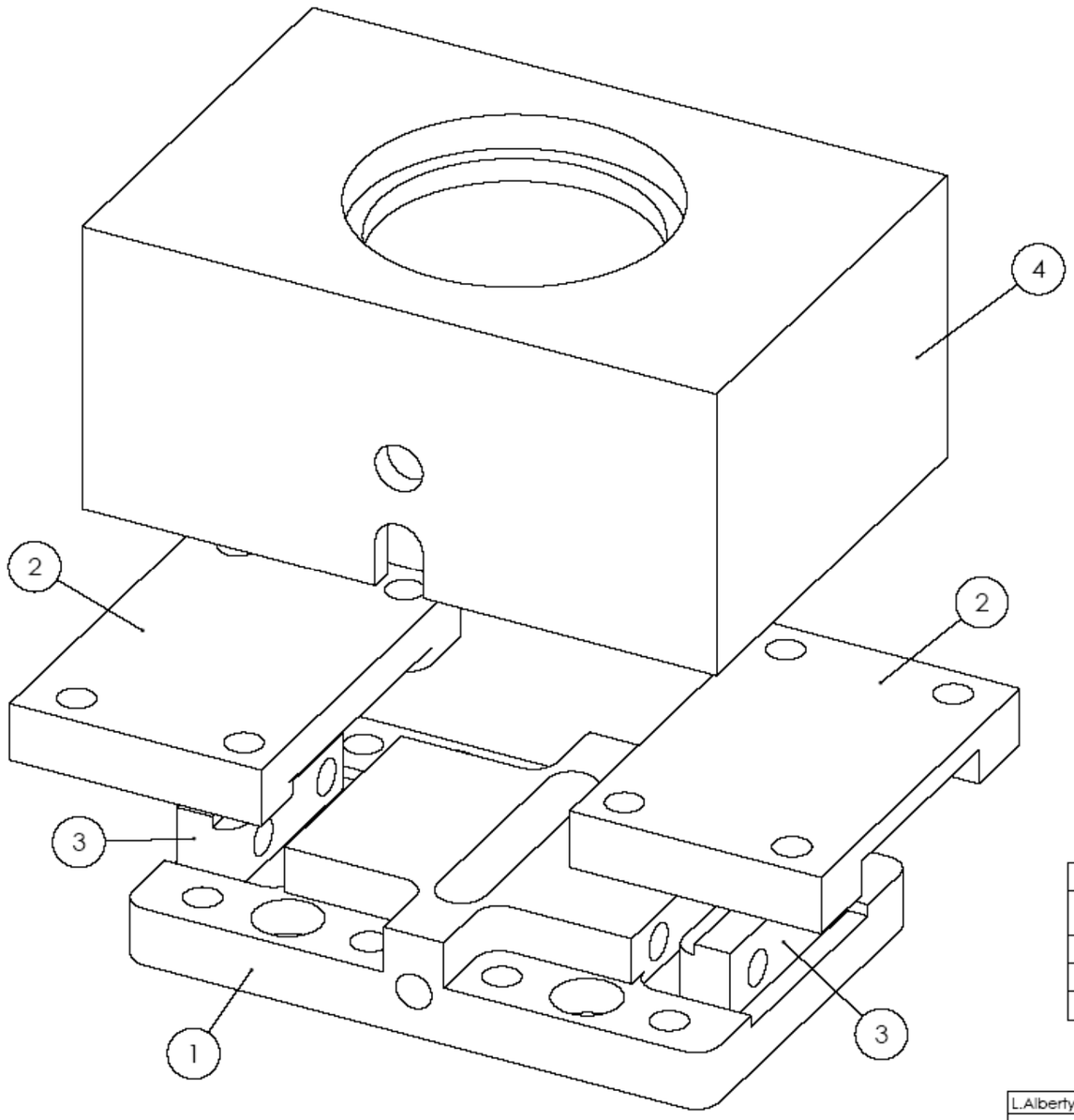

OTHER COMPONENTS		
COMPONENT	DESCRIPTION	QTY
M6X20	HEX SOCKET BOLT	8
M6X15		4

ITEM NO.	PART NUMBER	MATERIAL	QTY.
1	MAIN BODY	MILD STEEL	1
2	HOLDER	MILD STEEL	2
3	BATCH	MILD STEEL	2
4	CHAMBER	NECURON 400	1

L.Alberty 24/09/10		JIG - FIXTURE SYSTEM LASER WELDING of SMAs	FCT-UNL
	3:2 ISO 2768-m	WELDING CHAMBER	

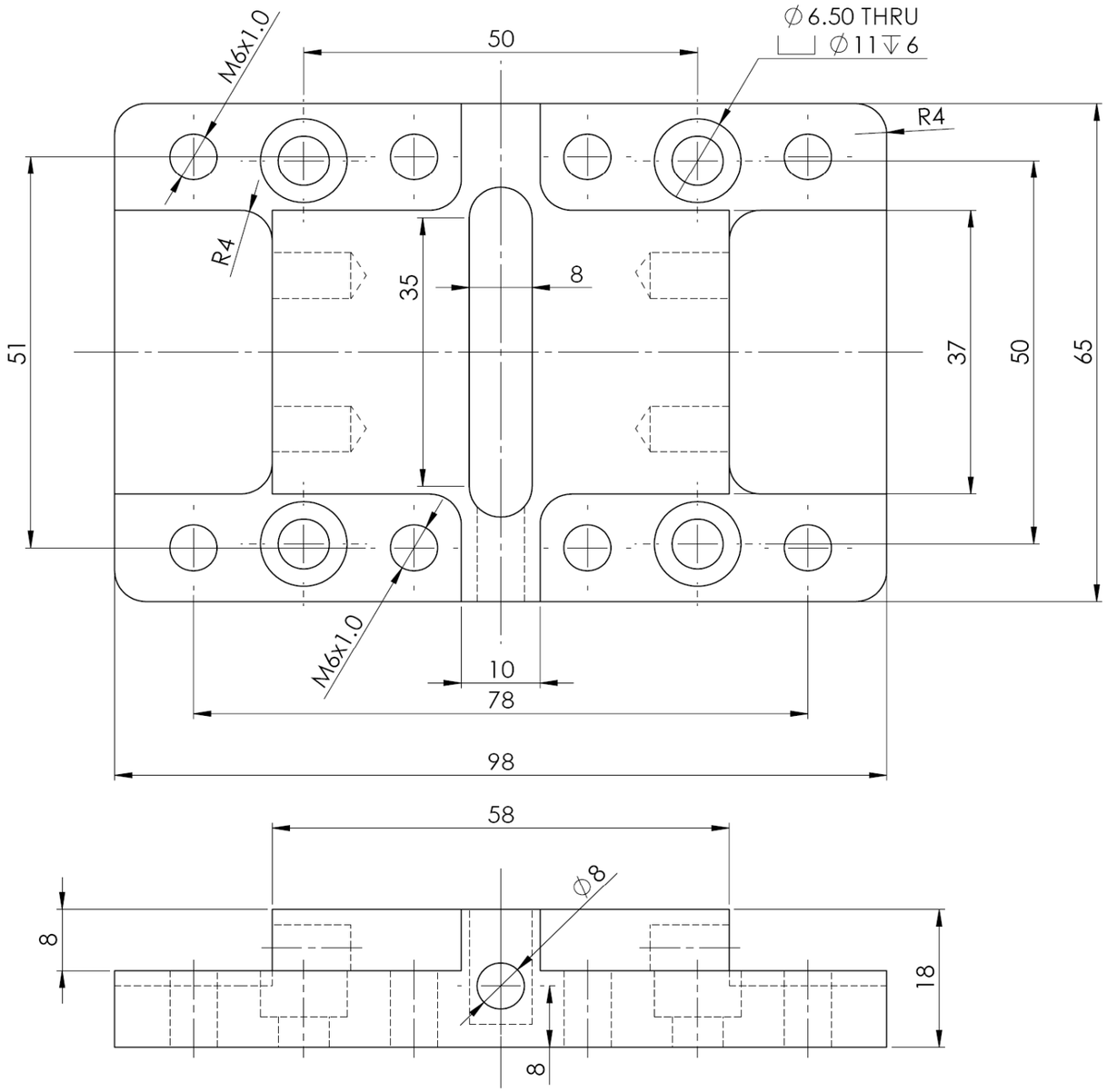

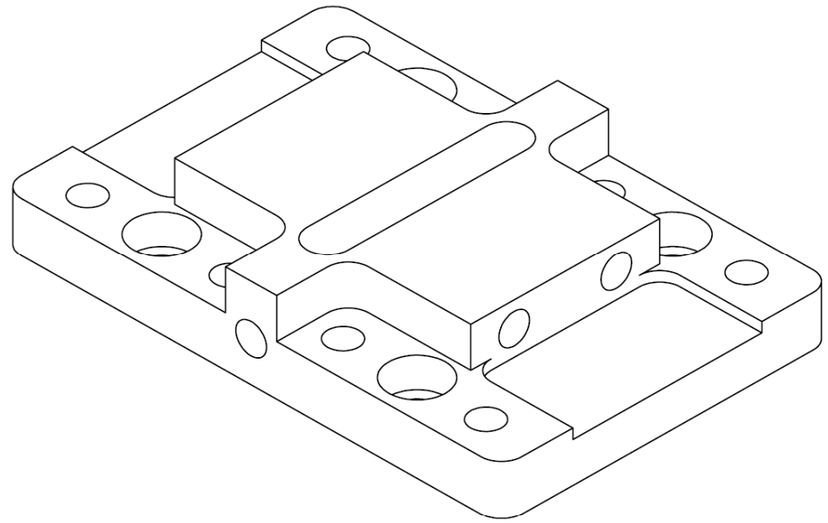

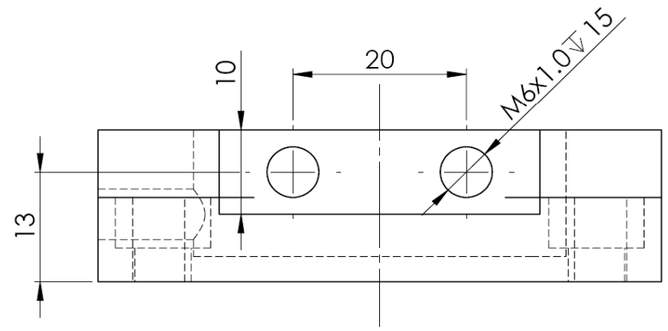

L.Alberty 24/09/10	JIG - FIXTURE SYSTEM LASER WELDING of SMAs	FCT-UNL	
3:2 ISO 2768-m	MAIN BODY		

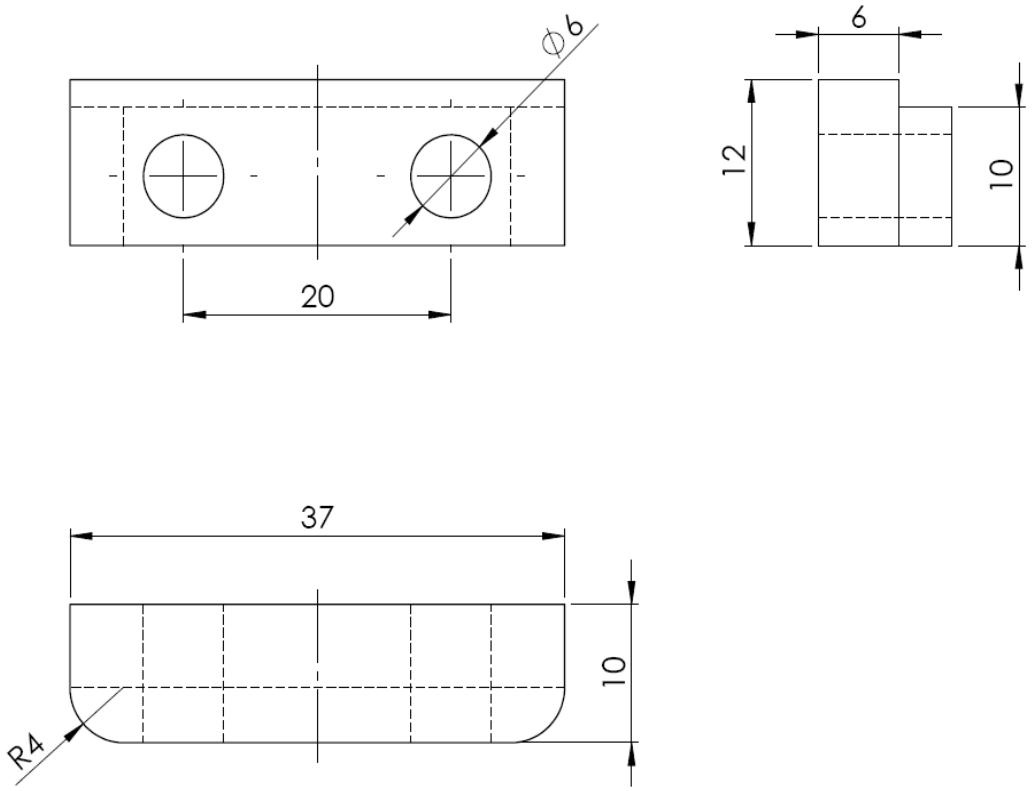

L.Alberty 24/09/10	JIG - FIXTURE SYSTEM LASER WELDING of SMAs	FCT-UNL
2:1 ISO 2768-m	BATCH	

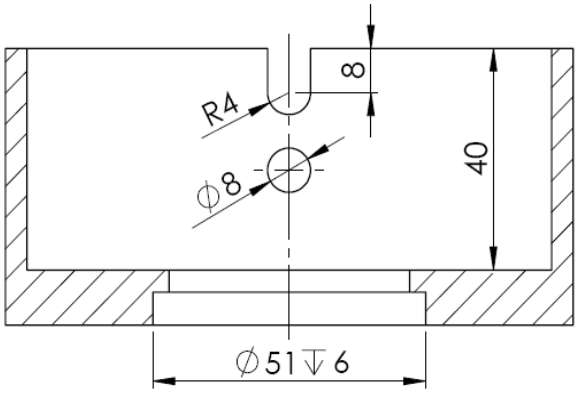

SECTION A-A
SCALE 4 : 5

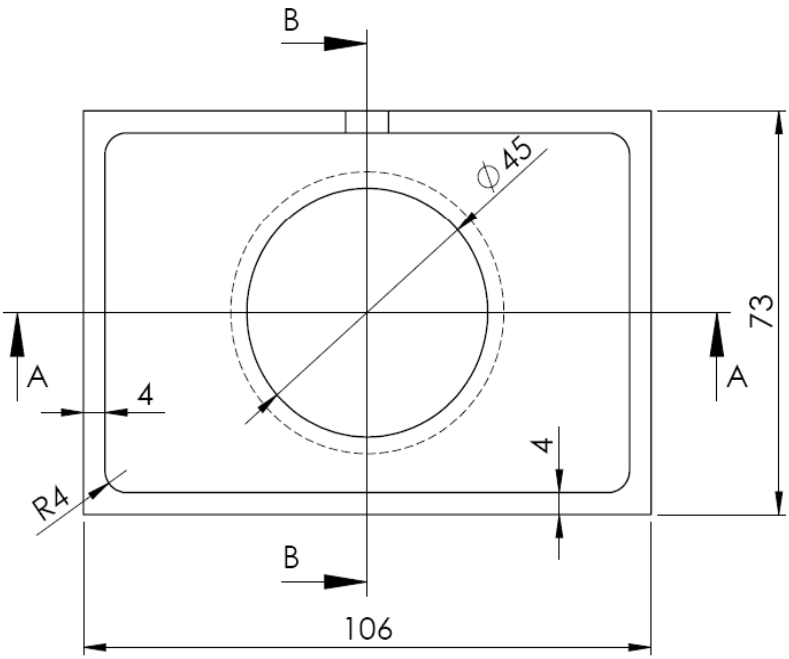

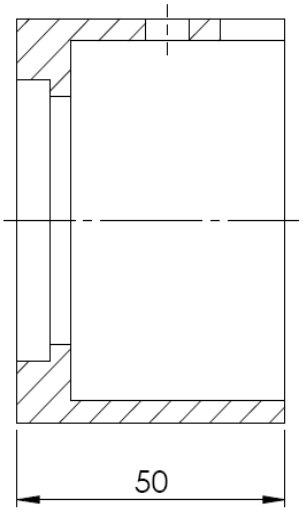

SECTION B-B
SCALE 4 : 5

L.Alberty 24/09/10	JIG - FIXTURE SYSTEM LASER WELDING of SMAs	FCT-UNL
3:2 ISO 2768-m	CHAMBER	

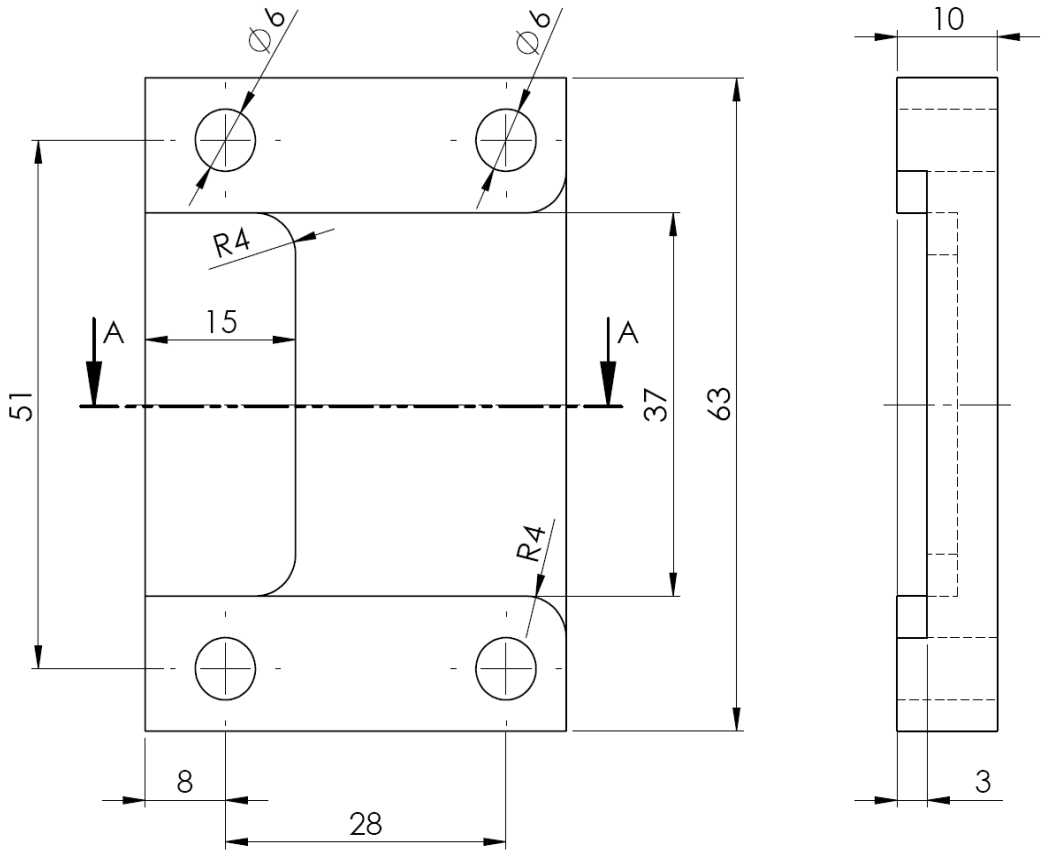

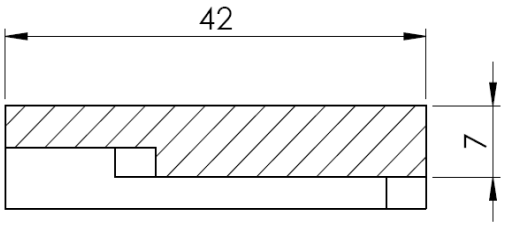

SECTION A-A
SCALE 3 : 2

L.Alberty 24/09/10	JIG - FIXTURE SYSTEM LASER WELDING of SMAs	FCT-UNL
3:2 ISO 2768-m	HOLDER	

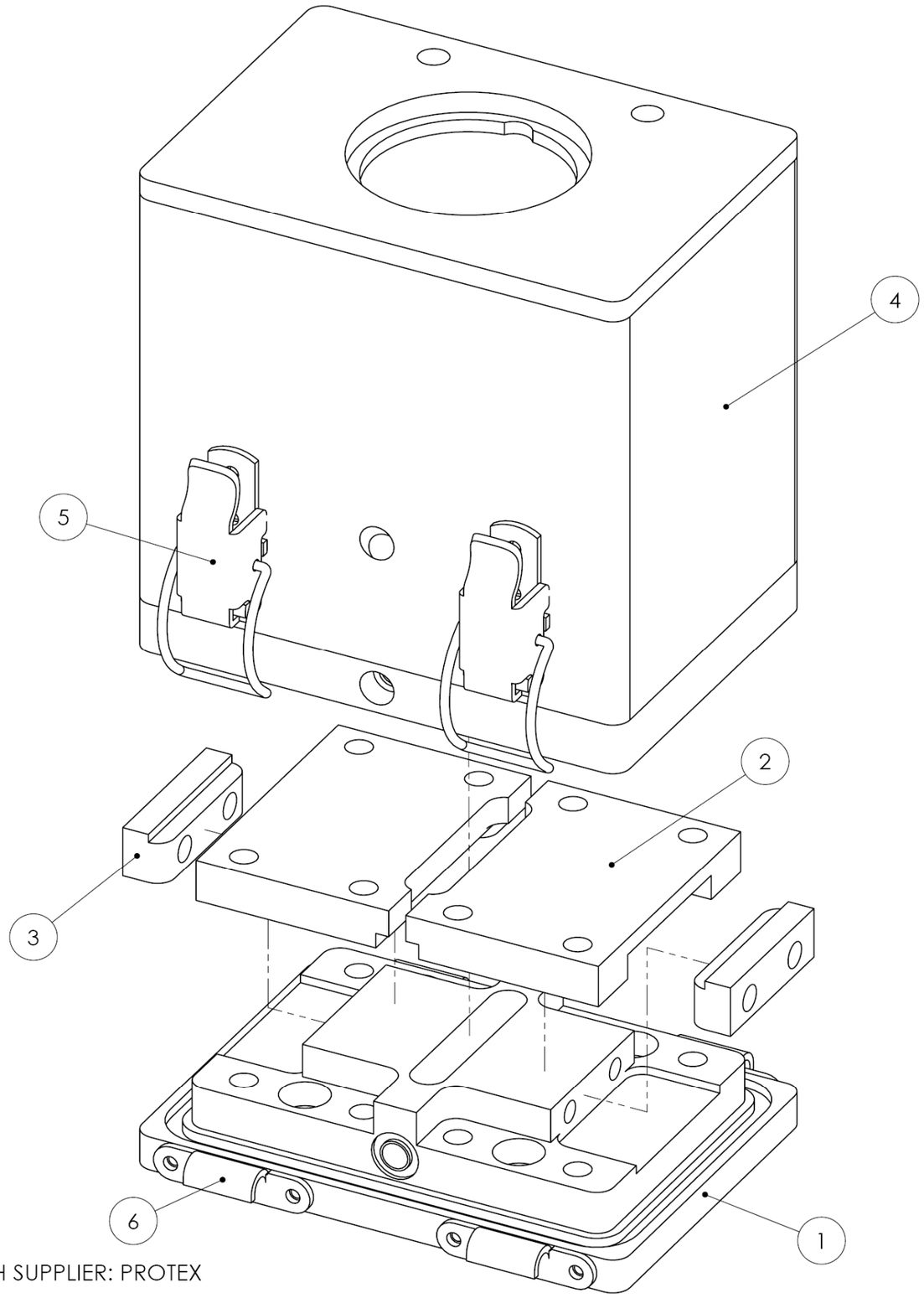

NOTE:
LATCH SUPPLIER: PROTEX

DESCRIPTION	SUPPLIER/DESCRIPTION	QUANTITY
O-RING ∅i=105 t=3.0mm NITRILE	COLUMBIA O-RINGS	1
O-RING ∅i=7,0 t=2.0mm NITRILE	COLUMBIA O-RINGS	1
M8X10	HEX SOCKET BOLT	2
M6X20		8
M6X15		4
M3X10		8
M3X5		8

ITEM NO.	PART NUMBER/ REFERENCE	DESCRIPTION/MATERIAL	QTY.
1	MAIN BODY	MILD STEEL	1
2	HOLDER	MILD STEEL	2
3	BATCH	MILD STEEL	2
4	CHAMBER	Al 5052	1
	CHAMBER #1	Al 5052	1
	CHAMBER #2		1
	CHAMBER #3 CHAMBER #4		1 2
	CHAMBER #5		1
	CHAMBER #6		1
5	20-1015	20-50414MSZN	4
	504A	BASE	1
	504B	LEVER	1
	623C	CLAW	1
6	01-504	CATCH PLATE	4

L.Alberty 23/06/10	JIG - FIXTURE SYSTEM LASER WELDING of SMAs	FCT-UNL
1:1	FINAL ASSEMBLY	

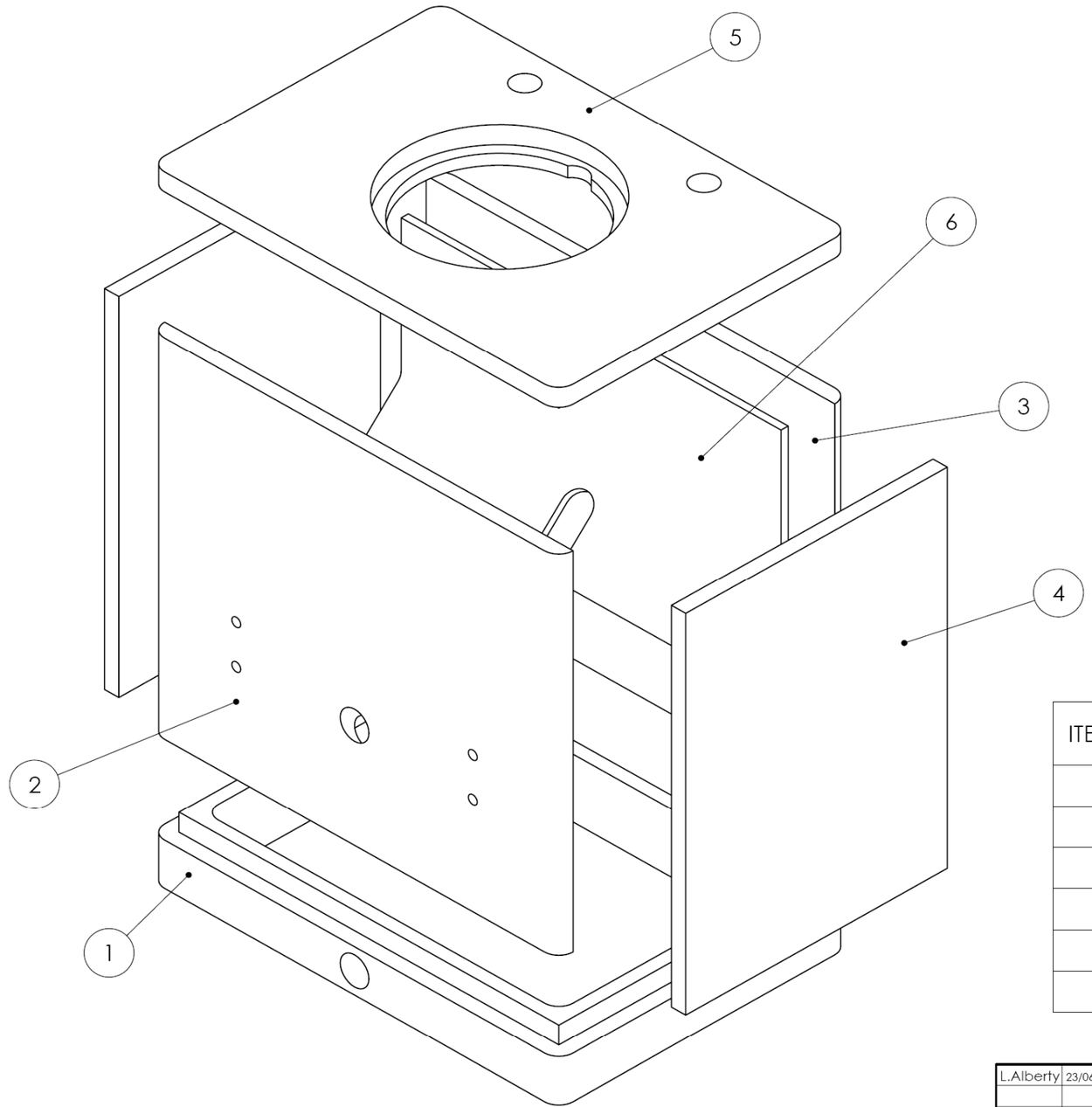

ITEM NO.	DRAWING REFERENCE	MATERIAL	QTY.
1	CHAMBER PART 1	Al 5052 H32 or H34	1
2	CHAMBER PART 2		1
3	CHAMBER PART 3		1
4	CHAMBER PART 4		2
5	CHAMBER PART 5		1
6	CHAMBER PART 6		1

NOTES:
FILLETS OF PARTS 2 & 3 CAN BE HANDMADE AFTER WELDMENTS - HIGH GEOMETRICAL ACCURACY IS NOT REQUIRED

FINAL FINISH: ANODIZED

L.Alberty	23/06/10	JIG - FIXTURE SYSTEM LASER WELDING of SMAs	FCT-UNL
	1:1	CHAMBER ASSEMBLY	

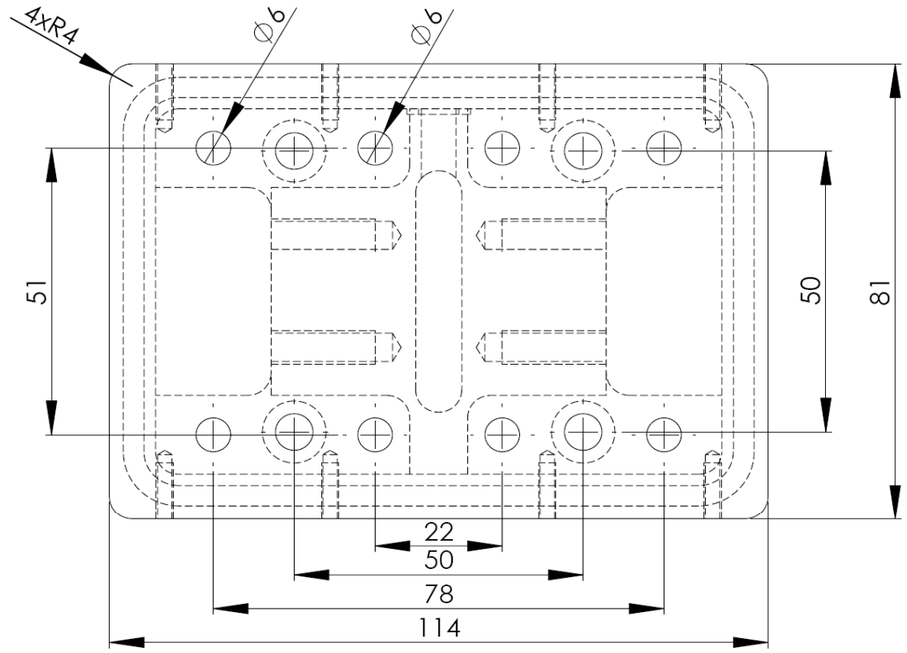

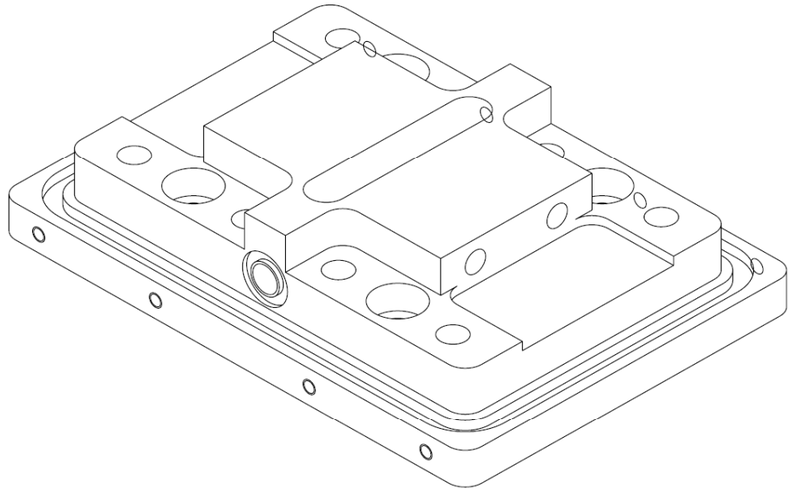

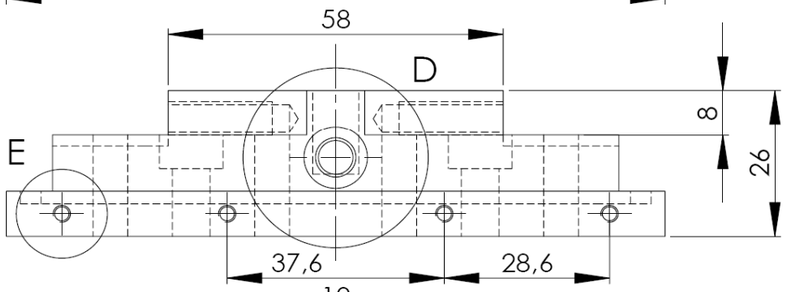

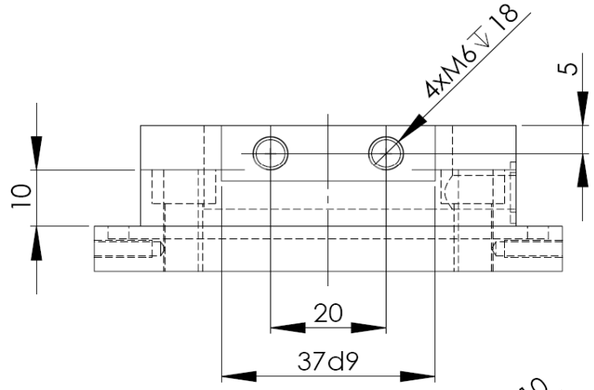

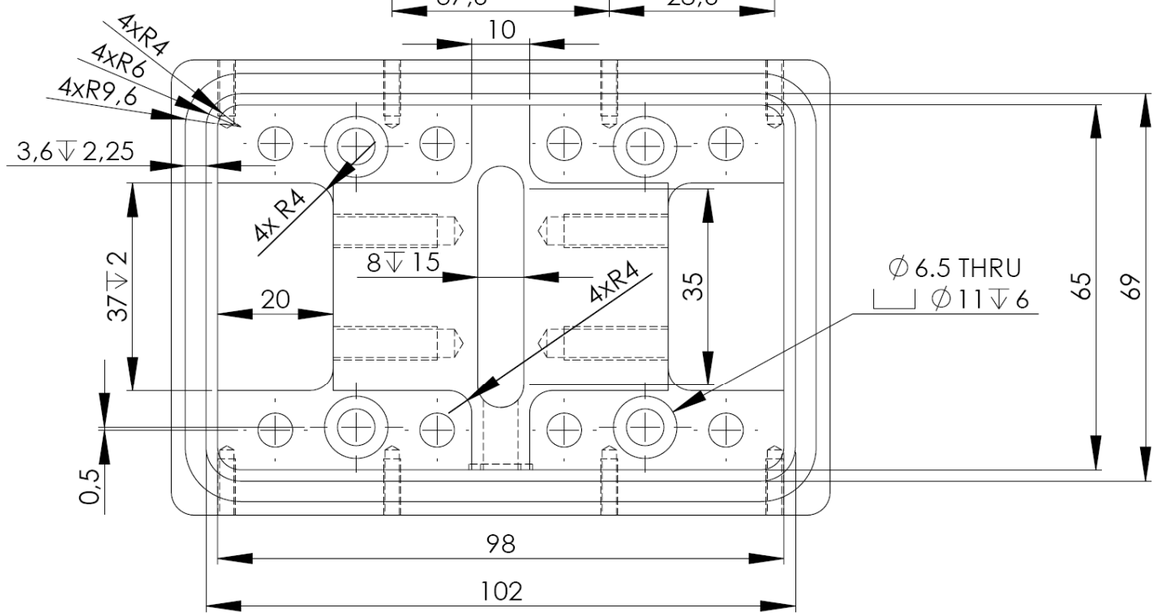

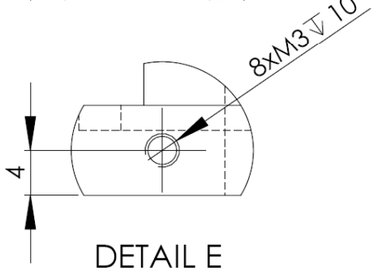

DETAIL E
SCALE 2 : 1

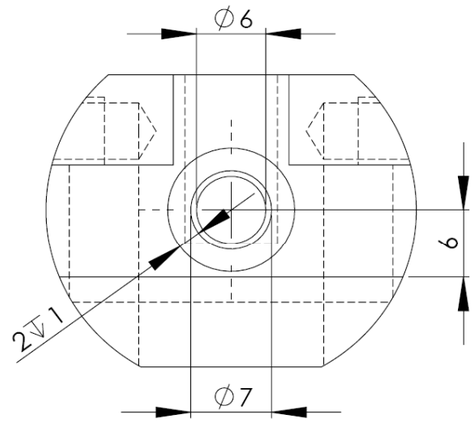

DETAIL D
SCALE 2 : 1

L.Alberty	21/06/10		JIG - FIXTURE SYSTEM LASER WELDING of SMAs	FCT-UNL
		1:1 ISO 2768-m	MAIN BODY	

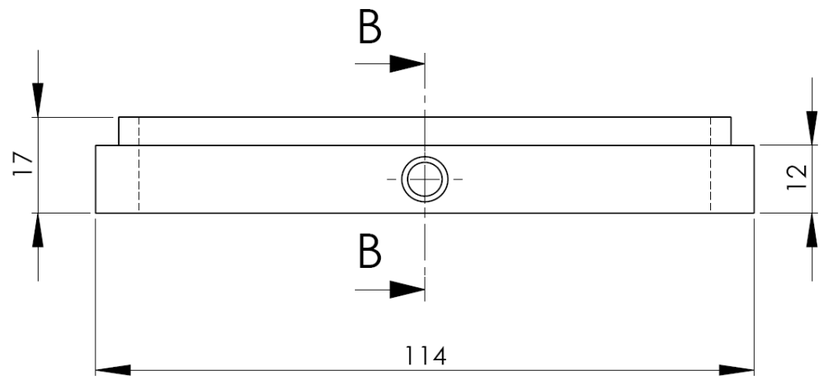

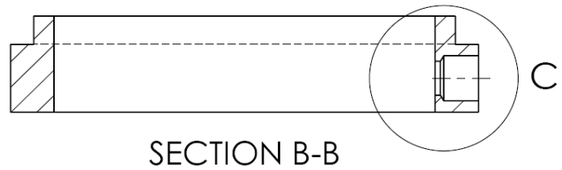

SECTION B-B

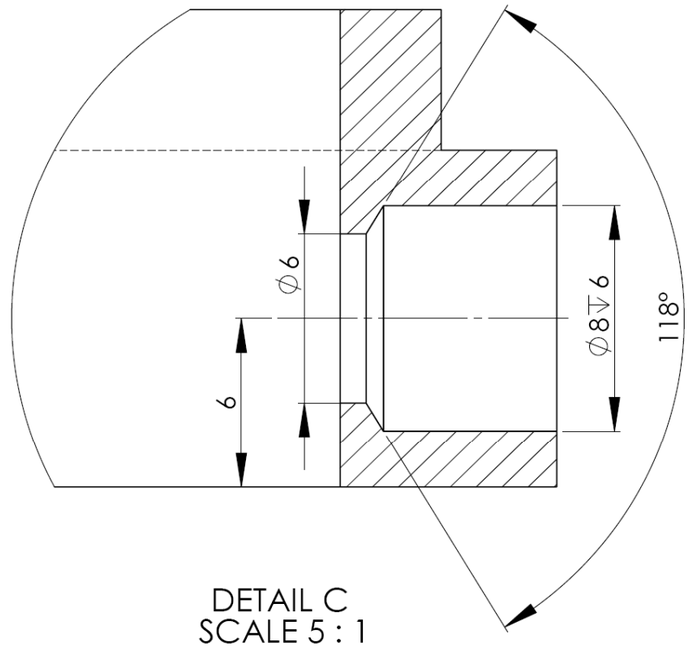

DETAIL C
SCALE 5 : 1

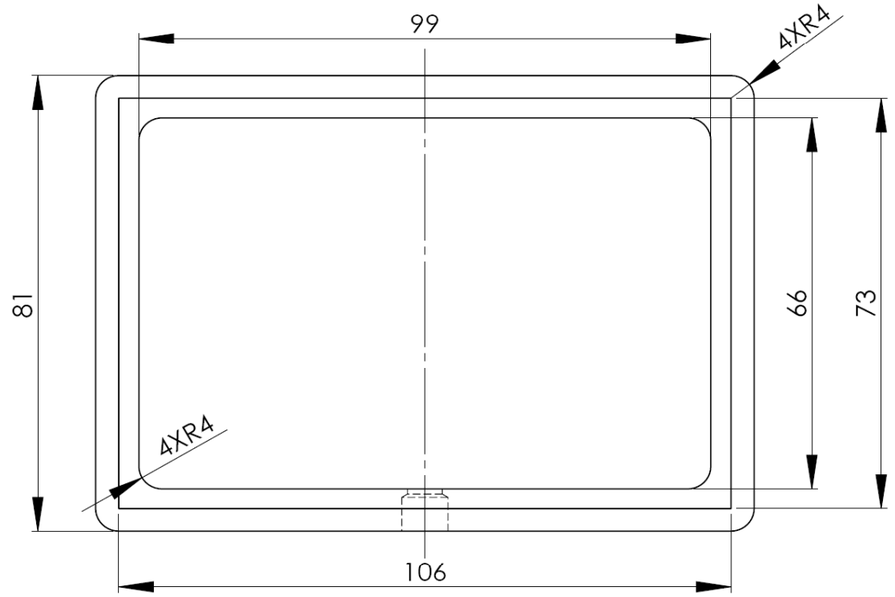

L.Alberty 22/06/10		JIG - FIXTURE SYSTEM LASER WELDING of SMAs	FCT-UNL
	1:1 ISO 2768-m	CHAMBER PART1	

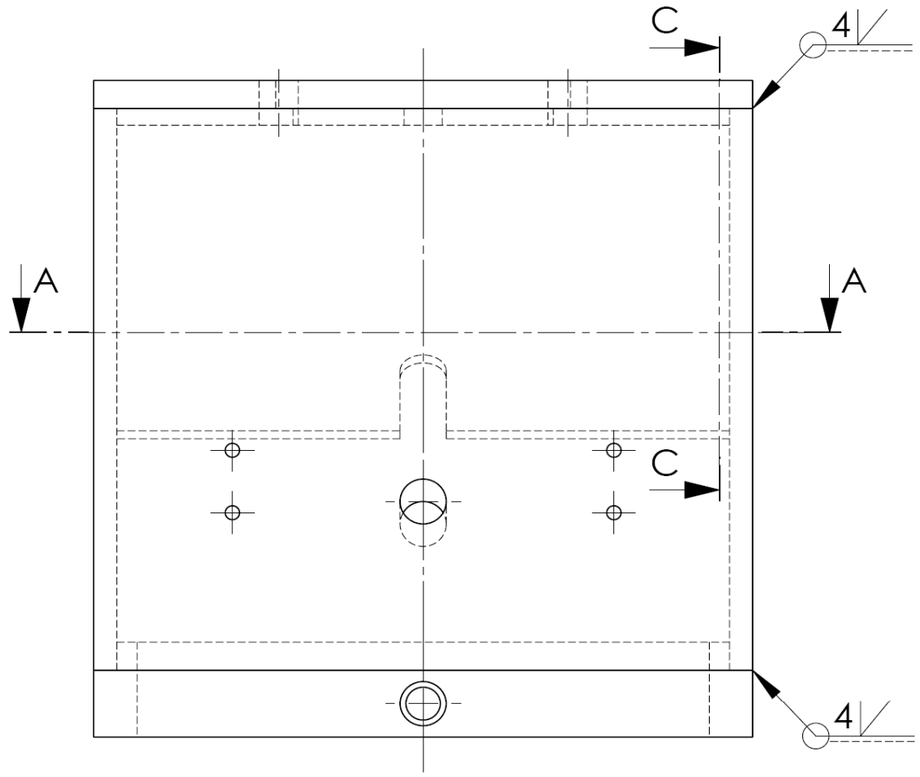

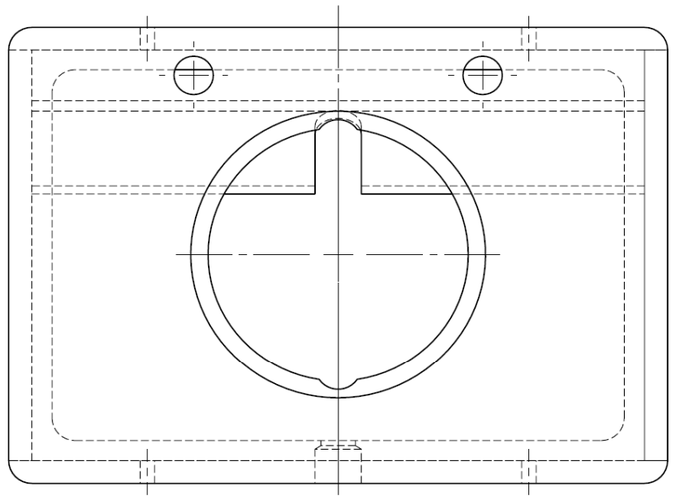

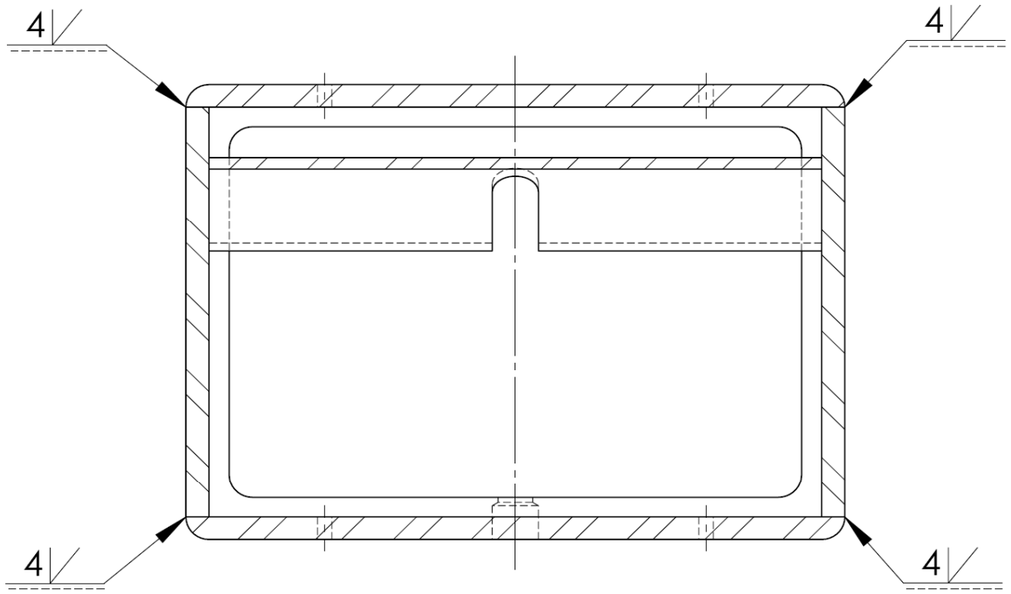

SECTION A-A
SCALE 1 : 1

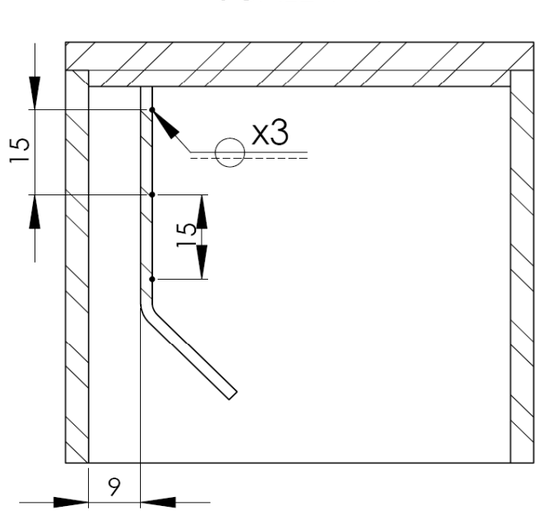

SECTION C-C
SCALE 1 : 1

L.Alberty 22/06/10	JIG - FIXTURE SYSTEM LASER WELDING of SMAs	FCT-UNL
1:1 ISO 2768-m	CHAMBER WELDMENTS	

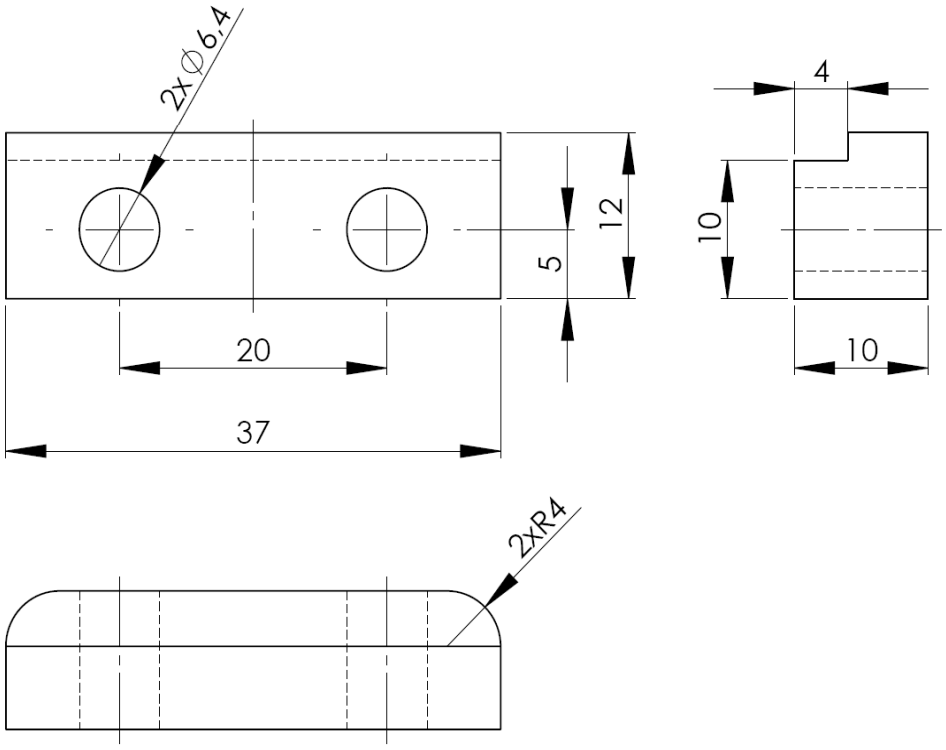

L.Alberty 22/06/10	JIG - FIXTURE SYSTEM LASER WELDING of SMAs	FCT-UNL
2:1 ISO 2768-m	BATCH	

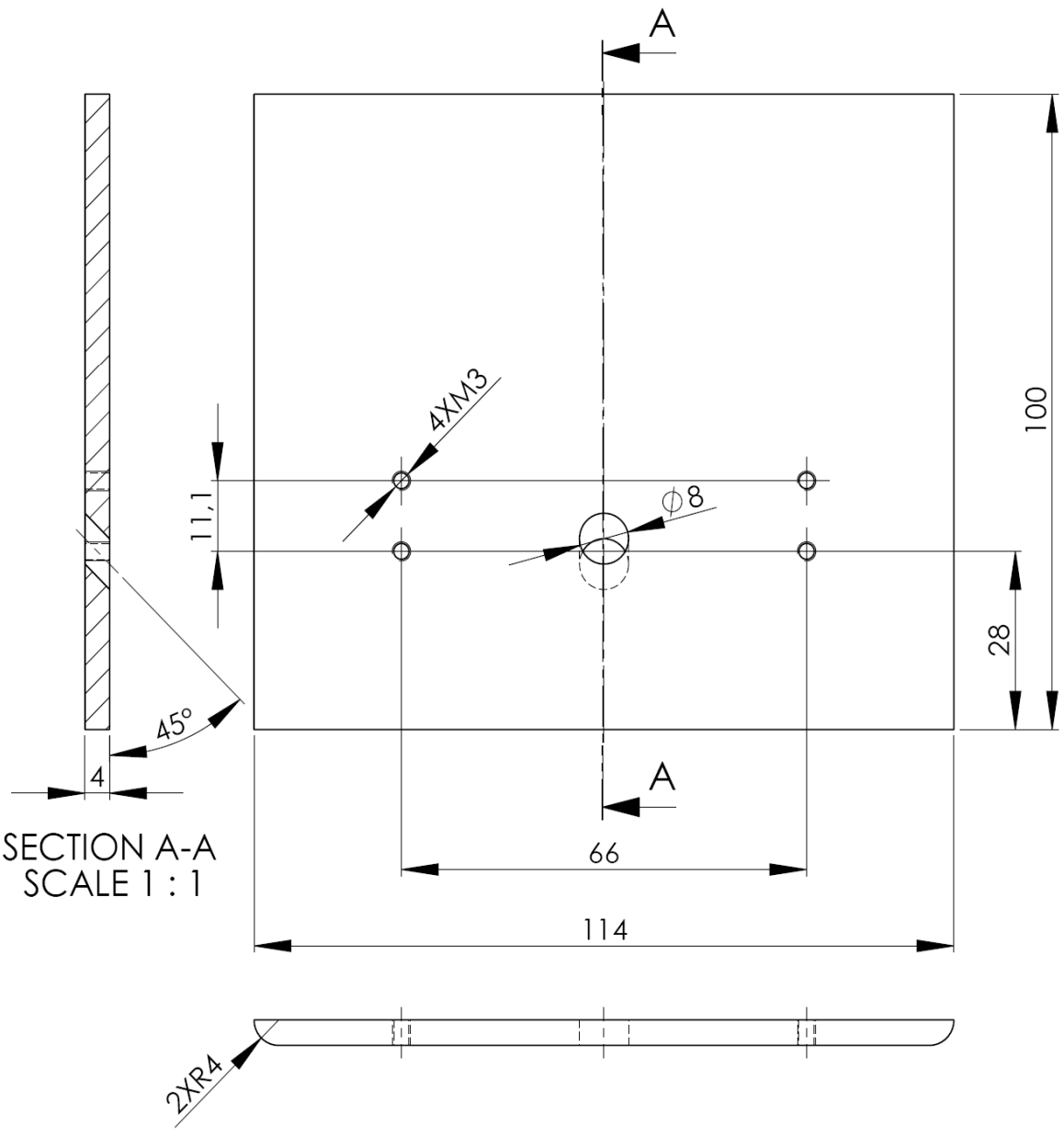

L.Alberty 22/06/10	JIG - FIXTURE SYSTEM LASER WELDING of SMAs	FCT-UNL
1:1 ISO 2768-m	CHAMBER PART2	

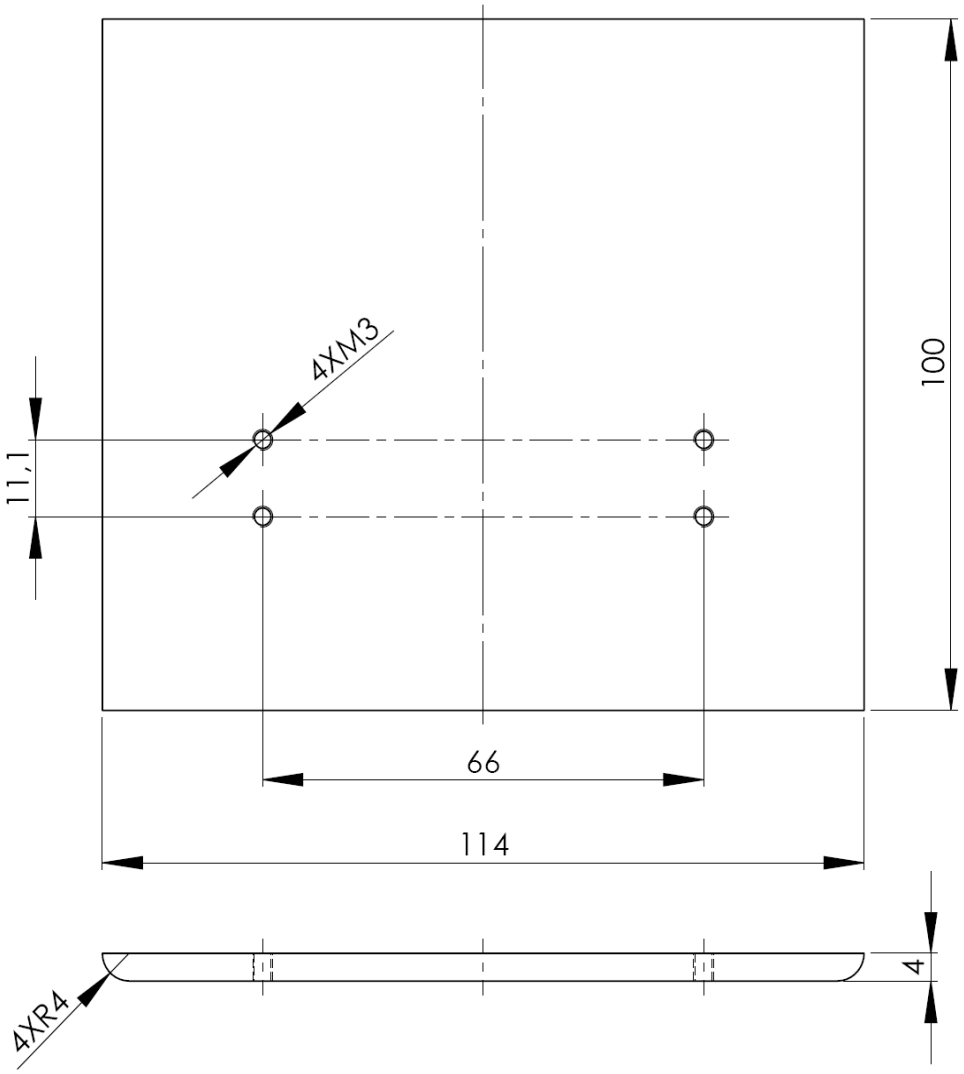

L.Alberty 22/06/10		JIG - FIXTURE SYSTEM LASER WELDING of SMAs	FCT-UNL
	1:1 ISO 2768-m	CHAMBER PART3	

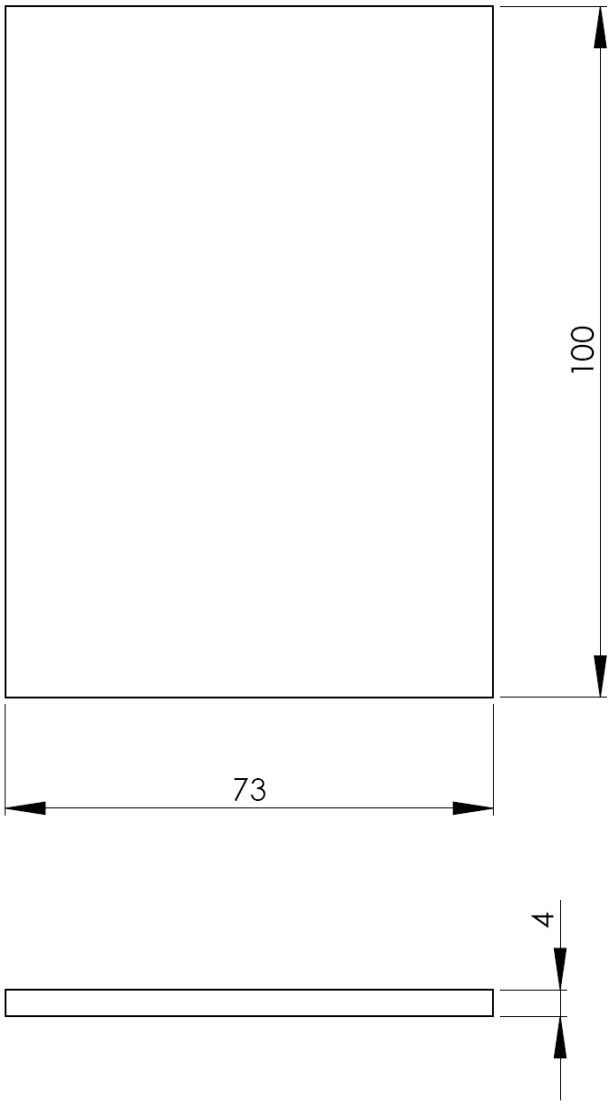

L.Alberty 22/06/10		JIG - FIXTURE SYSTEM LASER WELDING of SMAs	FCT-UNL
	1:1 ISO 2768-m	CHAMBER PART4	

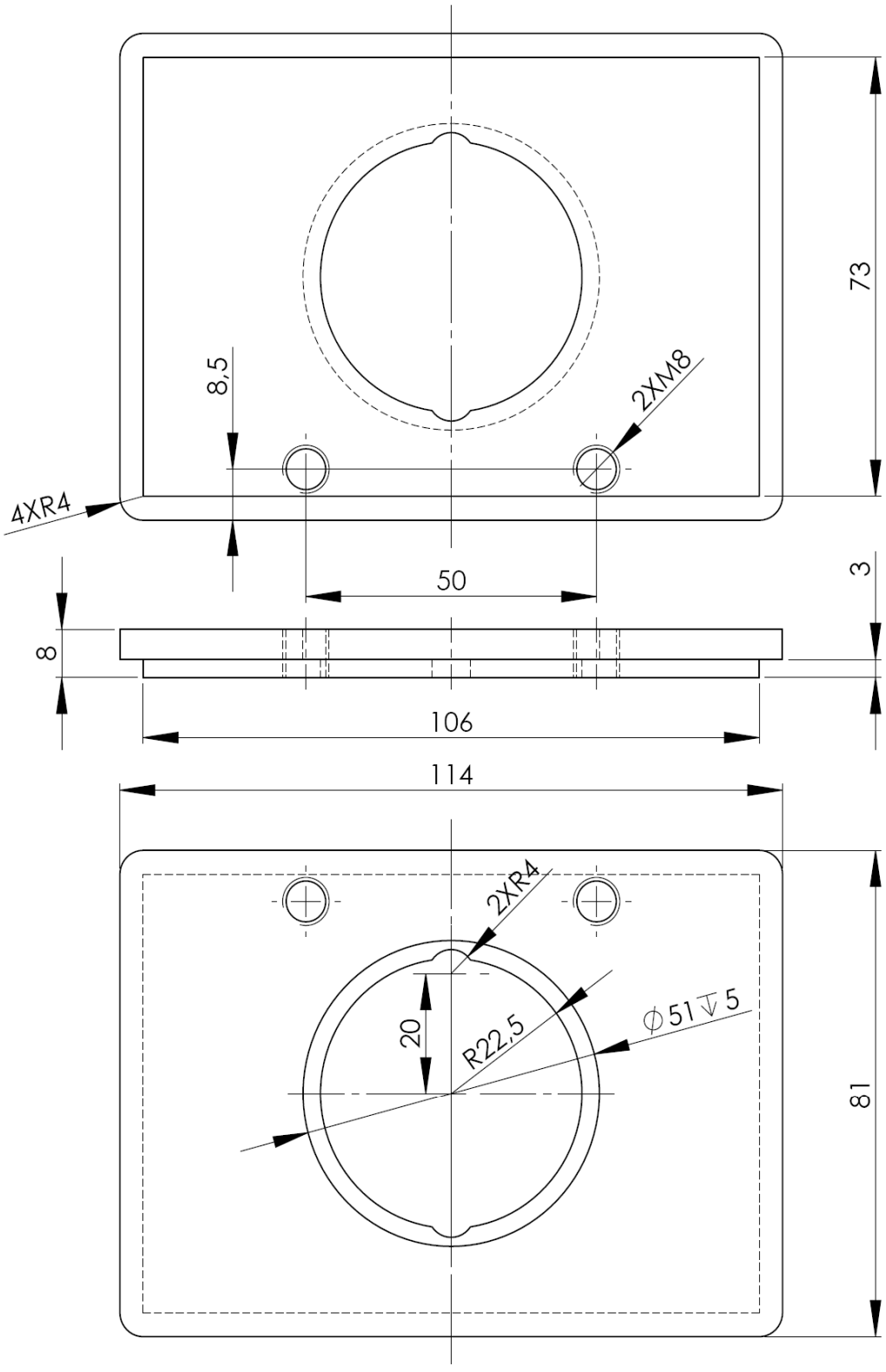

L.Alberty 22/06/10	JIG - FIXTURE SYSTEM LASER WELDING of SMAs	FCT-UNL
1:1 ISO 2768-m	CHAMBER PART5	

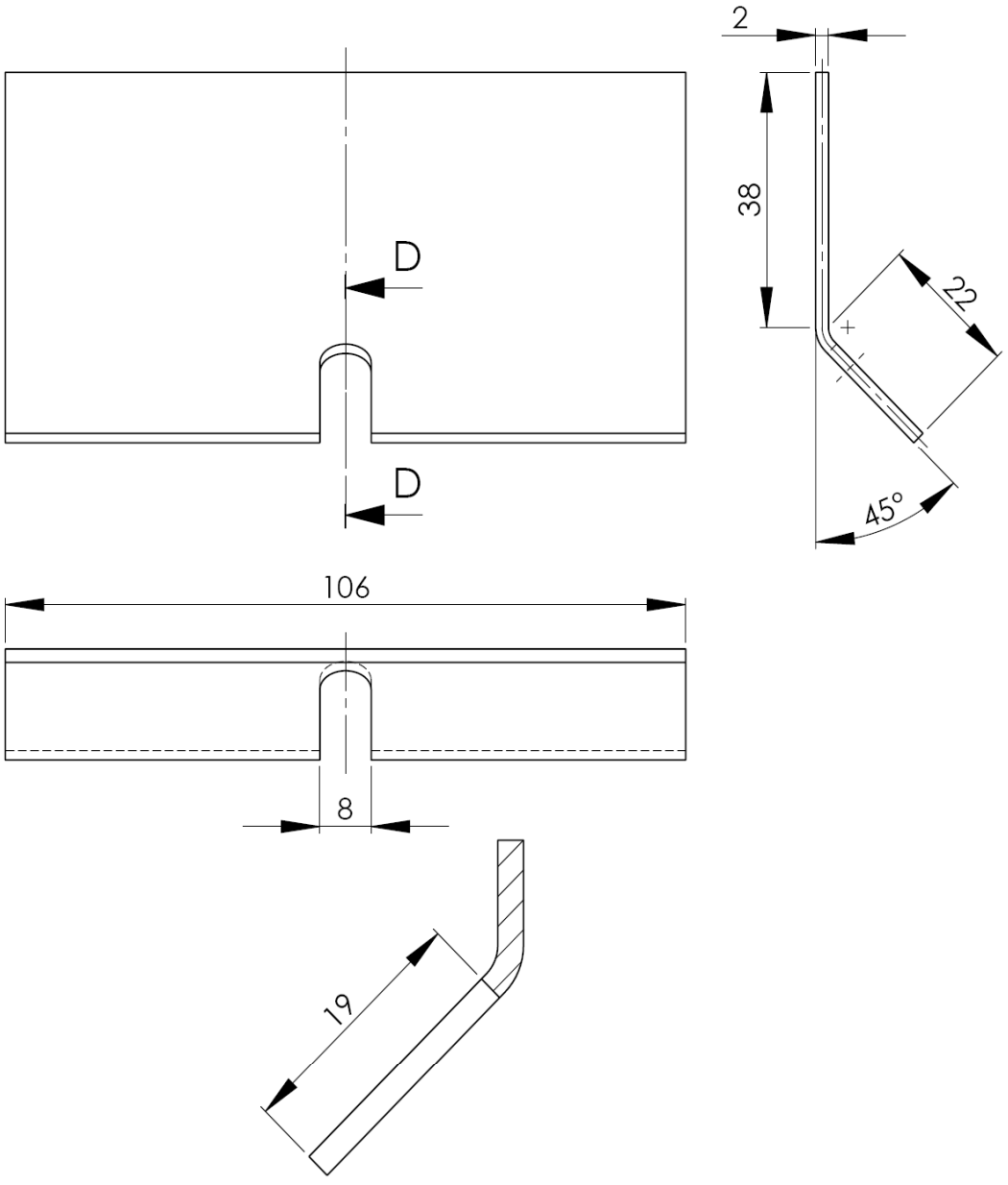

SECTION D-D
SCALE 2 : 1

SLOT END: ∅8

L.Alberty 22/06/10	JIG - FIXTURE SYSTEM LASER WELDING of SMAs	FCT-UNL
1:1 ISO 2768-m	CHAMBER PART6	

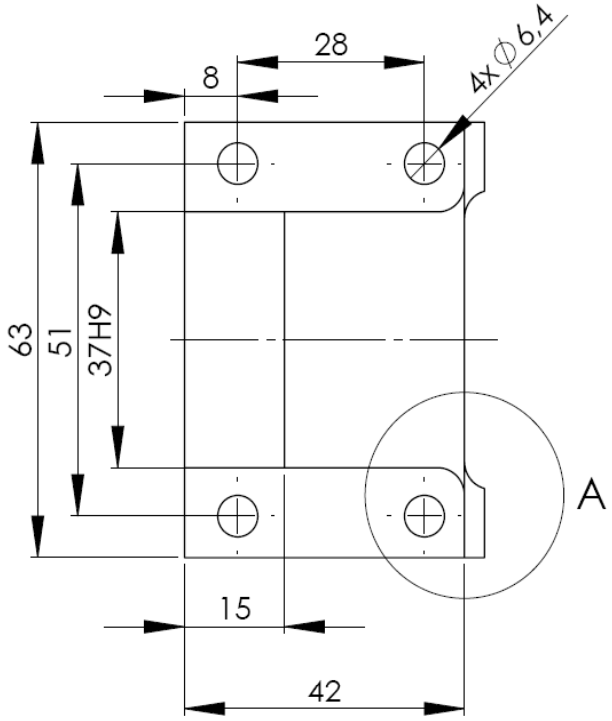

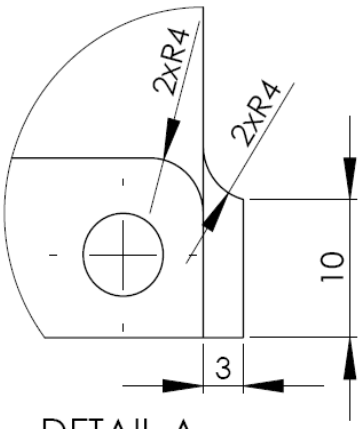

DETAIL A
SCALE 2 : 1

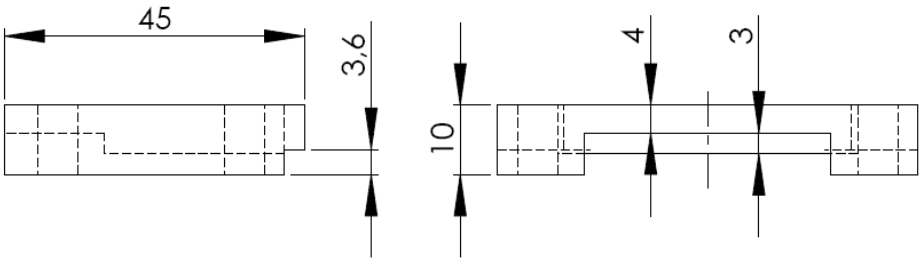

L.Alberty 21/06/10	JIG - FIXTURE SYSTEM LASER WELDING of SMAs	FCT-UNL
1:1 ISO 2768-m	HOLDER	

C – Metallographic procedures

Samples for both optical and electronic microscopy were prepared from transversal sections of welded joints, using an *ATM Brilliant* precision cut-off machine with the following parameters: rotational speed – 3500 rpm, feed rate – 3 mm/min, cooling – abundant cutting fluid. *Buehler's* epoxy cold casting resin was used to mount the specimens, as retaining plastic clips were used to keep the samples in place.

Mounted specimens were then grinded with SiC paper while cooling and lubrication was attained with abundant water, according to the following sequence of grit numbers:

180 / 240 / 400 / 600 / 1200 / 2500

Polishing was carried out using a multi-purpose micro polishing cloth with diamond paste and respective lubricant, according to the following sequence:

6 µm / 1 µm / ¼ µm

Careful optical microscope examination was carried on polished samples, looking for imperfections and rough grinding marks. Good samples were cleaned in an ultrasonic bath of pure ethanol for five minutes, in order to remove any grinding or polishing residues. The polished surfaces were then clean with pure acetone before etching.

According to [**6**] etching was attained using a heavy acid etchant solution with the following volumetric composition: HF 10% + HNO_3 45% + H_2O 45%. The etching procedure is described below:

The specimen was immersed in the etchant for about 10s, in a plastic container.

1. The Etchant solution was removed by flushing the surface with forced water.
2. Water was removed forcing ethyl alcohol on the surface.
3. Gaseous Nitrogen was blown to dry the sample.
4. The previous procedure was repeated until achieved the desired etching level.

Etched samples could be easily prepared for optical observation at any time; the only procedure is using a cotton swab with trichloroethylene to gently wipe the etched surface, removing dust, grass or drying marks left by ethanol. Attention should be paid to cotton fibbers.

Samples for SEM were cleaned in an ultrasonic bath of acetone for 5 min. By blowing nitrogen on the surface, the samples were dried, and after that coated with gold or carbon. Either carbon tape or silver paint were used to establish an electrical connection between the samples and the mounting plate, allowing the sample to discharge.

D – EDM tool and SME testing device – technical drawings

The technical drawings of the EDM tool designed and produced to obtain tensile specimens from welded joints are first presented.

Secondly the technical drawings of the Shape Memory Effect bending and free-recovery tester are presented.

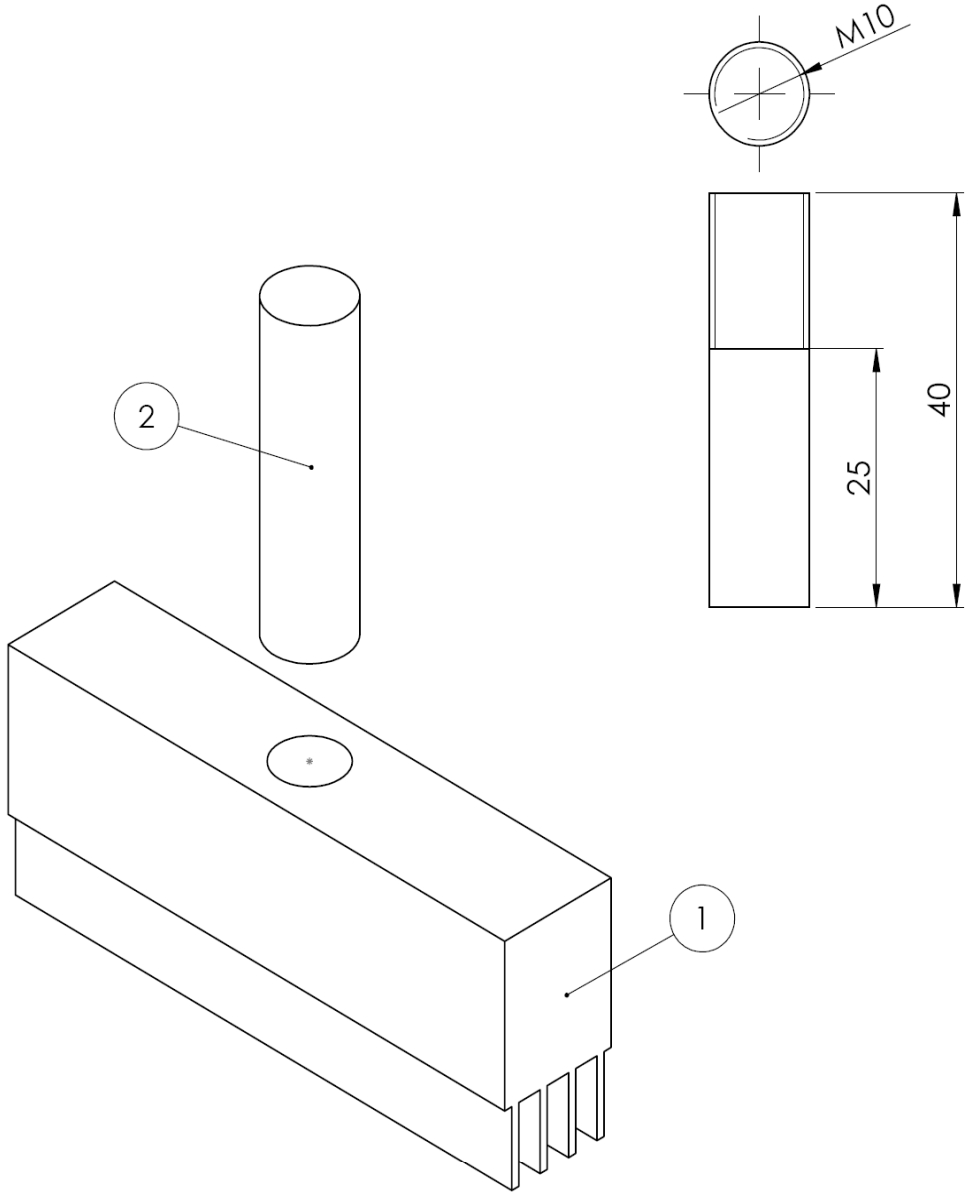

ITEM NO.	PART	MATERIAL	QTY.
1	EDM HEAD	ELECTROLYTIC COPPER	1
2	FIXTURE ROD	COPPER	1

L.Alberty 24/09/10		JIG - FIXTURE SYSTEM LASER WELDING of SMAs	FCT-UNL
	3:2 ISO 2768-m	EDM TOOL	

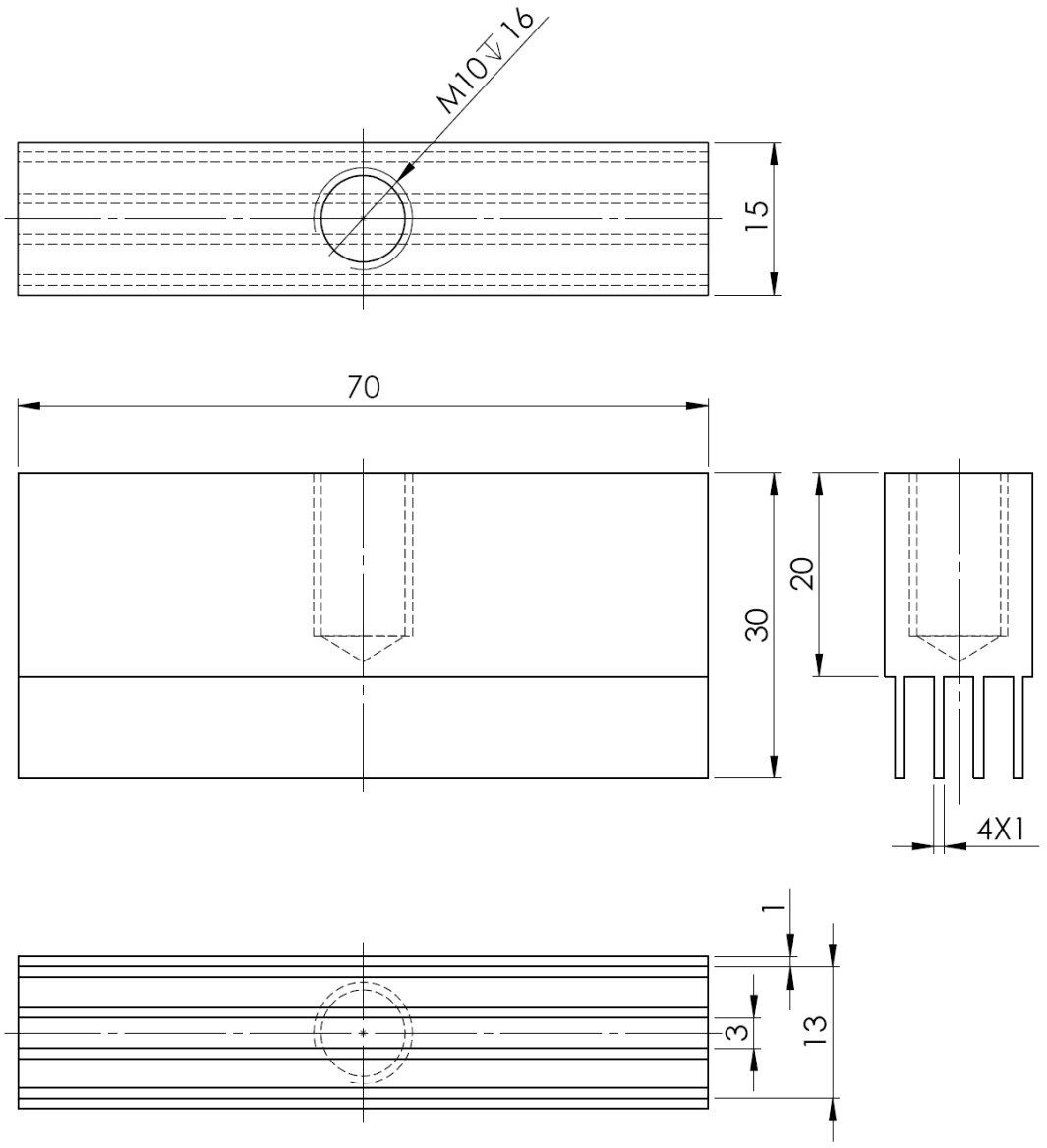

L.Alberty 24/09/10	JIG - FIXTURE SYSTEM LASER WELDING of SMAs	FCT-UNL
3:2 ISO 2768-m	EDM HEAD	

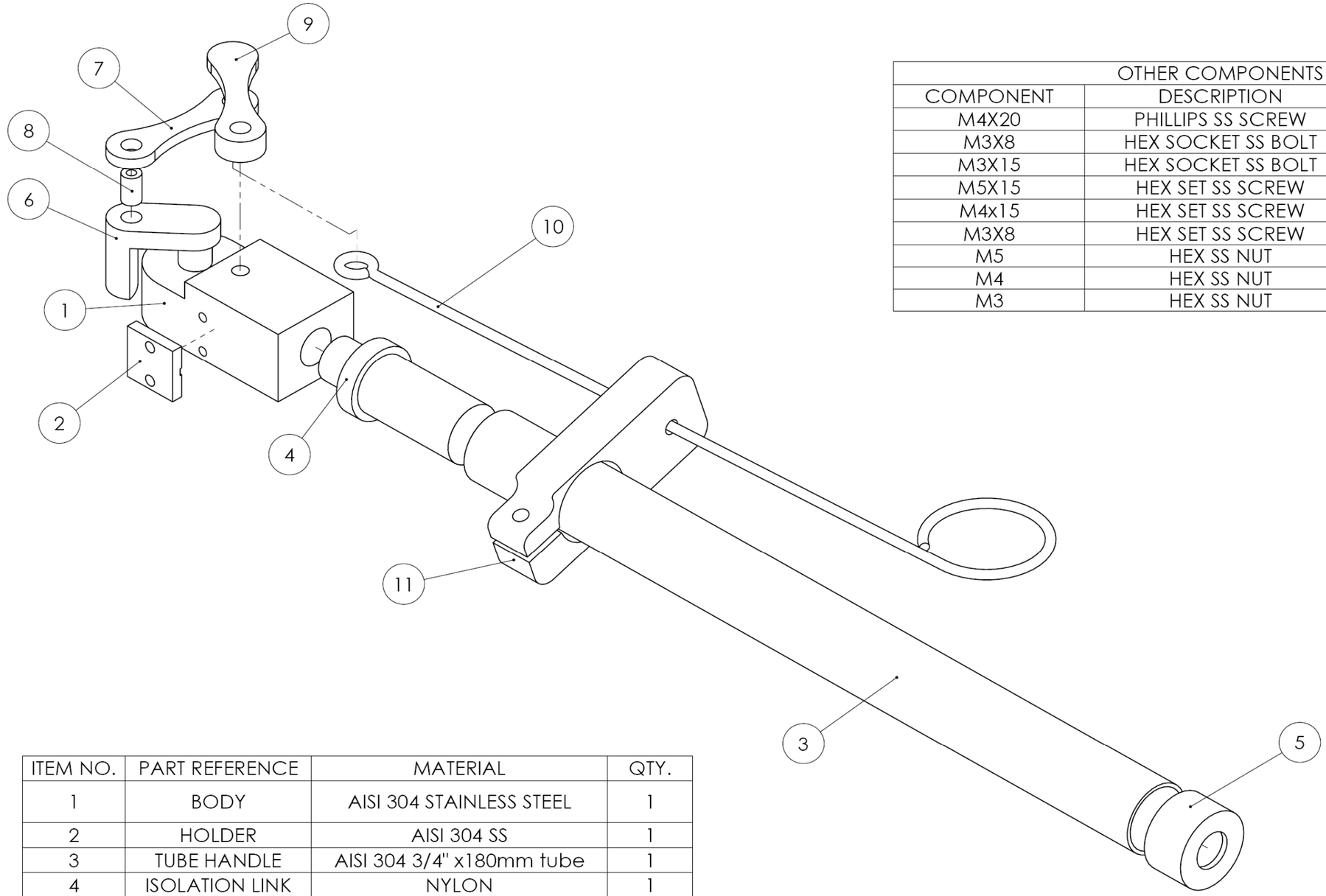

OTHER COMPONENTS		
COMPONENT	DESCRIPTION	QTY
M4X20	PHILLIPS SS SCREW	1
M3X8	HEX SOCKET SS BOLT	2
M3X15	HEX SOCKET SS BOLT	1
M5X15	HEX SET SS SCREW	1
M4x15	HEX SET SS SCREW	1
M3X8	HEX SET SS SCREW	3
M5	HEX SS NUT	1
M4	HEX SS NUT	1
M3	HEX SS NUT	1

ITEM NO.	PART REFERENCE	MATERIAL	QTY.
1	BODY	AISI 304 STAINLESS STEEL	1
2	HOLDER	AISI 304 SS	1
3	TUBE HANDLE	AISI 304 3/4" x180mm tube	1
4	ISOLATION LINK	NYLON	1
5	CAP	RUBBER	1
6	FLYWHEEL	AISI 304 SS	1
7	TIE ROD TYPE 2	AISI 304 SS	1
8	LINK	AISI 304 SS	1
9	TIE ROD TYPE 1	AISI 304 SS	1
10	PULL ROD	AISI 304 SS	1
11	HANDLER	ALUMINIUM 1100	1

L.Alberty 27/09/10		SME BENDING TESTER	FCT-UNL
	1:1	TESTER ASSEMBLY	

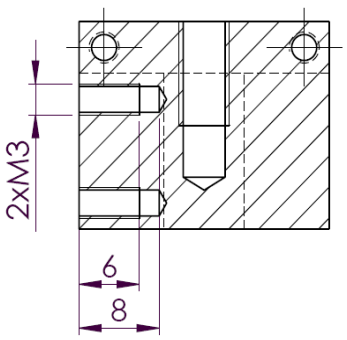

SECTION C-C
SCALE 3 : 2

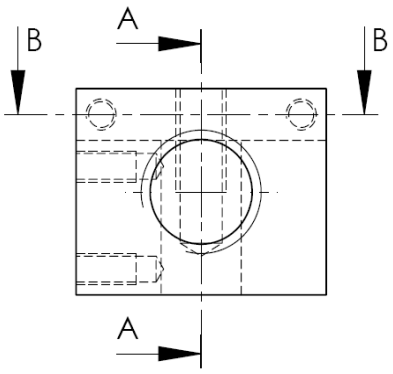

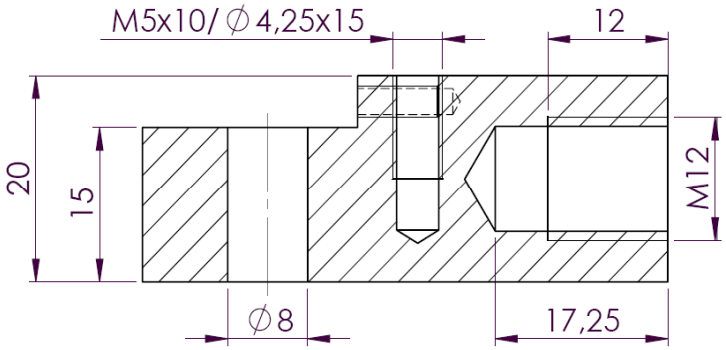

SECTION A-A
SCALE 3 : 2

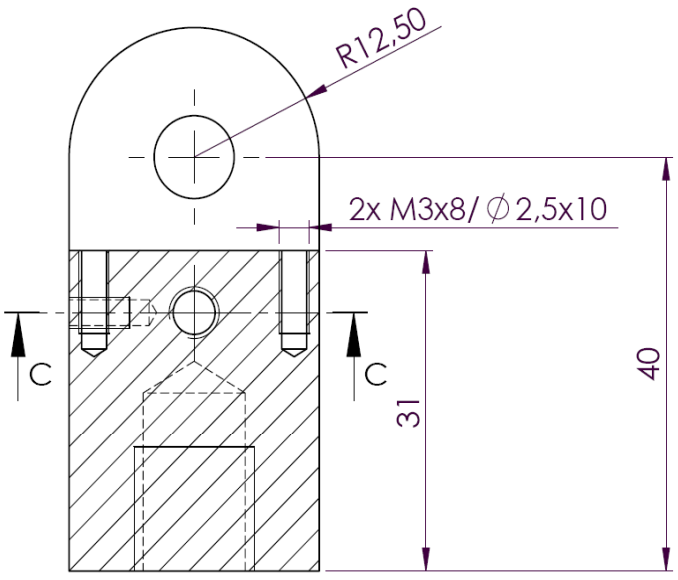

SECTION B-B
SCALE 3 : 2

L.Alberty 27/09/10	SME BENDING TESTER	FCT-UNL
3:2 ISO 2768-m	BODY	

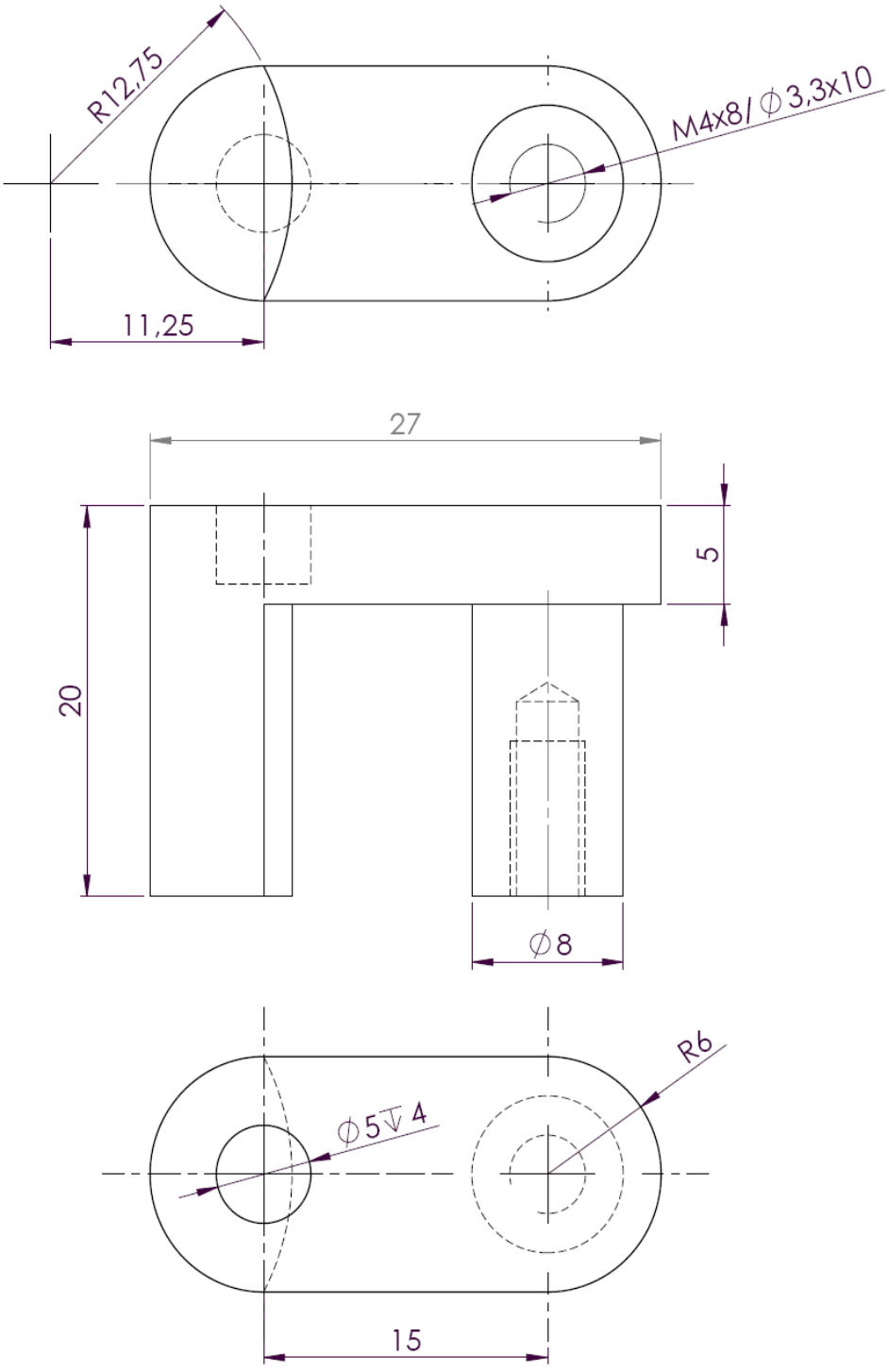

L.Alberty 27/09/10		SME BENDING TESTER	FCT-UNL
	1:1 ISO 2768-m	FLYWHEEL	

SECTION A-A
SCALE 2 : 1

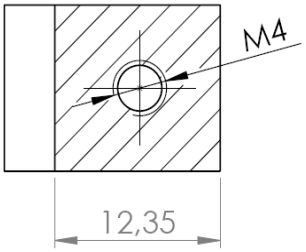

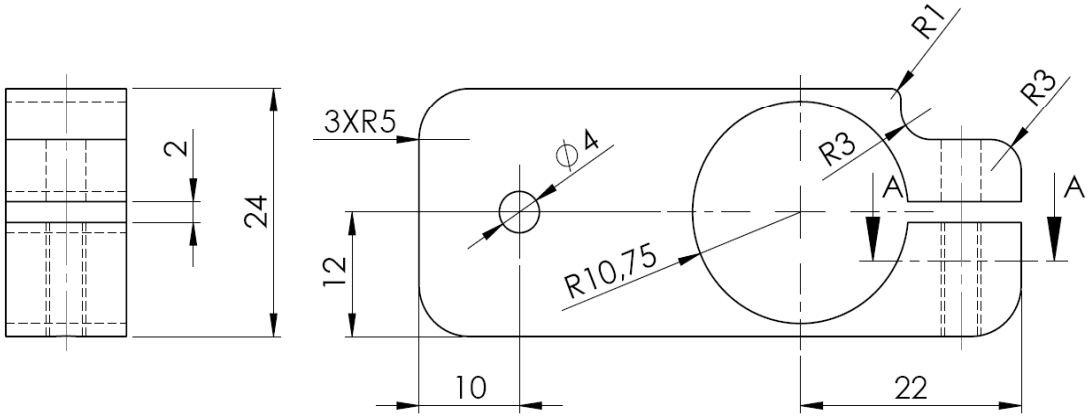

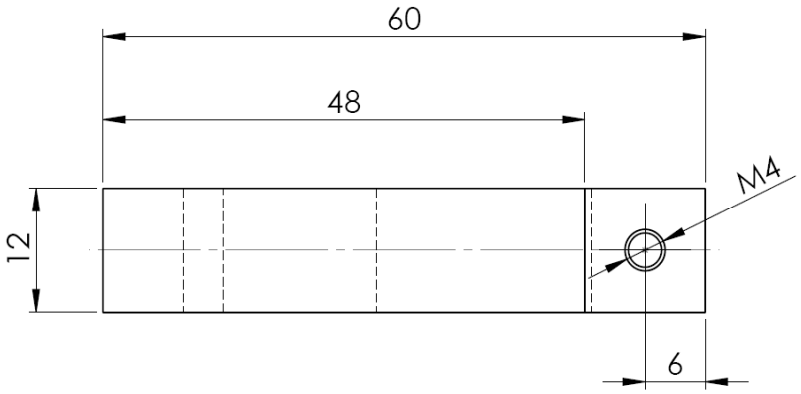

L.Alberty 27/09/10		SME BENDING TESTER	FCT-UNL
	3:2	HANDLER	
	ISO 2768-m		

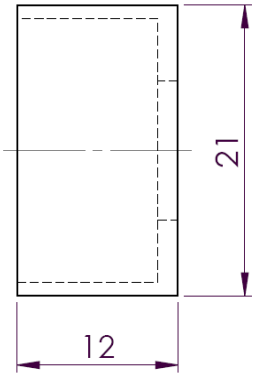

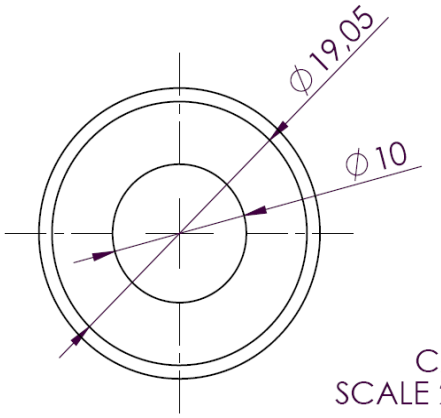

CAP
SCALE 2:1

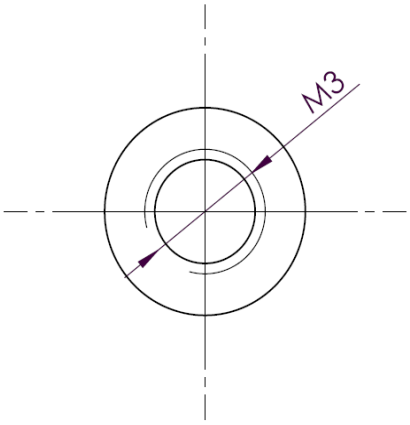

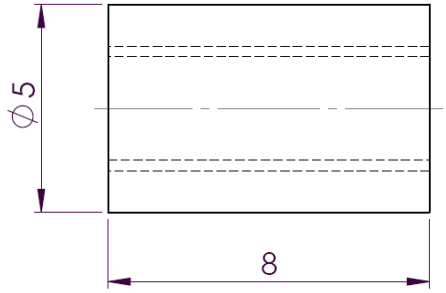

LINK
SCALE 6:1

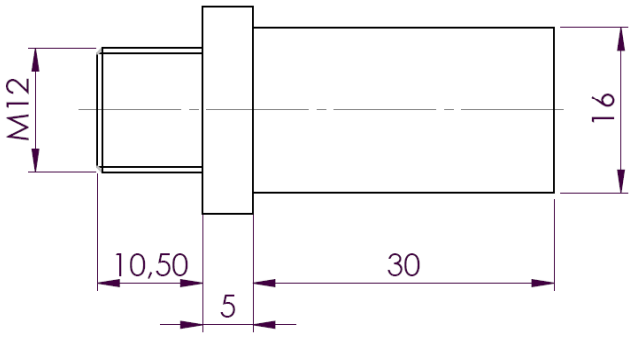

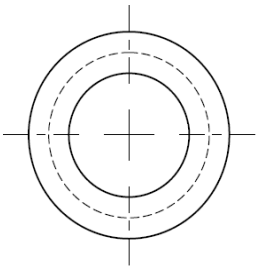

ISULATOR LINK
SCALE 3:2

L.Alberty 27/09/10	SME BENDING TESTER	FCT-UNL
ISO 2768-m	PARTS	

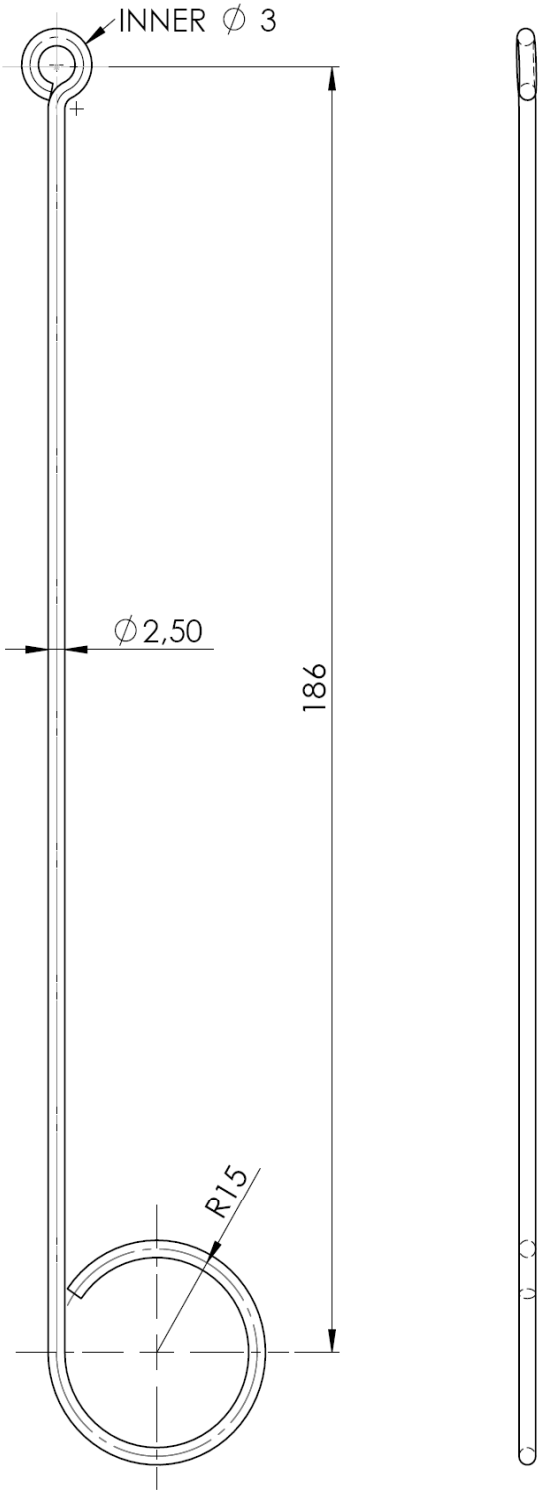

L.Alberty	27/09/10		SME BENDING TESTER	FCT-UNL
		1:1 ISO 2768-m	PULL ROD	

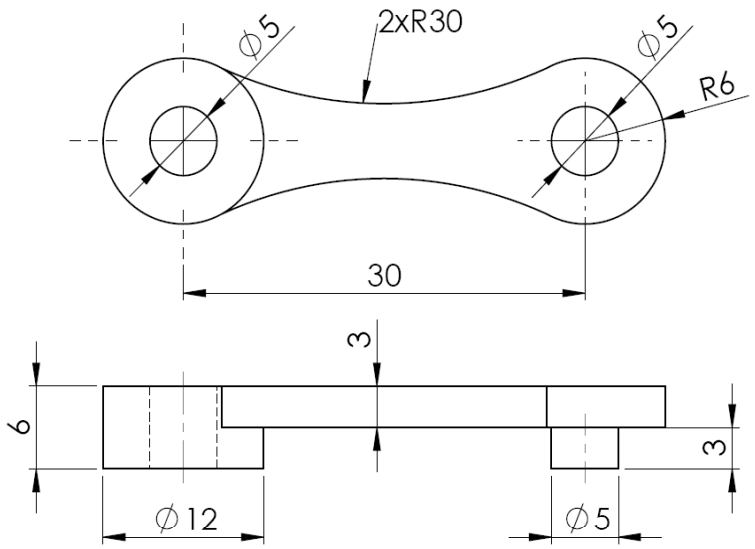

Type 1

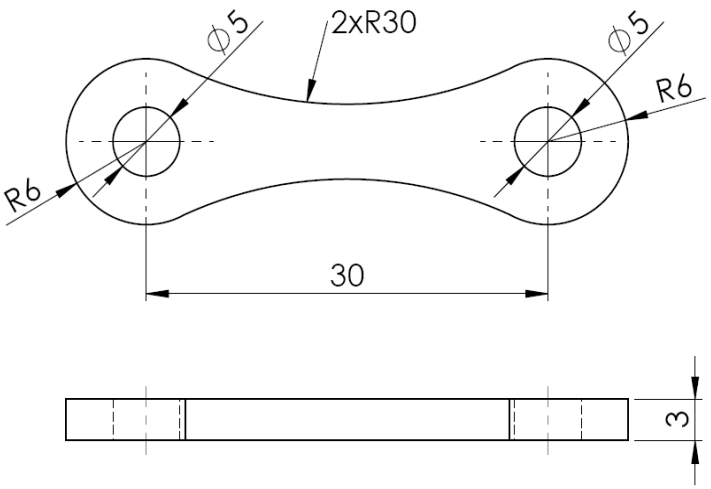

Type 2

L.Alberty	27/09/10		SME BENDING TESTER	FCT-UNL
		2:1	TIE RODS	
		ISO 2768-m		

E – Measurements for the weld bead geometry study

The width of both face and root of welded specimens for parameters evaluation was measured by means of optical microscopy combined with measuring software. Both the 0.5 and 1.0 thick butt welds were evaluated. Three measurements were performed in each side of welded specimens along the weld beads and results are presented (in millimeters) in table 1. The mean value and the square deviation were obtained from experimental results (as can be seen in table 1).

Reference		Face			Root			Face mean	σ_{face}	root mean	σ_{back}
		1st	2nd	3rd	1st	2nd	3rd				
1.0mm	A-A	2.029	2.015	2.037	0.55	0.491	0.387	2.027	0.0002	0.476	0.0136
	B-B	2.371	2.371	2.371	0.623	0.466	0.494	2.371	0.0000	0.527	0.0140
	C-C	2.924	2.871	2.823	0.825	0.631	0.696	2.872	0.0051	0.717	0.0195
	D-D	2.565	2.560	2.554	1.246	1.131	1.086	2.559	6.0666	1.154	0.0136
	E-E	2.983	3.025	3.048	1.440	1.426	1.414	3.018	0.0021	1.426	0.0003
	F-F	2.242	2.183	2.186	1.052	0.946	0.943	2.203	0.0022	0.980	0.0077
	G-G	2.484	2.467	2.506	1.187	1.254	1.28	2.485	0.0007	1.240	0.0046
	H-H	2.604	2.517	2.500	1.434	1.184	1.148	2.540	0.0062	1.255	0.0485
	I-I	2.882	3.098	3.098	1.499	1.308	1.283	3.026	0.0311	1.363	0.0279
0.5 mm	F-F	1.333	1.422	1.441	0.767	0.818	0.718	1.398	0.0066	0.767	0.0050
	G-G	1.000	1.267	1.293	0.544	0.405	0.486	1.000	0.0027	0.478	0.0097
	H-H	1.129	1.121	1.100	0.128	0.151	0.122	1.116	0.0004	0.133	0.0004
	I-I	1.716	1.932	1.743	1.587	1.097	1.304	1.797	0.0277	1.329	0.1210
	K-K	1.362	1.383	1.417	0.803	0.872	0.878	1.387	0.0015	0.851	0.0034
	L-L	1.726	1.680	1.650	1.083	1.068	1.126	1.685	0.0029	1.092	0.0018
	M-M	1.369	1.361	1.427	0.886	0.898	0.954	1.385	0.0025	0.912	0.0026
	N-N	1.279	1.284	1.248	0.728	0.633	0.73	1.270	0.0007	0.697	0.0061
	O-O	1.139	1.143	1.143	0.558	0.52	0.577	1.141	1.0666	0.551	0.0016

Annex E Table 1 measured face and root width values for weld bead geometry study – dimensions in millimeters

F – Programs

A routine was programmed in *MATLAB* to analyze the accumulation of inelastic strain over successive cycles, from long tensile cycling data files. The programming code is presented below.

```
clear all;
name=input('Which is the file containing the data?');
l=input('Which is, in mm, the initial length?');
Data=load(name); carga=Data(:,2);
carga2=carga*1000; carga3=round(carga2); % Load in N
deformacao=Dados(:,3); j=size(carga3);
k=1; m=0;
permdef(1,k)=0;
for i=1:1:j-1
    if  m >= carga3(i,1)
        continue
    end
    if  (carga3(i,1)*carga3(i+1,1))<=0
        k=k+1;
    end
    if  (carga3(i,1)*carga3(i+1,1))<=0
        permdef(1,k)=deformacao(i,1);
    end
    if  (carga3(i,1)*carga3(i+1,1))<=0
        m=200;
        m=0;
    end
end
x=0;
for n=2:1:30
    x=x+1;
    incredef(1,x)=permdef(1,n)-permdef(1,n-1);
end
strain_inc=incredef/l*100; permstrain=permdef/l*100;
strain=deformacao/l*100;
```

G – Micrographs of welded joints for parameters evaluation

Complementary micrographs of welded joints for parameters evaluation are now presented in figures 1 to 8.

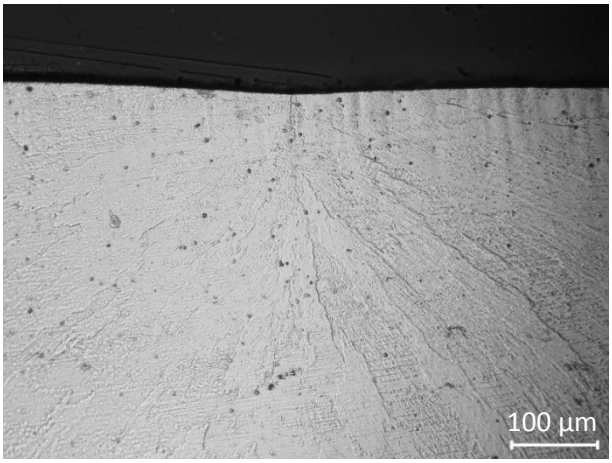

Annex G Figure 1 Micrograph of A-A 1.0 mm thick similar joint showing the weld bead centre

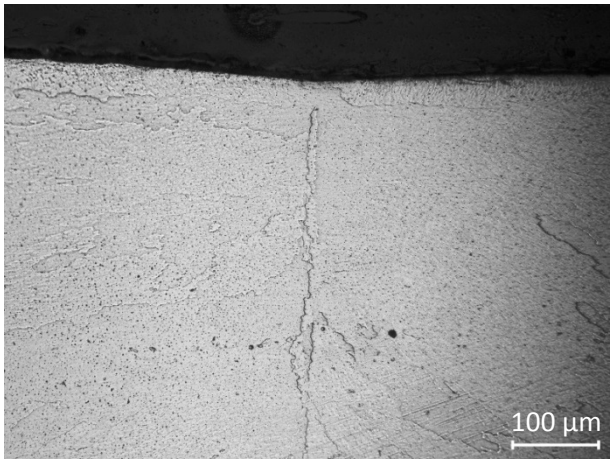

Annex G Figure 2 Micrograph of C-C 1.0 mm thick similar joint showing the weld bead centre

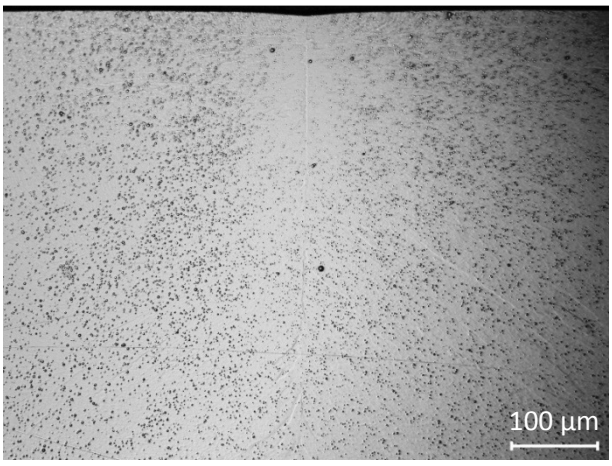

Annex G Figure 3 Micrograph of F-F 1.0 mm thick similar joint showing the weld bead centre

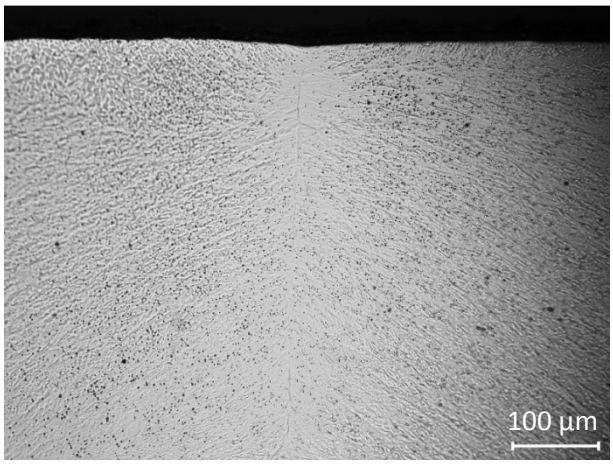

Annex G Figure 4 Micrograph of H-H 1.0 mm thick similar joint showing the weld bead centre

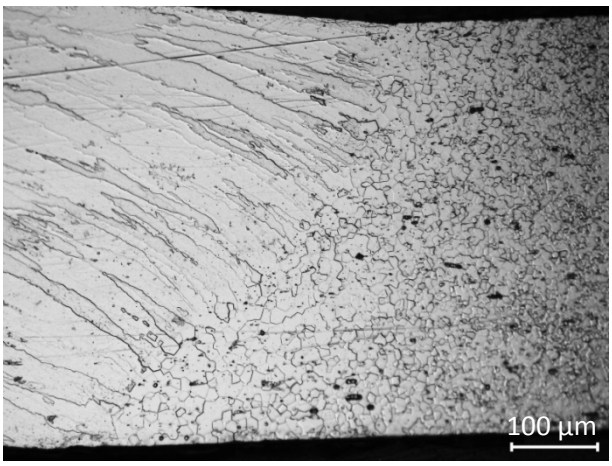

Annex G Figure 5 Micrograph of F-F 0.5 mm thick similar joint showing the transition zone

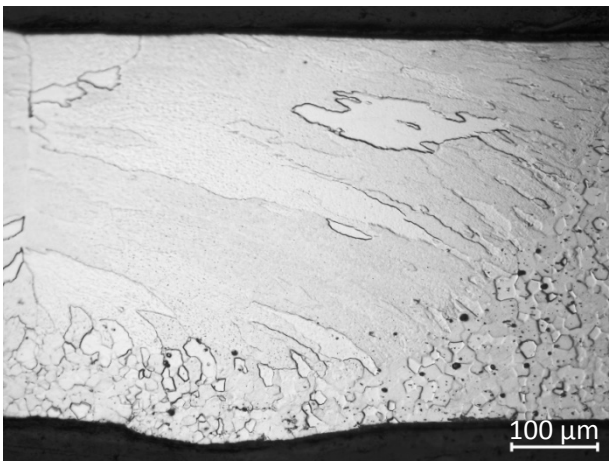

Annex G Figure 6 Micrograph of G-G 0.5 mm thick similar joint showing the transition zone

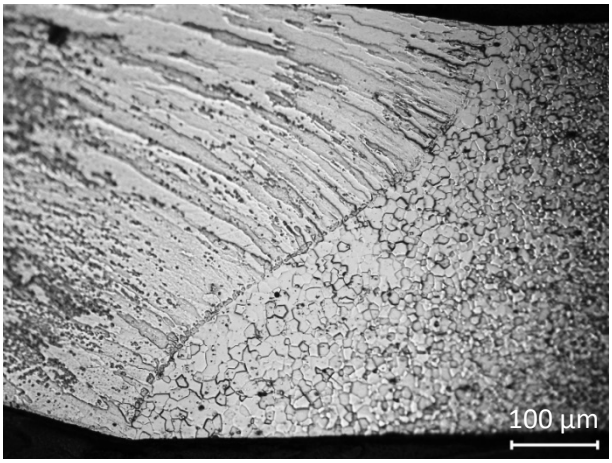

Annex G Figure 7 Micrograph of N-N 0.5 mm thick similar joint showing the transition zone

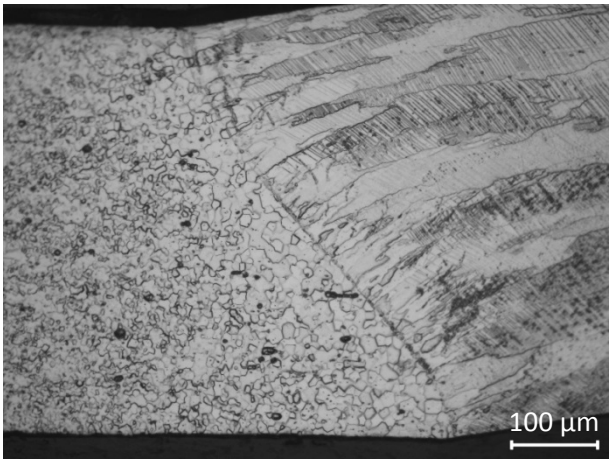

Annex G Figure 8 Micrograph of O-O 0.5 mm thick similar joint showing the transition zone

H – Tensile testing plots from welded joints for parameters evaluation

Complementary tensile testing plots are now presented in figures 1 to 10. Results from these tests were used to conclude about process parameters and tensile strength.

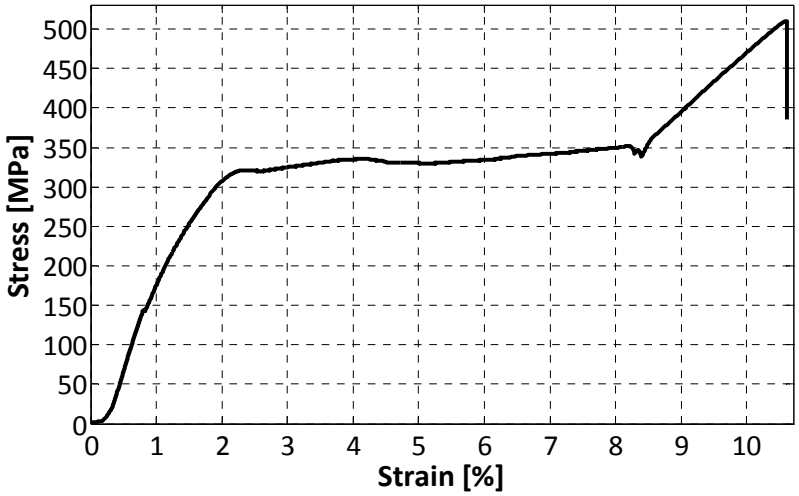

Annex H Figure 1 Tensile test result of the 1.0 mm thick B – B # 2 specimen

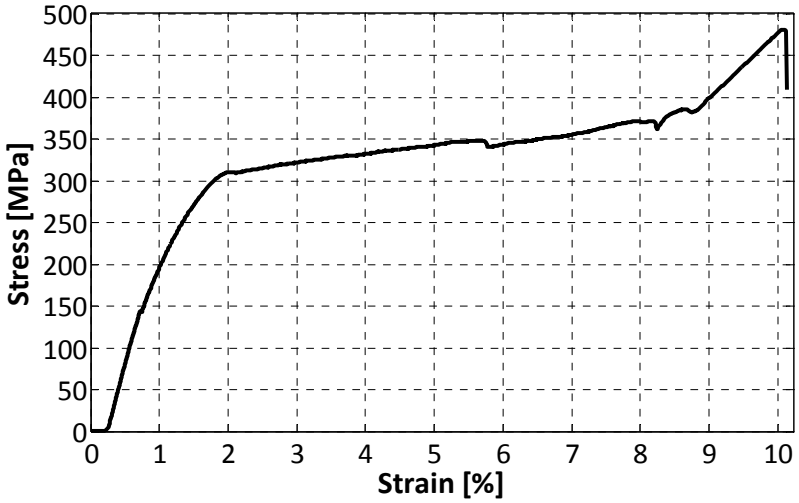

Annex H Figure 2 Tensile test result of the 1.0 mm thick D – D # 1 specimen

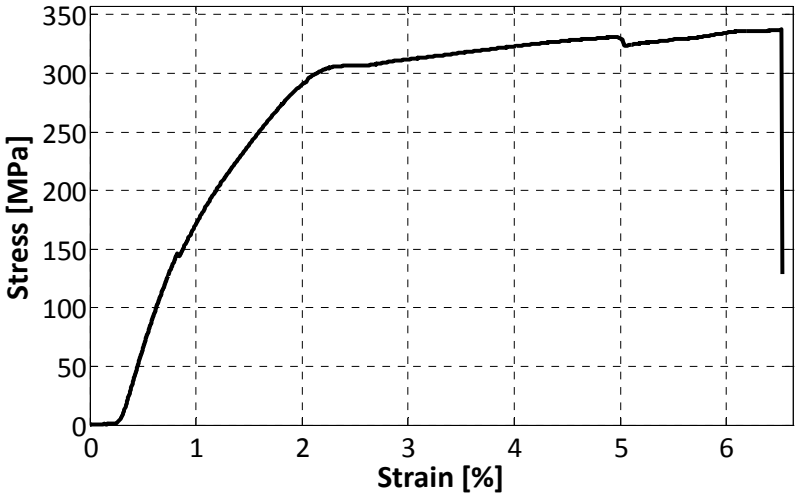

Annex H Figure 3 Tensile test result of the 1.0 mm thick E – E # 1 specimen

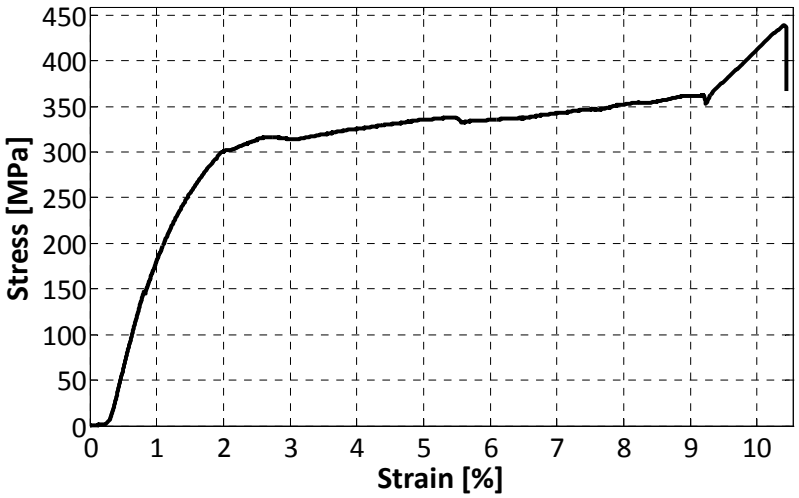

Annex H Figure 4 Tensile test result of the 1.0 mm thick G – G # 1 specimen

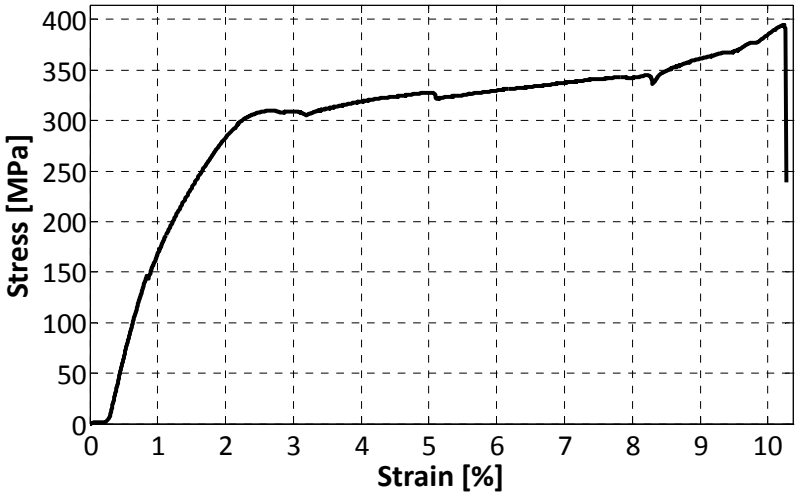

Annex H Figure 5 Tensile test result of the 1.0 mm thick I – I # 2 specimen

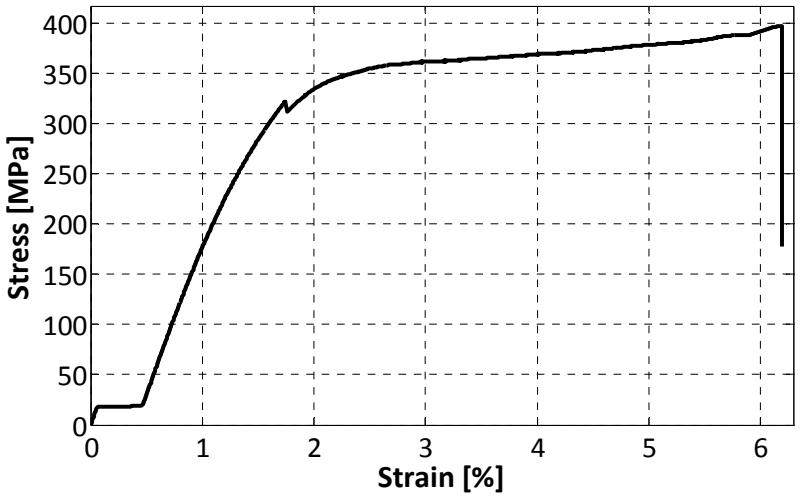

Annex H Figure 6 Tensile test result of the 0.5 mm thick H – H # 2 specimen

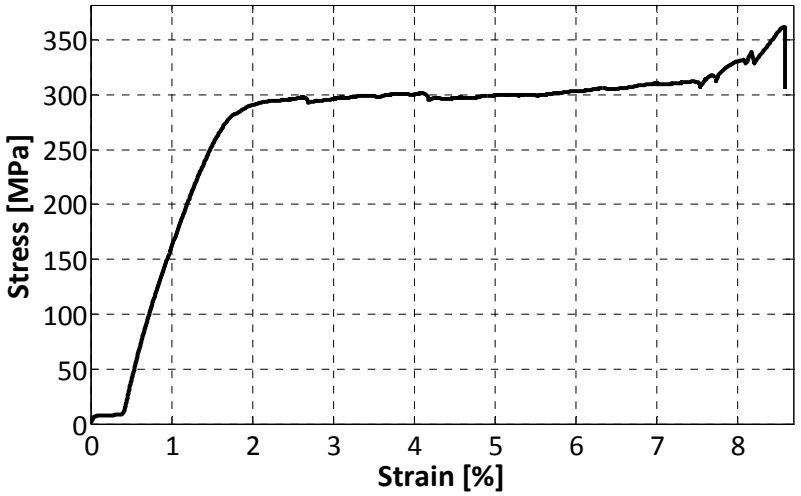

Annex H Figure 7 Tensile test result of the 0.5 mm thick I – I # 1 specimen

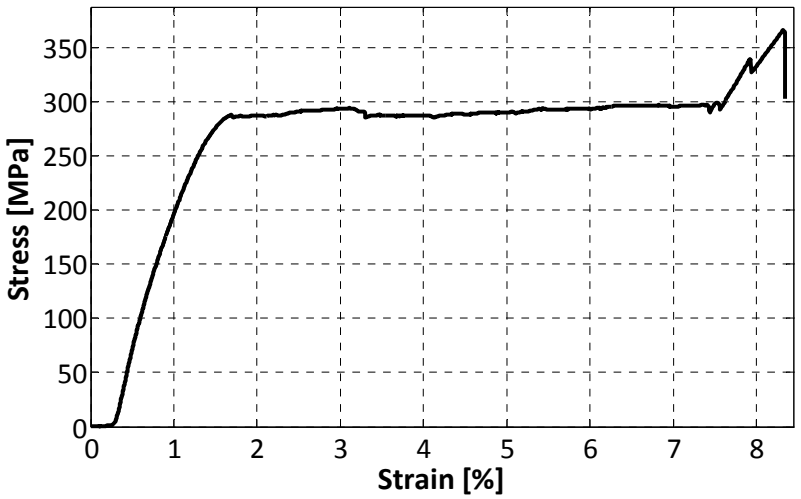

Annex H Figure 8 Tensile test result of the 0.5 mm thick K – K # 2 specimen

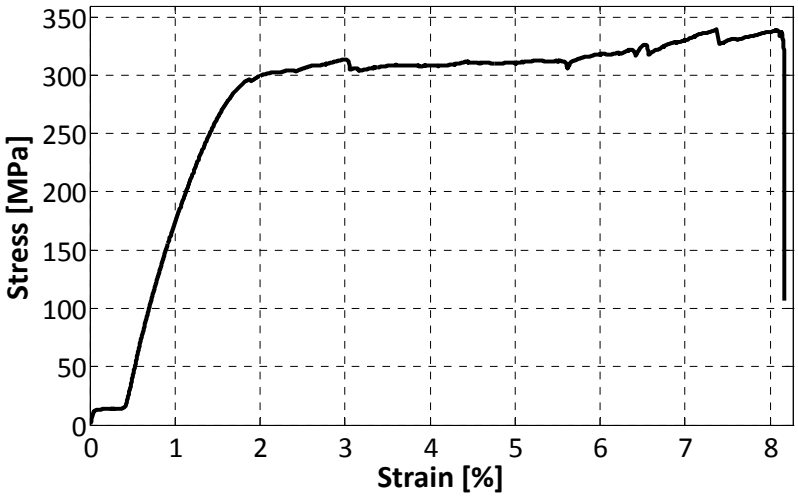

Annex H Figure 9 Tensile test result of the 0.5 mm thick L – L # 1 specimen

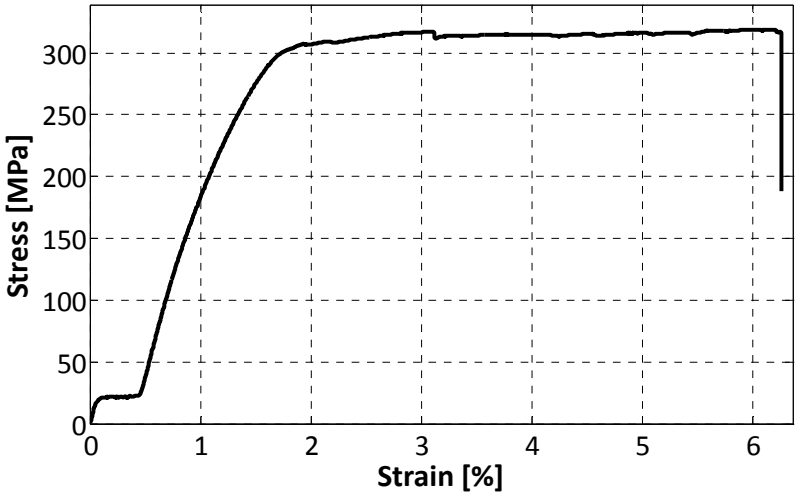

Annex H Figure 10 Tensile test result of the 0.5 mm thick M – M # 1 specimen

I – Optical observations from the preliminary study in pulsed mode

Complementary optical observations carried on both NiTi and Ti-6Al-4V are now presented. NiTi autogenous welds are presented in figures 1 to 17. Ti-6Al-4V preliminary welds are shown in figures 18 to 21.

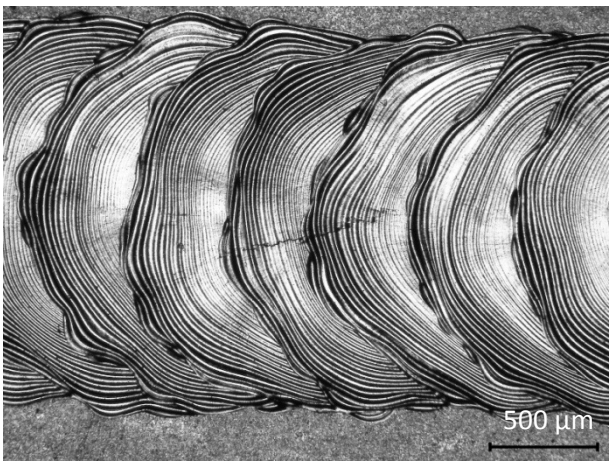

Annex I Figure 1 NiTi pulsed mode weld - 1st series - bead on plate # 3 – top observation

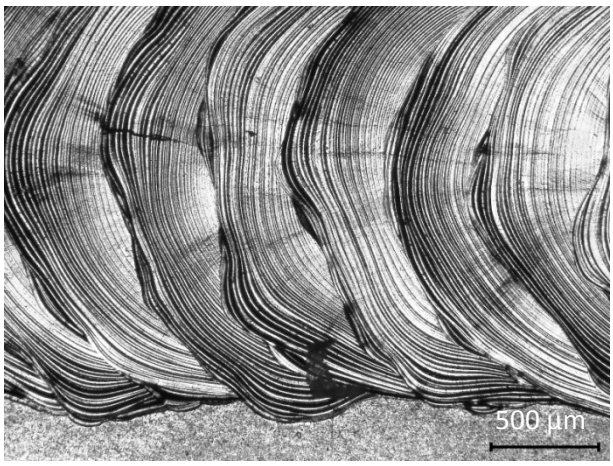

Annex I Figure 2 NiTi pulsed mode weld - 1st series - bead on plate # 4 – top observation

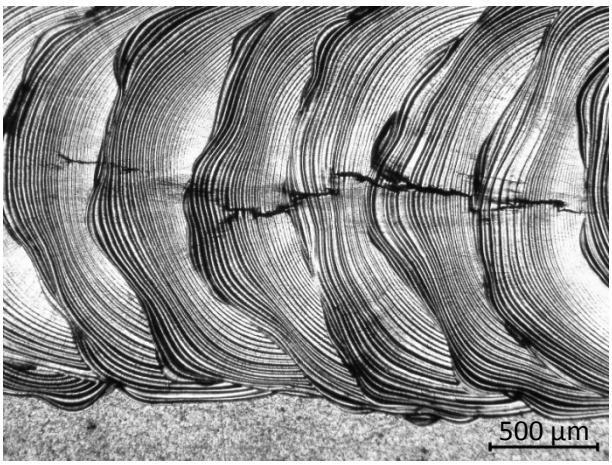

Annex I Figure 3 NiTi pulsed mode weld - 1st series - bead on plate # 7 – top observation

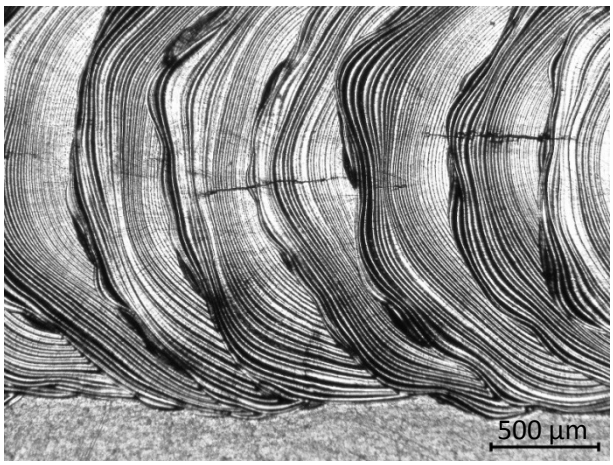

Annex I Figure 4 NiTi pulsed mode weld - 1st series - bead on plate # 8 – top observation

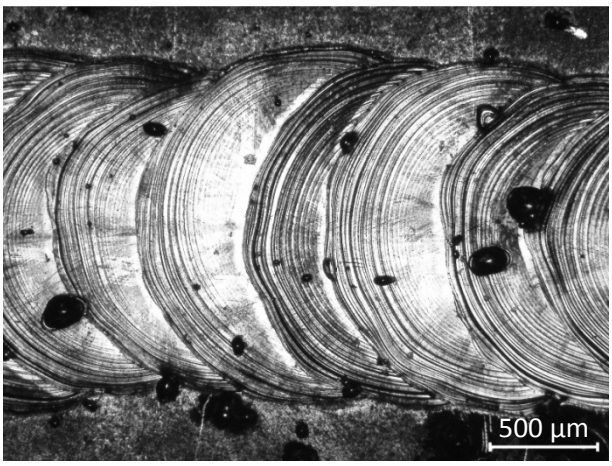

Annex I Figure 5 NiTi pulsed mode weld - 1st series - bead on plate # 4 – back observation

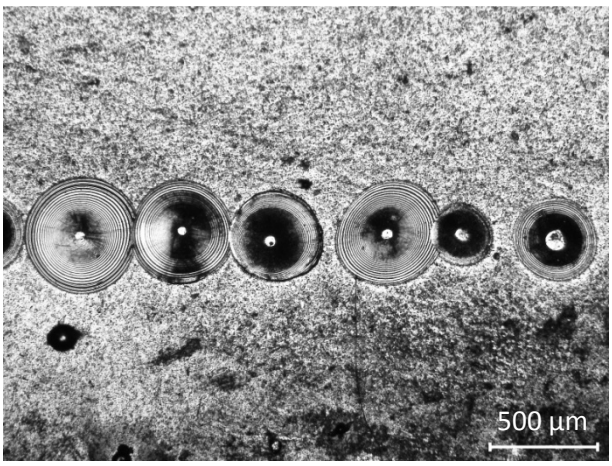

Annex I Figure 6 NiTi pulsed mode weld - 1st series - bead on plate # 7 – back observation

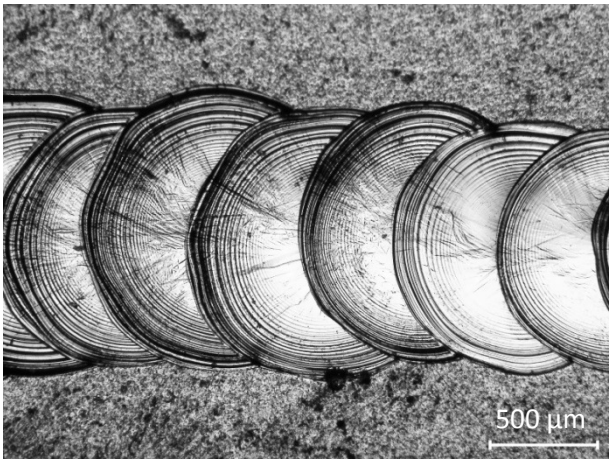

Annex I Figure 7 NiTi pulsed mode weld - 1st series - bead on plate # 8 – back observation

Annex I Figure 8 NiTi pulsed mode weld - 2nd series - bead on plate # 2 – top observation

Annex I Figure 9 NiTi pulsed mode weld - 2nd series - bead on plate # 3 – top observation

Annex I Figure 10 NiTi pulsed mode weld - 2nd series - bead on plate # 4 – top observation

Annex I Figure 11 NiTi pulsed mode weld - 2nd series - bead on plate # 5 – top observation

Annex I Figure 12 NiTi pulsed mode weld - 2nd series - bead on plate # 7 – top observation

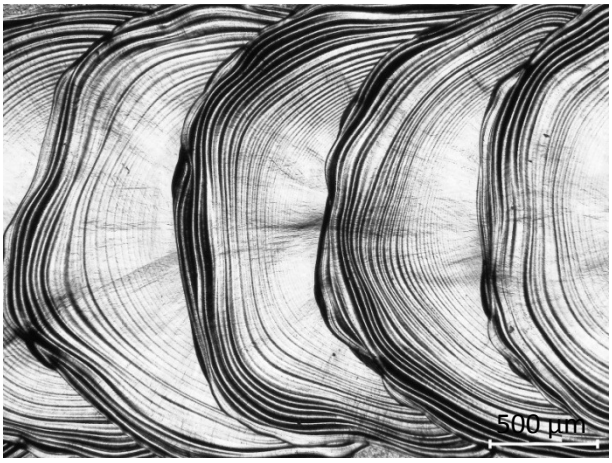

Annex I Figure 13 NiTi pulsed mode weld - 3rd series - bead on plate # 2 – top observation

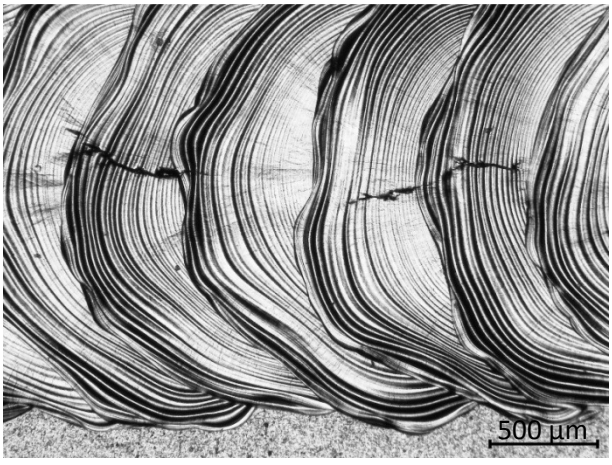

Annex I Figure 14 NiTi pulsed mode weld - 3rd series - bead on plate # 4 – top observation

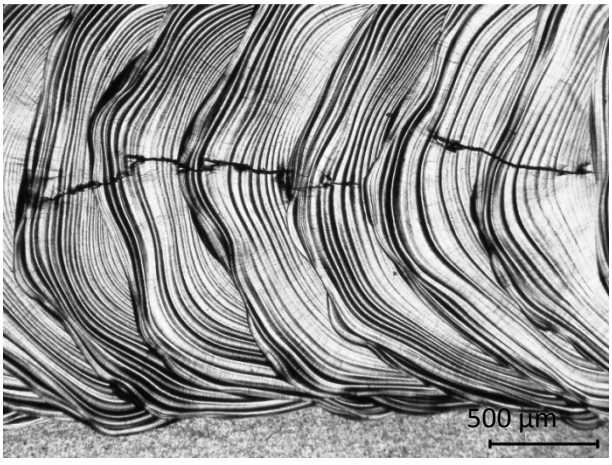

Annex I Figure 15 NiTi pulsed mode weld - 3rd series - bead on plate # 5 – top observation

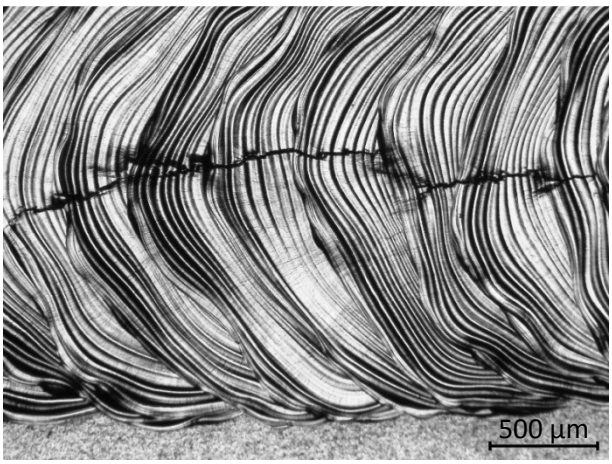

Annex I Figure 16 NiTi pulsed mode weld - 3rd series - bead on plate # 6 – top observation

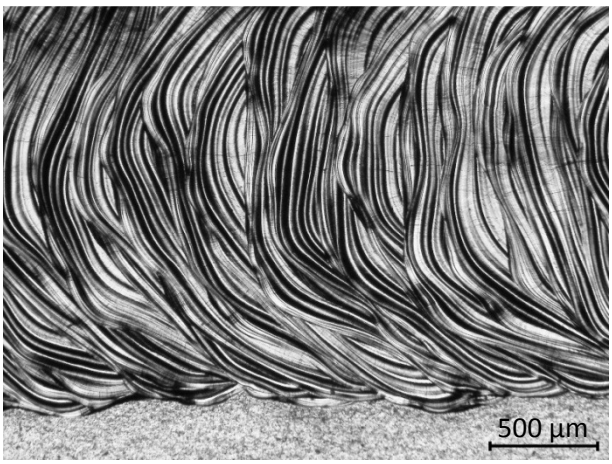

Annex I Figure 17 NiTi pulsed mode weld - 3rd series - bead on plate # 8 – top observation

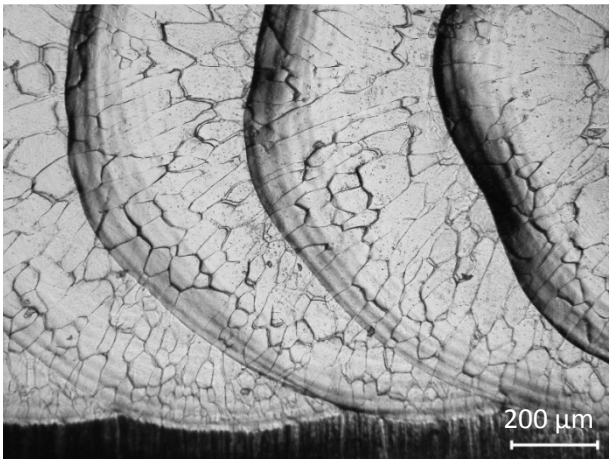

Annex I Figure 18 Optical observation of the Ti-6Al-4V bead on plate weld #1 showing top face

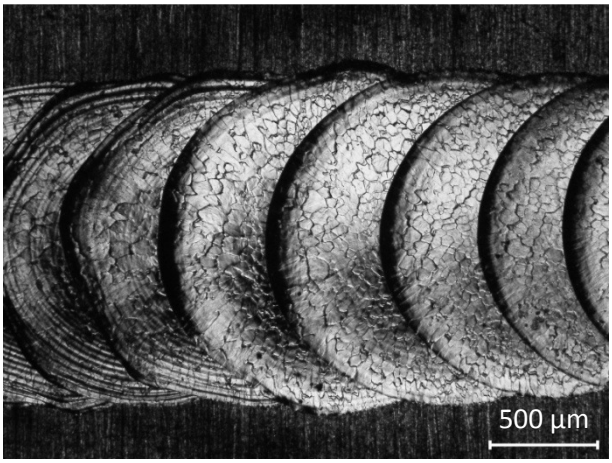

Annex I Figure 19 Optical observation of the Ti-6Al-4V bead on plate weld #2 showing top face

Annex I Figure 20 Optical observation of the Ti-6Al-4V bead on plate weld #2 showing top face

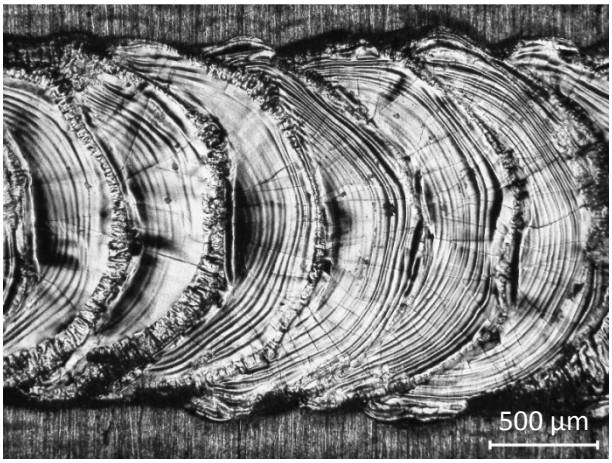

Annex I Figure 21 Optical observation of the Ti-6Al-4V bead on plate weld #8 showing top face